ELECTRONIC TRANSPORT PROPERTIES OF THERMOELECTRIC MATERIALS WITH A FOCUS ON CLATHRATE COMPOUNDS

Dissertation

zur Erlangung des akademischen Grades

doctor rerum naturalium (Dr. rer. nat.)

im Fach: Physik

Spezialisierung: Theoretische Physik

eingereicht an der

Mathematisch-Naturwissenschaftlichen Fakultät

der Humboldt-Universtität zu Berlin

von

M.Sc. Maria Troppenz

Präsidentin der Humboldt-Universität zu Berlin

Prof. Dr. Sabine Kunst

Dekan der Mathematisch-Naturwissenschaftlichen Fakultät

Prof. Dr. Elmar Kulke

GutachterInnen:	1. Prof. Dr. Dr. h.c. Claudia Draxl
	2. Prof. Dr. Jorge O. Sofo
	3. Prof. Dr. Sabine Klapp
Tag der mündlichen Prüfung:	30.07.2021

SUMMARY

Thermoelectric devices provide the possibility to generate electricity from waste heat, that is produced in large amounts in all kinds of energy-conversion processes. Their efficiency compared to other energy resources is, however, rather low. To make them profitable, materials with a high thermoelectric figure of merit, ZT, need to be discovered. ZT is determined by the electronic and thermal transport properties. In the context of this thesis, we study the electronic transport properties of two emerging thermoelectric materials, the two-dimensional material SnSe and a complex type-I clathrate alloy. Their reliable description requires different methodology, that has been implemented or developed during this PhD project.

For SnSe, the origin of its unprecedented high ZT for a wide temperature range was thus far puzzling. We study the temperature dependence of the conductivity and the Seebeck coefficient of its low-temperature phase using the Boltzmann transport (BT) approach in the relaxation time approximation (RTA). We show that only by simultaneously accounting for thermal lattice expansion and electron-phonon coupling, good agreement with experiment is reached for both, Na-doped and undoped SnSe. In preparation of this work, the BT approach has been implemented and demonstrated on Bi_2Te_3.

Type-I clathrates are inclusion compounds that have an enormous compositional space, thus offering a good playground to tailor their properties towards a high thermoelectric performance. For $Ba_8Al_xSi_{46-x}$, besides the composition, the properties are also affected by the configuration, *i.e.*, the arrangement of Al atoms in the host lattice Al_xSi_{46-x}. At the charge-compensated composition $x = 16$, the ground-state configuration is found to be a semiconductor, while configurations with energies only a few meV/atom above the ground state are metallic. We obtain a realistic description of the electronic, structural, and transport properties of $Ba_8Al_xSi_{46-x}$ at finite-temperature by performing configurational averages, using Metropolis Monte-Carlo and Wang-Landau samplings, combined with the cluster expansion method. From a newly developed method to compute the finite-temperature effective band structure of alloys, we observe a temperature-driven closing of the band gap for $x = 16$. This is concomitant with a partial order-disorder phase transition, whose macroscopic transition temperature is found at $582\,\mathrm{K}$. Such a phase transition can have a dramatic impact on the thermoelectric efficiency, for which semiconducting behavior is favorable. The closing of a band gap below the Fermi energy originating from a partial order-disorder phase transition is also observed for n-doped clathrates. For the example of $x = 15$, the electronic transport coefficients are calculated by the BT approach in the constant RTA. Again, performing a configurational average of them, we find that they agree well with experiment.

We further present a novel *ab initio* memory-function approach for solids to calculate the electrical conductivity of disordered solids. This method, originally used for the homogeneous electron gas, is able to describe disordered systems at all coupling strengths. An application of the developed formalism is demonstrated on the example of sodium. For this system, a metal-to-insulator transition is observed, as expected for this nearly-free electron system.

ZUSAMMENFASSUNG

Thermoelektrische Bauelemente ermöglichen die Generierung von Elektrizität aus überschüssiger Wärme, die in großer Menge in Geräten und Prozessen erzeugt wird. Deren Effizienz ist allerdings sehr gering im Vergleich zu anderen Energiequellen. Um Thermoelektrika profitabel zu machen, bedarf es noch der Entdeckung von Materialien mit einer hohen Gütezahl. Die Gütezahl ergibt sich aus den elektronischen und thermischen Transporteigenschaften. Im Rahmen dieser Dissertation werden die elektronischen Transporteigenschaften von zwei hochaktuellen thermoelektrischen Materialien untersucht. Es handelt sich um das Schichtsystem SnSe und um eine komplexe Klathrat-Legierung. Deren zuverlässige physikalische Beschreibung benötigt verschiedene Methoden, die während dieses Dissertationsprojektes entwickelt oder implementiert wurden.

Der Ursprung der beispiellos hohen Gütezahl von SnSe über einen großen Temperaturbereich war bisher rätselhaft. Wir untersuchen die Temperaturabhängigkeit der Leitfähigkeit und des Seebeck-Koeffizienten für die Niedrigtemperaturphase unter Verwendung der Boltzmann-Transportmethode in der Relaxationszeitnäherung. Wir zeigen, dass für Na-dotiertes und undotiertes SnSe nur bei gleichzeitiger Einbeziehung der thermischen Ausdehnung des Kristallgitters und der Elektron-Phonon-Streuprozesse eine gute Übereinstimmung mit Experimenten erreicht wird. In Vorbereitung auf diese Arbeit wurde die Boltzmann-Transportmethode implementiert und an Bi_2Te_3 veranschaulicht.

Typ-I-Klathrate sind Einschlussverbindungen mit einer Vielzahl an möglichen Zusammensetzungen. Sie bieten somit einen guten Spielraum, um ihre Eigenschaften hin zu einer hohen thermoelektrischen Effizienz zu optimieren. Die Eigenschaften der hier untersuchten Verbindung $Ba_8Al_xSi_{46-x}$ hängen neben dessen Zusammensetzung auch von dessen Konfiguration, d.h. der Anordnung der Al-Atome im Wirtsgitter, ab. Für die Al-Konzentration $x = 16$ wurde bereits festgestellt, dass der Grundzustand ein Halbleiter ist, während Konfigurationen mit einer Energie von nur wenigen meV/atom über dem Grundzustand metallisch sind. Wir erhalten eine zuverlässige Beschreibung der elektronischen, strukturellen und Transporteigenschaften von $Ba_8Al_xSi_{46-x}$ bei endlichen Temperaturen durch Mittlungen über Konfigurationen. Hierfür werden *Metropolis Monte-Carlo* und *Wang-Landau Samplings* in Kombination mit der *Cluster Expansion Method* verwendet. Mittels einer neu entwickelten Methode zur Berechnung der temperaturabhängigen effektiven Bandstruktur von Legierungen beobachten wir ein temperaturbedingtes Schließen der Bandlücke für $x = 16$. Dies geht mit einem partiellen Ordnung-/Unordnungsphasenübergang einher, dessen Übergangstemperatur bei $582\,\mathrm{K}$ liegt. Solch ein Phasenübergang kann dramatische Auswirkungen auf die thermoelektrische Effizienz haben, da für diese die Eigenschaften eines Halbleiters von Vorteil sind. Das Schließen einer Bandlücke unterhalb des Fermi-Niveaus, verursacht durch einen partiellen Ordnung-/Unordnungsübergang, beobachten wir auch für n-dotierte Klathrate. Für die Al-Konzentration $x = 15$ berechnen wir die elektrischen Transporteigenschaften unter der Verwendung der Boltzmann-Transportmethode in der Relaxationszeitnäherung mit der Annahme einer konstanten Relaxationszeit. Hier erreichen wir mit Hilfe der Mittelung über Konfigurationen eine gute Übereinstimmung mit dem Experiment.

Des Weiteren präsentieren wir eine neue *Ab-initio*-Methode basierend auf einer Gedächtnisfunktion zur Berechnung der elektrischen Leitfähigkeit ungeordneter Festkörper. Diese wurde ursprünglich für das homogene Elektronengas entwickelt. Wir zeigen, dass der entwickelte Formalismus in der Lage ist, ungeordnete Systeme für jede Kopplungsstärke zu beschreiben. Das wird anhand des Beispiels von Natrium gezeigt. Für dieses System, das sich ähnlich einem freien Elektrongas verhält, wird erwartungsgemäß ein Metal-Isolator-Übergang gefunden.

Ich erkläre, dass ich die Dissertation selbständig und nur unter Verwendung der von mir gemäß § 7 Abs. 3 der Promotionsordnung der Mathematisch-Naturwissenschaftlichen Fakultät, veröffentlicht im Amtlichen Mitteilungsblatt der Humboldt-Universität zu Berlin Nr. 42/2018 am 11.07.2018 angegebenen Hilfsmittel angefertigt habe.

Berlin, den 05. Oktober 2021

ELECTRONIC TRANSPORT PROPERTIES OF THERMOELECTRIC MATERIALS WITH A FOCUS ON CLATHRATE COMPOUNDS

Ph.D. Thesis
by Maria Troppenz

Supervisor: Prof. Dr. Dr. h.c. Claudia Draxl

To Stephan.

CONTENTS

ACRONYMS

APW	Augmented plane wave
BT	Boltzmann transport
CE	Cluster expansion
CVS	Cross validation score
DC	Direct-current
DFT	Density-functional theory
DOS	Density of states
FEG	Free-electron gas
GS	Ground state
IR	Interstitial region
KS	Kohn-Sham
LAPW	Linearized augmented plane wave
LASSO	Least Absolute Shrinkage and Selection Operator
lmo-CVS	Leave-many-out cross validation score
loo-CVS	Leave-one-out cross validation score
LO	Local orbital
MMC	Metropolis Monte-Carlo
MT	Muffin tin
PD	Partial disorder
QD	Quasi degenerate
RMSE	Root mean squared error
RTA	Relaxation time approximation
TD-EBS	Temperature-dependent effective band structure
WL	Wang-Landau

1

INTRODUCTION

The exploration of sustainable energy sources is of considerable concern for our society, since carbon-intensive fossil fuels are highly detrimental to the environment and need to be replaced. A substantial contribution to the sustainable energy generation can be achieved by recovering the waste heat, which is produced in large amounts by all kind of engines, including industrial processes, cars, refrigerators, *etc.* [1, 2]. Thermoelectric devices provide the possibility to harvest this waste heat and convert it into electricity [3–10]. Their extensive use is, however, hampered by their low efficiency in comparison to other energy resources. Thus, the discovery of promising candidates for high-efficient thermoelectric materials is required.

The thermoelectric figure of merit of a material depends on electronic and thermal transport coefficients. This thesis focuses on the electronic ones, namely the conductivity, the Seebeck coefficient, and the electronic part of the thermal conductivity. They can drastically change with temperature, and, especially for alloys, they can be highly affected by the material's degree of disorder. Since (dis)order is not properly treated in current methodologies available for computing the electronic transport coefficients, its reliable theoretical description remains very challenging. In this PhD project, we study the electronic transport properties of SnSe [11–13] and the complex type-I clathrate alloy $Ba_8Al_xSi_{46-x}$ [14–18], where the main focus lies on the latter. For their calculation, a combination of different methodologies is employed, covering density-functional theory (DFT) [19, 20] to access the structural and electronic ground-state properties of those materials, statistical thermodynamics to access finite-temperature properties of alloys, Boltzmann transport (BT) [21, 22], and the memory-function approach [23]. The latter two are used to compute the electronic transport coefficients. In the context of my thesis, these different methodologies have been implemented, extended or developed.

For SnSe, an unprecedented high figure of merit (above 2) has been reported for a wide temperature range [11–13]. Even though, comprehensive studies about several properties of this compound, as *e.g.* lattice anharmonicities [24], quasi-particle bands [25], electron-phonon interactions [26], and transport properties [25, 27, 28] can be found in literature, understanding the origin of this optimal thermoelectric performance at these temperatures is still lacking. To explore the temperature dependence of the electrical conductivity and the Seebeck coefficient, we employ the BT equation in the relaxation-time approximation (RTA) and successively add different temperature effects to this result. In

preparation of this work, the BT equation in the RTA has been implemented in the full-potential all-electron DFT package **exciting** [29] and demonstrated on Bi_2Te_3.

Intermetallic type-I clathrates [15, 17, 18, 30] are inclusion compounds that offer an excellent playground for tailoring their properties towards a high thermoelectric performance due to their huge compositional space. In the case of $Ba_8Al_xSi_{46-x}$ [31–36], heavy Ba atoms are encapsulated inside a crystal framework built by covalently bonded Si atoms, where some of them are substituted by Al. Here, besides the composition, it is found that the configuration, *i.e.*, the arrangement of the substituted Al atoms in the crystal framework, can have a dramatic impact on the compound's properties, especially its electronic structure [37–41]. The number of configurations available at a given composition presents a combinatorial explosion, thus computing all of them from first principles is out of reach. In addition, experimentally, the actual configurations present in thermal equilibrium can hardly be determined in x-ray diffraction due to the low scattering contrast between Al and Si [33, 36, 42, 43]. While, at low temperature, the system has a large probability to be in the most stable and ordered state, the degree of disorder increases with temperature, and the system represents a thermodynamic average on configurations. We study in detail the degree of (dis)order with respect to temperature. In this context, a realistic description of the structural, electronic, and transport properties at finite-temperature is obtained by performing finite-temperature simulations. They involve Metropolis Monte-Carlo [44] and Wang-Landau samplings [45, 46], combined with the cluster-expansion method [47] to access the configuration's energy at a computational cost that is much lower than the one spent for an *ab initio* calculation.

While the procedure for obtaining thermal averages of structural properties is well-defined, a strategy that accurately describes temperature-driven effects of disorder on the electronic structure of complex alloys is missing. Typical approaches consider either singles structures, *e.g.* the most stable structure [37, 39] or a fully disordered one [48–50] representing the high temperature limit, or resort to effective-medium theories [51–54]. Here, effective-medium theories, such as the virtual-crystal approximation [53] or the coherent-potential approximation [51, 52], are challenged by properly accounting for the local-environment effects present due to the different species in the crystal. We devise a novel method that enables the calculation of the electronic energy spectrum at finite temperature. It accurately incorporates short-range order effects, as atom relaxations and dopant-dopant correlations, as well as configurational disorder effects at elevated temperature by performing ensemble averages. We further apply such ensemble averages on the configurations for the calculation of transport coefficients.

In the determination of electronic transport coefficients, the conventional approaches, as the BT [21, 22] and the Kubo-Greenwood method [55], have

several limitations. For example, BT depends on an empirical parameter, the relaxation time, and delivers good results mainly for elastic and weak scattering mechanisms, the Kubo-Greenwood formula gives unreliable results for the direct-current limit (zero frequency limit). We go beyond and explore the memory-function approach [23] for calculating the conductivity of disordered solids. This method, initially developed for the homogeneous electron gas [56–58], is able to describe disordered systems at all coupling strengths. We derive the memory-function formalism for solids by including the periodicity of the crystal lattice. By careful treatment of the singularities of the response functions, which appear for small frequency and electron momentum, explicit expressions for the direct-current limit are obtained. The applicability of the developed formalism is demonstrated on the example of sodium. Since the electronic structure of sodium is similar to the free-electron gas, that has been studied by Götze [58], it can be explored to which extent they deviate from each other.

This thesis is organized as follows: In Chapter 2, basics of thermoelectricity and an overview about current state-of-the-art thermoelectric materials are presented. In Chapter 3, the methodologies used in this PhD thesis are introduced. It starts with the main concepts of DFT, followed by an introduction to the cluster-expansion method together with configurational sampling procedures, and an overview of electronic transport, including the BT equation and the memory-function approach. Chapter 4 presents the results obtained for the electronic transport coefficients of SnSe. The finite-temperature properties of the type-I clathrate $Ba_8Al_xSi_{46-x}$ are discussed in Chapter 5. In Chapter 6, the memory-function approach for calculating the electrical conductivity for disordered solids is presented and exemplified on bulk sodium. Each main chapter ends with a summary and short outlook.

2

THERMOELECTRIC MATERIALS

Thermoelectricity is the conversion of heat into electricity or vice versa [3–7, 16]. It enables the reuse of the waste heat generated by all kind of machines and processes, ranging from laptops to high-performance computers, from cars to airplanes and many more [1, 2]. Thermoelectric devices used for energy conversion are scalable in size and free of moving parts, thus making them suitable for distributed power generation. They consist of thermoelectric couples that are built from an n- and a p-type material placed in parallel between a heat source and a heat sink. A single thermoelectric couple used in the power generation mode is depicted in Fig. 2.1(a). Due to the temperature difference $\Delta T = T_h - T_c$ between the heat source with temperature T_h (h for hot) and the heat sink with temperature T_c (c for cold), the free charge carriers in the materials diffuse from the hot to the cold end, thus inducing a current I from the hot to the cold end in the p-type material (moving holes indicated with black circles) and from the cold to the hot end in the n-type material (moving electrons indicated black dots in Fig. 2.1(a)). The build-up voltage ΔV at the junction connecting the cold ends is proportional to the temperature difference as

$$\Delta V = S\Delta T \ . \tag{1}$$

The proportionality factor S is the Seebeck coefficient, named after the discoverer of this effect, Thomas J. Seebeck [59, 60]. The use of the thermoelectric couple in reverse order, *i.e.* a voltage is applied at the heat sink, leads to a cooling of the material on the opposite junction (Peltier effect) [61].

The efficiency of the energy conversion is determined by the dimensionless figure of merit

$$ZT = \frac{S^2\sigma}{\kappa}T \, , \tag{2}$$

where T is the absolute temperature, σ the electrical conductivity, and κ the thermal conductivity. The aim is to achieve large ZT's in the operating temperature range $[T_c, T_h]$ of the thermoelectric couple. The maximum power-generation efficiency is determined by the average value ZT_{avg} over the range $[T_c, T_h]$ as [16, 63]

$$\eta_{\max} = \frac{\Delta T}{T_h}\frac{\sqrt{1+ZT_{\text{avg}}}-1}{\sqrt{1+ZT_{\text{avg}}}+\frac{T_c}{T_h}} \ . \tag{3}$$

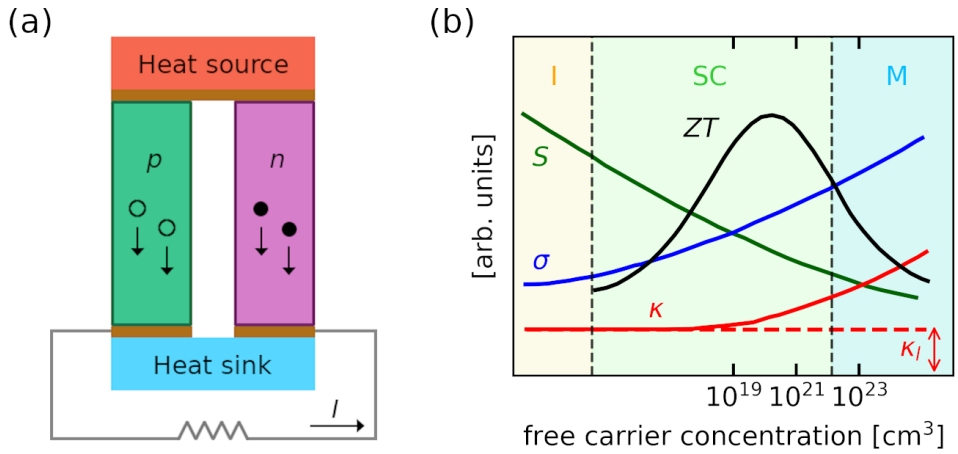

Figure 2.1: (a) Principle of thermoelectric power generation. (b) Thermoelectric coefficients, namely the Seebeck coefficient S (green), the electronic conductivity σ (blue), and the thermal conductivity κ (red), together with the figure of merit ZT with respect to the charge carrier concentration. The lattice part of the thermal conductivity κ_l is shown with a red dashed line. The insulator (I) regime is indicated with a yellow shaded area, the semiconductor region (SC) region with a green shaded area, and the metallic (M) region with a blue shaded. Model system of PbTe adapted from Ref. [62].

This efficiency is limited by the Carnot factor $\Delta T/T_h$. To give an example, by applying $T_h = 900\,\mathrm{K}$ at the heat source and $T_c = 300\,\mathrm{K}$ at the heat sink, a ZT_{avg} of 1.5 leads to $\eta_{\max} \approx 20\%$. ZT_{avg} and ZT are the same only under the assumptions that S, σ, and κ are constant across the temperature range, the properties match in the n- and p-type materials, and the presence of a 1-dimensional heat flow with no other losses.

The transport coefficients together with the corresponding ZT as a function of the charge carrier concentration n are depicted for the model system PbTe in Fig. 2.1(b) [62]. S is large in the insulator regime (yellow shaded area, denoted by I) and decreases with n. In contrast, σ increases with n, as suggested by the relationship $\sigma = ne\mu_n$ with μ_n as the carrier mobility. Therefore, it is typically large in the metallic regime (light blue shaded area, denoted by M). The product σS^2, being in the enumerator of Eq. (2), is called power factor. The thermal conductivity κ in the denominator of Eq. (2) consists of a lattice contribution κ_l, arising from the phonons traveling through the lattice, and an electronic contribution κ_e, arising from charge carriers transporting heat, *i.e.* $\kappa = \kappa_l + \kappa_e$. κ_e is directly proportional to σ through the Wiedemann-Franz law [64], given by $\kappa_e = L\sigma T$ with L as the Lorenz factor. Accordingly, the total thermal conductivity κ increases with n (red solid line in Fig. 2.1(b)). The lattice part κ_l usually remains constant with n (red dashed line). Combining the coefficients to ZT (black solid line), the maximum of ZT is typically reached for carrier concentrations around $10^{19} - 10^{21}\,\mathrm{cm}^{-3}$, which are usually found for heavily-doped semiconductors (semiconductor regime indicated with the light green shaded area, denoted by SC).

From above, it is evident that thermoelectric materials need to accomplish contradicting properties. To reach a high σ and a high S one seeks for crystalline small-band-gap semiconductors (band gap $\lesssim 1\,\mathrm{eV}$) with only one type of carrier (n- or p-type) for conduction. Preferably, the band structure has multiple valleys in the conduction band and/or multiple peaks in the valence band, thus each valley/peak can contribute to the increase of ZT [7]. Low thermal conductivities are observed for amorphous (non-crystalline) materials, such as glasses, where phonons travel randomly through the crystal [65–67]. Comprising both, a good performance in the electronic properties and a glass-like thermal conductivity leads to the concept of the phonon-glass electron-crystal (glass for phonons and crystal for electrons) [3].

The first materials, reaching a good thermoelectric efficiency, are Bi-Te and Pb-Te alloys (discovered in the late 1950s) [7, 16, 17]. They are narrow band-gap semiconductors, composed of heavy elements to reduce κ_l [68, 69], and reach maximum ZTs around one. Alloying these compounds, *e.g.* with Sb_2Te_3 and Bi_2Se_3 in the case of Bi_2Te_3, allows for a further reduction of κ_l and a tuning of the charge carrier concentration. Although defects in these alloys lead to a reduction of σ, the adjustment of the carrier concentration enables to change the ZT peak to temperatures that are relevant in specific applications [70]. Despite the fact that Bi and Pb are highly toxic materials, those compounds are widely used until now.

In the design of new state-of-the-art thermoelectrics, different approaches to optimize ZT are employed [4, 7, 8, 71–74]. One approach is to explore new classes of bulk materials with complex crystal structures that realize the PGEC concept. Those compounds typically have a cage-like crystal structure formed by atoms with covalent bonds to ensure a high performance in the electronic properties (high S and high σ). Inside its cavities, guest atoms can be encapsulated. They are loosely bound to the crystal framework and act as so called "rattlers", on which phonons are scattered to reduce the lattice thermal conductivity. Those inclusion compounds often have a complex unit cell with many atoms. Typical examples for such inclusion compounds are skutterudites and clathrates. For skutterudites, ZTs around or slightly larger than one have been achieved so far [75–79]. In the case of the skutterudite $CoSb_3$, a good performance in the electronic properties is observed ($\sigma S^2 \sim 20\,\mu\mathrm{W\,cm^{-1}K^{-2}}$ and $S \gtrsim 150\,\mu\mathrm{V\,K^{-1}}$ at $300\,K$), but also large κ ($\gtrsim 10\,\mathrm{W\,m^{-1}K^{-1}}$) [75, 77]. Here, filling the cavities with different elements (increase of disorder) reduces κ ($\sim 3\,\mathrm{W\,m^{-1}K^{-1}}$), leading to a maximal ZT of around 1.7 [78]. Clathrate compounds with heavy elements as guests, *e.g.* Ba or Sr, demonstrate low thermal conductivities $\sim 1\,\mathrm{Wm^{-1}K^{-1}}$ [16, 30, 80–84], however they lack a good performance of the electronic properties [14, 15, 17, 18, 85]. A considerably large value of $ZT \sim 1.35$ is reached for the clathrate $Ba_8Ga_{16}Ge_{30}$ [85]. The advantage of such inclusion compounds is that they offer a good playground for tuning the properties to the optimal performance.

Another approach to reach high ZTs is to reduce the dimensionality for the electrons and phonons traveling through the material by introducing nanostructures such as, *e.g.*, superlattices, quantum dots, nanowires, and nanocomposites [71, 86–88]. The interfaces of the nanostructures enhance phonon scattering, when the distance between them is shorter than the mean free path of the phonons, but still larger than the mean free path of the electrons. Furthermore, a sharp slope of the density of the states at the Fermi level can be produced with nanostructures, leading to an enhancement of S [4, 86, 88, 89]. For the quantum well superlattices Bi_2Te_3-Sb_2Te_3 [90], a high ZT of 2.4 has been achieved so far [90]. For quantum wires and nanotubes, the enhancement of ZT is predicted to be even better due to the additional reduction of dimensionality. Silicon nanowires with $50\,\mathrm{nm}$ diameters have a 60-fold increased ZT compared to the bulk material, resulting in a ZT of ~ 0.6 [91]. In the studies of low-dimensional materials without nanostructures, a remarkable ZT of 2.6 is obtained for the single crystal SnSe [11]. Its anisotropic crystal structure consisting of weakly-bonded and two-atoms-thin layers exhibits one of the lowest thermal conductivities ($\leq 0.4\,\mathrm{W\,m^{-1}K^{-1}}$) and a semiconductor-like Seebeck coefficient ($\geq 400\,\mu\mathrm{V\,K^{-1}}$). These properties are realized for a large temperatures range, making this material most promising for technology applications.

In this thesis, we study a traditional, a complex and a two-dimensional material, namely Bi_2Te_3, the type-I clathrate $Ba_8Al_xSi_{x-46}$, and SnSe.

3

THEORETICAL BACKGROUND

3.1 DENSITY-FUNCTIONAL THEORY

The properties of a solid-state material, composed of interacting electrons and nuclei, can be obtained from the many-body Schrödinger equation. However, solving the full equation is a very demanding and often impossible task due to the high amount of degrees of freedom of the system. Thus, approximations are required. As a first one, commonly, the Born-Oppenheimer approximation [92] is introduced, which decouples the motion of the electrons from the motion of the nuclei. Since the heavy nuclei move much at much larger time scales, they can be considered as stationary in comparison to the electrons. Now, what remains to be solved is the electronic many-body Schrödinger equation:

$$\left[-\sum_i\left(\frac{\nabla_i^2}{2}\right)+\frac{1}{2}\sum_{i\neq j}\frac{1}{|\boldsymbol{r}_i-\boldsymbol{r}_j|}-\sum_{i,I}\frac{Z_I}{|\boldsymbol{r}_i-\boldsymbol{R}_I|}\right]\Psi(\boldsymbol{r}_1,\boldsymbol{r}_2,\ldots,\boldsymbol{r}_N) = E\ \Psi(\boldsymbol{r}_1,\boldsymbol{r}_2,\ldots,\boldsymbol{r}_N)\ . \quad (4)$$

Its solution determines the electronic many-body wave function $\Psi(\boldsymbol{r}_1,\boldsymbol{r}_2,\ldots,\boldsymbol{r}_N)$ of a system consisting of N interacting electrons at positions $\boldsymbol{r}_i$ in a potential of the nuclei with atomic number Z_I at positions $\boldsymbol{R}_I$.

The numerical solution of the N-electron Schrödinger equation (Eq. (4)) can be determined *e.g.* by the configuration interaction method, that uses a linear combination of Slater determinants to describe $\Psi(\boldsymbol{r}_1,\boldsymbol{r}_2,\ldots,\boldsymbol{r}_N)$. Since its computational effort grows exponentially with N, it is only suitable for small systems. A good alternative is provided by DFT [19, 20, 93, 94]. In this theory, the problem of the determination of $\Psi(\boldsymbol{r}_1,\boldsymbol{r}_2,\ldots,\boldsymbol{r}_N)$ is avoided and reformulated in terms of the electronic density of the ground state (GS). This enables a reduction of the many-body problem to an effective single-particle problem (having only 3 spatial coordinates), leading to an excellent scalability for handling large and complex systems.

DFT within the Kohn-Sham (KS) scheme is introduced in Sec. 3.1.1. In this thesis, the DFT-based *ab initio* calculations are performed with the full-potential all-electron DFT package **`exciting`** [29]. The linearized augmented plane-wave (LAPW) method as implemented in **`exciting`** is shortly presented in Sec. 3.1.2.

3.1.1 *Density-functional theory in the Kohn-Sham scheme*

The fundamental theorem of DFT has been introduced by Hohenberg and Kohn [95]. They demonstrated that the external potential $v_{\mathrm{ext}}(\boldsymbol{r})$ is a unique functional of the electronic GS density and *vice versa*. Thus, the total energy E_v of the system of interacting electrons in the external potential $v_{\mathrm{ext}}(\boldsymbol{r})$ can be considered as a universal functional of the electronic density $n(\boldsymbol{r})$

$$E_v\left[n\right] = F\left[n\right] + \int \mathrm{d}\boldsymbol{r}\, v_{\mathrm{ext}}(\boldsymbol{r})\, n(\boldsymbol{r}) \ , \tag{5}$$

where $F\left[n\right]$ is a functional that accounts for the kinetic energy and the interaction between the electrons. The GS energy E_0 of the system described with Hamiltonian H can then be determined by the Rayleigh-Ritz variational principle as

$$E_0 = \min_{\tilde{\Psi}} \langle \tilde{\Psi} \left| \hat{H} \right| \tilde{\Psi} \rangle \equiv \min_{\tilde{n}(\boldsymbol{r})} E_v\left[\tilde{n}\right] \ . \tag{6}$$

Here, $\tilde{\Psi}$ is a trial wave function. According to Hohenberg and Kohn, this minimization with respect to $\tilde{\Psi}$ can be replaced by a minimization with respect to a trial density $\tilde{n}(\boldsymbol{r})$.

To determine the GS energy (and the GS electronic density) from the variational principle, an expression for $F\left[n\right]$ is required. Kohn and Sham (KS) decomposed $F\left[n\right]$ as follows [96]:

$$F\left[n\right] = T_0\left[n\right] + E_{\mathrm{H}}\left[n\right] + E_{\mathrm{xc}}\left[n\right] \ . \tag{7}$$

Here, $T_0\left[n\right]$ is the kinetic energy of the system of non-interacting electrons, $E_{\mathrm{H}}\left[n\right]$ the Hartree energy, and $E_{\mathrm{xc}}\left[n\right]$ the exchange-correlation energy. $E_{\mathrm{xc}}\left[n\right]$ gathers the energy contributions from the kinetic-energy difference between the interacting and the non-interacting system, as well as the electron-electron interactions that are not represented by the Hartree energy. Within the KS approach, the system of interacting electrons is mapped to a fictitious system of non-interacting particles that has the same GS electronic density as the interacting one.

Now, the total energy functional, defined by Eq. (5) using Eq. (7) for $F\left[n\right]$, can be minimized under the assumption that the number of particles N is conserved. It results a set of single-particle Schrödinger equations for the fictitious non-interacting system:

$$\left[-\frac{1}{2}\nabla^2 + v_{\mathsf{KS}}(\boldsymbol{r})\right] \psi_i(\boldsymbol{r}) = \epsilon_i\, \psi_i(\boldsymbol{r}) \ . \tag{8}$$

This is called KS equation. Here, $\psi_i(\boldsymbol{r})$ are the single-particle KS wave functions, ϵ_i their corresponding energies, and $v_{\mathsf{KS}}(\boldsymbol{r})$ the potential of the fictitious KS system given by

$$v_{\mathsf{KS}}(\boldsymbol{r}) = v_{\mathrm{ext}}(\boldsymbol{r}) + \frac{\delta E_{\mathrm{H}}\,[n]}{\delta n(\boldsymbol{r})} + \frac{\delta E_{\mathrm{xc}}\,[n]}{\delta n(\boldsymbol{r})}\ , \tag{9}$$

where the first term represents the external potential, the second term the mean-field interaction of the electrons $v_H(\boldsymbol{r})$, and the third term the exchange-correlation potential $v_{\mathrm{xc}}(\boldsymbol{r})$.

The GS electronic density is obtained from the single-particle KS wave functions as

$$n(\boldsymbol{r}) = \sum_{i=1}^{N} |\psi_i(\boldsymbol{r})|^2\,. \tag{10}$$

Since $v_{\mathsf{KS}}(\boldsymbol{r})$ depends on the electronic density, the KS equation (Eq. (8)) and the electronic density (Eq. (10)) need to be solved self-consistently. The self-consistent KS scheme starts with an initial guess for $n(\boldsymbol{r})$, *e.g.* obtained from a superposition of the atomic densities. Subsequently, the KS equations are solved to determine the $\psi_i(\boldsymbol{r})$'s, and from those wave functions the new $n(\boldsymbol{r})$ is calculated. This self-consistent field cycle stops when the convergence criterion is fulfilled. The converged density is the GS density. From it, the GS properties are calculated.

The KS scheme gives the exact GS energy and GS electronic density if the exact $v_{\mathrm{xc}}(\boldsymbol{r})$ is known. However, the exact form of $E_{\mathrm{xc}}[n]$ or $v_{\mathrm{xc}}(\boldsymbol{r})$ is not known and needs to be approximated. Due to this, the accuracy of the DFT calculation depends on the level of the approximation chosen for the exchange-correlation functional. There are several levels of approximations available with increasing complexity [97, 98]. The simplest approximation for $E_{\mathrm{xc}}[n]$ is given by the local-density approximation (LDA) as

$$E_{\mathrm{xc}}^{\mathsf{LDA}}\,[n] = \int e_{\mathrm{xc}}^{\mathrm{hom}}\Big(n(\boldsymbol{r})\Big)\, n(\boldsymbol{r})\,\mathrm{d}\boldsymbol{r}\ . \tag{11}$$

Here, $e_{\mathrm{ex}}^{\mathrm{hom}}(n)$ is the exchange-correlation energy per particle of a homogeneous electron gas with density n. The exchange part of $e_{\mathrm{xc}}^{\mathrm{hom}}(n)$ is analytically known and the correlation part can be estimated with high-accuracy Quantum-Monte-Carlo methods [99, 100]). The generalized-gradient approximation (GGA) accounts for some non-locality of the exchange-correlation functional. In GGA, the exchange-correlation energy is given by

$$E_{\mathrm{xc}}^{\mathsf{GGA}}\,[n] = \int f\Big(n(\boldsymbol{r}), |\nabla n(\boldsymbol{r})|\Big)\, n(\boldsymbol{r})\,\mathrm{d}\boldsymbol{r}\ , \tag{12}$$

where the function f depends not only on $n(\boldsymbol{r})$ but also on the gradient $\nabla n(\boldsymbol{r})$. One of the most widely used GGA functionals was proposed by Perdew, Burke, and Ernzerhof (PBE) [101]. A GGA functional optimized for solids is called PBEsol [102]. Semi-local functionals give quantitatively better results than LDA for various properties, as *e.g.* binding energies and lattice parameters. However, the suitability of both functionals is limited for particular properties, especially for the band gap that is typically underestimated and is not even expected to be correct for the exact KS functional [103, 104]. Semi-local functionals have formal deficiencies in their construction, such as the absence of the derivative discontinuity [105, 106] and the presence of self-interaction in the exchange-correlation energy [107]. Addressing the latter, improved results can be yielded by hybrid functionals [103, 108–111] realized in generalized DFT. Here, in the expression for a local or semi-local functional, a fraction α of the exchange part E_x is replaced by a non-local exchange. Then, E_{xc} reads as

$$E_{\mathrm{xc}}^{\mathsf{hybrid}} = E_{\mathrm{xc}}^{\mathsf{local/semi\text{-}local}} + \alpha \left(E_{\mathrm{x}}^{\mathsf{non\text{-}local}} - E_{\mathrm{x}}^{\mathsf{local/semi\text{-}local}} \right) \ . \tag{13}$$

For $E_{\mathrm{x}}^{\mathsf{non\text{-}local}}$, usually the Hartree-Fock exchange energy $E_{\mathrm{x}}^{\mathsf{HF}}$ is employed. A famous hybrid functional is, for instance, PBE0 [112, 113] whose E_{xc} has the following form:

$$E_{\mathrm{xc}}^{\mathsf{PBE0}} = E_{\mathrm{xc}}^{\mathsf{PBE}} + 0.25 \left(E_{\mathrm{x}}^{\mathsf{HF}} - E_{\mathrm{x}}^{\mathsf{PBE}} \right) \ . \tag{14}$$

Here, the fraction is fixed to 0.25. By separating the long-range from the short-range interactions, further improvements can be achieved [114, 115].

Beyond DFT, many-body perturbation theory provides further concepts, as *e.g.* the GW approximation [116, 117], to obtain good estimates for band gaps, as well as precise descriptions of excited states [118]. They are not subject of this thesis, thus they are not further discussed at this point.

3.1.2 *Linearized augmented plane-wave method in* `exciting`

In the software package `exciting` [29], the KS equations (Eq. 8) are solved by expanding the $\psi_i(\boldsymbol{r})$ in terms of a set of basis functions, composed of (linearized) augmented plane waves ((L)APWs) and local orbitals (LOs) (details are given in Ref. [29] and references therein).

In particular, the KS wave functions are expanded as:

$$\psi_{i\boldsymbol{k}}(\boldsymbol{r}) = \sum_{\boldsymbol{G}}^{|\boldsymbol{G}|<G_{\max}} C_{i\boldsymbol{G}}^{\boldsymbol{k}} \, \varphi_{\boldsymbol{G}+\boldsymbol{k}}(\boldsymbol{r}) \ . \tag{15}$$

Here, $\boldsymbol{k}$ are the wave vectors in the first Brillouin zone and $\boldsymbol{G}$ are reciprocal lattice vectors. The space is partitioned into muffin-tin (MT) regions and an

interstitial region (IR). The MT regions are defined by spheres with radius R^{α}_{MT} around the nuclei α located at $\boldsymbol{R}_{\alpha}$. In this region, the wave functions are expected to be atomic-like wave functions and can be expanded in terms of spherical harmonics $Y_{lm}(\hat{\boldsymbol{r}}_{\alpha})$ and radial functions $u_{l\alpha}(r_{\alpha})$. In the IR, that is defined as the region between the MTs, the electrons are expected to move almost freely, thus the wave functions can be approximated by plane waves. Accordingly, a dual representation of the APW basis functions is used and defined as follows:

$$\varphi_{\boldsymbol{G}+\boldsymbol{k}}(\boldsymbol{r}) = \begin{cases} \sum_{lm} A^{\boldsymbol{G}+\boldsymbol{k}}_{lm\alpha}\, u_{l\alpha}(r_{\alpha};\epsilon)\, Y_{lm}(\hat{\boldsymbol{r}}_{\alpha}) \ , & r_{\alpha} = |\boldsymbol{r}-\boldsymbol{R}_{\alpha}| \leq R^{\alpha}_{\mathrm{MT}} \\ \frac{1}{\sqrt{\Omega}} e^{\mathrm{i}(\boldsymbol{G}+\boldsymbol{k})\cdot\boldsymbol{r}} \ , & \boldsymbol{r} \in \mathrm{IR} \ . \end{cases} \tag{16}$$

The coefficients $A^{\boldsymbol{G}+\boldsymbol{k}}_{lm\alpha}$ are defined by the continuity condition of $\varphi_{\boldsymbol{G}+\boldsymbol{k}}(\boldsymbol{r})$ at the boundary of MT spheres.

Finding a solution for the KS equations using the APW basis, as defined in Eq. (16), is a non-linear eigenvalue problem, since the radial part $u_{l\alpha}$ depends on the eigenenergies of the KS system. To linearize the eigenvalue problem, two methods are used in **exciting**: The linearized APW (LAPW) method and the APW+local-orbital (APW+lo) method. For the first approach, a straightforward way would be an expansion of the energy-dependent radial functions as

$$u_{l\alpha}(r_{\alpha};\epsilon) \approx u_{l\alpha}(r_{\alpha};\epsilon_{l\alpha}) + (\epsilon_{l\alpha}-\epsilon)\dot{u}_{l\alpha}(r_{\alpha};\epsilon_{l\alpha}) \ , \tag{17}$$

where $\dot{u}_{l\alpha}(r_{\alpha};\epsilon_{l\alpha})$ is the derivative of the radial function with respect to the energy. Inspired by this, the LAPW functions in the MT region are defined as:

$$\varphi_{\boldsymbol{G}+\boldsymbol{k}}(\boldsymbol{r}) = \sum_{lm} \left[A^{\boldsymbol{G}+\boldsymbol{k}}_{lm\alpha}\, u_{l\alpha}(r_{\alpha};\epsilon_{l\alpha}) + B^{\boldsymbol{G}+\boldsymbol{k}}_{lm\alpha}\, \dot{u}_{l\alpha}(r_{\alpha};\epsilon_{l\alpha}) \right] Y_{lm}(\hat{\boldsymbol{r}}_{\alpha}) \ . \tag{18}$$

The coefficients $A^{\boldsymbol{G}+\boldsymbol{k}}_{lm\alpha}$ and $B^{\boldsymbol{G}+\boldsymbol{k}}_{lm\alpha}$ are determined by the continuity condition of $\varphi_{\boldsymbol{G}+\boldsymbol{k}}(\boldsymbol{r})$ and its spatial derivative at the boundary of the MT spheres.

The alternative scheme keeps the APW form of Eq. (16), but uses frozen energy parameters for the radial functions, *i.e.*, $u_{l\alpha}(r_{\alpha};\epsilon) \approx u_{l\alpha}(r_{\alpha};\epsilon_{l\alpha})$, and adds linearly-independent LOs to Eq. (15). The LOs are defined within the MT region as

$$\varphi_{\beta}(\boldsymbol{r}) = \delta_{\alpha\alpha_{\beta}}\delta_{ll_{\beta}}\delta_{mm_{\beta}} \left[a_{\beta} u_{l\alpha}(r_{\alpha},\epsilon_{l\alpha}) + b_{\beta}\dot{u}_{l\alpha}(r_{\alpha},\epsilon_{l\alpha}) \right] Y_{lm}(\hat{\boldsymbol{r}}_{\alpha}) \tag{19}$$

and are zero in the IR. The coefficients a_{β} and b_{β} are determined by the condition $\varphi_{\beta}(\boldsymbol{r}) = 0$ at the MT boundary and the normalization to one, *i.e.*, $\int_{\Omega} |\varphi_{\beta}(\boldsymbol{r})|^2 \, \mathrm{d}\boldsymbol{r} = 1$, with Ω being the cell volume. The APW+lo basis can be improved by adding high-order terms in $u_{l\alpha}(r_{\alpha};\epsilon)$, *i.e.*, including high-order derivatives, as *e.g.* $\ddot{u}$, $\dddot{u}$, *etc.* The APW+lo method provides more flexibility

and yields smaller errors in the eigenvalues than the LAPW methods using the same basis set size [29].

The basis set used to construct the KS wave functions (Eq. (15)) is truncated by the plane-wave cutoff $G_{\max}$ with $G_{\max} > |\boldsymbol{G} + \boldsymbol{k}|$. As seen from Eq. (16), the basis is not solely dependent on $G_{\max}$, but also on the MT radius R_{MT}. The MT radii can differ for each species. For a small R_{MT}, the wave function in the IR varies more rapidly in some parts and a larger $G_{\max}$ is needed to reach the same accuracy as for a large R_{MT}. Therefore, the dimensionless parameter $R_{\mathrm{MT,min}}G_{\max}$ is defined, with $R_{\mathrm{MT,min}}$ as the smallest MT radius of a species in the crystal. In the **exciting** code, $G_{\max}$ and $R_{\mathrm{MT,min}}G_{\max}$ are specified as input parameters. Furthermore, the accuracy of the DFT calculation is determined by the discretization of the $\boldsymbol{k}$-space in the Brillouin zone, usually referred to as the $\boldsymbol{k}$-grid or $\boldsymbol{k}$-point mesh.

3.2 SAMPLING THE CONFIGURATION SPACE

For alloys, a reliable description of the structural and thermodynamic properties at finite temperature is obtained from thermal averages over several configurations. The set of configurations used to calculate these averages can be generated from Monte-Carlo samplings. During a Monte-Carlo sampling, the energy of every new proposed configuration needs to be determined. Here, a DFT calculation would be computationally very demanding, especially for large (super)cells. An efficient tool to predict the energy and other properties at low computational cost is the cluster expansion (CE) technique [47]. It makes use of the unique dependence of the property of interest on the configuration.

The CE technique is explained in Sec. 3.2.1. The Monte-Carlo sampling methods used for configurational thermodynamics are discussed in Sec. 3.2.2.

3.2.1 *Cluster expansion method*

The CE method aims at the relation between the concentration and configuration of the substitutional species in the lattice as well as the physical property P of the system. We consider a crystal with N lattice sites. Each of these sites i is occupied by an atomic species. Having M_i different type of species in the lattice, the species type at site i can be represented by an occupation variable σ_i that takes integer values from 0 to $M_i - 1$. For instance, in case of the binary alloy with species A and B, σ_i can take the values 0 and 1, respectively. Thus, an arbitrary arrangement of the species in the lattice can be represented

by the vector $\boldsymbol{\sigma}_s = \{\sigma_{s1}, \sigma_{s2}, \ldots, \sigma_{sN}\}$. Based on this, the general form of the CE for a configuration-dependent property P is given by

$$P(\boldsymbol{\sigma}) = \sum_{\alpha} m_\alpha J_\alpha X_\alpha(\boldsymbol{\sigma}) \ . \tag{20}$$

Here, the sum runs over a set of symmetrically distinct clusters α. A cluster is a set of crystal sites $\{i_1, i_2, \ldots\}$. The coefficient J_α is the effective cluster interaction (ECI) for cluster α, and $X_\alpha(\boldsymbol{\sigma})$ is the correlation function between α and the structure $\boldsymbol{\sigma}$, calculated as

$$X_\alpha(\boldsymbol{\sigma}) = \frac{1}{m_\alpha} \sum_{\beta \in \mathcal{O}(\alpha)} f_\beta(\boldsymbol{\sigma}) \ . \tag{21}$$

Here, the *cluster functions* $f_\beta(\boldsymbol{\sigma})$ form a complete and orthonormal set of basis functions [47, 119]. In Eq. (21), these functions are averaged over *cluster orbits* $\mathcal{O}(\alpha)$, *i.e.*, the set of clusters β which are symmetrically equivalent to α by the symmetry operations of the space group of the pristine (non-substituted) lattice. m_α is the cluster multiplicity, *i.e.*, the number of clusters β in $\mathcal{O}(\alpha)$. In the case of a binary alloy, a convenient set of the cluster functions is the product of the occupation variables σ_i, *i.e.*, $f_\beta(\boldsymbol{\sigma}) = \prod_{i \in \beta} \sigma_i$, with $\sigma_i = 0, 1$.

In order to apply the CE formalism, one needs to specify the lattice positions of the system and the species types at each position. They is defined in the so-called *parent lattice*. Such a *coarse-grained* model is able to represent all possible configurations of the system, thus includes all configurational degrees of freedom. Additional effects arising, *e.g.*, from electronic and vibrational degrees of freedom are neglected [120]. The summation in Eq. (20) is in principle infinite, and, using a complete basis, an exact expansion of any structure-property relation can be obtained. However, in practice, a summation over all possible α is not feasible, since the number of clusters, as the number of configurations, rapidly grows with the size of the supercell (*combinatorial explosion*). It has been found that for most alloys, the CE model of the energy rapidly converges with respect to the number of clusters [40, 41, 120–123]. In most cases, a set of around 10 to 20 clusters, that consists mainly of short-range pairs and triples, is sufficient to obtain an accurate description of the system's property.

A CE model of a property of interest can be obtained from the following ingredients:

- Set of N_s structures (*training set*): $\mathcal{S} = \left\{\boldsymbol{\sigma}_{s_1}, \boldsymbol{\sigma}_{s_2}, \ldots, \boldsymbol{\sigma}_{s_{N_s}}\right\}$
- *Ab initio* properties of $\mathcal{S}$ calculated, *e.g.*, from DFT: $\boldsymbol{P}^T = (P_1, P_2, \ldots, P_{N_s})$
- Set of N_α clusters: $\mathcal{C} = \{\alpha_1, \alpha_2, \ldots, \alpha_{N_\alpha}\}$

To simplify the notation, we define a $N_\mathcal{S} \times N_\alpha$ matrix, $\boldsymbol{X}$, containing as elements the correlations $X_{s\alpha} = X_\alpha(\boldsymbol{\sigma}_s)$ between the structure s in S and the clus-

ter α in $\mathcal{C}$. We also define the vector $\tilde{\boldsymbol{J}}_\alpha^T = \left(m_{\alpha_1} J_{\alpha_1}, m_{\alpha_2} J_{\alpha_2}, \ldots, m_{\alpha_{N_\alpha}} J_{\alpha_{N_\alpha}}\right)$, containing the cluster interactions J_α multiplied by their multiplicities m_α. Then, Eq. (20) can be recast in a matrix-vector representation:

$$\begin{pmatrix} \hat{P}_1 \\ \hat{P}_2 \\ \vdots \\ \hat{P}_{N_s} \end{pmatrix} = \begin{pmatrix} X_{1\alpha_1} & X_{1\alpha_2} & \ldots & X_{1\alpha_{N_\alpha}} \\ X_{2\alpha_1} & X_{2\alpha_2} & \ldots & X_{2\alpha_{N_\alpha}} \\ \vdots & \vdots & \ddots & \vdots \\ X_{N_s\alpha_1} & X_{N_s\alpha_2} & \ldots & X_{N_s\alpha_{N_\alpha}} \end{pmatrix} \cdot \begin{pmatrix} m_{\alpha_1} J_{\alpha_1} \\ m_{\alpha_2} J_{\alpha_2} \\ \vdots \\ m_{\alpha_{N_\alpha}} J_{\alpha_{N_\alpha}} \end{pmatrix} \tag{22}$$

or, equivalently,

$$\hat{\boldsymbol{P}} = \boldsymbol{X}\tilde{\boldsymbol{J}}\,. \tag{23}$$

Here, the vector $\hat{\boldsymbol{P}}^T = \left(\hat{P}_1, \hat{P}_2, ..., \hat{P}_{N_s}\right)$ contains the predicted property $\hat{P}_s$ for each structure s in $\mathcal{S}$. The hat symbol $\hat{}$ on top of P indicates that it is the predicted value of property P.

The optimal ECIs for a given set $\mathcal{C}$ are obtained by minimizing the mean squared error (MSE) of the predictions $\hat{\boldsymbol{P}}$ in the training set $\mathcal{S}$:

$$\tilde{\boldsymbol{J}} = \underset{\tilde{\boldsymbol{J}}^*}{\operatorname{argmin}} \, ||\boldsymbol{P} - \boldsymbol{X}\tilde{\boldsymbol{J}}^*||_2^2 \,. \tag{24}$$

A solution of this objective function can be found, if the number of clusters N_α is smaller or equal than the number of structures N_s ($N_\alpha \leq N_s$) and the columns of the matrix $\boldsymbol{X}$ are linear independent (*i.e.*, full column rank of $\boldsymbol{X}$). If $N_\alpha > N_{\mathcal{S}}$, the set of linear equations from Eq. (24) is underdetermined (more parameters than equations), and no solution or infinitely many solutions are found. In this case, the optimization problem needs to be "regularized", *e.g.*, by adding ℓ_p norms in Eq. (24), that controls the coefficients J_α's [124–126]. Then, the objective function reads

$$\tilde{\boldsymbol{J}} = \underset{\tilde{\boldsymbol{J}}^*}{\operatorname{argmin}} \, \left(||\boldsymbol{P} - \boldsymbol{X}\tilde{\boldsymbol{J}}^*||_2^2 + \lambda||\tilde{\boldsymbol{J}}||_p\right) \,, \tag{25}$$

with $||\boldsymbol{u}||_p = (\sum_i |u_i|^p)^{\frac{1}{p}}$ being the ℓ_p norm and $\lambda \in \mathbb{R}$ a regularization hyperparameter. An ℓ_2 regularization (ridge regression) in Eq. (25) penalizes large ECIs, *i.e.*, a small λ has small effects on the ECIs and serves mainly the purpose of regularizing the optimization problem, while for a large λ the regression coefficients are shrunken and, thus, uniform solutions are obtained. The use of an ℓ_1 regularization leads to sparse solutions, *i.e.*, a few non-zero ECIs, since it causes a shrinking of the actual values of the coefficients. Sparse solutions result naturally by employing an ℓ_0 norm, since it simply penalizes the number of non-zero coefficients. Here, no shrinkage of the coefficients occurs. Finding the solution by using the ℓ_0 norm is an NP-hard problem, thus it can only be applied to a small pool of clusters. If the clusters pool is large, sufficiently good

solutions can be obtained by using the ℓ_1 norm solved with the 'Least Absolute Shrinkage and Selection Operator' (LASSO) method [124, 127].

The solutions found by optimizing Eq. (25) may not give good predictions $\hat{P}$ of new structures, *i.e.*, structures that are not used to train the CE model. A good estimate of the predictive power is obtained by the cross validation score (CVS) [128–130]. The CVS is calculated with the use of one or several *validation sets*. The *validation set* is a set of N_V structures $\mathcal{V} = \{\boldsymbol{\sigma}_{s1}, \boldsymbol{\sigma}_{s2}, \ldots, \boldsymbol{\sigma}_{N_V}\}$ with known *ab initio* properties $\boldsymbol{P}_{\mathcal{V}}^T = (P_1, P_2, \ldots, P_{N_V})$, which do not belong to the *training set*. The mean squared error of the predictions $\hat{\boldsymbol{P}}_{\mathcal{V}}$, obtained by the CE for a given set $\mathcal{C}$ and hyperparameter λ, with respect to $\boldsymbol{P}_{\mathcal{V}}$ gives the CVS:

$$\text{CVS} = ||\boldsymbol{P}_{\mathcal{V}} - \hat{\boldsymbol{P}}_{\mathcal{V}}|| \ . \tag{26}$$

Here, $||\bullet||$ means $||\bullet||_2^2$. Usually, extra data for validation is not available. Thus, in practice, a data set of N *ab initio* properties is split into a *training* and *validation set* ($N_V + N_S = N$). From several distinct splits, a CVS is obtained by averaging the residual sum of squares on these splits. For instance, a widely used CVS is the leave-one-out CVS, short loo-CVS [120, 122, 128]. As the name already suggests, one out of the N structures at a time is taken as *validation set*, and the remaining $N-1$ structures are used as *training set*. This is done for every structure, thus, there are N splits used for the average. Taking several structures out at a time is called the leave-many-out CVS (lmo-CVS) [131]. The minimum of loo-CVS or lmo-CVS is found by evaluating them on different subsets of clusters $\mathcal{C}$ and values of λ.

3.2.2 *Configurational thermodynamics*

In the following, we explain two sampling methods, the Metropolis Monte-Carlo (MMC) sampling method [44] and the Wang-Landau (WL) method [45, 46], which allow us to access structural and thermodynamic properties at finite temperature. Here, we focus on sampling procedures performed in the canonical ensemble (NVT ensemble), *i.e.*, the number of particles N, the temperature T, and the volume V remain unchanged during the sampling.

The MMC and the WL method are Markov-Chain Monte Carlo simulation methods [132, 133]. In such a simulation, a sequence of configurations is generated in a stochastic manner, specifically at each sampling step n, the current configuration σ_n with energy E_n is modified by a swap of two randomly-chosen species in the lattice (Monte-Carlo swap or trial move). In general, it can be also multiple swaps per sampling step. The acceptance of this new proposed (or trial) configuration σ_{n+1} with energy E_{n+1} is decided by a probability distribution p_A. For Markov Chains, p_A depends solely on the current and the new proposed configuration, $\boldsymbol{\sigma}_n$ and $\boldsymbol{\sigma}_{n+1}$, respectively. Specifically, one can write

Table 3.1: Sampling methods with their acceptance probability p_A, the formula of the resulting histogram H and a possible shape of H.

Sampling Method	$\boldsymbol{p_A\,(E_n \to E_{n+1})}$	**Histogram $\boldsymbol{H}$**	
Random-walk Monte Carlo	1	$g(E) \cdot 1$	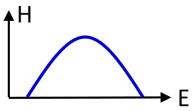
Canonical Metropolis Monte-Carlo	$\min\left[1, e^{-\frac{E_{n+1}-E_n}{k_B T}}\right]$	$g(E) \cdot e^{E/k_B T}$	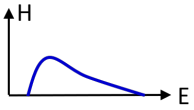
Wang-Landau	$\min\left[1, \frac{g(E_n)}{g(E_{n+1})}\right]$	$g(E) \cdot \frac{1}{g(E)}$	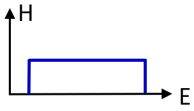

$p_A\,(E_n\,(\boldsymbol{\sigma}_n) \to E_{n+1}\,(\boldsymbol{\sigma}_{n+1}))$, or short $p_A\,(E_n \to E_{n+1})$, with $E_n \to E_{n+1}$ denoting that $\boldsymbol{\sigma}_n$ with E_n changes to $\boldsymbol{\sigma}_{n+1}$ with E_{n+1}.

The acceptance probabilities p_A of the MMC and the WL method are shown schematically together with a possible sampling histogram in Table 3.1. For comparison, the unbiased random-walk Monte-Carlo method with $p_A = 1$ is also added. In the limit of a very long sampling procedure, the histogram of a random walk converges to the configurational density-of-states $g(E)$, which represents the number of accessible configurations at energy E. A possible shape of $g(E)$ versus E is depicted in the first row on the right of Table 3.1.

In an MMC sampling (second row in Table 3.1), p_A depends on temperature T through the Boltzmann distribution $\exp\left(-\frac{\Delta E}{k_B T}\right)$ with the Boltzmann constant k_B and the energy difference $\Delta E = E_{n+1} - E_n$. The histogram generated from this sampling procedure is proportional to the Boltzmann distribution, and its maximum depends on T. We can use the MMC sampling method to estimate a temperature-dependent property P_T from a sampling performed at T, provided that P is calculated or predicted at each visited configuration σ_n, for instance, by using a CE model for P. P_T is obtained by the average

$$P_T = \langle P \rangle_T = \frac{1}{N_{\text{avg}}} \sum_{i=1}^{N_{\text{avg}}} P_i(\boldsymbol{\sigma}_i)\ . \tag{27}$$

Here, N_{avg} is the number of sampling steps used for the average after discarding N_{eq} equilibration steps at the beginning of the sampling trajectory with, in total, N_{steps} sampling steps ($N_{\text{steps}} = N_{\text{eq}} + N_{\text{avg}}$). After N_{eq}, the system is in the equilibrium state. As an example for a thermodynamic property, calculated by

using Eq. (27), the internal energy $U(T) = \langle E \rangle_T$ is obtained by averaging the energy $E_i = E(\boldsymbol{\sigma}_i)$ of each visited configuration $\boldsymbol{\sigma}_i$ in an MMC sampling performed at given T. One of the disadvantages of the MMC sampling method is that the temperature dependence of the property $P(T)$ over the temperature range of interest can be only achieved from several sampling procedures, one at each temperature. Furthermore, at low temperatures, the sampling easily gets trapped in local minima and often does not find all possible states at a given T.

An alternative to the MMC method is the WL method. The goal of this method is to obtain the temperature-independent $g(E)$ from a single sampling procedure directly. Once the $g(E)$ is known, the thermodynamic properties at any T can be calculated directly without the need of another sampling procedure. As mentioned before, $g(E)$ is, in principle, generated by an unbiased random-walk Monte Carlo method. However, achieving a converged $g(E)$ with this method is practically impossible since an enormous number of sampling steps is required. In the WL sampling, the energy space is sampled with an acceptance probability p_A that is directly proportional to $1/g(E)$. If the true $g(E)$ is used for p_A, such a sampling produces a flat histogram, as shown in Table 3.1. Reversely, it means that if a sampling procedure generates a flat histogram in energy, we use a sufficiently accurate $g(E)$. To obtain a flat histogram, $g(E)$ is updated during the sampling procedure, as explained in the following.

The workflow scheme of the WL method is depicted in Fig. 3.1. The procedure samples the full energy space that is possible to be visited during the canonical sampling. This energy space is discretized into energy bins with a predefined width ΔE. Each energy bin should be visited nearly equally in the sampling to achieve the flat histogram. At the beginning of the sampling procedure $g(E)$ is unknown, thus, initially, $g(E) = 1$ and the histogram $H(E) = 0$ (no visits) for all energy bins. In addition, the algorithm employs a modification factor f that is used after each sampling step to update $g(E)$ of the energy bin E, containing the energy of the visited configuration, and is set initially to $f_0 = e^1$. Starting from these settings and an initial configuration $\boldsymbol{\sigma}_0$ with energy E_0 (blue frame in Fig. 3.1), the sampling procedure performs a nested loop consisting of an inner loop to generate a flat histogram and an outer loop to increase the accuracy of $g(E)$ by lowering f. Both loops are framed in green in Fig. 3.1. In the inner loop, the configurational space is sampled by swapping species and, after each sampling step, the $g(E_\mathrm{V})$ of the currently visited energy bin E_V is multiplied by f, and the corresponding $H(E_\mathrm{V})$ is incremented by 1. The inner loop stops if the histogram satisfies the flatness criterion (light red diamond box in the inner green frame). As flatness criterion, $\min H(E) > \frac{x}{100} \cdot \bar{H}(E)$ is usually used, meaning that the minimum of $H(E)$ has to be larger than $x\%$ of the mean value of $H(E)$. The optimal percentage $x\%$ depends on the size and complexity of the system, and is usually

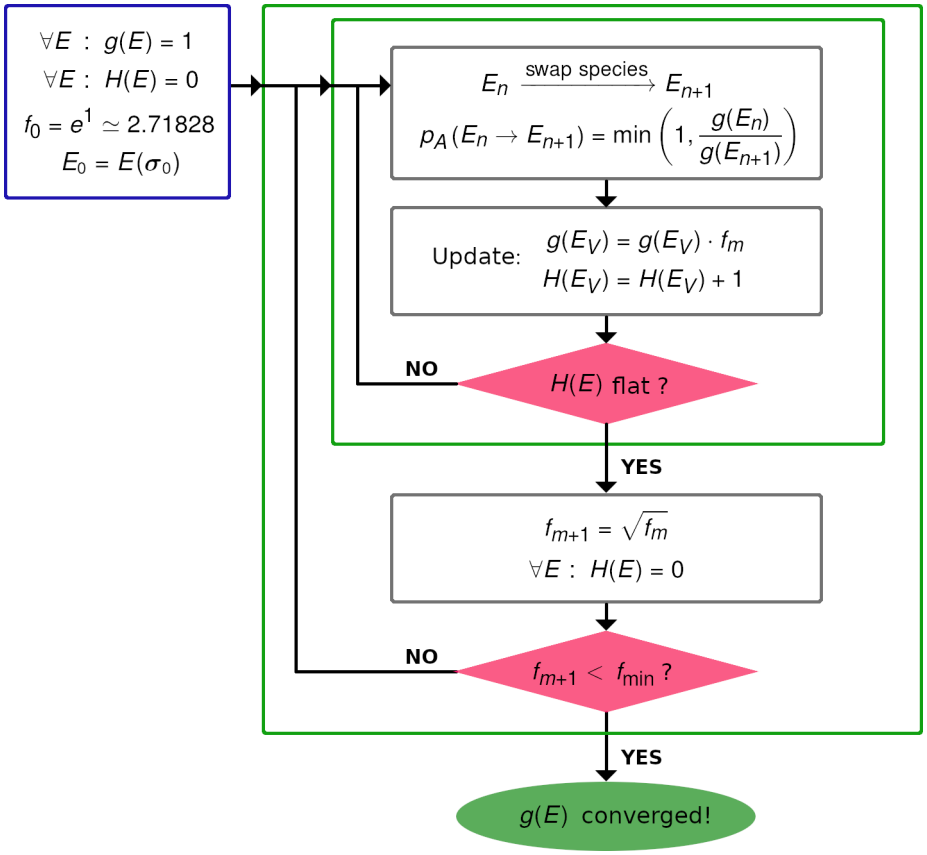

Figure 3.1: Workflow of Wang-Landau algorithm.

increased before a next iteration m of the outer loop begins. Starting usually with $x\% = 50\%$ at $m = 0$, $x\%$ can be increased in the last iterations up to 95% for simple systems, as *e.g.* for the Ising model, while for more complex systems 50-60% is already sufficient to get an accurate $g(E)$ [46, 134, 135]. Larger flatness criteria in those cases are difficult to achieve. In the outer loop, the modification factor is reduced by $f_{m+1} = \sqrt{f_i}$ (other choice is also possible), and eventually the percentage $x\%$ is increased. If f is below a predefined threshold $f_{\min}$, the nested loop stops and the converged $g(E)$ is achieved (for all energy bins). The accuracy of the final $g(E)$ depends on the flatness condition and the final modification factor. Details of the WL algorithm are given in Refs. [45, 46, 136], and examples of applications are found in Refs. [135–138].

From the converged $g(E)$, the thermodynamic properties can be calculated directly at an arbitrary temperature with low computational cost. For instance, the partition function Z and the internal energy U can be evaluated as

$$Z(T) \equiv \sum_E g(E) e^{-\frac{E}{kT}} \tag{28}$$

$$U(T) \equiv \langle E \rangle_T = \frac{1}{Z(T)} \sum_E E\, g(E)\, e^{-\frac{E}{kT}} \ . \tag{29}$$

(Note: In this thesis, sometimes the temperature dependence of Z is highlighted by using the notation Z_T instead.) Having these functions available, the free energy F, the entropy S, and the isobaric specific heat C_p can be calculated as

$$F(T) = k_B T \ln(Z) \tag{30}$$

$$S(T) = \frac{U(T) - F(T)}{T} \tag{31}$$

$$C_p(T) = \frac{\langle E^2 \rangle_T - \langle E \rangle_T^2}{k_B T^2} \ . \tag{32}$$

Here, $\langle E^2 \rangle_T - \langle E \rangle_T^2$ is the fluctuation or dispersion of the energy.

The MMC and the WL sampling methods are powerful tools to estimate thermal averages and predict stable structures. A prerequisite of these methods is that the system is ergodic, *i.e.*, all possible configurations should be attainable during the sampling [133, 139, 140]. This is not fulfilled if the phase space consists of two well-separated phases.

3.3 ELECTRONIC TRANSPORT

A simple and notable model to calculate the electronic conductivity is the classical Drude model, developed in 1900 [141, 142]. Inspired by kinetic gas theory [143–145], it assumes that electrons are non-interacting classical particles that scatter with static ion cores within an average *relaxation time* τ_{D}. The motion of each electron is randomized after a scattering event, *i.e.*, if no electric field is applied the average electron velocity is zero, thus, also the current is zero. In the presence of an electric field, the electrons drift in the direction opposite to the field, and the average electron velocity is different from zero, resulting in a net direct current (DC). The DC conductivity is then given by the Drude formula [146–148]

$$\sigma_{\mathrm{D}} = \frac{e^2 n}{m_e} \tau_{\mathrm{D}} \ , \tag{33}$$

with e as the electron charge, n the electronic density, and m_e the electron mass. Even though good agreement with experiment can be reached with this model in some cases [146, 149], this classical theory is not able to describe the quantum mechanical behavior of electrons together with the complex scattering mechanisms present in solids. Extensions of this model, *e.g.*, made by replacing the Maxwell-Boltzmann distribution by the Fermi-Dirac distribution (Sommerfeld theory developed in 1927 [146, 150]), could predict the correct value of the electronic heat capacity. This model, however, fails to explain the temperature dependence of σ and other transport coefficients.

The most employed approach to obtain the electronic transport coefficients is based on the semi-classical BT equation [21, 22, 151], which is explained in detail in Sec. 3.3.1. In this approach, the electrons are treated as wavepackets, which obey Newton's laws of motion, and the electrical field is a classical field. Aspects of quantum mechanics are introduced by, *e.g.*, using the Fermi-Dirac distribution for the electrons and employing the Bloch theorem. In presence of elastic and weak inelastic scattering processes, the scattering term in the BT equation can be approximated by an empirical relaxation time, that is independent of the non-equilibrium distribution function (relaxation-time approximation). This enables solving the BT equation analytically. For strong inelastic scattering processes, this approximation can not be applied, and the BT equation needs to be solved numerically.

First-principles quantum-mechanical approaches are the Kubo-Greenwood and the memory-function approach, which are based on linear-response theory [55, 152]. The Kubo-Greenwood formula gives, in principle, the exact linear response of the system, however, in practice, the calculation of the DC limit is often unreliable, as discussed in Sec. 3.3.2. The memory-function method, discussed in detail in Sec. 3.3.3, is a generalized form of the Langevin equation in the framework of quantum mechanics [23]. It does not suffer from the problem of determining the DC limit accurately.

3.3.1 *Boltzmann transport equation*

We consider the distribution function $f_{\boldsymbol{k}}(\boldsymbol{r},t)$, which is the probability of finding an electron with wave vector $\boldsymbol{k}$ at position $\boldsymbol{r}$ at time t. For a non-interacting system at thermal equilibrium, $f_{\boldsymbol{k}}(\boldsymbol{r},t)$ is the Fermi-Dirac distribution

$$f^{(0)}_{\boldsymbol{k}}(\boldsymbol{r},t) = \frac{1}{e^{\frac{1}{k_B T}(\epsilon_{\boldsymbol{k}}-\mu)}+1} \tag{34}$$

with μ being the chemical potential, $\epsilon_{\boldsymbol{k}}$ the energy at $\boldsymbol{k}$, k_B the Boltzmann constant, and T the temperature. Since the system is in thermal equilibrium, μ is constant throughout the medium and, thus, it is independent of $\boldsymbol{r}$.

Using $f_{\boldsymbol{k}}(\boldsymbol{r},t)$, the electrical current density $\boldsymbol{j}$ and the heat current density $\boldsymbol{j}_Q$ are defined by the following integrals

$$\boldsymbol{j} = e\sum_{\boldsymbol{k}} \boldsymbol{v}_{\boldsymbol{k}}\, f_{\boldsymbol{k}}(\boldsymbol{r},t) \tag{35}$$

$$\boldsymbol{j}_Q = \sum_{\boldsymbol{k}} (\epsilon_{\boldsymbol{k}}-\mu)\, \boldsymbol{v}_{\boldsymbol{k}}\, f_{\boldsymbol{k}}(\boldsymbol{r},t)\ , \tag{36}$$

with e being the electron charge. In equilibrium, with $f_{\boldsymbol{k}}(\boldsymbol{r},t) = f^{(0)}_{\boldsymbol{k}}(\boldsymbol{r},t)$, no net current flows, and $\boldsymbol{j}$ and $\boldsymbol{j}_Q$ are zero. By applying an external perturbation,

e.g., an electro-magnetic field or a temperature gradient $\nabla_{\boldsymbol{r}} T$, the system is changed away from equilibrium and, thus, a net current is built up. The variation of $f_{\boldsymbol{k}}(\boldsymbol{r}, t)$ with time due to the perturbation can be found by calculating its total time derivative as

$$\frac{\mathrm{d}}{\mathrm{d}t} f_{\boldsymbol{k}}(\boldsymbol{r}, t) = \frac{\partial}{\partial t} f_{\boldsymbol{k}}(\boldsymbol{r}, t) + \frac{\mathrm{d}\boldsymbol{r}}{\mathrm{d}t} \nabla_{\boldsymbol{r}} f_{\boldsymbol{k}}(\boldsymbol{r}, t) + \frac{\mathrm{d}\boldsymbol{k}}{\mathrm{d}t} \nabla_{\boldsymbol{k}} f_{\boldsymbol{k}}(\boldsymbol{r}, t) + \left(\frac{\partial f}{\partial t}\right)_{\text{scatt.}} . \quad (37)$$

The last term is the scattering term, which describes the change of the momentum due to scattering events, *e.g.*, with defects, phonons, and other electrons in the system. In Eq. (37), the time derivative of $\boldsymbol{r}$ is the electron velocity $\boldsymbol{v}$. Furthermore, the time derivative of $\boldsymbol{k}$ can be replaced by the applied external force $\boldsymbol{F}_{\text{ext}} = \hbar \, \mathrm{d}\boldsymbol{k}/\,\mathrm{d}t$. $\boldsymbol{F}_{\text{ext}}$ is the force acting on an electron with charge e due to an electric field $\boldsymbol{E}$ and magnetic field $\boldsymbol{B}$, and it is given by $e\,[\boldsymbol{E} + \boldsymbol{v} \times \boldsymbol{B}]$. According to Liouville's Theorem [153, 154], the total time variation is zero. Hence, it follows:

$$0 = \frac{\partial}{\partial t} f_{\boldsymbol{k}}(\boldsymbol{r}, t) + \boldsymbol{v} \nabla_{\boldsymbol{r}} f_{\boldsymbol{k}}(\boldsymbol{r}, t) + \frac{e}{\hbar} [\boldsymbol{E} + \boldsymbol{v} \times \boldsymbol{B}] \nabla_{\boldsymbol{k}} f_{\boldsymbol{k}}(\boldsymbol{r}, t) + \left(\frac{\partial f}{\partial t}\right)_{\text{scatt.}} . \quad (38)$$

This equation is called Boltzmann transport (BT) equation [21, 22]. In a steady state, *i.e.*, in the presence of a steady current, the term with the explicit time dependence $\partial f_{\boldsymbol{k}}/\partial t$ vanishes.

The change of the distribution function $f_{\boldsymbol{k}}$ away from equilibrium can be defined as $\delta f_{\boldsymbol{k}} = f_{\boldsymbol{k}} - f_{\boldsymbol{k}}^{(0)}$. We derive the linearized BT equation by keeping in Eq. (38) only terms that are first-order in the perturbation. With this, the derivatives $\nabla_{\boldsymbol{r}} f_{\boldsymbol{k}}$ and $\nabla_{\boldsymbol{k}} f_{\boldsymbol{k}}$ give [151]

$$\nabla_{\boldsymbol{r}} f_{\boldsymbol{k}} = \frac{\epsilon_{\boldsymbol{k}} - \mu}{T} \nabla_{\boldsymbol{r}} T \left(-\frac{\partial f_{\boldsymbol{k}}^{(0)}}{\partial \epsilon_{\boldsymbol{k}}}\right) \quad (39)$$

$$\nabla_{\boldsymbol{k}} f_{\boldsymbol{k}} = \hbar \boldsymbol{v}_{\boldsymbol{k}} \frac{\partial f_{\boldsymbol{k}}^{(0)}}{\partial \epsilon_{\boldsymbol{k}}} . \quad (40)$$

To obtain these equations, the chemical potential is assumed to be uniform ($\nabla_{\boldsymbol{r}} \mu = 0$). Inserting Eqs. (39) and (40) in Eq. (38), the term containing the magnetic field $\boldsymbol{B}$ vanishes identically, since $\boldsymbol{v}_{\boldsymbol{k}} \cdot (\boldsymbol{v}_{\boldsymbol{k}} \times \boldsymbol{B}) = 0$. Hence, we arrive at the linearized BT equation

$$\left(\frac{\partial f}{\partial t}\right)_{\text{scatt.}} = -\frac{\partial f_{\boldsymbol{k}}^{(0)}}{\partial \epsilon_{\boldsymbol{k}}} \boldsymbol{v}_{\boldsymbol{k}} \left(e\boldsymbol{E} - \frac{\epsilon_{\boldsymbol{k}} - \mu}{T} \nabla_{\boldsymbol{r}} T\right) . \quad (41)$$

In the relaxation-time approximation (RTA), the scattering term on the left side of Eq. (41) takes the simple form [21, 22]

$$\left(\frac{\partial f}{\partial t}\right)_{\text{scatt.}} = -\frac{f_{\boldsymbol{k}} - f_{\boldsymbol{k}}^{(0)}}{\tau_{\boldsymbol{k}}} = -\frac{\delta f_{\boldsymbol{k}}}{\tau_{\boldsymbol{k}}} \ . \tag{42}$$

It implies that the perturbed $f_{\boldsymbol{k}}$ will relax to its equilibrium state, with the relaxation time constant $\tau_{\boldsymbol{k}}$, after the perturbing field is removed. Thus, the RTA can only be applied in the absence of inelastic scattering processes. Inserting Eq. (42) into Eq. (41), we obtain an explicit expression for the change of $f_{\boldsymbol{k}}$:

$$\delta f_{\boldsymbol{k}} = f_{\boldsymbol{k}} - f_{\boldsymbol{k}}^{(0)} = -\frac{\partial f_{\boldsymbol{k}}^{(0)}}{\partial \epsilon_{\boldsymbol{k}}} \tau_{\boldsymbol{k}} \ \boldsymbol{v}_{\boldsymbol{k}} \left(e\boldsymbol{E} - \frac{\epsilon_{\boldsymbol{k}} - \mu}{T} \ \nabla_{\boldsymbol{r}} \, T \right) \ . \tag{43}$$

This is the linearized BT equation in the RTA.

Inserting Eq. (43) in Eqs. (35) and (36), $\boldsymbol{j}$ and $\boldsymbol{j}_Q$ can be expressed in terms of three transport coefficients, namely the electrical conductivity $\boldsymbol{\sigma}$, the Seebeck coefficient $\boldsymbol{S}$, and the electronic thermal conductivity $\boldsymbol{\kappa}_e'$, as

$$\boldsymbol{j} = \boldsymbol{\sigma} \left(\boldsymbol{E} - \boldsymbol{S} \nabla T \right) \tag{44}$$

$$\boldsymbol{j}_Q = \boldsymbol{\sigma} \boldsymbol{S} \, T \, \boldsymbol{E} - \boldsymbol{\kappa}_e' \nabla T \tag{45}$$

with

$$\boldsymbol{\sigma} = -e \sum_{\boldsymbol{k}} \frac{\partial f_{\boldsymbol{k}}^{(0)}}{\partial \epsilon_{\boldsymbol{k}}} \tau_{\boldsymbol{k}} \ \boldsymbol{v}_{\boldsymbol{k}} \otimes \boldsymbol{v}_{\boldsymbol{k}} \tag{46}$$

$$\boldsymbol{\sigma} \boldsymbol{S} = -e \, k_B \sum_{\boldsymbol{k}} \frac{\partial f_{\boldsymbol{k}}^{(0)}}{\partial \epsilon_{\boldsymbol{k}}} \tau_{\boldsymbol{k}} \ \boldsymbol{v}_{\boldsymbol{k}} \otimes \boldsymbol{v}_{\boldsymbol{k}} \, \frac{\epsilon_{\boldsymbol{k}} - \mu}{k_B T} \tag{47}$$

$$\boldsymbol{\kappa}_e' = -k_B^2 T \sum_{\boldsymbol{k}} \frac{\partial f_{\boldsymbol{k}}^{(0)}}{\partial \epsilon_{\boldsymbol{k}}} \tau_{\boldsymbol{k}} \ \boldsymbol{v}_{\boldsymbol{k}} \otimes \boldsymbol{v}_{\boldsymbol{k}} \left(\frac{\epsilon_{\boldsymbol{k}} - \mu}{k_B T} \right)^2 \ . \tag{48}$$

These transport coefficients are tensors as evident from the dyadic product of the velocities $\boldsymbol{v}_{\boldsymbol{k}}$. The summation runs over all states in $\boldsymbol{k}$-space. In solids, these states depend also on the band index n, which has been omitted for simplicity so far. In the following, we write $n\boldsymbol{k}$ instead of $\boldsymbol{k}$.

While $\boldsymbol{\kappa}_e'$ is the electronic thermal conductivity for zero electrochemical potential gradient inside the sample, the conventional electronic thermal conductivity $\boldsymbol{\kappa}_e$ is defined for $\boldsymbol{j} = 0$ [155]. Inserting $\boldsymbol{\sigma} \boldsymbol{E} = \boldsymbol{j} + \boldsymbol{\sigma} \boldsymbol{S} \nabla T$ (Eq. (44)) in Eq. (45), we obtain

$$\boldsymbol{j}_Q = \boldsymbol{S} T \boldsymbol{j} - \boldsymbol{\kappa}_e \nabla T \ . \tag{49}$$

Thus, $\boldsymbol{\kappa}_e$ is given by

$$\boldsymbol{\kappa}_e \;=\; \boldsymbol{\kappa}'_e - \boldsymbol{\sigma}\boldsymbol{S}^2 T \;. \tag{50}$$

The integrals in Eqs. (46), (47), and (48) can be written in a way that is more convenient for calculations by defining the energy-dependent transport distribution function,

$$\boldsymbol{\Xi}(\epsilon) = \sum_{n\boldsymbol{k}} \tau_{n\boldsymbol{k}}\; \boldsymbol{v}_{n\boldsymbol{k}} \otimes \boldsymbol{v}_{n\boldsymbol{k}}\, \delta(\epsilon - \epsilon_{n\boldsymbol{k}}) \;. \tag{51}$$

Using this kernel, the transport coefficients can be recast as

$$\boldsymbol{\sigma} \;=\; -e^2 \int \mathrm{d}\epsilon\; \frac{\partial f^{(0)}}{\partial \epsilon}\; \boldsymbol{\Xi}(\epsilon) \tag{52}$$

$$\boldsymbol{\sigma}\boldsymbol{S} \;=\; -e\, k_B \int \mathrm{d}\epsilon\; \frac{\partial f^{(0)}}{\partial \epsilon}\; \boldsymbol{\Xi}(\epsilon)\; \frac{\epsilon - \mu}{k_B T} \tag{53}$$

$$\boldsymbol{\kappa}'_e \;=\; -k_B^2 T \int \mathrm{d}\epsilon\; \frac{\partial f^{(0)}}{\partial \epsilon}\; \boldsymbol{\Xi}(\epsilon)\; \left(\frac{\epsilon - \mu}{k_B T}\right)^2 \;. \tag{54}$$

In practice, the transport coefficients are evaluated for a given temperature T and chemical potential μ. A doped material can be simulated by adjusting the chemical potential according to the material's charge concentration, while the electronic band structure remain unaffected (rigid band model [156, 157]).

We note at this point that the classical Drude formula, as defined in Eq. (33), can be recovered from Eq. (52) evaluated at very low temperature. For $k_B T \ll \mu$, the derivative $\partial f^{(0)}/\partial\epsilon$ turns effectively into a delta around μ, $\delta(\epsilon - \mu)$. Employing, in addition, some relations from the free-electron gas (FEG), $\epsilon_{\boldsymbol{k}} = \hbar^2 k^2/(2m_e)$ and $n = k_F^3/(3\pi^2)$ with k_F as the Fermi wave vector, we obtain $\tau = \tau_{\mathrm{D}}$. Consequently, the rate $1/\tau_{\mathrm{D}}$ at which the velocity reduces is the same as the rate at which the electron distribution relaxes to its equilibrium state.

3.3.2 *Kubo-Greenwood approach*

The electrical and heat current densities, as defined by Eqs. (44) and (45), can be rewritten using Onsager's reciprocal relations [158] as:

$$\boldsymbol{j} \;=\; \frac{1}{e}\left(eL_{11}\boldsymbol{E} + \frac{L_{12}\nabla T}{T}\right) \tag{55}$$

$$\boldsymbol{j}_Q \;=\; \frac{1}{e}\left(eL_{21}\boldsymbol{E} + \frac{L_{22}\nabla T}{T}\right) \;. \tag{56}$$

Here, $L_{\nu l}$ ($\nu, l = 1, 2$) are called Onsager coefficients [159]. In general, they are tensors, *i.e.* $\boldsymbol{L}_{\nu l}$. For simplicity, we restrict the discussion to scalar coefficients. Using Eqs. (55) and (56), the transport coefficients σ, S, and κ are given by:

$$\sigma = L_{11}\,, \qquad S = \frac{L_{12}}{TL_{11}}\,, \qquad \kappa = \frac{1}{T}\left(L_{22} - \frac{L_{12}^2}{TL_{11}}\right)\,. \tag{57}$$

Within Kubo's linear-response theory [55], the frequency-dependent Onsager coefficients $L_{\nu l}(\omega)$ are obtained from the following expression [159]:

$$L_{\nu l}(\omega) = \frac{2\pi(-e)^{4-\nu-l}}{3V\omega} \sum_{\boldsymbol{k}nm} |\langle n\boldsymbol{k}|\boldsymbol{v}|m\boldsymbol{k}\rangle|^2 \left(f_{n\boldsymbol{k}} - f_{m\boldsymbol{k}}\right) \times \left(\frac{\epsilon_{m\boldsymbol{k}} + \epsilon_{n\boldsymbol{k}}}{2} - h_e\right)^{\nu+l-2} \delta(\epsilon_{m\boldsymbol{k}} - \epsilon_{n\boldsymbol{k}} - \hbar\omega)\,. \tag{58}$$

Here, $\langle n\boldsymbol{k}|\boldsymbol{v}|m\boldsymbol{k}\rangle$ are the matrix elements of the velocity operator $\boldsymbol{v}$, $f_{n\boldsymbol{k}}$ the Fermi occupation factor of Block state $|n\boldsymbol{k}\rangle$ with wave vector $\boldsymbol{k}$ and band index n, $\epsilon_{n\boldsymbol{k}}$ the eigenenergies, and h_e the enthalpy per electron, which is defined as $h_e = \mu + Ts$ with s as the entropy per electron. (h_e stems from the definition of the heat current operator according to Ref. [160].) The expression for $L_{11}(\omega)$ is identical to the Kubo-Greenwood formula [55, 161]. The static DC Onsager coefficients $L_{\nu l}$ are obtained by the zero-frequency limit of $L_{\nu l}(\omega)$ as

$$L_{\nu l} = \lim_{\omega\to 0} L_{\nu l}(\omega)\,. \tag{59}$$

The calculation of the transport coefficients using Kubo's linear-response formalism is free of phenomenological parameters: In contrast to BT, in the Kubo-Greenwood approach disorder is simulated by building supercells and replacing some of the atoms in the crystal by a different species (substitutional disorder in alloys). However, to obtain non-zero contributions in the sum of Eq. (58) for ω's close to zero, the energy difference between discretized states near the Fermi level needs to be indefinitely small. This can be realized by very large supercells, since here the discretization of the energy states $\epsilon_{n\boldsymbol{k}}$ is refined due to band structure folding. The computation of very large supercells, however, is often out of reach. To obtain the DC limit from a supercell, whose size is still accessible at reasonable computational cost, a broadening of the δ-function in Eq. (58) is used in real calculations. The drawback of this broadening is that its type and width may highly affect the result of the limit $\omega \to 0$, as it is demonstrated for σ in Ref. [162].

So far, the Kubo-Greenwood approach has been applied to study fluid systems at extreme conditions (high temperature and high pressure) [159, 163–167] and recently also for solids [162, 168].

3.3.3 *Memory-function formalism for homogeneous systems*

The memory-function approach, developed by Mori [23], is able to describe systems in a disorder potential at all coupling strengths, thus it can be used to examine transitions from a metallic to an insulting regime (Anderson transition). Further advantages are that it does not suffer from the limiting procedure to calculate the DC conductivity as the Kubo-Greenwood approach, and it can account for finite-temperature effects. In the mode coupling approximation, this approach was applied to the homogeneous electron gas by Götze [56–58]. Thereafter, applications have been demonstrated for two-dimensional [169–173] and three-dimensional systems [173, 174].

In this section, we start by introducing concepts used in the memory-function approach [23]. They comprise Kubo's internal product [23, 55], that provides a general expression for correlation functions, the time evolution operator in reciprocal space, and its equation of motion projected onto the subspace of interest (relevant subspace). Having these concepts at hand, we present the memory-function approach for the homogeneous electron gas in a static random disorder potential, as discussed by Götze in Ref. [58]. Here, the Hamiltonian of the disordered system is defined and its equation of motion is derived. This equation can be solved self-consistently. At the end, we arrive at an expression for the conductivity for disordered systems.

The equations and results published by Götze in Ref. [58] are sometimes difficult to access. Thus, in the following, we give more details about their interpretation and derivation in some parts. These details were worked out within a joint collaboration with Prof. Sofo and his group from Pennsylvania State University.

Kubo's internal product

We consider a system in thermodynamic equilibrium described by the Hamiltonian H_0. In this system, the expectation value of a dynamical variable A is given by

$$\langle A\rangle_0 = \frac{1}{Z_0}\,\mathrm{Tr}(e^{-\beta H_0}A)\ , \tag{60}$$

with $Z_0 = \mathrm{Tr}(e^{-\beta H_0})$ being the partition function in equilibrium and $\beta = 1/\left(k_B T\right)$. With this, Kubo's internal product between A and another dynamical variable B is defined as [23, 55]

$$(B^\dagger|A) = \int_0^\beta \mathrm{d}\lambda\,\langle e^{\lambda H_0}[B^\dagger - \langle B\rangle_0]e^{-\lambda H_0}\,[A - \langle A\rangle_0]\rangle_0\ . \tag{61}$$

It has all properties of a scalar product in vector space, *i.e.*, $(A|A) \geq 0$ for all A (positivity), $(A|A) = 0$ only if $A = 0$ (definiteness), $(A + B|C) = (A|C) + (B|C)$ (additivity), $(\gamma A|B) = \gamma(A|B)$ with $\gamma \in \mathbb{C}$ (homogeneity), and $\overline{(B^\dagger|A)} = (A^\dagger|B)$ (conjugate symmetry). In the following, Kubo's internal product is also named correlation function or relaxation function. In what follows, it is assumed that $\langle A\rangle_0$ and $\langle B\rangle_0$ are zero.

Relation between internal product and linear-response function

Before we introduce the memory-function formalism, we discuss the relation of Kubo's internal product to the retarded Kubo's linear-response function, defined as (here and in the following, $\hbar = 1$)

$$\chi_{AB}(t) = -\mathrm{i}\,\Theta(t)\left\langle\left[A^\dagger(t), B(0)\right]\right\rangle_0 \ . \tag{62}$$

Here, $\Theta(t)$ is the Heaviside step function, which is one for $t \geq 0$ and zero for $t < 0$. The time derivative of Kubo's internal product $\phi_{AB}(t) = (A^\dagger(t)|B)$ between the variables A and B can be expressed in terms of the expectation value of their commutator as (derivation shown in Appendix A.2.1):

$$\begin{aligned} \frac{\mathrm{d}}{\mathrm{d}t}\phi_{AB}(t) &= \frac{\partial}{\partial t}(A^\dagger(t)|B) && (63)\\ &= i\langle[A^\dagger(t), B]\rangle \ . && (64) \end{aligned}$$

Using Eq. (62), it follows:

$$-\,\Theta(t)\,\frac{\mathrm{d}}{\mathrm{d}t}\phi_{AB}(t) = \chi_{AB}(t) \ . \tag{65}$$

The Laplace transform of $\phi_{AB}(t)$ then gives

$$\begin{aligned} \phi_{AB}(z) &= \int_0^\infty \mathrm{d}t\, e^{-zt}\phi_{AB}(t) && (66)\\ &= \int_0^\infty \mathrm{d}t\, \left[\frac{\mathrm{d}}{\mathrm{d}t}\left(-\frac{e^{-zt}}{z}\phi_{AB}(t)\right) + \frac{e^{-zt}}{z}\left(\frac{\mathrm{d}}{\mathrm{d}t}\phi_{AB}\right)\right] && (67)\\ &= \left(-\frac{e^{-zt}}{z}\phi_{AB}(t)\right)\Bigg|_0^\infty - \frac{1}{z}\int_0^\infty \mathrm{d}t\, e^{-zt}\chi_{AB}(t) && (68)\\ &= \frac{1}{z}\phi(0) - \frac{1}{z}\chi_{AB}(z) \ . && (69) \end{aligned}$$

Here, we use that $\phi(t \to \infty)$ approaches zero by assuming that the system relaxes back to equilibrium at infinite time. Furthermore, we note that

$$\chi(z=0) = \int_0^\infty \mathrm{d}t \ \chi(t) \tag{70}$$

$$= -\int_0^\infty \mathrm{d}t \, \frac{\partial \phi(t)}{\partial t} = -\phi(t \to \infty) + \phi(0) = \phi(0) \ . \tag{71}$$

Thus, we obtain the relation

$$\phi_{AB}(z) = -\frac{1}{z} \left[\chi_{AB}(z) - \chi_{AB}(z=0) \right] \ . \tag{72}$$

Time evolution

The time evolution of a dynamical variable $A(t)$ in the Heisenberg picture is given by

$$\frac{\mathrm{d}}{\mathrm{d}t} A(t) = \mathrm{i} \left[H, A \right] := \mathrm{i}\mathcal{L} A(t) \ , \tag{73}$$

where $\mathcal{L}$ is the Liouville operator. Its formal solution is described as

$$A(t) = e^{\mathrm{i}Ht} A e^{-iHt} := e^{\mathrm{i}\mathcal{L}t} A \ . \tag{74}$$

Using this, the time dependence in the correlation function $\tilde{\phi}$ between the variables $A(t)$ and B can be expressed as

$$\tilde{\phi}(t) = (A^\dagger(t)|B) = \left(A^\dagger | e^{-\mathrm{i}\mathcal{L}t} | B \right) \ . \tag{75}$$

Its Laplace transform gives

$$\phi(z) = \int_0^\infty \mathrm{d}t e^{-\mathrm{i}zt} \tilde{\phi}(t) = \mathrm{i} \int_0^\infty \mathrm{d}t \left(A^\dagger \left| e^{-\mathrm{i}(z-\mathcal{L})t} \right| B \right) \tag{76}$$

$$= \left(A^\dagger \left| \frac{1}{\mathcal{L} - z} \right| B \right) \ , \tag{77}$$

with z being a complex frequency. From this we can define the resolvent in reciprocal space

$$\mathcal{R}(z) = \frac{1}{\mathcal{L} - z} \ . \tag{78}$$

It embodies the full time evolution of the system. The time-dependent resolvent $\mathcal{R}(t)$ is obtained from the inverse Laplace transform and is given by

$$\mathcal{R}(t) = e^{\mathrm{i}\mathcal{L}t} \ . \tag{79}$$

The resulting equation of motion for $\mathcal{R}(t)$ reads:

$$\frac{\mathrm{d}}{\mathrm{d}t}\mathcal{R}(t) = \mathrm{i}\mathcal{L}R(t) \ . \tag{80}$$

Equation of motion projected onto the relevant subspace

Monitoring the time evolution of all variables of the system is not always reasonable, since usually we are interested in only a small subset of them, as *e.g.* the current along $\boldsymbol{q}$. This subset can be considered as the relevant subspace, while the remaining variables form the "bath" (also called outer space).

From the mathematical side, these two orthogonal subspaces can be described by projectors. The relevant subspace is represented by the projector $\mathcal{P}$ and the complement by $\mathcal{Q}$. Together, they define the whole space, *i.e.*:

$$\mathcal{P} + \mathcal{Q} = 1 \ . \tag{81}$$

Since they are projectors, it follows $\mathcal{P}^2 = \mathcal{P}$ and $\mathcal{Q}^2 = \mathcal{Q}$. Employing these projectors in the equation of motion for the resolvent in reciprocal space $\mathcal{R}(z)$ (derivation shown in Appendix A.2.2), we obtain:

$$\mathcal{P}\mathcal{R}(z)\mathcal{P} = \frac{\mathcal{P}}{\mathcal{P}(\mathcal{L}-z)\mathcal{P} - \mathcal{P}\mathcal{L}\mathcal{Q}(\mathcal{Q}\mathcal{L}\mathcal{Q}-z)^{-1}\mathcal{Q}\mathcal{L}\mathcal{P}} \ . \tag{82}$$

This equation describes the dynamics of the system in the relevant subspace. Having a closer look to the denominator of Eq. (82), the first part $\mathcal{P}(\mathcal{L}-z)\mathcal{P}$ describes the dynamics of the system ignoring the "bath", and the second part $\mathcal{P}\mathcal{L}\mathcal{Q}(\mathcal{Q}\mathcal{L}\mathcal{Q}-z)^{-1}\mathcal{Q}\mathcal{L}\mathcal{P}$ accounts for the interaction of the system with the "bath" by projecting the time evolution $\mathcal{L}$ first onto the outer space $\mathcal{Q}$ and then back to $\mathcal{P}$.

Similar kinds of propagators have been introduced implicitly in damping theory [23, 175, 176]. We will make use of Eq. (82) later to derive the equation of motion for a disordered system.

Hamiltonian of a disordered system

Within the memory-function formalism, we study in this section a three-dimensional non-interacting electron gas in a static random disorder potential. The Hamiltonian of this system is defined as

$$H = H_0 + H' \ , \tag{83}$$

with

$$H_0 = \sum_{\boldsymbol{k}} \left[\frac{\hbar^2 k^2}{2m_e} - \epsilon_F \right] c^\dagger_{\boldsymbol{k}} c_{\boldsymbol{k}} = \sum_{\boldsymbol{k}} \epsilon_{\boldsymbol{k}} c^\dagger_{\boldsymbol{k}} c_{\boldsymbol{k}} \tag{84}$$

and

$$H' = \sum_{\boldsymbol{q}} U(\boldsymbol{q}) \rho^\dagger(\boldsymbol{q}) \ . \tag{85}$$

H_0 is the Hamiltonian of the homogeneous non-interacting electron gas with $\epsilon_{\boldsymbol{k}} = \hbar^2 k^2/(2m_e)$ as the energy at wave vector $\boldsymbol{k}$ given with respect to the Fermi energy ϵ_F, and $c^\dagger_{\boldsymbol{k}}$ ($c_{\boldsymbol{k}}$) as the creation (annihilation) operator of an electron at state $\boldsymbol{k}$. H' describes the interaction of the density fluctuation $\rho(\boldsymbol{q})$ of the electron gas with the impurity disorder potential given by the Fourier transform $U(\boldsymbol{q})$. The potential square average $\langle |U(\boldsymbol{q})|^2 \rangle$ is defined as a well-behaved function of the wave vector modulus $|\boldsymbol{q}| = q$. Further, we introduce the following quantities: the electronic gas density n, the electron mass m_e, the Fermi wave vector $k_F = (3\pi^2 n)^{1/3}$, the Fermi energy $\epsilon_F = k_F^2/(2m_e)$, and the density of states at the Fermi level $\rho_F = m_e k_F/\pi^2$.

The Fourier transform of density fluctuation operator for wave vector $\boldsymbol{q}$ is

$$\rho(\boldsymbol{q}) = \sum_{\boldsymbol{k}} \xi_{\boldsymbol{k}}(\boldsymbol{q}) \ , \tag{86}$$

with the dynamical variable

$$\xi_{\boldsymbol{k}}(\boldsymbol{q}) = c^\dagger_{\boldsymbol{k}-\boldsymbol{q}/2} c_{\boldsymbol{k}+\boldsymbol{q}/2} \ . \tag{87}$$

The operator $\xi_{\boldsymbol{k}}$ annihilates a fermion at $\boldsymbol{k}+\boldsymbol{q}/2$ and creates one at $\boldsymbol{k}-\boldsymbol{q}/2$, thus $\rho(\boldsymbol{q})$ is a linear superposition of electron-hole pairs.

Current operator

To calculate the current $\boldsymbol{j}$ originating from the density fluctuations of the system, we use the continuity equation

$$\frac{\partial}{\partial t} \rho(\boldsymbol{q}, t) = \mathrm{i}\mathcal{L}\rho(\boldsymbol{q}) = -\boldsymbol{q}\, \boldsymbol{j}(\boldsymbol{q}) \ . \tag{88}$$

Using the definition of $\mathcal{L}$ (see Eq. (73)), the Liouville operator acting on the density gives the following

$$\mathcal{L}\rho(\boldsymbol{q}) = [H, \rho(\boldsymbol{q})] = [H_0, \rho(\boldsymbol{q})] + [H_1, \rho(\boldsymbol{q})] \tag{89}$$

$$[H_0, \rho(\boldsymbol{q})] = \sum_{\boldsymbol{k}} \epsilon_{\boldsymbol{k}}(\boldsymbol{q}) \xi_{\boldsymbol{k}}(\boldsymbol{q}) = \sum_{\boldsymbol{k}} \frac{\boldsymbol{q}\boldsymbol{k}}{m_e} \xi_{\boldsymbol{k}}(\boldsymbol{q}) \tag{90}$$

$$[H_1, \rho(\boldsymbol{q})] = 0 \ , \tag{91}$$

with $\epsilon_{\boldsymbol{k}}(\boldsymbol{q}) = \epsilon_{\boldsymbol{k}-\boldsymbol{q}/2} - \epsilon_{\boldsymbol{k}+\boldsymbol{q}/2} = \boldsymbol{q}\boldsymbol{k}/m_e$. Projecting Eq. (88) along the direction of $\boldsymbol{q}$ gives the longitudinal current as

$$j(\boldsymbol{q}) = \frac{1}{q}\sum_{\boldsymbol{k}} \epsilon_{\boldsymbol{k}}(\boldsymbol{q})\xi_{\boldsymbol{k}}(\boldsymbol{q}) = \sum_{\boldsymbol{k}} \frac{\boldsymbol{q}\boldsymbol{k}}{qm}\xi_{\boldsymbol{k}}(\boldsymbol{q}) \ . \tag{92}$$

Defining the relevant operator subspace

Now, we investigate the time evolution of the disordered system with the Hamiltonian in Eq. (83). For this, we make use of the projected equation of motion (see Eq. (82)). Before this equation can be applied, the two projectors $\mathcal{P}$ and $\mathcal{Q}$, that project onto the relevant subspace and the outer space, respectively, need to be defined. The projector $\mathcal{P}$ can be written as

$$\mathcal{P}_{\boldsymbol{q}} \bullet = \sum_{\alpha} |A_\alpha(\boldsymbol{q})) \, (A_\alpha(\boldsymbol{q})| \bullet) \ , \tag{93}$$

with

$$A_\alpha(\boldsymbol{q}) = \sum_{\boldsymbol{k}} a_\alpha^{\boldsymbol{q}}(\boldsymbol{k})\xi_{\boldsymbol{k}}(\boldsymbol{q}) \ . \tag{94}$$

The operators $A_\alpha(\boldsymbol{q})$ ($\alpha = 0, 1, \dots$) are built from the operators $\xi_{\boldsymbol{k}}$ and are chosen such that they fulfill the orthogonality condition

$$(A_\alpha | A_\beta) = \delta_{\alpha\beta} \ . \tag{95}$$

At this point, we note that $\mathcal{P}_{\boldsymbol{q}}$ is defined for a given $\boldsymbol{q}$ (indicated by index $\boldsymbol{q}$). Wave vectors different from $\boldsymbol{q}$ are not part of the relevant subspace and are contained in the outer subspace $\mathcal{Q}$.

The longitudinal current $j(\boldsymbol{q})$ and the density $\rho(\boldsymbol{q})$ have the same form as $A_\alpha(\boldsymbol{q})$ (built from $\xi_{\boldsymbol{k}}$) and are orthogonal:

$$(\rho(\boldsymbol{q})|j(\boldsymbol{q})) \sim (\rho(\boldsymbol{q})|\mathcal{L}\rho(\boldsymbol{q})) = \langle [\boldsymbol{\rho}(\boldsymbol{q}), \boldsymbol{\rho}[\boldsymbol{q}]\rangle = 0 \ . \tag{96}$$

Thus, we use $j(\boldsymbol{q})$ and $\rho(\boldsymbol{q})$ to define the projector $\mathcal{P}$ (see Eq. (93)), *i.e.*,

$$A_0(\boldsymbol{q}) = (g(\boldsymbol{q}))^{-1/2} \, \rho(\boldsymbol{q}) \tag{97}$$

$$A_1(\boldsymbol{q}) = \left(\frac{m_e}{n}\right)^{1/2} j(\boldsymbol{q}) \ . \tag{98}$$

The prefactors here originate from the normalization of the A_α's and are obtained as $(\rho(\boldsymbol{q})|\rho(\boldsymbol{q})) = g(\boldsymbol{q})$ and $(j(\boldsymbol{q})|j(\boldsymbol{q})) = n/m_e$.

Equation of motion of a disordered system

Using Eq. (93) for $\mathcal{P}$ in Eq. (82), the projected equation of motion takes the following form:

$$\sum_{\beta} \left[\omega_{\alpha\beta} - z\delta_{\alpha\beta} - m_{\alpha\beta}(\boldsymbol{q}, z)\right] \phi_{\beta\gamma}(\boldsymbol{q}, z) = \delta_{\alpha\gamma}] \ , \tag{99}$$

with

$$\begin{aligned} \phi_{\alpha\beta} &= (A_\alpha(\boldsymbol{q})|\mathcal{R}(z)|A_\beta(\boldsymbol{q})) & (100)\\ \omega_{\alpha\beta} &= (A_\alpha(\boldsymbol{q})|\mathcal{L}|A_\beta(\boldsymbol{q})) & (101)\\ m_{\alpha\beta}(\boldsymbol{q}, z) &= (A_\alpha(\boldsymbol{q})|\mathcal{L}\mathcal{Q}\tilde{\mathcal{R}}(z)\mathcal{Q}\mathcal{L}|A_\beta(\boldsymbol{q})) \ . & (102) \end{aligned}$$

Here, $\tilde{\mathcal{R}}(z) = (\mathcal{Q}\mathcal{L}\mathcal{Q} - z)^{-1}$. $\phi_{\alpha\beta}$ is the correlation function between $A_\alpha(\boldsymbol{q})$ and $A_\beta(\boldsymbol{q})$, and $m_{\alpha\beta}(\boldsymbol{q}, z)$ is the memory function. $m_{\alpha\beta}(\boldsymbol{q}, z)$ originates from the second term in the denominator of Eq. (82), $\mathcal{P}\mathcal{L}\mathcal{Q}\tilde{\mathcal{R}}(z)\mathcal{Q}\mathcal{L}\mathcal{P}$. It performs the time evolution of the dynamical variable in the outer space, *i.e.*, for $\boldsymbol{q}' \neq \boldsymbol{q}$ components. $m_{\alpha\beta}$ can be rewritten as

$$m_{\alpha\beta} = (F_\alpha(\boldsymbol{q})|\tilde{\mathcal{R}}(z)|F_\beta(\boldsymbol{q})) \ , \tag{103}$$

with $F_\alpha(\boldsymbol{q})$ being the so-called fluctuating forces

$$F_\alpha(\boldsymbol{q}) = \mathcal{Q}\mathcal{L}A_\alpha(\boldsymbol{q}) \ . \tag{104}$$

Inserting Eq. (94) in Eq. (104), we obtain

$$F_\alpha(\boldsymbol{q}) = \sum_{\boldsymbol{k}} a_\alpha^{\boldsymbol{q}}(\boldsymbol{k}) F_{\boldsymbol{k}}(\boldsymbol{q}) \ , \tag{105}$$

with

$$F_{\boldsymbol{k}}(\boldsymbol{q}) = \mathcal{Q}\mathcal{L}\xi_{\boldsymbol{k}}(\boldsymbol{q}) = \sum_{\boldsymbol{l}} U(\boldsymbol{q} - \boldsymbol{l}) \left[\xi_{\boldsymbol{k}+(\boldsymbol{q}-\boldsymbol{l})/2}(\boldsymbol{l}) - \xi_{\boldsymbol{k}-(\boldsymbol{q}-\boldsymbol{l})/2}(\boldsymbol{l})\right] \ . \tag{106}$$

Where does the name "memory function" come from?

To gain more insight into Eq. (99), we perform the inverse Laplace transform of it:

$$\frac{\mathrm{d}}{\mathrm{d}t}\phi_{\alpha\gamma}(\boldsymbol{q}, t) = \sum_{\beta} \left[-i\omega_{\alpha\beta}\phi_{\beta\gamma}(\boldsymbol{q}, t) - \int_0^t \mathrm{d}t' m_{\alpha\beta}(\boldsymbol{q}, t - t')\phi_{\beta\gamma}(\boldsymbol{q}, t')\right] \ . \tag{107}$$

Expressed in words, the time derivative of the correlation function at time t is equal to the sum of a term containing correlation functions evaluated at the same time t, and a second term which takes into account the past history of

the correlation function. How much the past times are relevant at the present time is measured by the memory function $m_{\alpha\beta}(\boldsymbol{q}, t-t')$. Hence, one can say that the memory function stores or "memorizes" the information of the past times. Since the dynamics in the subspace $\mathcal{P}$ depends on states of the system at past times, it is non-markovian. If you consider the time evolution of the whole system described by $\mathcal{P}+\mathcal{Q}$, the system's dynamics would become markovian and would not have a dependence on past times. Thus, the non-markovian behavior is introduced through separating the phase space into a relevant and outer space.

Approximate solution

In general, Eqs. (100), (101), and (102) are represented by infinite matrices. In order to apply the formalism and find a solution for Eq. (99), approximations are needed. As first approximation, we truncate the infinite matrices to finite $N_{\mathrm{var}} \times N_{\mathrm{var}}$ matrices (N_{var}th-order) by limiting the number of the linearly independent variables A_α ($\alpha = 0, 1, ..., N_{\mathrm{var}}$).

As demonstrated previously, the operators $\rho(\boldsymbol{q})$ and $j(\boldsymbol{q})$ can be used to define A_0 and A_1 through Eqs. (97) and (98), thus $N_{\mathrm{var}} = 1$. The corresponding expressions for their fluctuation forces are evaluated in the following. One can show that

$$
\begin{aligned}
F_0(\boldsymbol{q}) &= \mathcal{Q}\mathcal{L}A_0(\boldsymbol{q}) && (108)\\
&\underset{\sim}{\text{Eq. (97)}} \ \mathcal{Q}\mathcal{L}\rho(\boldsymbol{q}) && (109)\\
&\underset{\sim}{\text{Eq. (89) and Eq. (91)}} \ \mathcal{Q}\left[H_0, \rho(\boldsymbol{q})\right] && (110)\\
&\underset{\sim}{\text{Eq. (90)}} \ \sum_{\boldsymbol{k}} \epsilon_{\boldsymbol{k}}(\boldsymbol{q})\, \mathcal{Q}\, \xi_{\boldsymbol{k}}(\boldsymbol{q}) = 0\ . && (111)
\end{aligned}
$$

It gives zero, since $\xi_{\boldsymbol{k}}(\boldsymbol{q})$ builds the relevant subspace $\mathcal{P}$ while $\mathcal{Q}$ projects onto the outer space. Consequently, there is no fluctuating force acting on the density and the memory function matrix elements $m_{00} = m_{\alpha 0} = m_{\beta 0} = 0$. The fluctuation force $F_1(\boldsymbol{q})$ is given by

$$
F_1(\boldsymbol{q}) = \mathcal{Q}\mathcal{L}A_1(\boldsymbol{q}) = \frac{1}{(nm_e)^{1/2}} \sum_{\boldsymbol{p}} U(\boldsymbol{q}-\boldsymbol{p}) \left[\hat{\boldsymbol{q}}\,(\boldsymbol{q}-\boldsymbol{p})\right] \rho(\boldsymbol{p})\ . \qquad (112)
$$

This equation represents the force that the electronic cloud experiences due to the impurity potential.

According to Götze [58], we define $m = m(\boldsymbol{q}, z) = m_{11}(\boldsymbol{q}, z) = \Big(F_1(\boldsymbol{q})|\tilde{\mathcal{R}}(z)|F_1(\boldsymbol{q})\Big)$. Then, the memory function matrix $\boldsymbol{m}$ can be approximated as

$$\boldsymbol{m} = \begin{pmatrix} 0 & 0 & 0 & \dots \\ 0 & m & 0 & \\ 0 & 0 & m & \\ \vdots & & & \ddots \end{pmatrix} . \tag{113}$$

That means that $\boldsymbol{m}$ is a diagonal matrix with a zero head component. Or equivalently, the matrix elements $m_{\alpha\beta}$ can be expressed in terms of m as $m_{\alpha\beta} = m\delta_{\alpha\beta} - m\delta_{\alpha 0}\delta_{\beta 0}$. Using this, Eq. (99) can be reformulated as follows ($\boldsymbol{q}$- and z-dependence of m is omitted here):

$$\sum_{\beta} \left[(z+m)\delta_{\alpha\beta} - \omega_{\alpha\beta}(\boldsymbol{q})\right] \phi_{\beta\gamma}(\boldsymbol{q}, z) = -\delta_{\alpha\gamma} + m\,\delta_{\alpha 0}\phi_{0\gamma}(\boldsymbol{q}, z) \ . \tag{114}$$

For a system without disorder, *i.e.*, a non-interacting system with the Hamiltonian H_0 (Eq. (84), no perturbation), m is zero and we can write for Eq. (114):

$$\sum_{\beta} \left[z\delta_{\alpha\beta} - \omega_{\alpha\beta}(\boldsymbol{q})\right] \phi^{(0)}_{\beta\gamma}(\boldsymbol{q}, z) = -\delta_{\alpha\gamma} \ . \tag{115}$$

Here, $\phi^{(0)}_{\beta\gamma}$ is the correlation function of the non-interacting system. Now, since z is an arbitrary complex number, we can replace z by $z+m$ in Eq. (115). Writing Eq. (115) with replacing $z \to z+m$ and Eq. (114) in matrix form, we obtain:

$$\left[(z+m)\mathbb{1} - \boldsymbol{\omega}(\boldsymbol{q})\right] \boldsymbol{\phi}^{(0)}(\boldsymbol{q}, z+m) = -\mathbb{1} \tag{116}$$

$$\left[(z+m)\mathbb{1} - \boldsymbol{\omega}(\boldsymbol{q})\right] \boldsymbol{\phi}(\boldsymbol{q}, z) = -\mathbb{1} + m\,\boldsymbol{H}\boldsymbol{\phi}(\boldsymbol{q}, z) \ . \tag{117}$$

Here, $\mathbb{1}$ is the identity matrix, and $\boldsymbol{H}$ the head matrix with a one in the head component and zero in all others. The solution of Eqs. (116) and (117) for $\alpha = 0$ and $\beta = 0$ gives the density-density correlation function of the disordered system $\phi(\boldsymbol{q}, z) \equiv g(\boldsymbol{q})\phi_{00}(\boldsymbol{q}, z) = (\rho(\boldsymbol{q})|\mathcal{R}(z)|\rho(\boldsymbol{q}))$. It has the following form:

$$\phi(\boldsymbol{q}, z) = \frac{\phi^{(0)}(\boldsymbol{q}, z + m(\boldsymbol{q}, z))}{1 + m(\boldsymbol{q}, z)\phi^{(0)}(\boldsymbol{q}, z + m(\boldsymbol{q}, z))/g(\boldsymbol{q})} \ . \tag{118}$$

This is similar to a Dyson equation with the important difference that the kernel m appears in the frequency argument of $\phi^{(0)}$, thus effectively introducing a non-

linear dependence on the kernel. The density-density correlation function of the non-interacting system $\phi^{(0)}(\boldsymbol{q}, z)$ is calculated as

$$\begin{aligned} \phi^{(0)}(\boldsymbol{q}, z) &= g(\boldsymbol{q}, z)\phi_{00}^{(0)}(\boldsymbol{q}, z) && (119) \\ &= (\rho(\boldsymbol{q})|\mathcal{R}_0(z)|\rho(\boldsymbol{q})) && (120) \end{aligned}$$

with $\mathcal{R}_0(z) = (\mathcal{L}_0 - z)^{-1}$ and $\mathcal{L}_0$ representing the time evolution of the non-interacting system, *i.e.*, $\mathcal{L}_0 \bullet = [H_0, \bullet]$.

The mode-coupling approximation

To evaluate the expression for the kernel $m(\boldsymbol{q}, z)$ (Eq. (103) with $\alpha, \beta = 1$), further simplifications are needed. The fluctuating force $F_1(\boldsymbol{q})$, from which m is obtained, is composed of products of the disorder potential $U(\boldsymbol{q}-\boldsymbol{p})$ and the density fluctuations $\rho(\boldsymbol{p})$. Since $U(\boldsymbol{q}-\boldsymbol{p})$ is a static potential, the correlations between the frozen modes of the potential and the dynamical modes of the electronic system are neglected. This is called the mode-coupling approximation. Together with the assumption of macroscopic homogeneity, its leading order is [58]:

$$\begin{aligned} &\Big(U(\boldsymbol{q}-\boldsymbol{p})\rho(\boldsymbol{p}) \Big|\tilde{\mathcal{R}}(z)\Big| U(\boldsymbol{q}-\boldsymbol{p})\rho(\boldsymbol{p})\Big) \\ &\qquad \approx \langle U(\boldsymbol{q}-\boldsymbol{p})\, U(\boldsymbol{q}-\boldsymbol{p})\rangle_{\mathrm{dis}} \, \Big(\rho(\boldsymbol{p}) \Big|\tilde{\mathcal{R}}(z)\Big| \rho(\boldsymbol{p})\Big) \ . \end{aligned} \tag{121}$$

The index dis indicates that U is averaged over different realizations of disorder. The expression for the memory function is then given by [57, 177]

$$m(\boldsymbol{q}, z) = \frac{1}{nm_e}\frac{1}{V}\sum_{\boldsymbol{p}} \langle |U(\boldsymbol{q}-\boldsymbol{p})|^2\rangle_{\mathrm{dis}} \left[\hat{\boldsymbol{q}}\,(\boldsymbol{q}-\boldsymbol{p})\right]^2 \phi(\boldsymbol{p}, z) \ , \tag{122}$$

with $\hat{\boldsymbol{q}}$ being the unit vector in the direction of $\boldsymbol{q}$.

Further approximations

In the following, we introduce the explicit expressions used by Götze in Ref. [58] to study the insulator-conductor transition for the homogeneous electron gas using the memory-function formalism. Here, the expression for $m(\boldsymbol{q}, z)$ is further simplified by neglecting the $\boldsymbol{q}$-dependence in Eq. (122):

$$m(\boldsymbol{q}, z) \approx m(\boldsymbol{q} = 0, z) = M(z) \ . \tag{123}$$

This leads to the transcendental equation

$$M(z) = \frac{1}{3nm_e}\frac{1}{V}\sum_{\boldsymbol{q}} \langle |U(\boldsymbol{q})|^2\rangle \, q^2 \, \phi(\boldsymbol{q}, z) \ , \tag{124}$$

with $q = |\boldsymbol{q}|$ and V being the volume of the system.

To solve Eq. (124), it remains to determine the Fourier transform of the impurity potential $U(\boldsymbol{q})$. In Ref. [58], it is approximated by a square potential (in reciprocal space) with a scalar momentum cut-off at q_0. The potential square average is then defined as

$$\langle |U(\boldsymbol{q})|^2 \rangle = U^2 \frac{6\pi^2}{q_0^3} \theta(q_0 - q) \ . \tag{125}$$

Self-consistency equations

To evaluate $\phi(\boldsymbol{q}, z)$ using Eq. (118) for the homogeneous non-interacting electron gas (FEG), we need apart from $M(z)$ its density-density correlation function. From Eq. (72), it is obtained as

$$\phi^{(0)}(\boldsymbol{q}, z) = -\frac{\chi^{(0)}(\boldsymbol{q}, z) - \chi^{(0)}(\boldsymbol{q}, z = 0)}{z} \ . \tag{126}$$

$\chi^{(0)}(\boldsymbol{q}, z)$ is Kubo's linear-response function of the FEG given by

$$\chi^{(0)}(\boldsymbol{q}, z) = \frac{1}{V} \sum_{\boldsymbol{k}} \frac{f_{\boldsymbol{k}}(\boldsymbol{q})}{z + \epsilon_{\boldsymbol{k}}(\boldsymbol{q})} \ , \tag{127}$$

with $\epsilon_{\boldsymbol{k}}(\boldsymbol{q}) = \epsilon_{\boldsymbol{k}-\boldsymbol{q}/2} - \epsilon_{\boldsymbol{k}+\boldsymbol{q}/2}$ and $f_{\boldsymbol{k}}(\boldsymbol{q}) = f_{\boldsymbol{k}-\boldsymbol{q}/2} - f_{\boldsymbol{k}+\boldsymbol{q}/2}$. Using the simple conversion

$$-\frac{1}{z}\left(\frac{1}{z + \epsilon_{\boldsymbol{k}}(\boldsymbol{q})} - \frac{1}{\epsilon_{\boldsymbol{k}}}\right) = \frac{1}{z + \epsilon_{\boldsymbol{k}}(\boldsymbol{q})} \ \frac{1}{\epsilon_{\boldsymbol{k}}(\boldsymbol{q})} \ , \tag{128}$$

we arrive to the following expression for $\phi^{(0)}(\boldsymbol{q}, z)$:

$$\phi^{(0)}(\boldsymbol{q}, z) = \frac{1}{V} \sum_{\boldsymbol{k}} \frac{1}{z + \epsilon_{\boldsymbol{k}}(\boldsymbol{q})} \ \frac{f_{\boldsymbol{k}}(\boldsymbol{q})}{\epsilon_{\boldsymbol{k}}(\boldsymbol{q})} \ . \tag{129}$$

Carrying out the integral in $\boldsymbol{k}$ for $\chi^{(0)}(\boldsymbol{q}, z)$ (Eq. (127)), we obtain the following analytic expression [58, 152]:

$$\chi^{(0)}(\boldsymbol{q}, z) = \rho_F \frac{k_F}{q} \left[\psi\left(\frac{z}{q v_F} - \frac{q}{2k_F}\right) - \psi\left(\frac{z}{q v_F} + \frac{q}{2k_F}\right)\right] \ . \tag{130}$$

Here, $v_F = \hbar k_F / m_e$ is the Fermi velocity and the function $\psi(z)$ is given by:

$$\psi(z) = \frac{z}{2} + \frac{1 - z^2}{4} \ln \frac{z + 1}{z - 1} \ . \tag{131}$$

The static Kubo's linear-response function $\chi^{(0)}(\boldsymbol{q}, z=0)$ can be further simplified to [152]

$$\chi^{(0)}(\boldsymbol{q},0) = -\rho_F \left[\frac{1}{2} + \frac{(q/k_F)^2 - 4}{8\,(q/k_F)} \ln\left|\frac{(q/k_F)-2}{(q/k_F)+1}\right|\right] . \tag{132}$$

For the calculation of $\phi(\boldsymbol{q}, z)$, it remains to define $g(\boldsymbol{q})$, which is simply

$$g(\boldsymbol{q}) = (\rho(\boldsymbol{q})|\rho(\boldsymbol{q})) = -\chi(\boldsymbol{q}, z=0) . \tag{133}$$

The aim of the memory-function approach is to determine $M(z)$. It is obtained by solving $\phi(\boldsymbol{q}, z)$ in a self consistent manner. To summarize, the set of self-consistent equations are:

$$\phi(\boldsymbol{q},z) = \frac{\phi^{(0)}(\boldsymbol{q}, z+M(z))}{1 + M(z)\phi^{(0)}(\boldsymbol{q}, z+M(z))/g(\boldsymbol{q})} \tag{134}$$

$$M(z) = \frac{1}{3nm_e}\frac{1}{V}\sum_{\boldsymbol{q}} \langle|U(\boldsymbol{q})|^2\rangle\, q^2\, \phi(\boldsymbol{q}, z) , \tag{135}$$

with

$$\phi^{(0)}(\boldsymbol{q},z) = \frac{1}{V}\sum_{\boldsymbol{k}} \frac{1}{z+\epsilon_{\boldsymbol{k}}(\boldsymbol{q})}\,\frac{f_{\boldsymbol{k}}(\boldsymbol{q})}{\epsilon_{\boldsymbol{k}}(\boldsymbol{q})} \tag{136}$$

$$\langle|U(\boldsymbol{q})|^2\rangle = U^2 \frac{6\pi^2}{q_0^3}\theta(q_0 - q) . \tag{137}$$

As alternative, Eq. (136) can be exchanged by Eq. (126). Furthermore, analytic expressions can be used, *e.g.*, Eqs. (130) and (131) for the dynamical $\chi^{(0)}(\boldsymbol{q}, z)$ and Eq. (132) for the static $\chi^{(0)}(\boldsymbol{q}, 0)$.

In Ref. [58], Götze introduces dimensionless quantities units. The relation between his equations and the ones of this section are given in the Appendix A.2.3.

Conductivity

The macroscopic dynamical conductivity is obtained from the current-current correlation function [55]:

$$\sigma(z) = \lim_{\boldsymbol{q}\to 0} -\mathrm{i}\left(j(\boldsymbol{q})\left|(\mathcal{L}-z)^{-1}\right|j(\boldsymbol{q})\right) . \tag{138}$$

It can be expressed in terms of $\phi(\boldsymbol{q}, z)$ by using the continuity equation, Eq. (88). Then, according to Götze's theory [57, 58, 177], the zero-wave-vector limit $\boldsymbol{q} \to 0$ gives the macroscopic conductivity:

$$\sigma(z) = e^2 \frac{n}{m_e} \frac{\mathrm{i}}{z + M(z)} \ . \tag{139}$$

Thus, $\sigma(z)$ depends simply on $M(z)$. The DC conductivity is obtained from the $z \to 0$ limit. If $M(z)$ for $z \to 0$ is a finite imaginary number (*i.e.*, $\mathrm{Re}\, M(0) = 0$), $\sigma(z)$ is real, and the system is in the metallic phase (or conducting phase). If $\lim_{z\to 0} M(z)$ is purely real (*i.e.*, $\mathrm{Im}\, M(0) = 0$), $\mathrm{Re}\, \sigma(z)$ is zero, and the system is in the insulating phase.

Götze demonstrated in Ref. [58] that the homogeneous electron gas in a random disorder potential exhibits a metal-to-insulator transition. The metallic phase is characterized by extended electron states and occurs in the weak coupling regime (*i.e.*, weak disorder potential), while the insulating phase has localized electron states and is present in the strong coupling regime (*i.e.*, strong disorder potential). The transition point between the metallic and insulating phase is reflected in a drastic qualitative change of $M(z)$ at small z.

Comparison to Drude formula

The classical Drude result for the DC conductivity $\sigma(0)$, as defined in Eq. (33), is reproduced by the zero-order result for $M(0)$ in the weak coupling regime. It is derived by substituting the non-interacting correlation function at zero frequency,

$$\phi^{(0)}(\boldsymbol{q}, z = 0) = \mathrm{i} \frac{m_e^2}{\pi} \frac{1}{q} \, \Theta\left(\frac{4k_F^2}{q_0^2} - \frac{q^2}{q_0} \right) \ , \tag{140}$$

into Eq. (124) (instead of $\phi(\boldsymbol{q}, z)$) and evaluating this formula only once (no self-consistent cycle). The expression for $M(0)$ is then [58, 174]

$$M(0) = \mathrm{i} \, \frac{3}{2} \pi \left(\frac{U}{E_0} \right)^2 \left(\frac{2k_F}{q_0} \right) \min \left[1, \left(\frac{2k_F}{q_0} \right)^{-4} \right] \ , \tag{141}$$

with $E_0 = q_0^2 / m_e$. This is simply a constant. Comparing Eq. (139) to the Drude formula in Eq. (33), we obtain $M(0) = \mathrm{i}/\tau_{\mathrm{D}}$.

4

TEMPERATURE-DEPENDENT TRANSPORT PROPERTIES OF SnSe

Tin selenide (SnSe) has a layered, anisotropic, and low-symmetry crystal structure (Fig. 4.1). Its two-atom-thin layers are weakly bonded. SnSe undergoes a reversible displacive phase transition at about 750-$800\,\mathrm{K}$ from the low-temperature phase with space group $Pnma$ to the high-temperature phase with space group $Cmcm$. In the high-temperature phase, an unprecedented high figure of merit $ZT \sim 2.6$ at $T \approx 923\,\mathrm{K}$ is observed along the $\boldsymbol{b}$-axis [11]. In the low-temperature phase, ZT remains below one, however, it can be significantly enhanced by hole doping using Na atoms as acceptors. For hole-doped SnSe, a ZT around 2 is reached along the $\boldsymbol{b}$-axis at $T \geq 600\,\mathrm{K}$ [13]. For the temperature range between $300\,\mathrm{K}$ to $773\,\mathrm{K}$, the average figure of merit, ZT_{avg}, is ~ 1.34. This corresponds to an estimated maximum efficiency of $\eta_{\mathrm{max}} \sim 17\,\%$ (see Eq. (3)), which is one of the highest values observed for state-of-the-art p-type materials [11, 178, 179]. This exceptional performance arises from a high power factor ($\sim 40\,\mu\mathrm{W\,cm^{-1}K^{-2}}$ at $300\,\mathrm{K}$ and $\sim 14\,\mu\mathrm{W\,cm^{-1}K^{-2}}$ at $773\,\mathrm{K}$) together with a low κ ($\sim 1.6\,\mathrm{W\,m^{-1}K^{-1}}$ at $300\,\mathrm{K}$ and $\sim 0.55\,\mathrm{W\,m^{-1}K^{-1}}$ at $773\,\mathrm{K}$) present over a wide temperature range. Unraveling the origin of its peculiar temperature dependence is a key point in understanding the high-efficient thermoelectric performance of this material, and also in perspective of related compounds, as *e.g.* SnS, InSe, and PbSe.

In the following, we calculate the electrical conductivity σ and the Seebeck coefficient S for undoped and hole-doped SnSe in the low-temperature phase $Pnma$ using the BT approach in the RTA. In short, we find that good agree-

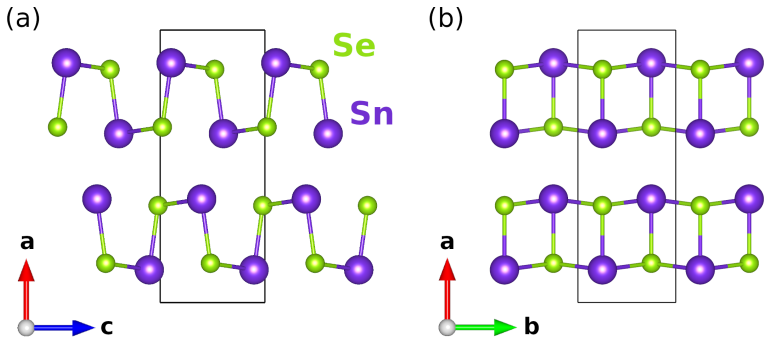

Figure 4.1: Crystal structure of SnSe (space group $Pnma$) perpendicular to (a) the $\boldsymbol{b}$-axis and (b) the $\boldsymbol{c}$-axis. Se atoms are shown in light green and Sn atoms in violet. The unit cell is framed by thin black lines.

ment with experiment is only reached after accounting for both, thermal expansion and electron-phonon coupling.

This chapter is organized as follows: First, in Sec. 4.1, we introduce the implementation of the BT approach in **exciting** and demonstrate its applicability to the well-studied thermoelectric material Bi_2Te_3. Computational details about the calculation of σ and S for undoped and holed-doped SnSe are given in Sec. 4.2. Results are presented in Sec. 4.3, summary and conclusions in Sec. 4.4.

4.1 BOLTZMANN TRANSPORT IN **exciting**

4.1.1 *Details about the implementation*

In the software package **exciting** [29], the electronic transport coefficients, namely the conductivity $\boldsymbol{\sigma}$, the Seebeck coefficient $\boldsymbol{S}$, and the electronic part of the thermal conductivity $\boldsymbol{\kappa_e}$, can be evaluated via the linearized BT equation in the RTA (see Eqs. (41) and (42) in Sec. 3.3.1). $\boldsymbol{\sigma}$, $\boldsymbol{S}$, and $\boldsymbol{\kappa}_e$ are calculated by using Eqs. (52), (53) and (54), respectively, together with the transport distribution function $\boldsymbol{\Xi}(\epsilon)$ in Eq. (51) being the kernel of these coefficients. Alternatively, they can be determined directly by using Eqs. (46), (47), and (48), which do not require the calculation of $\boldsymbol{\Xi}(\epsilon)$. This option is usually used to cross-check if the parameters of $\boldsymbol{\Xi}(\epsilon)$ are chosen appropriately. In both cases, the evaluation of one or several summations over states $n\boldsymbol{k}$ on a discrete $\boldsymbol{k}$-point mesh in the first BZ (n - band index) is performed. For each $n\boldsymbol{k}$, the eigenenergy $\epsilon_{n\boldsymbol{k}}$, the group velocity $\boldsymbol{v}_{n\boldsymbol{k}}$, and the relaxation time $\tau_{n\boldsymbol{k}}$ are required for the calculation. $\epsilon_{n\boldsymbol{k}}$ together with the wave functions $\Psi_{n\boldsymbol{k}}$ are direct outputs of the GS calculation in **exciting**, which is executed initially. $\boldsymbol{v}_{n\boldsymbol{k}}$ is obtained from the matrix elements of the momentum operator $\hat{\boldsymbol{p}}$:

$$\boldsymbol{v}_{n\boldsymbol{k}} = \frac{1}{m_e}\boldsymbol{p}_{n\boldsymbol{k}} = \langle \Psi_{n\boldsymbol{k}} | \hat{\boldsymbol{p}} | \Psi_{n\boldsymbol{k}} \rangle \ . \tag{142}$$

These momentum matrix elements are available in the `optics` package of **exciting**. The relaxation time $\tau_{n\boldsymbol{k}}$ is an empirical parameter. In general, it depends on the energy of state $n\boldsymbol{k}$. In our implementation, τ is assumed to be energy independent. By specifying temperature T and chemical potential μ, the transport coefficients can be evaluated. To simulate a given charge carrier concentration n at a given T, *e.g.* for doped materials, μ can be adjusted accordingly.

The largest contributions to the integrals in Eqs. (52), (53) and (54) stem from $\boldsymbol{k}$-points near the Fermi surface. Thus, an adequate sampling in this region is needed, which may be difficult to achieve with homogeneous $\boldsymbol{k}$-meshes. Therefore, our implementation provides the possibility to evaluate the BT co-

efficients on adaptive $\boldsymbol{k}$-meshes with high $\boldsymbol{k}$-point densities in relevant regions, generated in an iterative manner [180].

A detailed description of the performance of BT calculations in **exciting** can be found in the tutorial "Transport properties using the Boltzmann equation" on the **exciting** webpage [181]. In this tutorial, the example system is bulk silicon.

4.1.2 *Bi_2Te_3 as test system*

A suitable choice of a material to test the implementation of the Boltzmann transport coefficients in **exciting** is Bi_2Te_3, since its properties have already been studied with the BT approach implemented in other DFT packages, as *e.g.* `WIEN2k` [182, 183]. In the following, we compare our calculations with the results presented in Ref. [182].

The crystal structure of Bi_2Te_3 has 5 atoms in the unit cell (space group $R\bar{3}m$), as shown on the left side of Fig. 4.2(a). Known from experiments [184], its rhombohedral cell has a lattice constant of $a = 19.8\,a_B$ and an angle between the lattice vectors of $24.16°$. For the DFT calculation, we use the PBEsol functional [102] and include spin-orbit coupling, since Bi_2Te_3 is known to have large spin-orbit effects. The MT radii of Bi and Te are $R_{\text{MT}} = 2.8\,a_B$. The dimensionless parameter $R_{\text{MT}}|\boldsymbol{G}+\boldsymbol{k}|_{\max}$, determining the basis set size, is set to 10 and the plane-wave cutoff $G_{\max}$ for the density and the potential is set to $20\,a_B^{-1}$. We use a homogeneous $20\times20\times20$ $\boldsymbol{k}$-point mesh for GS calculation and a dense mesh of $50\times50\times50$ $\boldsymbol{k}$-points, giving $31\,902$ $\boldsymbol{k}$-points in the irreducible wedge of the Brillouin zone, for the BT calculations. This computational parameters are similar to the ones used in Ref. [182].

Figure 4.2(b) shows the electronic band structure of Bi_2Te_3. Due to spin-orbit effects, the band edges are moved away from the high-symmetry points. We obtain a band gap of 0.11 eV that is similar to the experimental value of about 0.13 eV [185]. This results are in good agreement to the results reported in Ref. [182].

The transport properties of Bi_2Te_3 are calculated using the relaxation times $\tau_{xx} = \tau_{yy} = 22$ fs in the basal plane (x-y plane) and $\tau_{zz} = 21$ fs in the trigonal axis (z-direction) (taken from Ref. [182]). Figure 4.2(c), (d), (e), (f), and (g) show, respectively, the transport distribution function, the electronic density of states, the Seebeck coefficient S, the power factor σS^2, and the figure of merit ZT at 300 K with respect to the chemical potential μ (here, the rigid band approximation is used [156, 157]). For calculating ZT, we use the experimental lattice thermal conductivity κ_l, which is $\kappa_{xx,l} = 1.5\,\text{W m}^{-1}\text{K}^{-1}$ in the basal plane and $\kappa_{zz,l} = 0.7\,\text{W m}^{-1}\text{K}^{-1}$ for the trigonal direction [186]. Overall, the shape and magnitude of the transport properties agree well with the results shown in Fig. 6 of Ref. [182].

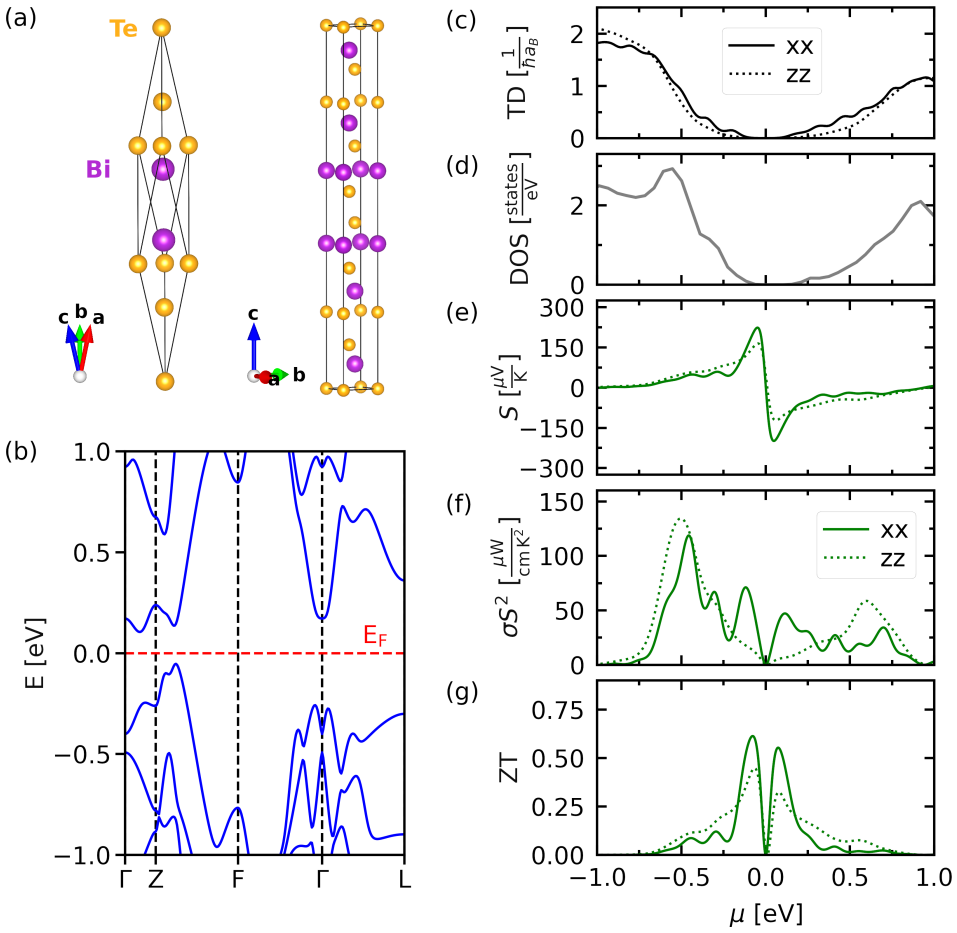

Figure 4.2: Crystal structure and properties of Bi_2Te_3 calculated with `exciting`: (a) Rhombohedral unit cell with space group $R\bar{3}m$ (left) and conventional hexagonal cell (right). Bi atoms are shown in purple and Te atoms in yellow. (b) Electronic band structure along high-symmetry lines. The red dashed line indicates the Fermi energy E_F. (c) Transport distribution function (TD), (d) electronic density of states (DOS), (e) Seebeck coefficient S, (f) power factor σS^2, and (g) figure of merit ZT versus chemical potential μ. Here, the temperature is $300\,\mathrm{K}$. The properties along the xx direction (basal plane) are shown with solid lines, and along the zz direction (trigonal axis) with dotted lines.

4.2 COMPUTATIONAL DETAILS

Using the BT approach, we calculate the conductivity σ and the Seebeck coefficient S between $300\,\mathrm{K}$ and $700\,\mathrm{K}$. In this temperature range, the crystal structure has the space group $Pnma$, as shown Fig. 4.1. The DFT calculations are performed using the PBE exchange-correlation functional [101], as also used in other works [11]. MT radii of $R_{\mathrm{MT}} = 2.0\,a_B$ for both species, Sn and Se, are used. The parameter $R_{\mathrm{MT}}|\boldsymbol{G}+\boldsymbol{k}|_{\max}$ is 10, and the plane-wave cutoff $G_{\max}$ for the density and the potential is $20\,a_B^{-1}$. We use a homogeneous $4 \times 12 \times 12$ $\boldsymbol{k}$-point mesh for the GS calculation, and a dense mesh of

$20 \times 60 \times 60$ $\boldsymbol{k}$-points, leading to $10\,571$ $\boldsymbol{k}$-points in the irreducible Brillouin zone, for the calculation of the transport coefficients.

4.3 RESULTS AND ANALYSIS

The electronic band structure of SnSe, shown in Fig. 4.3, displays multiple maxima below E_F. The degree to which they contribute to transport depends on the charge carrier concentration. We compute σ and S for undoped SnSe and hole-doped SnSe [12], for which experimental data are available in Ref. [12]. The undoped SnSe has intrinsically a hole concentration of $n_h = 4.5 \cdot 10^{17}\text{cm}^{-3}$ due to Sn vacancies in the crystal [28]. The hole-doped sample of Ref. [12] has a hole concentration of $n_\text{h} = 4.0 \cdot 10^{19}\text{cm}^{-3}$ (realized in experiment by introducing Na atoms as substitutional impurities). The chemical potentials at zero Kelvin related to $n_\text{h} = 4.5 \cdot 10^{17}\text{cm}^{-3}$ and $n_h = 4.0 \cdot 10^{19}\text{cm}^{-3}$ are indicated in Fig. 4.3 with a light red and an orange horizontal line, respectively. For hole-doped SnSe, μ lies below two local maxima along Z-Γ, thus, multiple maxima contribute to the transport [12].

The conductivity σ along the $\boldsymbol{b}$ axis for undoped and doped SnSe is shown in Figs. 4.4(b) and (c), respectively. We start by neglecting the temperature dependence of τ and set it to the constant value of $\tau = 20\,\text{fs}$ (light blue line, labeled with CRT for constant relaxation time). The calculated σ for both undoped and hole-doped SnSe increases with temperature. This behavior is

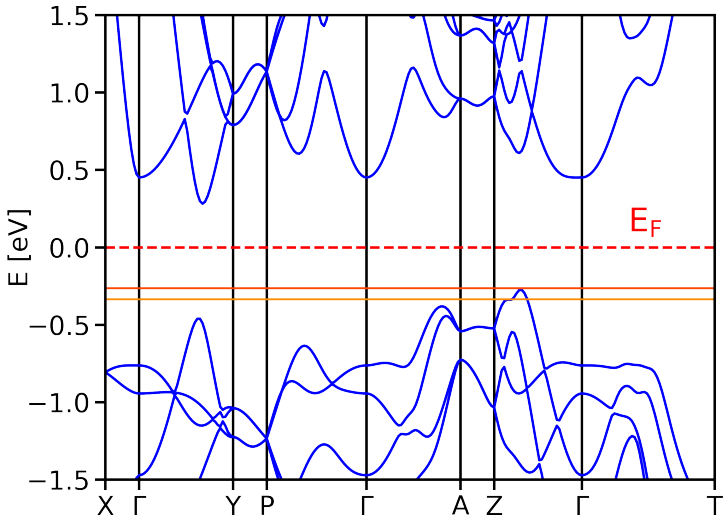

Figure 4.3: Electronic band structure of SnSe (space group $Pnma$). The red dashed line indicates the Fermi energy E_F. The solid lines indicate the chemical potential for undoped SnSe (light red) and for doped SnSe (orange), which correspond to hole concentrations of $n_h = 4.5 \cdot 10^{17}\,\text{cm}^{-3}$ and $n_h = 4.0 \cdot 10^{19}\,\text{cm}^{-3}$ at $T = 0$, respectively.

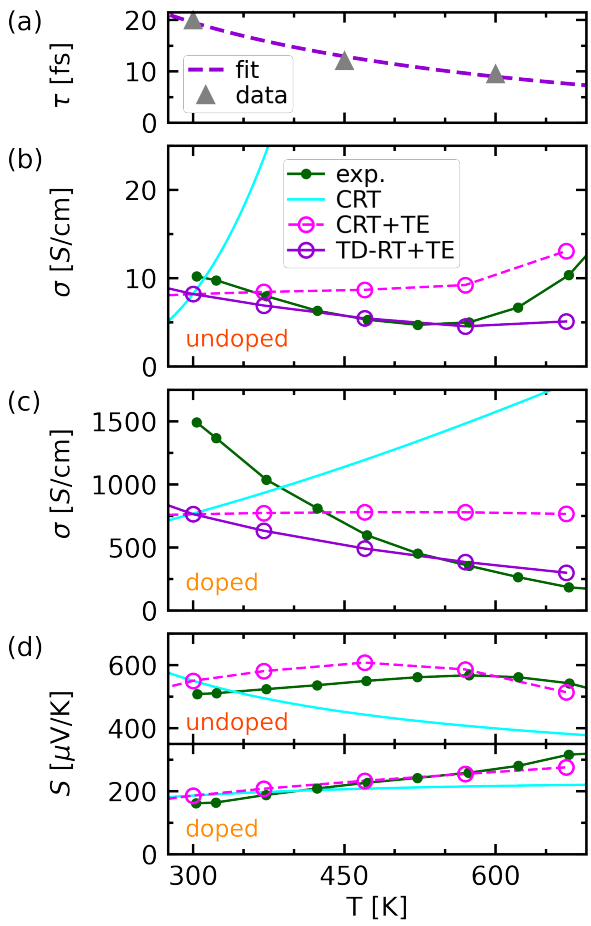

Figure 4.4: (a) Relaxation time τ for SnSe with respect to temperature obtained from a fit to four *ab-initio* data points (gray triangles, one at $80\,\mathrm{K}$ is not displayed here). (b) and (c) show the conductivity σ for undoped and doped SnSe, respectively. The result for constant $\tau = 20\,\mathrm{fs}$ is labeled with CRT (light-blue line), CRT including the thermal expansion of the lattice (TE) is labeled with CRT + TE (magenta circles), and the result including both, a temperature-dependent relaxation time and TE is labeled with TD-RT+TE (violet circles). (d) Seebeck coefficient S for the undoped (top) and doped case (bottom). Experimental data (dark-green dots) are taken from Ref. [12]. The lines connecting the symbols are guides to the eye.

in strong disagreement with experiment (green dots). The agreement with experiment is improved by including the thermal expansion (TE) of the crystal lattice (magenta circles, labeled as CRT+TE). Here, to account for the TE, we extract the lattice parameters from Ref. [187] for the temperatures $300\,\mathrm{K}$, $370\,\mathrm{K}$, $470\,\mathrm{K}$, $570\,\mathrm{K}$, and $670\,\mathrm{K}$ and perform for each temperature separate GS and BT calculations. Importantly, the agreement with experiment is further improved if, additionally, a temperature-dependent relaxation time $\tau(T)$ (TD-RT) is employed by accounting for the renormalization due to electron-phonon interaction. They are calculated at values $80\,\mathrm{K}$, $300\,\mathrm{K}$, $450\,\mathrm{K}$, using

the Fan-Migdal electron-phonon self-energy [188]. $\tau(T)$ is obtained by a least-squares fit of $\tau(T) = a + b/(T - c)$ to these data points [189], leading to the parameters $a = -6.74\,\text{fs}$, $b = 11743\,\text{fs K}$, and $c = -146.87\,\text{K}$. The data point and the fit are shown in Fig. 4.4(a). Combining the thermal expansion with the temperature-dependent relaxation time $\tau(T)$ (violet circles, labeled as TD-RT+TE), good agreement with experiment is achieved. The impact of other scattering mechanisms, *e.g.* due to impurities, electron-electron and electron-plasmon couplings [190], are not considered here.

The Seebeck coefficient S along the $\boldsymbol{b}$ axis is shown in Fig. 4.4(d). Since S has no τ-dependence in the RTA, its calculated value is only affected by the TE. Thus, there is no result for TD-RT + TE. The computed S without TE (light blue line) agrees with experiment for doped SnSe, but shows a rather different temperature behavior for undoped SnSe. Including the TE (magenta circles), S is in very good agreement with experiment for both, doped and undoped SnSe.

σ and S along all three crystallographic axes for undoped and doped SnSe are shown in Fig. 4.5. Since measurements of the charge carrier concentration have a large uncertainty, here, also a range of hole concentrations n_h (shaded areas) is explored. For undoped SnSe, the reported value in Refs. [12, 28] is $n_h = 4.49 \cdot 10^{17}\,\text{cm}^{-3}$, thus, a range from 10^{17} to $10^{18}\,\text{cm}^{-3}$ is considered. For hole-doped SnSe, the reported n_h is $4.0 \cdot 10^{19}\,\text{cm}^{-3}$, thus we consider the range from 10^{19} to $10^{20}\,\text{cm}^{-3}$. The range of possible values (shaded areas in Fig. (4.5)) covers the small discrepancies that remain between the experiment and the calculated results for all crystallographic axes.

4.4 CONCLUSION

The influence of thermal lattice expansion and electron-phonon coupling on the transport coefficients has been analyzed. While, by including the thermal expansion, the expected trend of a decreasing σ with increasing temperature is obtained, the thermal enhancement of the electron-phonon interaction leads to a further suppression of hole transport. Only by simultaneously accounting for both, the peculiar temperature dependence of the electronic transport coefficients S and σ can be understood.

Results presented in this section are published in Ref. [189], where I contributed with the calculation and analysis of the transport coefficients as presented above.

As a critical side remark, we want to mention that the BT approach in the RTA is based on a large set of assumptions and is in general known to be a good approximation for elastic and weak inelastic scattering mechanisms only [21, 22]. In the case of SnSe, phonons have a pronounced polaronic character [189], indicating the presents of strong (or at least not weak) inelastic scattering. Irre-

spective of this, as presented in this work, we have achieved a good agreement with experiment.

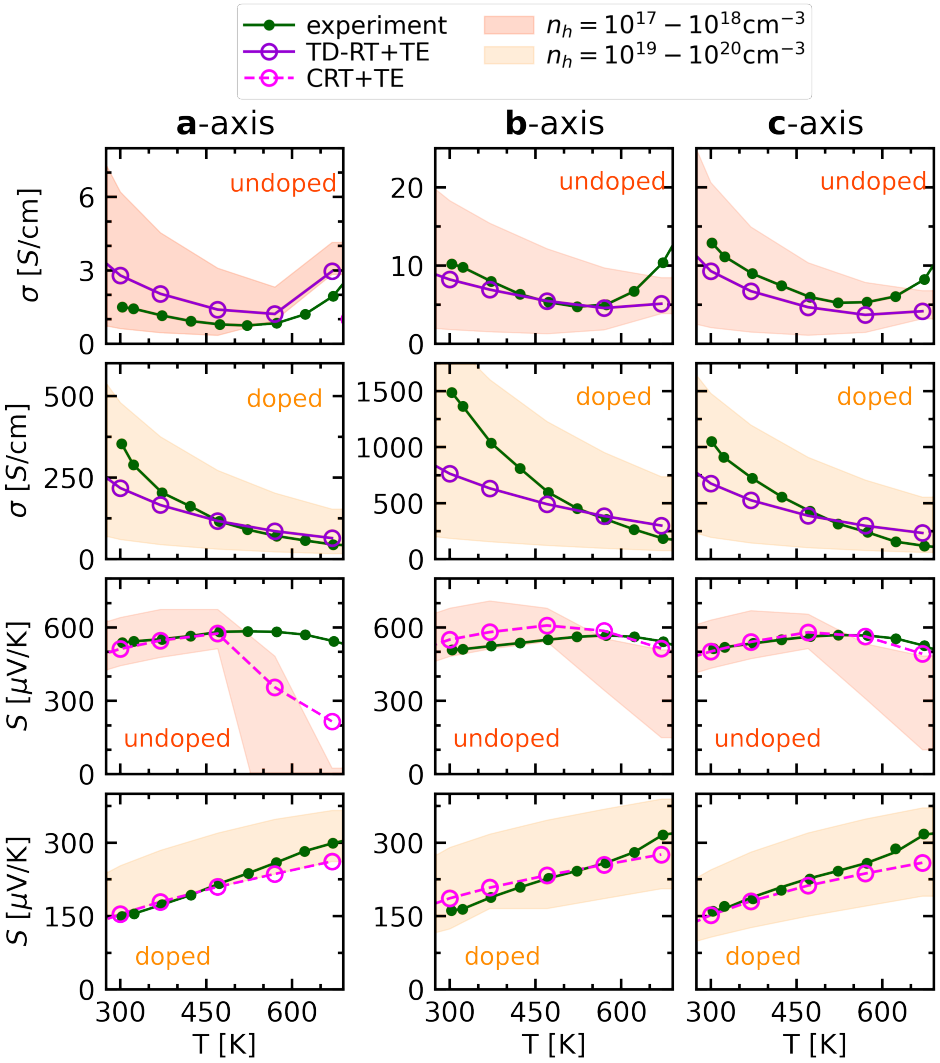

Figure 4.5: Conductivity σ (first and second row) and Seebeck coefficient S (third and fourth row) for undoped SnSe (plots indicated with light red label) and hole-doped SnSe (orange label). Each column shows the results for one crystallographic axis, from left to right: $\boldsymbol{a}$, $\boldsymbol{b}$, and $\boldsymbol{c}$. The calculated σ, obtained by accounting simultaneously for the thermal expansion (TE) and temperature-dependent relaxation time (TD-RT), is labeled with TD-RT+TE (violet circles). The calculated S, that is τ-independent and, thus, obtained by simply accounting for the TE, is label with CRT+TE (magenta circles). Experimental data (dark-green dots) are taken from Ref. [12]. The lines connecting the symbols are guides to the eye. The shaded area in each plot indicates the range of possible values due to a variation of the hole concentrations, n_h. For undoped SnSe, n_h is investigated in the range $n_h = 10^{17} - 10^{18}\,\mathrm{cm}^{-3}$, for hole-doped SnSe, in the range $n_h = 10^{19} - 10^{20}\,\mathrm{cm}^{-3}$.

5

TEMPERATURE-DEPENDENT TRANSPORT PROPERTIES OF TYPE-I CLATHRATES

In this chapter, the finite-temperature electronic, structural, and transport properties of type-I clathrates $Ba_8Al_xSi_{46-x}$ are investigated in the composition range $x \in [6, 16]$. They are obtained from configurational thermodynamic averages. For this, MMC and WL samplings of the configurational space are performed in the canonical ensemble. For predicting the configuration-dependent properties (*e.g.* total energies, bond lengths, *etc.*) of the structures visited during the sampling, the CE technique is used (see Sec. 3.2.1).

Intermetallic type-I clathrates are inorganic inclusion complexes containing guest atoms in the cavities formed by the host lattice. Their unit cell with the cubic space group $Pm\bar{3}n$ is shown in Fig. 5.1(a). It is composed of 46 tetrahedrally-coordinated group-IV species sitting at the Wyckoff sites $w = 24k$, $16i$, and $6c$. They form the host structure (also called framework) with eight cavities: six tetrakaidecahedra (light green) and two dodecahedra (light blue) with their centers at the Wyckoff sites $6d$ and $2a$, respectively. Those cavities can contain guest atoms, that are often alkali or alkaline-earth metals.

The covalently-bonded pristine clathrate Si_{46} is a semiconductor [191]. For Ba_8Si_{46}, 8 Ba atoms are introduced in the framework's cavities. They donate their two valence electrons to the crystal (n-doping), in total 16 free electrons, and turn the compound into a metal. The electronic properties of $Ba_8Al_xSi_{46-x}$,

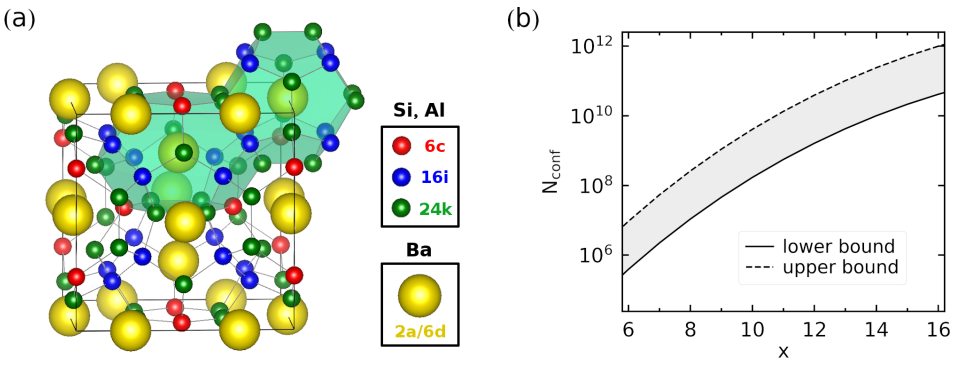

Figure 5.1: (a) Unit cell of the type-I clathrate structure $Ba_8Al_xSi_{46-x}$ (space group $Pm\bar{3}n$). Host atoms are at the Wyckoff sites of the pristine lattice $w = 24k$ (green), $16i$ (blue), and $6c$ (red), while guest atoms are at $2a$ and $6d$ sites (yellow). A tetrakaidecahedral and a dodecahedral guest-containing cavity is shown in light blue and light green, respectively. (b) Upper and lower bound of the total number of configurations N_{conf} available for compositions with Al content x.

in which some of the Si atoms are substituted by Al, can be understood by employing the so-called Zintl-Klemm concept [18, 192–195]. Following this concept, each free electron in the crystal can be compensated by one Al, that is a group-III element (p-doping). In this way, a completely charge-balanced composition can be achieved at $x = 16$, for which semiconducting behavior is expected. Although the Zintl-Klemm concept provides good guidelines for understanding the electronic behavior of clathrates compounds, it only takes into account the material's composition and ignores the effects of the dopant configuration. Indeed, it is found that the electronic behavior is not only determined by the composition, but it is also highly sensitive to the configuration, *i.e.* the arrangement of the Al atoms in the host lattice [37, 38, 40, 41]. In particular for $Ba_8Al_{16}Si_{30}$, the ground-state (GS) configuration is found to be a semiconductor (thus seemingly following the Zintl-Klemm concept) while configurations with an energy only slightly higher (a few meV/atom) than the GS are found to be metallic [41].

The number of configurations N_{conf} available at a given composition is enormous and increases rapidly with the number of substituents (combinatorial explosion). For $Ba_8Al_xSi_{46-x}$, the upper bound for N_{conf} can be estimated by the binomial coefficient $\binom{46}{x}$ with 46 as the number of substitutional sites. Its lower bound can be obtained by dividing $\binom{46}{x}$ by 24, that is the largest multiplicity among the Wyckoff sites. These bounds are shown in Fig. 5.1(b). In experiments, the actual configurations present in thermal equilibrium are difficult to determine, since the species occupying the host lattice typically give indistinguishable x-ray diffraction patterns [18]. This is the case, *e.g.*, for Si and Al in the compound $Ba_8Al_{16}Si_{30}$ [33, 36, 42, 43]. In addition, a measured sample represents a thermodynamic average on configurations. The annealing temperatures of several hundred Kelvin used during the compound's synthesis (lasting several days) [32, 33, 36, 196] and the fast cooling down to room temperature afterwards suggest that the system does not reach the most stable configuration.

This chapter is structured as follows: First, in Sec. 5.1, the tools for thermodynamic analysis as implemented within the CE package `CELL` are introduced. The CE models used to predict the properties of $Ba_8Al_xSi_{46-x}$ in MMC and WL samplings together with details about their construction are described in Sec. 5.2. A new approach to perform canonical-ensemble averages fully based on *ab initio* properties weighted by the configurational density of states (obtained from the WL method) is explained in Sec. 5.3. Computational details are given in Sec. 5.4. In the following sections, the results are presented. The temperature-dependent structural and electronic properties for different x are discussed in Sec. 5.5. Here, Sec. 5.5.1 is dedicated to the charge-compensated composition $x = 16$, and Sec. 5.5.2 discusses n-doped clathrates, *i.e.* compositions with $x < 16$. In Sec. 5.6, the temperate-dependent bond distances are accessed by MMC samplings and compared to experiments. The transport

properties are discussed in Sec. 5.7. Finally, summary and conclusions are given in Sec. 5.8.

5.1 STATISTICAL THERMODYNAMICS IN CELL

To access finite-temperature properties, we employ the MMC sampling and the WL method – described in Sec. 3.2.2 – that are implemented within the CE package CELL [197]. CELL is an object-oriented python package for the purpose of building CE models and performing configurational samplings for a broad variety of material classes. It is developed and maintained in our research group, and it has a special focus on complex alloys, such as the clathrate compound.

I implemented the `thermodynamics` package in CELL, containing the MMC and WL sampling methods. Important features of the `thermodynamics` package are outline in Sec. 5.1.1. Its application is demonstrated on the example of the Pt/Cu(111) surface alloy in Sec. 5.1.2. This example together with instructions about how to use the code is published in Ref. [198].

5.1.1 *Configurational samplings in* CELL

To obtain reliable thermal averages from samplings, a large number of sampling steps is usually required. The tools of the `thermodynamics` package in CELL allow for acceleration of the sampling. For instance, the cluster orbits $\mathcal{O}(\alpha)$ are precalculated before the sampling routine starts and reused in the prediction of the CE energy at every sampling step. Furthermore, computational time can be saved by evaluating a Monte-Carlo sampling step as follows: At sampling step n, a new proposed configuration with vector $\boldsymbol{\sigma}_{n+1}$ is generated from the current configuration with vector $\boldsymbol{\sigma}_n$ by performing a Monte-Carlo swap. To calculate the acceptance probability of $\boldsymbol{\sigma}_{n+1}$ (see Table 3.1), its total CE energy $\hat{E}_{n+1} = \hat{E}(\boldsymbol{\sigma}_{n+1})$ is required. However, a swap of atoms affects the occupation variables σ_i of the vector $\boldsymbol{\sigma}_n$ only at two sites. Thus, instead of evaluating $\hat{E}_{n+1}$ as $E(\boldsymbol{\sigma}_{n+1}) = \sum_\alpha m_\alpha J_\alpha X_\alpha(\boldsymbol{\sigma}_{n+1})$ (see Eq. (20) with $P = E$), which involves the calculation of the full correlation vector $X_\alpha(\boldsymbol{\sigma}_{n+1})$, it is more efficient to calculate the change in the CE energy, $\Delta\hat{E}$, with respect the total CE energy $\hat{E}_n = \hat{E}(\boldsymbol{\sigma}_n)$ of the previous configuration $\boldsymbol{\sigma}_n$ as:

$$\begin{aligned} \Delta\hat{E} &= \hat{E}_{n+1} - \hat{E}_n = \sum_\alpha m_\alpha J_\alpha \left[X_\alpha(\boldsymbol{\sigma}_{n+1}) - X_\alpha(\boldsymbol{\sigma}_n)\right] \\ &= \sum_\alpha J_\alpha \left[\sum_{\beta \in \mathcal{O}(\alpha)} \left(f_\beta(\boldsymbol{\sigma}_{n+1}) - f_\beta(\boldsymbol{\sigma}_n) \right) \right] . \end{aligned} \tag{143}$$

Here, the difference of the cluster functions f in the square brackets is zero, except for the clusters β which contain a swapped site. Using $\Delta\hat{E}$, the energy

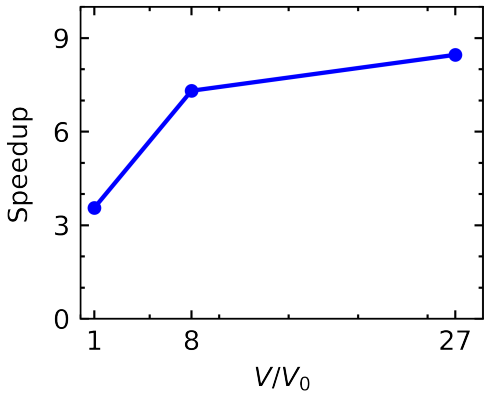

Figure 5.2: Speedup versus the supercell volume V (V_0 being the unit cell volume). It is calculated from the ratio between the time spent for $100\,000$ MMC steps using $\hat{E}$ and using $\Delta\hat{E}$ for predictions. In this example, the CE model for the energy of $Ba_8Al_{16}Si_{30}$ with 11 clusters is used (see Table 5.2).

at step n is obtained as $\hat{E}_{n+1} = \hat{E}_n + \Delta\hat{E}$, with $\hat{E}_n$ saved from the previous step. The speedup is demonstrated by means of an MMC sampling for the clathrate $Ba_8Al_{16}Si_{30}$, having, in total, $N_\alpha = 10$ clusters in its CE model (see Table 5.2). Figure 5.2 shows the speedup obtained for $100\,000$ MMC steps. It increases with the supercell size and reaches a factor of about 8.5 for a $3\times3\times3$ supercell with a volume of $V = 27\,V_0$ (V_0 being the unit cell volume).

5.1.2 *Pt/Cu(111) surface alloy as test system*

Thermodynamic analysis by using the MMC and WL sampling methods, as implemented in `CELL`, is carried out for the Pt/Cu(111) surface alloy. This alloy consists of a Cu fcc (111) surface that adsorbs Pt atoms into the top-most atomic layer. Its pristine surface and the fully substituted counterpart of the supercell with, in total, 16 top-most layer atoms are shown in Fig. 5.3(a) and (b), respectively.

In the samplings, the energy of every visited configuration is predicted with a CE model of the adsorption energy E_{ads}, which is defined as

$$E_{\mathrm{ads}}(\boldsymbol{\sigma}) = \frac{1}{N_{\mathrm{sites}}}\left[E(\boldsymbol{\sigma}) - n_{\mathrm{Pt}}\Delta\mu - E_{\mathrm{Cu,surface}}\right] \ . \tag{144}$$

Here, N_{sites} is the number of substitutional surface sites in the top-most layer of the supercell, E the total energy of the configuration $\boldsymbol{\sigma}$, n_{PT} the number of Pt atoms, $\Delta\mu = \mu_{\mathrm{Pt}} - \mu_{\mathrm{Cu}}$ with μ_{Pt} being the chemical potential of Pt and μ_{Cu} the chemical potential of Cu, and $E_{\mathrm{Cu,surface}}$ the total energy of the pristine Cu(111) surface. The advantage of using E_{ads} instead of the total energy $E(\boldsymbol{\sigma})$

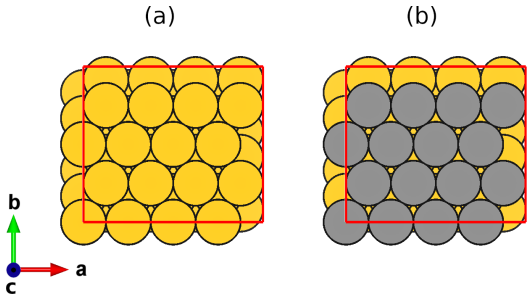

Figure 5.3: (a) Pristine Cu(111) surface and (b) Pt/Cu(111) surface with the fully Pt-substituted top-most atomic layer perpendicular to the z direction (top view). Yellow circles represent Cu atoms, gray circles Pt atoms. The red line indicates the supercell boundaries.

is that E_{ads} has a direct physical interpretation and is an intensive property, *i.e.* it does not scale with the supercell size.

The CE model of E_{ads} is trained by 100 random configurations generated at arbitrary Pt concentration in the Pt/Cu(111) surface with 16 substitutional surface sites (pristine surfaces shown in Fig. 5.3). The total energies of the structures in the training set are obtained with the effective medium theory calculator of ASE [199]. This calculator uses reasonably realistic parameters for the elements Pt and Cu, and requires much less computational resources than, *e.g.*, DFT calculations. The optimal CE model is found by applying the LASSO optimization method, *i.e.* an optimization using the ℓ_1 norm as regularization term in the objective function (see Eq. (25)). The regularization hyperparameter λ, determining the sparseness of the solution, is optimized in the range

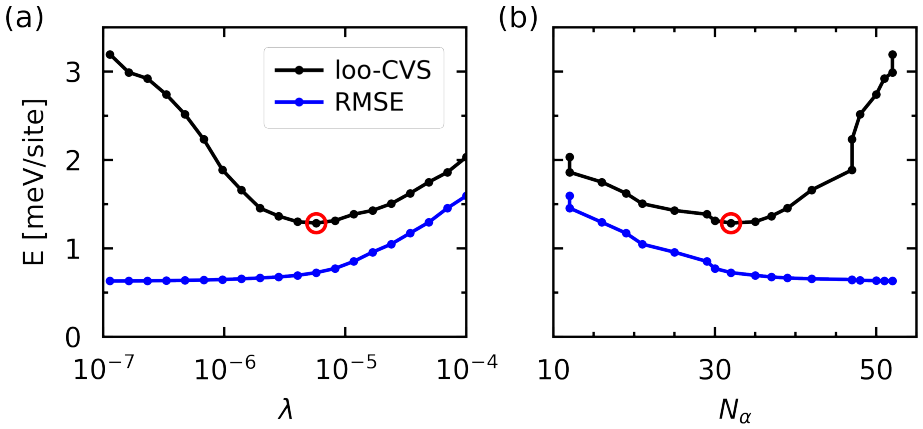

Figure 5.4: Cluster optimization performed with the LASSO method to obtain a CE model for the adsorption energy E_{ads} of the Pt/Cu(111) surface alloy: (a) E_{ads} versus the sparsity λ (regularization hyperparameter). (b) E_{ads} with respect to the number of clusters. The blue points indicate the RMSE of the fit, the black points indicate the loo-CVS, and the red circle the optimal value of the loo-CVS. The lines are guides to the eye.

$\lambda \in [10^{-7}, 10^{-4}]$. Figure 5.4(a) shows the loo-CV (black), and the root mean squared error (RMSE) (blue) with respect to λ. The lowest loo-CV is found for $\lambda = 6 \cdot 10^{-6}$ (red circle), indicating the optimal model. At this λ, the CE model consists of 32 out of 52 clusters, as it is revealed from Fig. 5.4(b), which shows the loo-CV with respect to the number of clusters. From a least-squares fit of this optimal set of 32 clusters to the training set (see Eq. (24)), the ECIs are obtained. The resulting optimal CE model has a RMSE of 0.7 meV/site and a loo-CVS of 1 meV/site.

For the stoichiometry of Cu_3Pt at the fcc (111) surface, we perform samplings in the canonical ensemble. First, we investigate the configurational ordering at different temperatures. For this, a simulated annealing procedure is performed, which consists of 15 sequential MMC samplings, with $100\,000$ sampling steps at each temperature T, starting from $1500\,\mathrm{K}$ and gradually decreasing T in steps of $100\,\mathrm{K}$ until reaching $100\,\mathrm{K}$. The most-visited configuration in MMC samplings for temperatures below $300\,\mathrm{K}$ is the GS configuration, *i.e.* the configuration with the lowest energy. The GS for the supercell with 64 surface sites is shown in Fig. 5.5(a). It has a $\mathrm{p}(2 \times 2)$ ordering of the Pt atoms. This ordered pattern is in agreement with experiment reported in Ref. [200]. As an example for a configuration present at high-temperature, a snapshot of the MMC trajectory at $1500\,\mathrm{K}$ is shown in Fig. 5.5(b). Here, no ordering pattern is visible.

The change of a well-ordered GS to a disordered state indicates a phase transition. Its signatures are investigated in the isobaric specific heat C_p (Eq. (32)), the internal energy U (Eq. (29)), and the configurational entropy S (Eq. (31)). These thermodynamic properties are shown in Fig. 5.6 for different supercell sizes. We discuss first the results obtained by the WL method (solid lines). The simulation parameters used for WL samplings are summarized in Table 5.1. As shown in Fig. 5.6(a), the C_p reveals a maximum, whose position typically indicates the transition temperature T_{trans} [133, 139, 201]. T_{trans} for

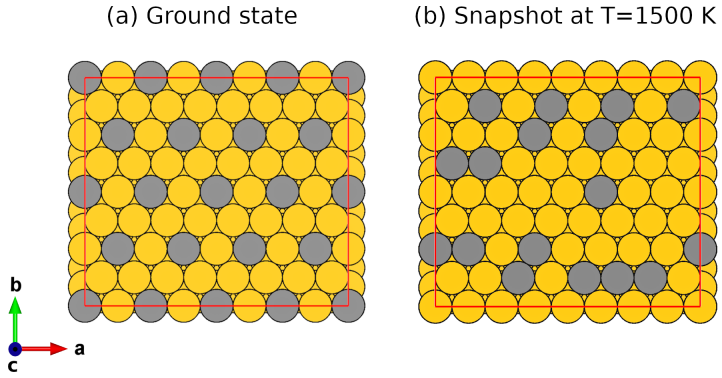

Figure 5.5: Simulation cell of the Pt/Cu(111) surface alloy with 64 surface sites: (left) the GS configuration and (right) a snapshot at $T = 1500\,\mathrm{K}$. Yellow circles represent Cu atoms, gray circles Pt atoms.

each supercell size is indicated by vertical dashed lines in Fig. 5.6 (values are displayed in Table 5.1). It decreases almost linearly with increasing supercell size, while the peak height increases. U and S, shown in Fig. 5.6(b) and (c), respectively, have a rather gradual increase with respect to temperature for the small simulation cell with 16 surface sites. For the simulation cell with 144 surface sites, they reveal a sudden change at T_{trans}. This jump in U and S, and a sharp delta-like peak in the C_p are signatures of a first-order phase transition.

Furthermore, C_p and U are calculated from MMC sampling trajectories of simulated annealing procedures for the simulation cells with 16 surface sites using $N_{\text{eq}} = 10\,000$ and with 64 surface sites using $N_{\text{eq}} = 12\,500$. The results,

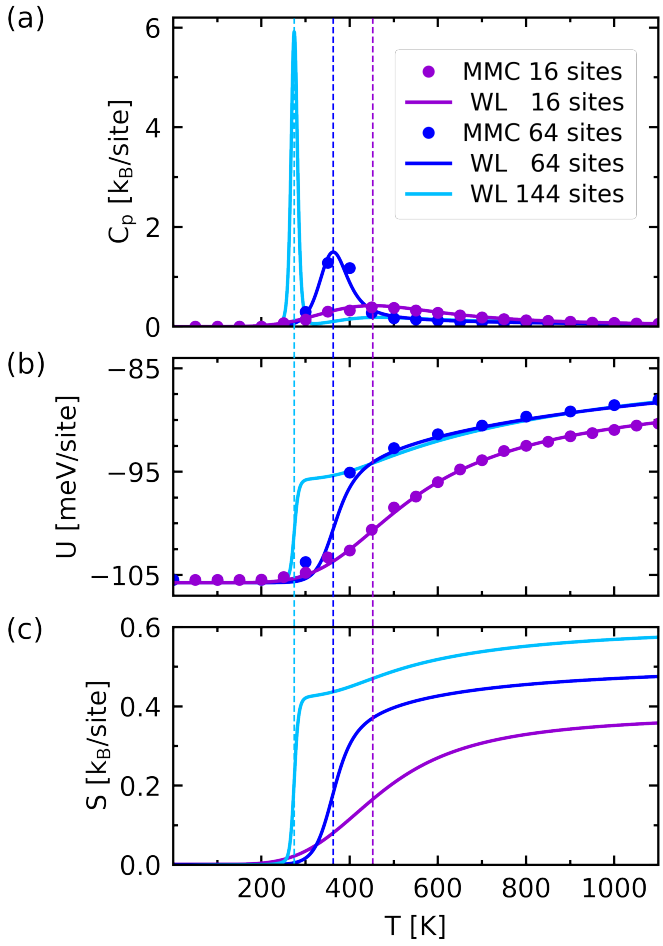

Figure 5.6: (a) Specific heat C_p, (b) internal energy U, and (c) entropy S with respect to temperature for the Pt/Cu(111) surface alloy with 16 (light blue), 64 (dark blue) and 144 (violet) surface sites of the simulation cell. Results obtained from WL method are shown with solid lines, results obtained by MMC samplings with dots in the corresponding color code. The transition temperatures T_{trans} from the ordered to disordered phase, indicated by the maximum of the C_p, are shown with vertical lines.

Table 5.1: Parameters of WL samplings for the Pt/Cu(111) surface for supercells of different sizes. From left to right: the number of surface sites of the supercell, the final modification factor f, the flatness citerion in the first ($m = 0$) and the final iteration, the total number of iterations, and the transition temperature T_{trans}. A general description of the parameters used in a WL sampling is given Sec. 3.2.2.

# surface sites	**final f**	**initial x%**	**final x%**	**iter.** m	$\mathbf{T_{trans}}$ **[K]**
16	$e^{1\cdot10^{-7}}$	0.5	0.95	23	452
64	$e^{6\cdot10^{-5}}$	0.5	0.9	14	363
144	$e^{6\cdot10^{-5}}$	0.5	0.9	14	274

shown with dots in Figs. 5.6(a) and (b), are in agreement with the results obtained from the WL method.

5.2 CLUSTER EXPANSION MODELS

In the configurational samplings performed for $Ba_8Al_xSi_{46-x}$, we use CE models for the energy E, the band gap E_{gap}, and the average bond distances between two neighboring k sites, b_{kk}, and between two neighboring i sites, b_{ii}. Their model parameters, as *e.g.* the ECIs, the loo-CV, and the RMSE are shown in Table 5.2. The CE model for E is obtained from an iterative scheme, developed as part of my Master thesis and published in Ref. [41]. In this study, it was found that the energy of mixing of GS configurations in the composition range $6 \leq x \leq 16$ decreases linearly with increasing x, but exhibits an abrupt change in slope at $x = 13$ [41]. To model this behavior accurately, one CE model was built from *ab initio* data at $x \in [6, 13]$ and another one from *ab initio* data at $x \in [13, 16]$ (details about building the CE models are given in Ref. [41]).

When we discuss the quantity E_{gap}, we refer to a gap in the KS band structure that can be found below the Fermi energy E_F for compositions $x < 16$ and that is the fundamental KS band gap for $x = 16$. Such gap is present in most of the GS configurations. At a fixed composition, this band gap is not present for all configurations (detailed discussion about the changes of band gap is given in Sec. 5.5.2). This can be problematic for constructing a CE model for E_{gap}, since CE builds linear models and, thus, is unable to fit a property that can take zero or positive values, but not negative ones, as the band gap. Therefore, the CE model for E_{gap} is trained using solely configurations with a band gap. Here, it turns out that a higher predictive power is achieved by building again two CE models, one for $x \in [6, 12]$ and one for $x \in [13, 16]$. We are particularly interested in the band gap at $x = 16$, thus at this composition, *ab initio* properties of 18 additional semiconducting structures are calculated

Table 5.2: Model parameters J_α, loo-CV, and RMSE of the CE models for the energy E, the band gap E_{gap}, and the average bond distances between neighboring k sites, b_{kk}, and between neighboring i sites, b_{ii}, for $Ba_8Al_xSi_{46-x}$. The model for E is taken from Ref. [41]. The models are trained from clathrate structures in the composition range $x \in [6, 16]$, which are calculated *ab initio* with the DFT package `exciting` [29] using the PBEsol exchange-correlation functional [102]. N_s indicates the number of structures used as training set. N_α indicates the number of clusters used for the CE model.

	E [meV/atom]		**E_{gap} [eV]**		**b_{kk} [Å]**	**b_{ii} [Å]**
x	$[6, 13]$	$[13, 16]$	$[6, 12]$	$[13, 16]$	$[6, 16]$	$[6, 16]$
N_s	25	17	16	25	40	40
N_α	8	10	4	5	4	4
J_0	-39510551.1	-39510606.9	-0.101	-0.077	2.4550	2.3097
J_k-J_c	4.86	3.82	-	0.035	0.0139	-0.0028
J_i-J_c	6.35	5.26	-0.069	-	0.0015	0.0066
J_c	23758.11	23763.06	0.084	-	-0.0051	0.0048
J_{kk}	4.93	4.29	-	-	-	-
J_{ii}	6.45	7.05	-	-	-	-
J_{ki}	4.53	5.45	-	-0.048	-	-
J_{kc}	5.23	5.12	-	-0.044	-	-
$J_{k(k)i}$	-	-	0.028	-	-	-
$J_{i(k)i}$	-	0.61	-	-0.026	-	-
$J_{k(k)c}$	-	0.21	-	-	-	-
loo-CV	1.13	0.59	0.038	0.038	0.0039	0.0023
RMSE	0.69	0.31	0.029	0.031	0.0035	0.0021

(using the same computational parameters and calculation procedure as in Ref. [41]) and added to the training set.

Furthermore, we build separate CE models for the bond distances b_{kk} and b_{ii}, since they are very sensitive to configurational changes [32, 41] (detailed discussion in Sec. 5.6). Here, we use as training set the average bond distances of the structures calculated in Ref. [41]. A separation of the training data set to build the CE models is not needed in theses cases, since a high predictive power with a low loo-CVS is already obtained by a single CE model for the full composition range $x \in [6, 16]$.

The optimal set of clusters $\mathcal{C}_{\text{opt}}$ with its corresponding ECIs of the CE model for E_{gap}, b_{kk} and b_{ii}, respectively, is obtained by executing two consecutive optimization procedures: First, a nested loop over sets of clusters with increasing cluster radius $R^{\max}$ and increasing cluster size N_p is performed, using as ob-

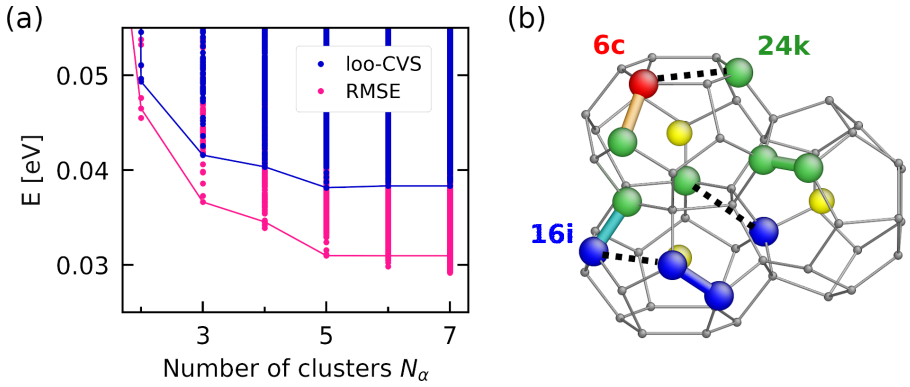

Figure 5.7: (a) Combinatorial optimization procedure for the CE model for the band gap, E_{gap}, with $x \in [13, 16]$: loo-CVS (blue) and RMSE (magenta) versus the number of clusters N_α of subsets selected from the clusters set $\mathcal{C}_1$. (b) Clusters of the optimal CE models, whose model parameters are given in Table 5.2. Host atoms in gray and guest atoms in yellow. 1-point clusters representing the Wyckoff sites $24k$, $16i$, and $6c$ are marked in green, blue, and red, respectively. The bonds between the nearest-neighbor 2-point clusters kk, ki, kc, and ii are marked in green, cyan, orange, and blue, respectively. Next-nearest-neighbor two-point clusters are indicated by dashed lines.

jective function Eq. (24) (see Sec. (3.2.1)). The cluster set size N_α increases with increasing $R^{\max}$ and N_p. From this optimization, the set of clusters $\mathcal{C}_1$ with the smallest loo-CVS is selected. In the second optimization procedure, a combinatorial search over all subsets of $\mathcal{C}_1$ is performed. This corresponds to solving the objective function of Eq. (25) with the ℓ_0-norm as regularization term. From all combinations, the subset with the smallest loo-CVS is identified as the optimal set $\mathcal{C}_{\text{opt}}$ for the CE model. For each CE model, the set of clusters $\mathcal{C}_1$ selected in the first optimization is defined by $R^{\max} = 4.32\,\text{Å}$ and $N_p = 2$, consisting, in total, of 16 clusters. An example of the subsequent combinatorial search is given in Fig. 5.7(a) for the CE model for E_{gap} in the composition range $x \in [13, 16]$. All possible subsets of $\mathcal{C}_1$ at a given number of clusters $N_\alpha < 16$ (x-axis) are considered, and the corresponding loo-CVS and RMSE are calculated (each point in Fig. 5.7(a) corresponds to one subset). The blue solid line connects the cluster subsets with the lowest loo-CVS for each N_α, while the magenta line connects their corresponding RMSE. The optimal CE model for E_{gap} having the lowest loo-CVS of $\sim 0.04\,\text{eV}$ is found for a subset with $N_\alpha = 5$ (corresponding ECIs are shown in Table 5.2).

Among the optimal set of clusters used in each CE model, are the empty cluster $\alpha = 0$, the three 1-point clusters $\alpha = k, i$, and c representing the three Wyckoff sites $w = 24k$, $16i$, and $6c$, respectively, the four 2-point clusters $\alpha = kk$, ii, ki, and kc of neighboring sites, and three 2-point clusters $\alpha = k(k)i$, $i(k)i$, and $k(k)c$ consisting of next-nearest neighbor sites (site in parenthesis indicates the Wyckoff site in between the two sites building the cluster). The ECIs J_α of the clusters α used for the CE models are given in Table 5.2. The

symbol "-" indicates that this cluster is not present in the CE model. The CE models are constructed using the cluster functions $f_\beta(\boldsymbol{\sigma}) = \prod_{i\in\beta}\sigma_i$ with $\sigma_i = 0, 1$. This non-orthogonal basis provides a convenient way to interpret configurational changes, since $f_\beta(\boldsymbol{\sigma})$ is one if every site of β is occupied with substitutional species (Al atoms in our case) and zero otherwise.

5.3 CANONICAL-ENSEMBLE AVERAGES USING THE CONFIGURATIONAL DENSITY OF STATES

In the following, a strategy to calculate canonical averages of any property P is devised by using $g(E)$ obtained from the WL method. This is particular useful for properties, for which a CE model is difficult to build. For instance, this is the case for the spectral function $A(\boldsymbol{k}, \epsilon)$. This quantity depends on two parameters, the wave vector $\boldsymbol{k}$ and the energy ϵ, thus, many CE models may be required for an accurate description of its probably complex behavior.

The canonical-ensemble average of P at temperature T is obtained from the following sum over the complete configuration space:

$$P_T \equiv \langle P\rangle_T = \frac{1}{Z_T}\sum_c P(\boldsymbol{\sigma}_c) e^{-\frac{E(\boldsymbol{\sigma}_c)}{k_B T}} \ . \tag{145}$$

Here, $P(\boldsymbol{\sigma}_c)$ is the property and $E(\boldsymbol{\sigma}_c)$ the energy of configuration c. $P(\boldsymbol{\sigma}_c)$ is weighted by the Boltzmann distribution $\exp\left(-\frac{E(\boldsymbol{\sigma}_c)}{k_B T}\right)$, and Z_T is the canonical partition function $Z_T = \sum_c \exp\left(-\frac{E(\boldsymbol{\sigma}_c)}{k_B T}\right)$. The configurations span the energy interval $[E_{\mathsf{GS}}, E_{\max}]$ with E_{GS} being the GS energy and $E_{\max}$ the maximum energy that is possible to attain in the configurational space. Dividing this energy interval into M intervals $\Delta_{E_j} = [E_j, E_j + \Delta_j[$ of width Δ_j with $E_{j+1} = E_j + \Delta_j$, the sum in Eq. (145) can be recast into a sum over these energy intervals as

$$P_T = \sum_j^M \langle P\rangle_{E_j}\, g(E_j)\Delta_j\, e^{-\frac{E_j}{k_B T}} \ . \tag{146}$$

Here, $\exp\left(-E(\boldsymbol{\sigma}_c)/k_B T\right) \approx \exp\left(-E_j/k_B T\right)$ for $E(\boldsymbol{\sigma}_c) \in \Delta_{E_j}$ under the assumption that the widths Δ_j are not too large. Furthermore, $g(E_j)\Delta_j$ is an estimate for the number of configurations N_j in interval Δ_{E_j}, and $\langle P\rangle_{E_j} = \sum_{E(\boldsymbol{\sigma}_c)\in\Delta_{E_j}} P(\boldsymbol{\sigma}_c)/N_j$ is the expectation value of P in Δ_{E_j}.

By using n_j configurations in each interval ΔE_j in Eq. (146) instead of the actual number N_j, a sampling error is introduced. This error can be estimated by a resampling procedure similar to the *bootstrap method* [202, 203]. Here, instead of obtaining $\langle P\rangle_{E_j}$ from the average of the n_j configurations, a subset of these n_j configurations is randomly generated and used to calculate $\langle P\rangle_{E_j}$. Performing several resamplings and calculating for them the canonical average,

as defined in Eq. (146), the uncertainty can be estimated by their standard deviation. This resampling technique is used in the calculation of the canonical-averaged transport coefficients, discussed in Sec. 5.7.

As a general remark, the underlying assumption for the average in Eq. (146) is spatial ergodicity [204], i.e. all possible configurations in a finite sample are realized in the infinite sample. Thus, the behavior of the infinite sample can be approximated by an average of many single finite samples.

5.4 COMPUTATIONAL DETAILS

The set of *ab initio* structures in the composition range $x \in [6, 16]$ from the iterative GS search performed in Ref. [41] is used for the analysis of their electronic properties. In addition to those structures, 38 configurations at composition $x = 16$ are computed with the same computational parameters and calculation procedure as for the previous configurations [41]. 15 of them are selected from a simulated annealing sampling retaining low-energy structures with energy less than 10 meV/atom above the GS energy $E_{\mathrm{GS}} = -39130344.71$ meV/atom. The set of 44 structures available at $x = 16$ is used to calculate canonical averages using Eq. (146).

The *ab initio* properties of these structures are calculated with the DFT package **exciting** [29]. From previous studies, we know that, independently from the choice of the exchange-correlation functional, LDA or PBEsol, the GS configuration remains the same [41]. For a few selected configurations of $x = 16$, the electronic structure is calculated with the DFT package FHIaims [205] using the hybrid functional HSE06 [206, 207]. In these calculations, the size of the fundamental band gap increases as expected, however, structures that have no fundamental band gap stay metallic. Thus, we conclude that the overall picture of the electronic and structural properties does not depend on the functional and choose PBEsol for our calculations. Each structure is optimized until the lattice parameter reaches an uncertainty of below 0.01Å and the atomic forces are below 34 meV/atom. To speed up convergence, the mixing algorithm of Ref. [208] is used for some of the structures. For the GS calculation, we use a homogeneous $4\times4\times4$ $\boldsymbol{k}$-point mesh, and the parameter $R_{\mathrm{MT,min}}|\boldsymbol{G}+\boldsymbol{k}|_{\max} = 8$ with R_{MT} of $2.0\,a_B$ for Al and Si and $2.3\,a_B$ for Ba. The plane-wave cutoff $\boldsymbol{G}$ for the density and the potential is $12\,a_B^{-1}$.

The transport coefficients are calculated using the BT approach as implemented in **exciting** (see Sec. 4.1). The transport integrals are evaluated on a dense mesh of $12 \times 12 \times 12$ $\boldsymbol{k}$-points. A convergence test with different $\boldsymbol{k}$-meshes (see in Fig. A.2 of Appendix A.1.2) demonstrates that this mesh is sufficient to achieve converged results for the clathrate compound $Ba_8Al_{16}Si_{30}$ ($x = 16$). In the Boltzmann approach, the only phenomenological parameter is the relaxation time τ, which accounts for various scattering processes. For

clathrates, typical estimates for τ in theoretical transport calculations range from 5 fs to 20 fs [34, 35, 37, 209, 210]. For the results presented in Sec. 5.7, we use the constant temperature-independent value $\tau = 5$ fs.

For the MMC simulations, we perform 10 million sampling steps at every temperature for the unit cell. For the $2 \times 2 \times 2$ supercell, which is 8 times larger than the unit cell, 80 million sampling steps are performed to reach the same level of convergence as for the unit cell. The first half of these sampling steps is taken for equilibration and the second half for averaging. For the $4 \times 4 \times 4$ supercell, 640 million sampling steps are out of reach, due to the very long sampling times that it would require. Here, we perform about 80 million sampling steps at every temperature and determine the number of equilibration steps N_{eq} for each temperature individually by analyzing its sampling trajectory. Typically, N_{eq} is around 60 million steps for low temperatures and 5 million steps for high temperatures.

The WL sampling (explained in Sec. 3.2.2), used to obtain the configurational density of states $g(E)$ at $x = 16$, is performed with the modification factors, $f_{m=0} = e^1$ in the first outer loop ($m = 0$) and $f_{m=27,\min} = e^{1.5 \cdot 10^{-8}}$ in the final outer loop after $m = 27$ iterations. The flatness criterion starts with $x\% = 50\%$ at $m = 0$ and reaches $x\% = 98\%$ at $m = 27$. For the energy space discretization, a bin width of $\Delta = 1$ meV/atom is chosen with the lowest energy bin centered at E_{GS}. The converged $g(E)$ is shown in Fig. 5.8(a).

5.5 PHASE TRANSITIONS

5.5.1 *Charge-compensated clathrate*

In this section, we study the temperature-dependent structural and electronic properties of the charge-compensated composition $Ba_8Al_{16}Si_{30}$. The results presented in this section are published in Ref. [138].

The DFT band gaps, E_{gap}, (right axis) of configurations with energies $E(\boldsymbol{\sigma}_c)$ are shown with black dots in Fig. 5.8(b). The x axis presents the energy E with respect to the GS energy E_{GS}. The band gap changes drastically with the Al configuration. Starting from the GS, which has an energy gap of $E_{\text{gap,GS}} = 0.36$ eV, E_{gap} decreases linearly with increasing E (red dash-dotted line) until reaching zero at around 5 meV/atom. Above 5 meV/atom, both semiconducting and metallic structures are present.

We proceed with analyzing the canonical probability distribution D_T in dependence of energy E and temperature T. For this, we employ the configu-

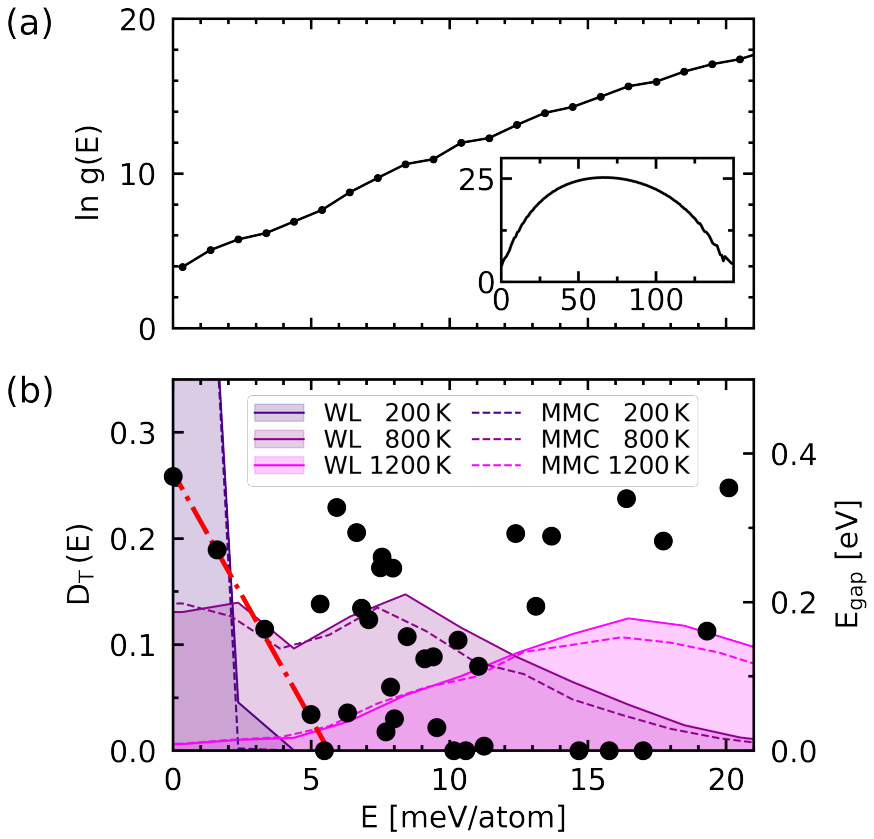

Figure 5.8: (a) Natural logarithm of the configurational density of states $\ln g(E)$ versus total energy E obtained from WL sampling in the unit cell for $Ba_8Al_{16}Si_{30}$. The inset shows the values for the full energy space that can be attained in the configurational space. (b) Canonical distribution $D_T(E)$ from Eq. (147) for $T = 200\,\mathrm{K}$, $800\,\mathrm{K}$, and $1200\,\mathrm{K}$ (left axis) and KS band gaps E_{gap} (black dots, right axis) versus E. The energy zero is the GS energy E_{GS}. The results for $D_T(E)$ obtained from the WL method are shown with shaded areas below solid lines, those from the MMC method with dashed lines. The linear decrease of the band gap at low energies is indicated by a red dash-dotted line.

rational density-of-states $g(E)$, obtained by a WL sampling as shown in Fig. 5.8(a)). Using $g(E)$, D_T is calculated as

$$D_T(E) = \frac{1}{Z_T}\, g(E)\Delta\, \exp\left(-\frac{E}{k_B T}\right) \quad . \tag{147}$$

Here, $Z_T = \sum_E g(E)\Delta\, \exp\left(-\frac{E}{k_B T}\right)$ is the partition function at temperature T, and k_B is the Boltzmann constant. D_T versus E is shown with solid lines and shaded areas in Fig. 5.8(b) (left) for the temperatures $200\,\mathrm{K}$, $800\,\mathrm{K}$, and $1200\,\mathrm{K}$. At low temperatures, *e.g.* $T = 200\,\mathrm{K}$ (dark violet), D_T has a single peak below $3\,\mathrm{meV/atom}$. Only semiconducting configurations are in this energy range. With increasing temperature, D_T becomes significant above $5\,\mathrm{meV/atom}$, where also

metallic configurations are present. At $T = 800\,\mathrm{K}$ (violet), D_T shows two maxima, one around $2\,\mathrm{meV/atom}$ and one around $8\,\mathrm{meV/atom}$. This double-peak distribution is indicating the coexistence of two phases, which are studied in more detail below when the temperature-dependent structural and thermodynamic properties are considered. For $T = 1200\,\mathrm{K}$ (magenta), D_T has a broad peak at high energies with metallic configurations. The distributions D_T can be reproduced by MMC samplings, as shown with dashed lines in Fig. 5.8(a).

For a detailed study of the electronic behavior at finite temperature, we calculate the temperature-dependent effective band structure (TD-EBS) from a canonical-ensemble average using the method presented in Sec. 5.3. Using the set of 44 computed configurations available at $x = 16$ (see Sec. 5.4), it is obtained from the following two averaging steps:

(*i*) For each configuration in the set, the symmetry of the pristine primitive cell is restored by an averaging procedure, according to Refs. [49, 50, 211]. The resulting symmetrized energy spectrum accounts for different local environments present due to the Al substituents in the host lattice.

(*ii*) Using $g(E)$, a statistical weight is assigned to each symmetrized energy spectrum. Then, a canonical-ensemble average is performed by applying the strategy described in Sec. 5.3.

A general method to obtain the TD-EBS of any alloy is described in Ref. [138]. For the clathrate alloy, we focus on the TD-EBS along the Γ-M path, since the GS has an indirect band gap along this direction, as can be seen from its band structure depicted in Fig. 5.9(a). This indirect band gap is not present for other configurations, as *e.g.* for the high-energy configuration with an energy $E(\boldsymbol{\sigma}_\mathrm{M}) = 64.74\,\mathrm{meV/atom}$ above the GS, shown in Fig. 5.9(b) (label M stands for metallic configuration).

Starting with point (*i*), for each of the 44 computed configurations at $x = 16$, we restore the symmetry of the pristine primitive cell, *i.e.* the non-substituted clathrate Ba_8Si_{46} with space group $Pm\bar{3}n$. The symmetry of the pristine primitive cell is at least partially broken due to Al substituents in the crystal, leading to, in general, different eigenvalues for different $\Gamma - M$ directions. However, the wave vector $\boldsymbol{k}_S$ of the substituted clathrate can be mapped to wave vector $\boldsymbol{k}$ of the pristine lattice by the relation $\boldsymbol{k}_S = S\boldsymbol{k}$, with S being a point-symmetry operation of the pristine primitive cell. Using this mapping, a symmetry-averaged spectral function for a configuration c can be defined as

$$A_c(\boldsymbol{k}, \epsilon) = \frac{1}{N_S} \sum_S \sum_n \delta_\xi(\epsilon - \epsilon_{c,n\boldsymbol{k}_S})\,. \tag{148}$$

Here, $\epsilon_{c,n\boldsymbol{k}_S}$ is the KS energy of band n and wave vector $\boldsymbol{k}_S$ for configuration c, and the sum runs over N_S operations S. ξ is a small number representing the discretization of ϵ. δ_ξ is 1 if the argument $(\epsilon - \epsilon_{c,n\boldsymbol{k}_S})$ is inside the interval $[-\xi, \xi[$ and 0 otherwise. The sum over S considers all point-symmetry

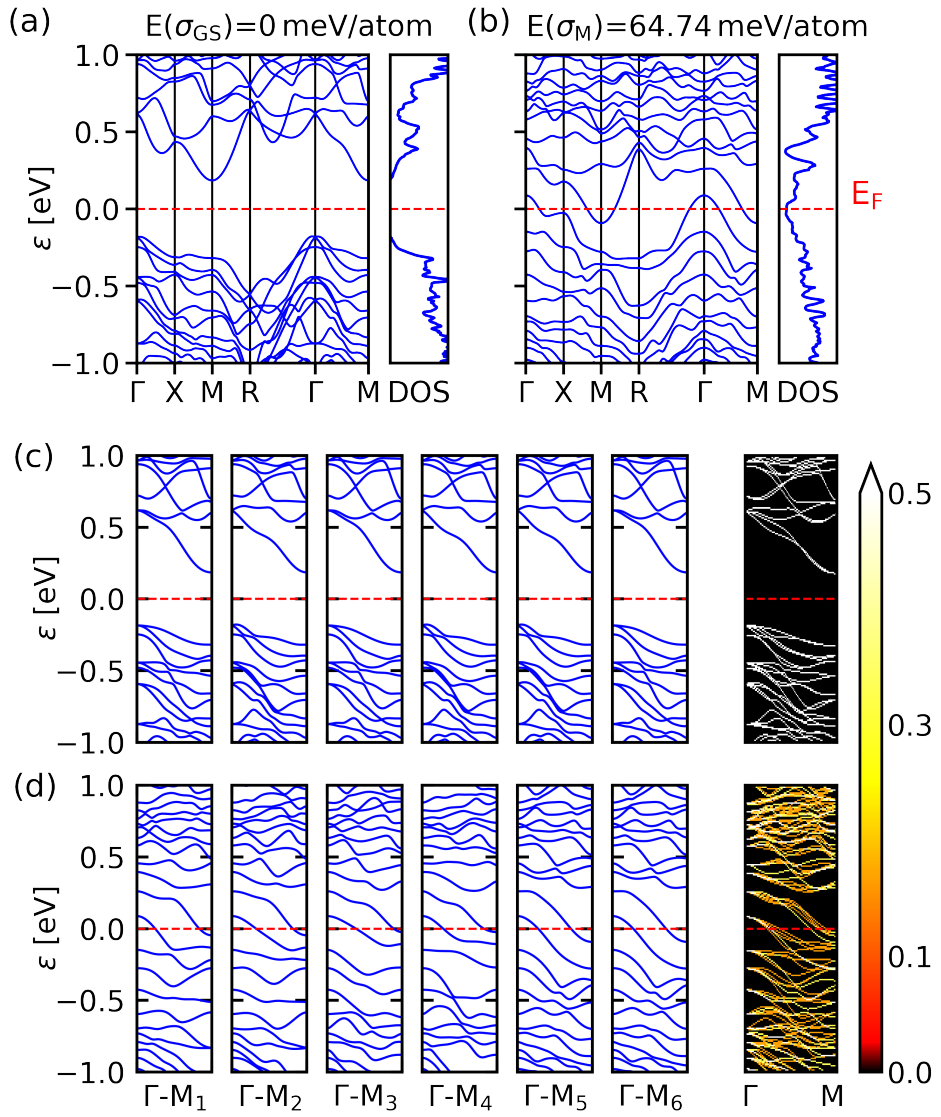

Figure 5.9: Band structure between high symmetry points and DOS for (a) the GS and (b) a high-energy configuration. Numbers on top of the band structure are the energies E of the structure with respect to E_{GS}. Band structure along the six different symmetry directions Γ-M (labeled with subscripts from 1 to 6) and resulting symmetry-averaged spectral function $A_c(\boldsymbol{k}, \epsilon)$ on the right are plotted for (c) the GS and (d) the high-energy configuration. Here, $A_c(\boldsymbol{k}, \epsilon) = 0$ is indicated in black, and $A_c(\boldsymbol{k}, \epsilon) > 0.5$ in white. The red dashed lines indicate the Fermi energy E_F.

operations. In the case of $Ba_8Al_{16}Si_{30}$, an unfolding of the band structure to recover the translational symmetry of the pristine primitive cell, as done in Refs. [49, 211], is not needed, since the lattice of the configurations has the same size as the pristine primitive cell. The cubic cell of $Ba_8Al_{16}Si_{30}$ has 6 distinct Γ-M directions. Figures 5.9(c) and (d) show the band structure for the GS and the high-energy structure along these directions, respectively. Both

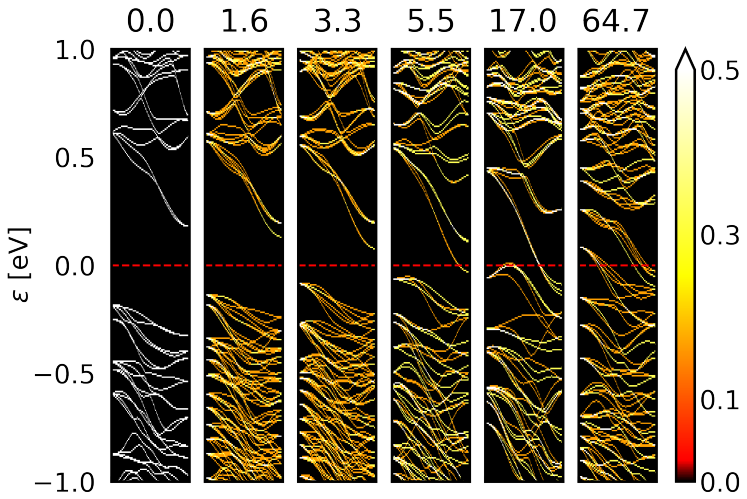

Figure 5.10: Symmetry-averaged spectral function $A_c(\boldsymbol{k}, \epsilon)$ of three semiconducting and two metallic configurations c at $x = 16$. The numbers on top of each panel indicate the energy E of the corresponding structure with respect to the energy of the ground state (E in meV/atom). Black corresponds to $A_c(\boldsymbol{k}, \epsilon) = 0$ and white to $A_c(\boldsymbol{k}, \epsilon) > 0.5$.

also show their resulting symmetry-averaged spectral functions (on the right). The symmetry-averaged spectral function for six further configurations with intermediate energies are shown in Fig. 5.10.

In point (*ii*), statistical weights are assigned to each $A_c(\boldsymbol{k}, \epsilon)$ by employing $g(E)$. With these, a canonical-ensemble average of these $A_c(\boldsymbol{k}, \epsilon)$'s can be calculated (see Eq. (146) in Sec. 5.3) as

$$A_T(\boldsymbol{k}, \epsilon) = \frac{1}{Z_T} \sum_{j}^{M} \langle A(\boldsymbol{k}, \epsilon) \rangle_{E_j} \, g(E_j) \Delta_j e^{-\frac{E_i}{k_B T}} \ . \tag{149}$$

Here,

$$\langle A(\boldsymbol{k}, \epsilon) \rangle_{E_j} = \frac{1}{n_j} \sum_{E(\boldsymbol{\sigma}_c) \in \Delta_{E_j}} A_c(\boldsymbol{k}, \epsilon) \tag{150}$$

is the configurational-averaged spectral weight of the energy interval Δ_{E_j}, obtained from the $A_c(\boldsymbol{k}, \epsilon)$'s of the n_j computed configurations whose energy $E(\boldsymbol{\sigma}_c)$ is in Δ_{E_j}. The TD-EBSs for temperatures from $200\,\mathrm{K}$ to $1200\,\mathrm{K}$, resulting from the corresponding $A_T(\boldsymbol{k}, \epsilon)$'s, are depicted in Fig. 5.11. At $200\,\mathrm{K}$, TD-EBS is similar to the symmetrized energy spectra of the GS (see Fig. 5.9(c), right), since it shows also an indirect effective band gap with the valence band maximum close to the Γ point and the conduction band minimum at the M point. With increasing temperature, the effective band gap decreases. For $T \geq 800\,\mathrm{K}$, $A_T(\boldsymbol{k}, \epsilon)$ at the Fermi energy is clearly non-zero, which indicates

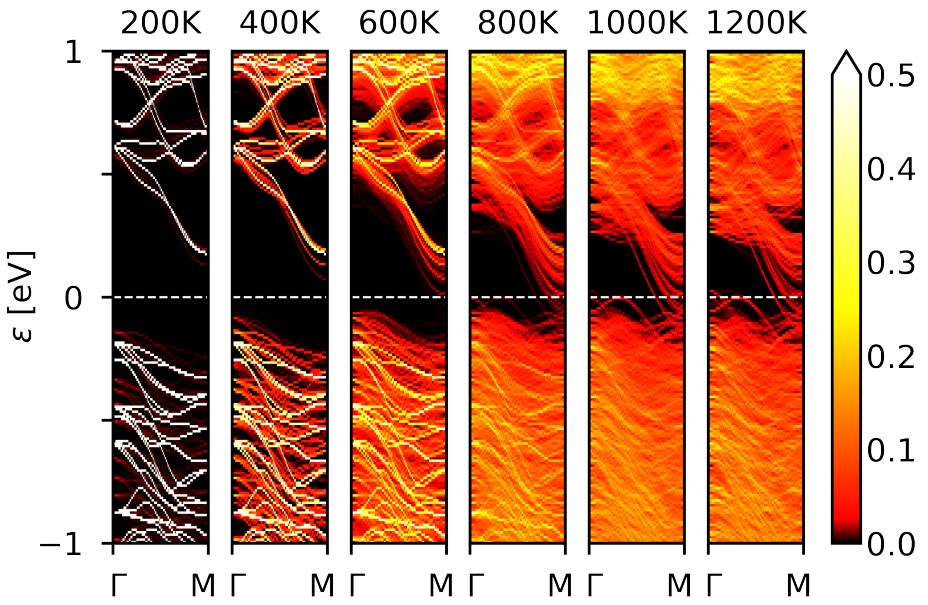

Figure 5.11: Temperature-dependent effective band structure along the Γ-M path for temperatures between 200 and 1200 K (from left to right). Black corresponds to $A_c(\boldsymbol{k}, \epsilon) = 0$ and white to $A_c(\boldsymbol{k}, \epsilon) > 0.5$. The white dashed lines indicate the Fermi energy E_F.

the onset of metallicity, under the assumption that no electron localization is present. (Disorder-driven localization can not be described by the method and model system used in this approach.)

Before we proceed with discussing the temperature-dependent density-of-states (TD-DOS), the effect of thermal lattice expansion on the electronic band structure is considered. It can have a significant impact, especially, on the band gap at elevated temperatures, as demonstrated, *e.g.*, for PbTe and SnTe in Ref. [212] and for $CuInTe_2$ in Ref. [213]. To estimate its effect for $Ba_8Al_{16}Si_{30}$, the electronic band structure of two different configurations using an expanded lattice (in analogy to Ref. [212]) is calculated. The thermal expansion coefficient α for Ba_8Si_{46} is $\alpha = 12 \cdot 10^{-6}\,\mathrm{K}^{-1}$ [214]. Using this value and the relation $\alpha = \Delta a/a \cdot (T_x - T_{0\mathrm{K}})^{-1}$, with a being the lattice constant at temperature $T_{0\mathrm{K}} = 0\,\mathrm{K}$ and Δa its change when going to temperature T_x, we obtain $\Delta a = 0.11\,\text{Å}$ for $T_x = 900\,\mathrm{K}$. Figure 5.12 shows the band structure at $0\,\mathrm{K}$ (no thermal expansion, blue lines) and at $900\,\mathrm{K}$ (expanded lattice with $\Delta a = 0.11\,\text{Å}$, dashed orange lines) for the GS (in Fig. 5.12(a)) and a high-energy configuration (in Fig. 5.12(b)). For both configurations, the result obtained for $900\,\mathrm{K}$ agrees well with the result for $0\,\mathrm{K}$. Thus, the effect of the thermal lattice expansion on the band structure is negligible.

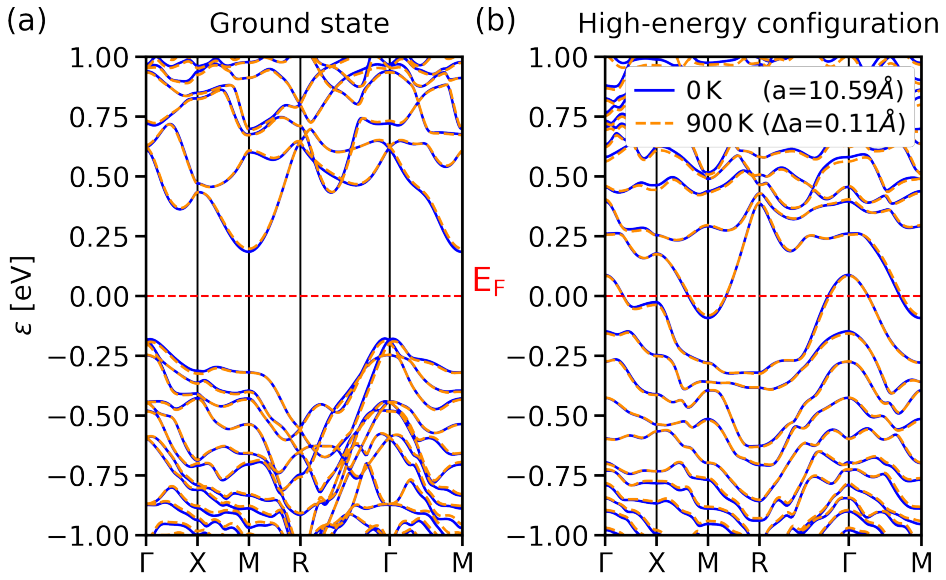

Figure 5.12: Band structure for (a) the ground state and (b) a high-energy configuration. Blue lines correspond to 0 K (lattice constant $a = 10.59\text{Å}$) and dashed orange lines to 900 K (lattice constant $a + \Delta a$ with $\Delta a = 0.11\text{Å}$). Here, only the thermal lattice expansion is considered.

The temperature-dependent density of states (TD-DOS) is obtained with a similar canonical average (Eq. (146)), as used for the spectral function:

$$\text{DOS}_T(\epsilon) = \frac{1}{Z_T} \sum_j^M \langle \text{DOS}(\epsilon) \rangle_{E_j} \, g(E_j) \Delta_j e^{-\frac{E_i}{k_B T}} \, . \tag{151}$$

Here,

$$\langle \text{DOS}(\epsilon) \rangle_{E_j} = \frac{1}{n_j} \sum_{E(\boldsymbol{\sigma}_c) \in \Delta_{E_j}} \text{DOS}_c(\epsilon) \tag{152}$$

is the configuration-averaged DOS of interval Δ_{E_j}, obtained from the DOS_c of the n_j computed configuration c whose energy $E(\boldsymbol{\sigma}_c)$ belongs to Δ_{E_j}. The TD-DOS, shown in Fig. 5.13, reveals also a closing of the effective band gap around 700 K, similar as obtained from the TD-EBS. The TD-DOS, shown for $200\,\text{K} \leq T \leq 1200\,\text{K}$ in Fig. 5.13(a) (left), exhibits the same narrowing of the band gap with increasing temperature as observed in the TD-EBS. The band gap closes at around 700 K.

After gaining knowledge about the temperature-dependent electronic properties, the discussion in the following paragraphs focuses on the temperature-dependent structural and thermodynamic properties.

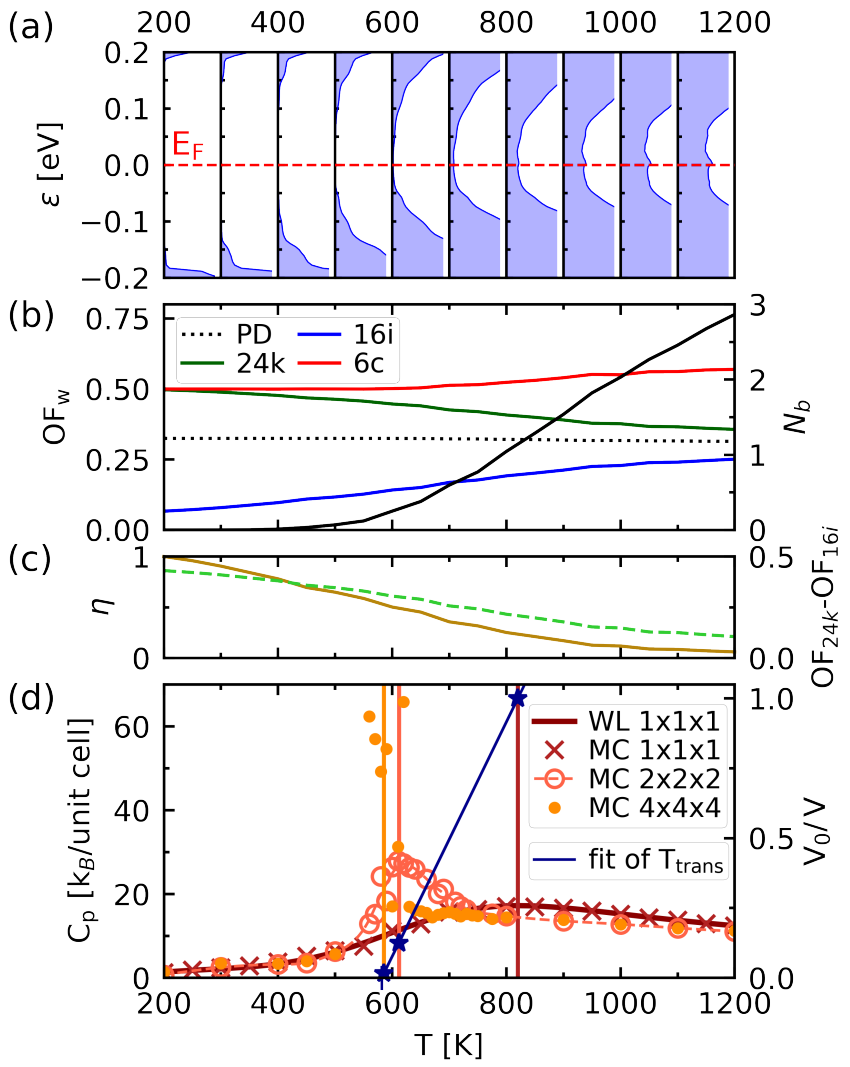

Figure 5.13: Signatures of the phase transition with respect to temperature: (a) Electronic density of states (blue shaded area). The Fermi level E_F is indicated with a red dashed line. (b) Occupation factors OF_w of the three Wyckoff sites $w = 24k$, $16i$, and $6c$, value of partial disorder $\mathrm{OF}_{\mathrm{PD}}$ (left axis), and number of Al-Al bonds N_b (black line, right axis). (c) Order parameter η (brown line, left axis), calculated from Eq. (155), and difference in occupation factors OF_{24k}-OF_{16i} (dashed light green line, right axis). (d) Specific heat C_p (left axis) for the single unit cell obtained from the WL method (dark-red solid line) and from the MMC method (dark-red crosses). Furthermore, C_p for the $2 \times 2 \times 2$ (dashed orange line, circles) and $4 \times 4 \times 4$ (yellow dots) supercells obtained from MMC simulations are shown. The transition temperature T_{trans} of the respective supercell size is indicated by a vertical line in the corresponding color. The dark-blue stars on top of these lines indicate the inverse of the supercell volume V^{-1} (right axis) and the solid dark-blue line the least-squares fit of Eq. (156).

From MMC samplings, we extract the total number of Al-Al bonds, N_b, and the fractional Al occupancy factors, OF_w, of the Wyckoff sites $w = 24k$, $16i$, and $6c$, which are calculated as

$$\mathrm{OF}_w(T) = \frac{1}{N_{\mathrm{avg}}} \sum_{i=1}^{N^i_{\mathrm{avg}}} \frac{N_{\mathrm{Al},w}(T)}{N^i_{\mathrm{sites},w}} \,. \tag{153}$$

Here, N_{avg} is the number of sampling steps used for the average, $N^i_{\text{Al},w}$ the number of Al atoms sitting at w in the visited configuration i, and N_{sites} the multiplicity of w. The result is shown in Fig. 5.13(b). At low temperatures ($T \leq 200\,\text{K}$), the structural properties agree well with the one of the GS configuration, that has twelve, one, and three Al atoms at the $24k$, $16i$, and $6c$ site, respectively, *i.e.* $\text{OF}_{24k} = 0.5$, $\text{OF}_{16i} = 0.0625$, and $\text{OF}_{6c} = 0.5$, and no Al-Al bonds [41]. The occupation of the $6c$ site, OF_{6c}, remains almost unaffected by the temperature and increases only to 0.57 at $T = 1200\,\text{K}$, *i.e.* there are ~ 0.4 Al atoms more in comparison to the GS configuration. OF_{24k} decreases, and OF_{16i} increases with temperature, approaching at $T \approx 1200\,\text{K}$ the value of partial disorder (PD), which can be calculated as

$$\text{OF}_{\text{PD}}(T) = \left[16 - \text{OF}_{6c}(T) \cdot 6\right]/40 \ . \tag{154}$$

This value, shown with a black dotted line in Fig. 5.13(b), corresponds to a partially disordered structure, that has a fully random Al-Si alloy in the sublattice $24k$-$16i$ and an ordered sublattice $6c$ due to the preference of the $6c$ site. The actual Al content in the $24k$-$16i$ sublattice depends on the occupation of the $6c$ site, thus, $\text{OF}_{\text{PD}}(T)$ changes slightly with respect to temperature from 0.325 at $200\,\text{K}$ to 0.315 at $1200\,\text{K}$. N_b increases with temperature due to the increase of disorder in the $24k$-$16i$ sublattice.

The transition from a well-ordered state to a (partially) disordered state can be characterized by an order parameter [215, 216]. With the use of OF_{PD}, the following order parameter is derived:

$$\eta(T) = \frac{1}{2} \sum_{w=24k,16i} \left[\frac{\text{OF}_w(T) - \text{OF}_{\text{PD}}(T)}{\text{OF}_w(0\,\text{K}) - \text{OF}_{\text{PD}}(0\,\text{K})} \right]^2 . \tag{155}$$

This order parameter is defined in such a way that it is one for the ordered phase at zero Kelvin, and zero for the perfect partially disordered phase being present at large temperatures. As shown in Fig. 5.13(c) (brown line, right axis), η decreases from $\sim$1 at $200\,\text{K}$ to almost zero at $1200\,\text{K}$. The simple difference of the $24k$ and $16i$ occupations factors, OF_{24k}-OF_{16i}, shown with a light green dashed line in Fig. 5.13(c), exhibits a similar decrease with temperature. Both parameters indicate the structural change from order to partial disorder, while η is a better definition of an order parameter, since it has appropriate low- and high-T limits.

The transition temperature T_{trans} of the phase transition is determined in the following from the signatures in the canonical probability distribution D_T (Eq. (147)) and the isobaric specific heat C_p (Eq. (32)). For first-order phase transitions, D_T at T_{trans} is expected to have a bimodal distribution with peaks of equal height [45, 133], and C_p is expected to exhibit a maximum at T_{trans} [133, 139, 140, 201]. As seen before in Fig. 5.8(a), the canonical distribution D_T has indeed two peaks with nearly equal height at $T_{\text{trans}} \approx 800\,\text{K}$. The C_p is calcu-

lated for different supercell sizes and shown in Fig. 5.13(d). For the unit cell, labeled as $1 \times 1 \times 1$ cell, C_p has a maximum at $820\,\mathrm{K}$ (dark-red vertical line). Here, for both methods, the WL (solid dark red line) and the MMC method (dark read crosses), indistinguishable results are obtained.

Due to the finite size of the simulation cell, the peaks of D_T and the C_p computed for the single unit cell are rounded (so-called "finite-size rounding" [133, 139, 217–220]), and it is expected that T_{trans} for the unit cell deviates systematically from the macroscopic limit [133, 201, 221]. This deviation is investigated in detail by calculating the C_p from MMC samplings for two further supercell sizes, a $2 \times 2 \times 2$ and a $4 \times 4 \times 4$ supercell with the simulation-cell volumes $V = 8\,V_0$ and $64\,V_0$, respectively (V_0 being the unit-cell volume). For the $2 \times 2 \times 2$ supercell (see Fig. 5.13(d), unfilled circles), the C_p has a single peak with a maximum that is larger and a distribution width that is smaller in comparison to that of the single unit cell. Here, we obtain $T_{\mathrm{trans}} = 621\,\mathrm{K}$. For the $4 \times 4 \times 4$ supercell, the computed C_p values have a large dispersion around $T = 600\,\mathrm{K}$ (Fig. 5.13(d), yellow dots), hampering an accurate identification of T_{trans} by the peak maximum. This is a frequent problem in simulations with increased supercell sizes, since for them very large sampling times are required near the transition region to obtain the correct probability distribution of the phases at those temperatures [133, 201, 222]. Nonetheless, we obtain an estimate of the transition temperature T_{trans} by an inspection of the MMC trajectories and the canonical probability distributions for temperatures near the transition, *i.e.* between $560\,\mathrm{K}$ and $610\,\mathrm{K}$. They are shown in Fig. 5.14. As seen from the MMC trajectories in Fig. 5.14(a), the system swaps between a low (violet) and high (magenta) energy phase and finally remains in one of the phases for a very long sampling time. Their corresponding canonical probability distributions, depicted in Fig. 5.14(b), reveal a double peak structure (phase coexistence) with preference of the low energy phase for $T \leq 580\,\mathrm{K}$ and preference of the high energy phase for $T \geq 590\,\mathrm{K}$. The change of preference is taken as indicator for the transition point. Thus, we take the mean value of those temperatures as estimate for T_{trans}, *i.e.* $T_{\mathrm{trans}} = 585\,\mathrm{K}$. The values of T_{trans} for each supercell size are indicated by vertical lines in Fig. 5.13(d). In general, we observe for the peak of the C_p that its height increases and its width decreases with increasing cell size, as typically observed for first-order phase transitions [133, 139]. For these, the transition temperature changes linearly with the inverse of the simulation-cell volume V^{-1} [133, 201] as

$$T_{\mathrm{trans}}(V) = T_{\mathrm{trans}}(\infty) + a\,V^{-1}\ . \tag{156}$$

Here, $T_{\mathrm{trans}}(\infty)$ is the transition temperature in the macroscopic limit, and a is a constant. $T_{\mathrm{trans}}(\infty)$ is determined by performing a least-squares fit of Eq. (156) to the values obtained for the three different supercell sizes. The obtained fit function, which is the straight dark-blue solid line in Fig. 5.13(d), agrees very well with the data points. We obtain $T_{\mathrm{trans}}(\infty) = 582\,\mathrm{K}$. This

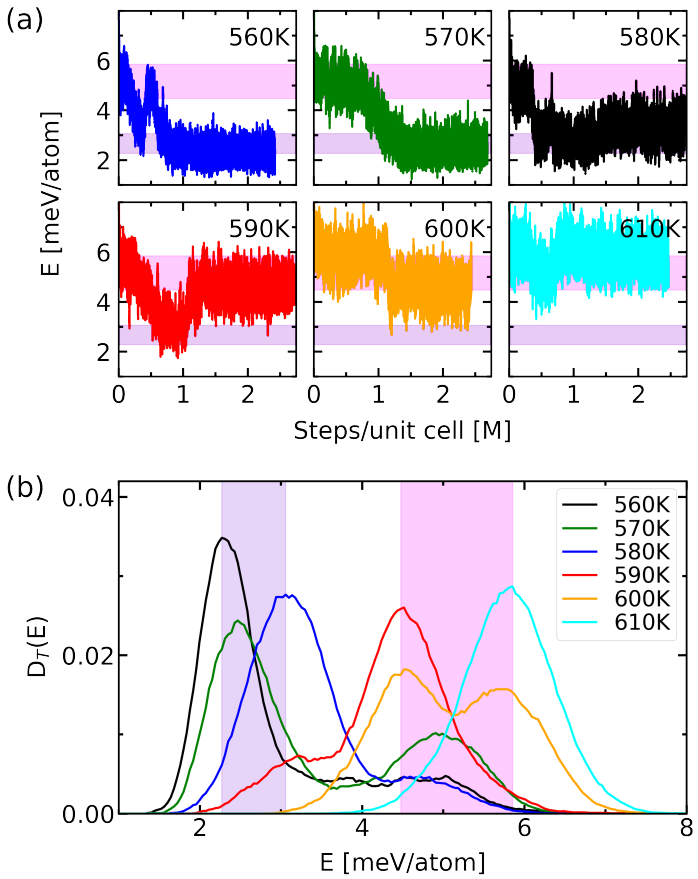

Figure 5.14: (a) Trajectory of the MMC samplings in the $4 \times 4 \times 4$ supercell and (b) their respective canonical probability distributions, $D_T(E)$ for various temperatures. The low-energy phase is indicated in violet, the high-energy phase in magenta.

temperature differs significantly from $T_{\text{trans}} = 820\,\text{K}$ of the unit cell, affirming the importance of a finite-size scaling.

A further indication that the partial order-disorder transition is a first-order phase transition is obtained by investigating the mircocanonical entropy $S(E)$ and its derivatives [223]. $S(E)$, shown in Fig. 5.15(a), is calculated as

$$S(E) = k_B \ln G(E) \; . \tag{157}$$

Here, $G(E)$ is the integrated density of states $G(E) = \int_{E_{\text{GS}}}^{E} g(E')dE'$ obtained from $g(E)$ for the single unit cell. The first derivative of S with respect to the energy E is the inverse of the temperature $T^{-1}(E) = \beta = (dS/dE)_{N,p}$. The result of $T^{-1}(E)$ is shown with a red solid line in Fig. 5.15(b)). The inflection point of $T^{-1}(E)$ appears at the inverse of the transition temperature for the unit cell, *i.e.* at $1/T_{\text{trans}} = 1/820\,\text{K}^{-1} = 0.00122$ (dark-blue horizontal line). At this inflection point, the second derivative $d\beta/dE = d^2S/dE^2$, shown with

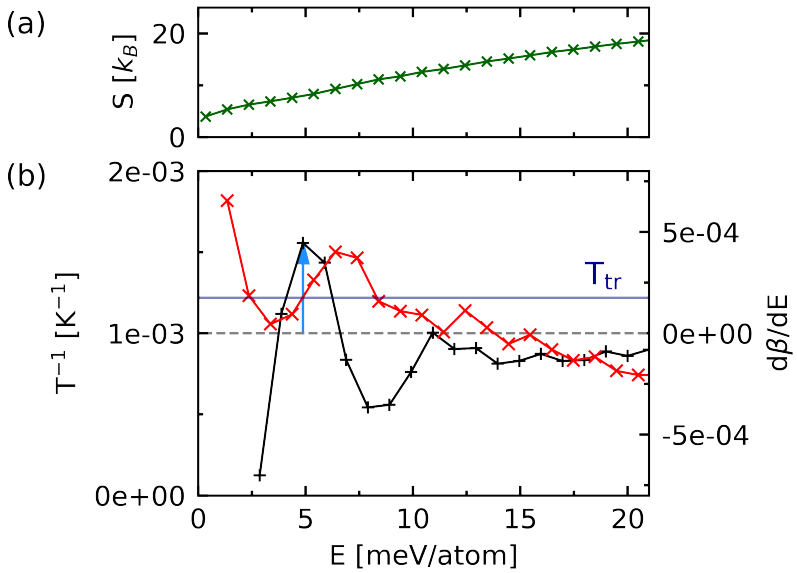

Figure 5.15: (a) Microcanonical entropy S and (b) its energy derivatives with respect to the total energy E. The first derivative, $T^{-1}(E) = \beta$, is shown in red (left axis) and the second derivative, $d\beta/dE$, in black (right axis). The inverse of the transition temperature for the unit cell $T_{\text{trans}}^{-1} = 1/820\,\text{K}^{-1} = 0.00122$, shown by the dark-blue horizontal line, matches the position of the inflection point of β (light-blue arrow).

the black solid line in Fig. 5.15(b), is positive (indicated by a light blue arrow). Both criteria point out that the phase transition is of first-order.

As last point regarding the phase transition temperature for $Ba_8Al_{16}Si_{30}$, we want to mention that the effect of the exchange-correlation functional on the transition temperature is negligible, as demonstrated in Fig. A.1 in Appendix A.1.1.

5.5.2 *n-doped clathrates*

Besides for the charge-compensated composition, phase transitions occur also for n-doped clathrates, *i.e.* $x \leq 16$. In the following, we discuss the electronic and structural changes with respect to temperature for $Ba_8Al_xSi_{46-x}$ in the composition range $x \in [6, 16]$.

Figure 5.16 shows the band structure and the DOS of the GS and a high-energy configuration for the compositions $x = 7$ (left panels, (a) and (c), respectively) and $x = 15$ (right panels, (b) and (d), respectively). For both compositions, the GS has a band gap below the Fermi energy, while the high-energy configuration does not reveal a gap in this region. When comparing the band structures of these GSs to the one of the GS at $x = 16$ (see Figs. 5.9(a) and (b)), it is observed that the features of the electronic bands above and below the energy gap are very similar. Thus, the change of composition from

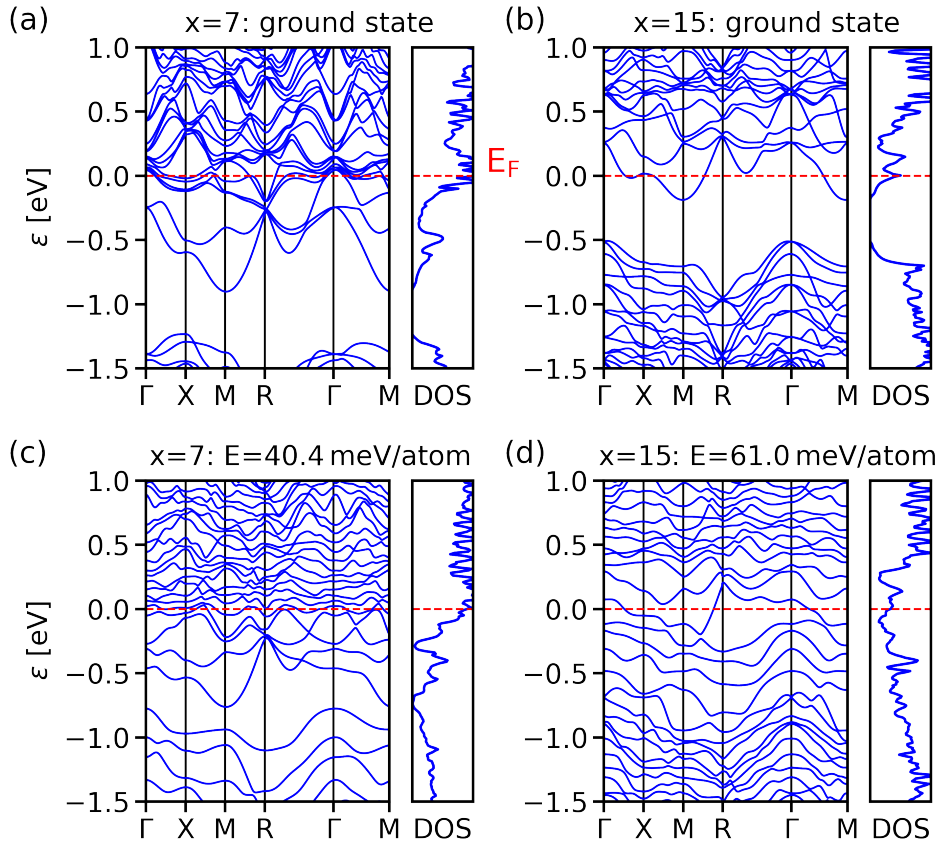

Figure 5.16: Band structure along high-symmetry points and DOS for the GS (upper panels) and a high-energy structure (lower panels) for the compositions $x = 7$ and $x = 15$, respectively. The energy E given on top of panels (c) and (d) indicates the total energy of the high-energy configuration with respect to the energy of the GS.

$x = 16$ to $x \leq 15$ can be understood in terms of the rigid band model [156], where the electronic structure is obtained by shifting up the Fermi level while the band features remain unchanged. At composition x, the Fermi level is shifted by the amount that corresponds to $16 - x$ extra electrons per unit cell.

The DFT band gaps, E_{gap}, of the computed configurations in the composition range $x \in [6, 16]$ are depicted in Fig. 5.17 (black dots). Similarly as observed for $x = 16$, E_{gap} for configurations of $x \leq 15$ can take zero or a positive value. At $x = 6$, the band gap of the GS is $0.45\,\text{eV}$. With increasing x, it decreases until reaching zero at $x = 12$. For $x > 12$, it increases again until arriving at $0.36\,\text{eV}$ for $x = 16$. We also indicate the band gaps of the quasi-degenerate (QD) configurations (light green dashed line), found for intermediate Al content ($x \in [9, 14]$) in Ref. [41]. QD configurations are configurations with an energy close to the GS energy (energy difference less than $2\,\text{meV/atom}$). Thus, at zero temperature, the GS and QD configurations could be simultaneously present in the material, and any average between those gaps

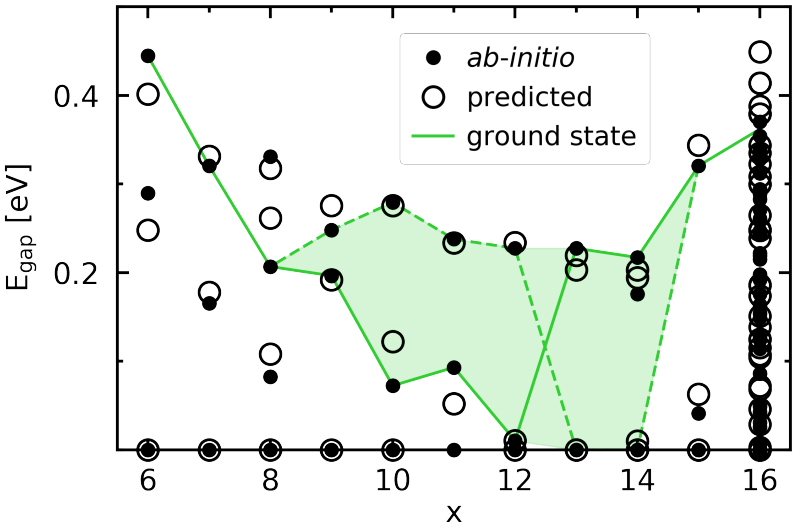

Figure 5.17: Kohn-Sham band gaps E_{gap} (black dots) and its predicted values using a CE model (black circles) for the computed structures with respect to Al content x. The GS configurations for each each x are joined with the light green solid line, the QD configurations of Ref. [41] with a light green dashed line. The range of possible values for E_{gap} at or close to $0\,\text{K}$, spanned by E_{gap} of the GS and the QD states, is indicated with the green shaded area.

can be taken, as indicated with the light green shaded area. At $x \in [12, 14]$, those values range from zero to finite positive values, leading to a possibly non-zero spectral weight for those compositions at $0\,\text{K}$. The mechanism behind the complex configurational reordering leading to QD states is explained in more detail below (see Fig. 5.20).

The predicted CE band gap $\hat{E}_{\text{gap}}$ for the computed configurations, shown with black circles in Fig. 5.17, match well with their *ab initio* values. We use the CE model for $\hat{E}_{\text{gap}}$ (see Sec. 5.2 and Table 5.2) in the following to examine trends in the change of the band gap with respect to temperature. From a canonical simulated annealing procedure with 10 million MMC sampling steps at every $50\,\text{K}$, the expected value of $\hat{E}_{\text{gap}}$ at temperature T and composition x is obtained and shown in Fig. 5.18(a). At this point, we note, that this averaged value can be regarded as the mean value of the gaps present in different local (configurational) phases. To obtain a macroscopic picture of the electronic behavior, the spectral function needs to be calculated, as done in Sec. 5.5.1. For low and high Al content, *i.e.* $x \leq 9$ and $x \leq 15$, $\hat{E}_{\text{gap}}$ is large at low temperatures and decreases with increasing temperature. This phenomenon of a vanishing band gap is similar to the one discussed for the charge-compensated composition $x = 16$ (see previous Sec. 5.5.1). For intermediate compositions ($x \in [10, 14]$), $\hat{E}_{\text{gap}}$ is zero or small for all temperatures, since there exists always a configuration (either the GS or the QD configuration, see Fig. 5.17) with zero band gap.

Table 5.3: Transition temperatures, T_{trans}, of the phase transitions with respect to temperature for $Ba_8Al_xSi_{46-x}$ with $x \in [6, 16]$.

x	6	7	8	9	10	11	12	13	14	15	16
T_{trans} [K]	780	883	986	1015	1039	896	871	886	880	892	820

In the following, we explore the structural and thermodynamic properties that are concomitant to the changes in the electronic properties. From the MMC sampling trajectories of simulated annealing procedures (same as used to calculate the temperature-dependent E_{gap}), we extract the fractional occupation factors, OF_w, of the three Wyckoff sites ($w = 24$, $16i$, and $6c$) and the number of Al-Al bonds N_b. The difference in occupation factors OF_{24k}-OF_{16i}, N_b, and OF_{6c} are shown in Fig. 5.18(b), (c), and (d), respectively, with respect to temperature T and composition x. For the possible structural phase transitions at composition x, being identified from these structural properties, their transition temperature T_{trans} can be extracted from the maximum of the isobaric specific heat C_p, shown in Fig. 5.19 and are given in Table 5.3. For $x = 15$, at low temperatures, *i.e.* $T \leq 200\,\text{K}$, OF_{24k}-OF_{16i} is around 0.5, N_b zero, and OF_{6c} around 0.5. With increasing T, OF_{24k}-OF_{16i} approaches zero, the number of Al-Al bonds increases, and OF_{6c} remains almost unaffected around 0.5. Those characteristics are very similar to the ones observed for $x = 16$ (see Sec. 5.5.1). This is expected, since also the GS ($0\,\text{K}$) for $x = 15$ resembles the one for $x = 16$. Their occupation factors are the same, except for the $16i$ site, which is occupied by no Al atoms for $x = 15$ ($\text{OF}_{16i} = 0$) but with one Al atoms for $x = 16$ ($\text{OF}_{16i} = 0.0625$). As indicated by the C_p for $x = 15$, shown with the green solid line in the right panel of Fig. 5.19, the transition temperature is $892\,\text{K}$ (vertical green dashed line). This temperature is slightly larger than $T_{\text{trans}} = 820\,\text{K}$ at $x = 16$ (dark purple dashed line in the right panel of Fig. 5.19).

For low Al content, *i.e.* $x \in [6, 11]$, the characteristics of the structural changes are different than for $x \in [15, 16]$. As shown in Fig. 5.18(d), OF_{6c} is one at $T \leq 200\,\text{K}$ (all $6c$ sites are occupied). It decreases with increasing T, and reaches 0.5 at $T = 1200\,\text{K}$ (3 Al atoms at the $6c$ site). This value is well above the composition-dependent disorder value, calculated as $(x/46)$ and ranging from 0.13 for $x = 6$ to 0.24 for $x = 11$. Thus, there is a clear preference of the $6c$ site for all temperatures. N_b remains around zero for all temperatures (see Fig. 5.18(c)). In the high-temperature limit, this is due to the low probability for creating Al-Al bonds. This probability can be estimated by $(x/46)^2 \cdot 100\%$, and ranges from 2% for $x = 6$ to 6% for $x = 11$, while being 11% for $x = 15$. For $6 < x \leq 11$, OF_{24k}-OF_{16i} is negative at low temperatures (blue area in Fig. 5.18(b)), indicating that the $16i$ site is preferred over the $24k$ site in this region. The occupation of site $16i$ instead of $24k$ for low Al content can be explained by the coordination of the Wyckoff sites (shown in Fig. 5.20(a)).

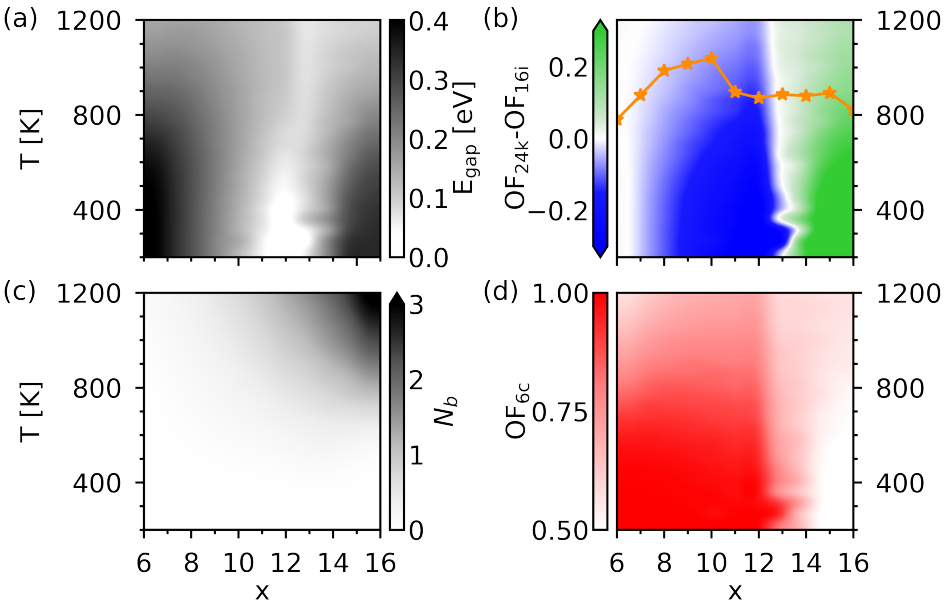

Figure 5.18: (a) Kohn-Sham band gap, E_{gap}, (b) difference of the $24k$ and $16i$ occupation factors, OF_{24k}-OF_{16i}, (c) number of Al-Al bonds, N_b, and (d) occupation factor of the $6c$ site, OF_{6c}, with respect to composition x and temperature T. For E_{gap}, white corresponds to a zero band gap, black to a band gap above $0.4\,\text{eV}$. For OF_{24k}-OF_{16i}, blue indicates a preference of the $16i$ site, green a preference of the $24k$ site. For N_b, white corresponds to no Al-Al bonds, black to more than three Al-Al bonds. For OF_{6c}, white corresponds to half occupation, red to full occupation. The orange stars connected by an orange solid line indicate the transition temperatures T_{trans} from order to partial disorder at given x, extracted from the maximum of the isobaric specific heat C_p depicted in Fig. 5.19.

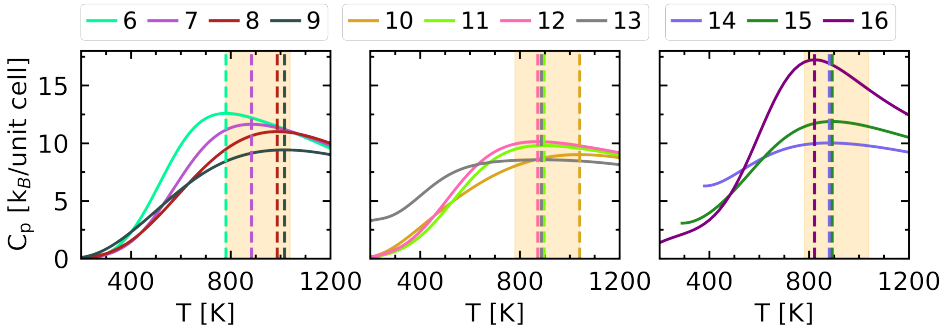

Figure 5.19: Specific heat, C_p, with respect to temperature T for compositions $x \in [6, 16]$ (labels in the legend). The transition temperatures, T_{trans}, are indicated by vertical dashed lines in the corresponding color.

Every $24k$ position has a $6c$ position as neighbor. Since all $6c$ positions are occupied at $T \leq 200\,\text{K}$, the addition of an Al atom to the $24k$ site would lead to a structure with Al-Al bonds. However, Al-Al bonds are energetically not favorable [41], thus, for the compositions $x \leq 11$, the remaining $x - 6$ Al atoms need to occupy $16i$ positions. The preference of $16i$ vanishes at

high temperature ($T \geq 1000\,\mathrm{K}$), since OF_{24k}-OF_{16i} approaches zero. In other words, for those temperatures, the $24k$-$16i$ sublattice hosts a fully random Al-Si alloy while the preference of the $6c$ is kept. Thus, OF_{24k}-OF_{16i} can be used as an order parameter to characterize the phase transition from a well-ordered state at low T (with $\mathrm{OF}_{6c} = 1$ and for $x > 6$, OF_{24k}-$\mathrm{OF}_{16i} > 0$) to a partially disordered state. Looking at the C_p with respect to T for fixed x, shown in Figs. 5.19(a) and (b), we obtain similar transition temperatures as for $x \in [15, 16]$ (orange shaded area in Fig. 5.19). For all compositions, T_{trans} is also shown with orange stars in Fig. 5.18(b) (their values are given in Table 5.3).

For $x \in [12, 14]$, OF_{24k}-OF_{16i} alternates between positive and negative values, and OF_{6c} stays around 0.5 in the full temperature range. Thus, the structural properties at low temperatures do not show a clear ordering pattern. This is due to the QD states with rather different structural ordering present in those compositions. The complex configurational reordering leading to the QD states is exemplified in Fig. 5.20(b) for the composition $x = 9$, for which the reordering can be demonstrated in a clear way. Here, the GS has zero, three and six Al atoms at the $24k$, $16i$, and $6c$ site, respectively, and no Al-Al bonds. Representing this configuration by the notation $(N_{\mathrm{Al},24k}, N_{\mathrm{Al},16i}, N_{\mathrm{Al},6c})\ N_b$ with $N_{\mathrm{Al},w}$ indicating the number of Al atoms sitting at Wyckoff position w, the GS is (0,3,6) 0. Moving of an Al atom from the $16i$ site to the $24k$ site lowers the energy by $J_i - J_k$ since $J_k < J_i$ (see cluster interactions in Table 5.2), but increases the energy by J_{kc} since an Al-Al bond is created between a $24k$ and $6c$

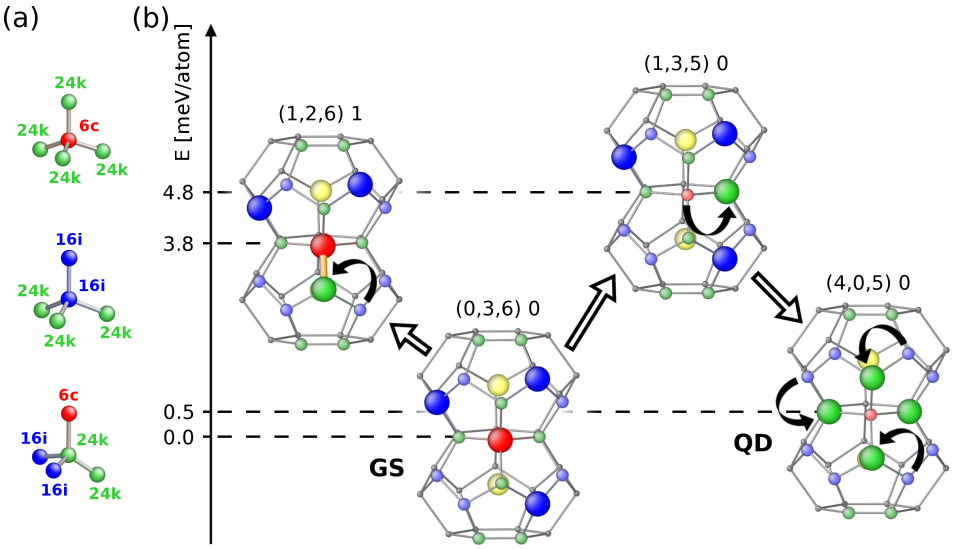

Figure 5.20: (a) Wyckoff sites and their tetrahedral bonding to the neighboring atoms. (b) Favored low-energy configurations with respect to the GS energy, exemplified for $x = 9$. The sites occupied by Al atoms are indicated by large spheres. Each composition is represented by the notation $(N_{\mathrm{Al},24k}, N_{\mathrm{Al},16i}, N_{\mathrm{Al},6c})\ N_b$, with $N_{\mathrm{Al},w}$ being the Al occupation $N_{\mathrm{Al},w}$ of site w and N_b the number of Al-Al bonds. The energies are given with respect to the energy of the GS.

position. This results in a non-QD configuration with an energy $3.8\,\text{meV/atom}$ above the GS energy, since its energy is larger than the threshold of $2\,\text{meV/atom}$ for a QD configuration (threshold chosen according to the precision of the *ab initio* energies used to train the CE model). However, moving one Al atom away from a $6c$ position and putting it to a $24k$ position allows for the Al atoms sitting at $16i$ positions to move to $24k$ positions surrounding an "empty" $6c$ position (empty means here occupied by a Si atom) without creating an Al-Al bond (neighboring atoms connected to a site are explicitly shown in Fig. 5.20(a)). This multiple exchange of Al atoms lead to a QD configuration with an energy only $0.5\,\text{meV/atom}$ above the GS energy and notably different occupation factors. Especially for the composition $x = 13$, there are several possibilities for those multiple exchanges and the pronounced occupation of the $24k$ or $16i$ site disappears not only at high, but also at low temperatures [41]. Here, also the C_p remains almost constant for $T > 500\,\text{K}$ and does not show a clear maximum as for the other compositions.

The examination of the structural phases present at low T in dependence of the composition reveal a transition of the ordering pattern around $x = 13$ (see Figs. 5.18(b), (c), and (d)). For $x \leq 12$, the $16i$ site is preferred over the $24k$ site, and the $6c$ site is fully occupied, while for $x \geq 14$ the $24k$ site is preferred over the $16i$, and the $6c$ site is half occupied. The preference of the $6c$ site is maintained at any composition and temperature. Also around $x = 13$, the band gap is zero for all temperatures (see Fig. 5.18(a)). The preference of the $6c$ site is maintained at any composition and temperature.

5.6 TEMPERATURE-DEPENDENT BOND DISTANCES

For $Ba_8Al_xSi_{46-x}$, the bond length between two host positions is expected to increase when an Al atom sits at one (or both) of these positions, due the larger covalent radius of Al in comparison to Si [224]. Therefore, the bond distances correlate with the Al occupations of the Wyckoff positions. Especially those between two k sites (b_{kk}) and between two i sites (b_{kk}) are very sensitive to the Al configuration, while these between the k and i site and between the k and c site (b_{ki} and b_{kc}) are less sensitive (maximum change $\approx 0.02\,\text{Å}$), exhibiting simply a monotonic, almost linear, increase with the Al content [32, 41]. To investigate the changes in b_{kk} and b_{ii} originating from the configurational (dis)order present at finite temperature, we perform a canonical MMC simulated annealing procedure for every $x \in [6, 16]$, in which b_{kk} and b_{ii} of each visited configuration are predicted by using CE models (see Sec. 5.2 and Table 5.2). From this, we obtain the temperature-dependent average bond distances $b_{kk}(T)$ and $b_{ii}(T)$.

Figure 5.21 shows $b_{kk}(T)$ and $b_{ii}(T)$ with respect to the Al content x. Here, colors are used to indicate the temperature. In addition, b_{kk} and b_{ii} of the

GSs and their experimental values are displayed. As reported in Ref. [41], the discrepancies between the GS bond distances and available experiments can be explained for $x \geq 9$ by QD structures, however not for b_{kk} at $x < 9$. At T below 200 K, the temperature-dependent b_{kk} and b_{ii} agree well with the bond distances of the GSs. For $x \leq 13$, b_{kk} increases with T, leading to a very good agreement with experiment at $T \geq 1000$ K for these compositions, especially now also for $x < 9$. For $x \geq 14$, b_{kk} decreases with T. This leads for $x = 15$ at $T \geq 1000$ K to a better agreement with experiment Exp. 2, but not with Exp. 4, which in turn matches with b_{kk} of the GS. Regarding b_{ii}, the variation with T is very small for $x < 9$. For $9 \leq x \leq 12$, it decreases only slightly with T and agrees well with experiment (similar as the GSs). For $x \geq 13$ at $T \geq 1000$ K, it coincides with the experiment Exp. 2, while the GSs at those compositions differs from it. The experimental data point at $x = 15$ from Exp. 1 [33] (blue triangle at $x = 15$) does not match the calculated values, neither $b_i i(T)$ nor b_{ii} of the GS (a QD configuration is not present at this composition).

The better agreement of the bond distances with experiments at elevated temperatures than the ones of the GSs suggests that the measured samples do not resemble the GS configuration, but adopted rather partially disordered configurations present at high annealing temperatures, *e.g.* 900 K, that are used for the compound's synthesis [32, 33, 36, 225]. Due to the indistinguishable x-ray diffraction patterns of Si and Al atoms in the host sites [33, 36, 42, 43], the sample's actual occupation factors cannot be determined directly. However,

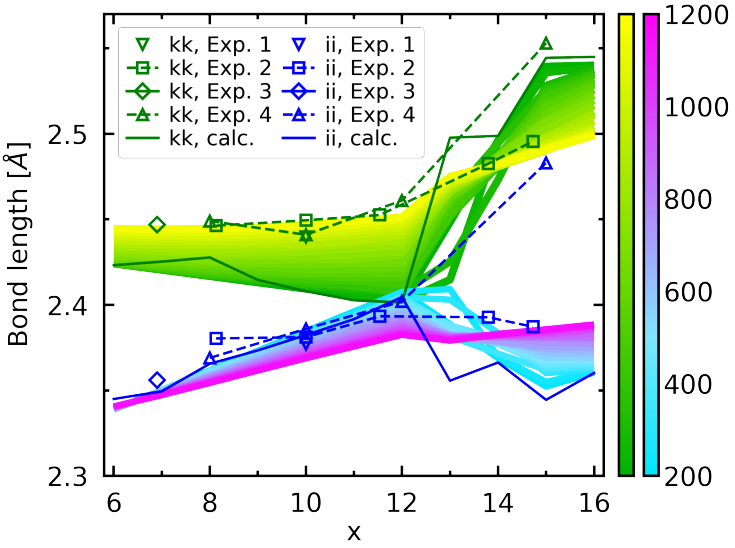

Figure 5.21: Temperature-dependent average bond distances $b_{kk}(T)$ and $b_{ii}(T)$ obtained from MMC samplings. They are shown at $T = 200$ K in green and light blue, respectively, while at $T = 1200$ K in yellow and violet, respectively. b_{kk} and b_{ii} of the GS configurations are indicated by dark green and dark blue solid lines, respectively. Experimental data (unfilled symbols) are taken from Refs. [33], [36], [32], and [225], labeled as Exp. 1, Exp. 2, Exp. 3, and Exp. 4, respectively.

the average bond distances can be monitored. Thus, the CE model describing correctly the bond distances at finite temperature is a useful tool that can help to identify the site occupations of synthesized samples.

5.7 THERMOELECTRIC TRANSPORT COEFFICIENTS

After studying the interplay between the temperature-dependent configurational ordering and electronic properties, we analyze now configurational effects on the transport properties.

For the set of *ab initio* configurations available for $x = 16$, the transport coefficients are calculated using the BT approach as implemented in **exciting** (see Sec. 4.1.1). Here, for each configuration c, the chemical potential μ is adjusted according to the electron concentration $n_{e,1e} = 8.415 \cdot 10^{20}\,\text{cm}^{-3}$, that corresponds to one free electron in the volume of the unit cell, thus effectively composition $x = 15$. We have a particular interest in $x = 15$, since near and at this composition experimental data are available. Such a simple adjustment of μ assumes that the removal of one Al atom in the crystal structure does not affect the electronic bands (rigid band model) [156, 157]. A cross-check of this plausible assumption is obtained by computing the transport coefficients of the actual GS at $x = 15$ for comparison. As shown in Fig. A.4 (Appendix A.1.2), the results are almost identical. Furthermore, the temperature-dependent electronic and structural properties of both compositions reveal very similar signatures, as *e.g.* the closing of the band gap with increasing temperature, the preference of the $24k$ site over the $16i$ site at low temperature, and a partially disordered state at high temperature. Thus, configurations at $x = 16$ with adjusted doping concentration can be used to describe the temperature-dependent properties for compositions near and at $x = 15$. For the relaxation time τ, we use the constant temperature-independent value $\tau = 5\,\text{fs}$. Typical estimates for the clathrate compounds range from $5\,\text{fs}$ to $20\,\text{fs}$ [34, 35, 37, 209, 210].

Figure 5.22 shows the transport coefficients of the GS (green line) and a configuration with a closed band gap having an energy around $5\,\text{meV/atom}$ higher than the GS energy (red solid line), as well as the canonical-ensemble-averaged transport coefficients (blue solid line) obtained from the set of 44 *ab initio* configurations at $x = 16$. Exemplified for the Seebeck coefficient S, the canonical-ensemble average is calculated as

$$S_T(\mu) = \sum_j^M \langle S(\mu,T)\rangle_{E_j}\, g(E_j)\Delta_j e^{-\frac{E_i}{k_B T}}\ , \tag{158}$$

with $\langle S(\mu,T)\rangle_{E_j} = \frac{1}{n_j}\sum_{E(\boldsymbol{\sigma}_c)\in\Delta_{E_j}} S_c(\mu,T)$ now being the temperature-dependent configurationally averaged Seebeck coefficient of the energy interval Δ_{E_j} ($S_c(\mu,T)$ is the Seebeck coefficient of configuration c). We further

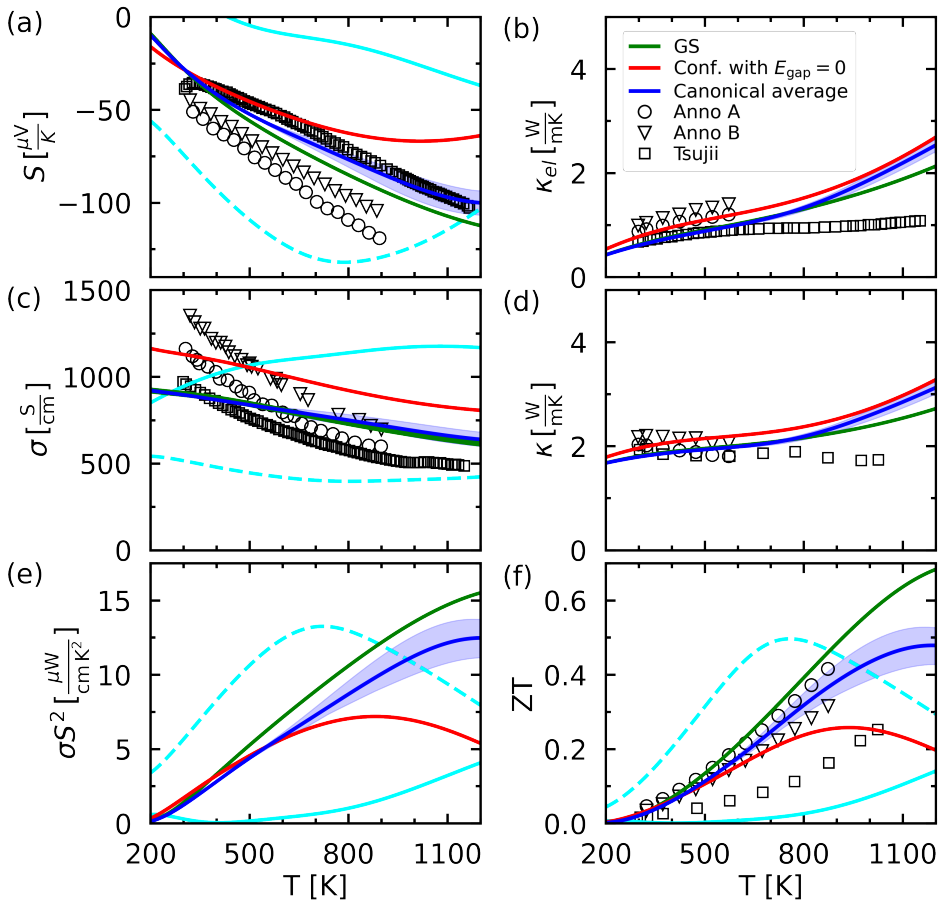

Figure 5.22: (a) Seebeck coefficient S, (b) electronic part of the thermal conductivity κ_e, (c) electrical conductivity σ, (d) total thermal conductivity κ, (e) power factor $S^2\sigma$, and (f) figure of merit ZT of the n-doped clathrate corresponding to $Ba_8Al_{15}Si_{30}$ ($x = 15$), calculated with the BT approach, using configurations of $x = 16$ and setting the charge carrier concentration to $n_{e,1e} = 8.415 \cdot 10^{20}\,\mathrm{cm}^{-3}$ (corresponding to one free electron in the unit cell). The results obtained from the GS configuration, a zero-band-gap configuration (labeled as "conf. with $E_{gap} = 0$"), and the canonical-ensemble average are shown with green, red, and blue solid lines, respectively. The blue shaded area indicates the uncertainty of the canonical average obtained by resamplings. Experimental data from Refs. [34] and [226] are shown with black unfilled symbols. Samples Anno A and B of Ref. [34] have $n_{e,\text{Anno A}} = 9.71 \cdot 10^{20}\,\mathrm{cm}^{-3}$ and $n_{e,\text{Anno B}} = 1.28 \cdot 10^{21}\,\mathrm{cm}^{-3}$, respectively. Sample Tsujii of Ref. [226] has $n_{e,\text{Tsujii}} \sim 3 \cdot 10^{21}\,\mathrm{cm}^{-3}$. The canonical-ensemble average calculated for the carrier concentrations $n_{e,\text{low}} = 3 \cdot 10^{20}\,\mathrm{cm}^{-3}$ and $n_{e,\text{high}} = 3 \cdot 10^{21}\,\mathrm{cm}^{-3}$ are shown with light blue dashed and solid lines, respectively.

estimate an uncertainty for the canonically averaged values by applying the resampling technique described in Sec. 5.3. The coefficients obtained from 50 resamplings are shown for the example of S in Fig. A.3 (Appendix A.1.2). The uncertainty is estimated by the difference between the maximal and minimal $S_T(\mu)$ at given T obtained from the resamplings.

The results for S and the electrical conductivity σ, shown in Fig. 5.22(a) and (c), respectively, obtained for the GS and the zero-band-gap configuration differ from one another. The canonical average takes an intermediate value, being closer to the result of the GS. The power factor $S^2\sigma$, resulting from S and σ and shown in Fig. 5.22(e), is the largest for the GS, with its maximum at $T \gtrsim 1200\,\mathrm{K}$. The maximum of the canonical average appears at the same temperature, but is lower. For the zero-band-gap configuration, the maximal σS^2 is reached at a much lower temperature around at $T \sim 850\,\mathrm{K}$, and its value is significantly smaller. The results obtained for the electronic part of the thermal conductivity κ_{el}, shown in Fig. 5.22(b), are very similar irrespective of their configuration, thus κ_e is largely insensitive to configurational changes. The same is observed for the total thermal conductivity κ (see Fig. 5.22(d)). Here, its lattice part $\kappa_{l,\text{exp. fit}}$ is estimated by a linear fit to the experimental values of Ref. [226], *i.e.* $\kappa = \kappa_e + \kappa_{l,\text{exp. fit}}$.

In addition to the calculations, Fig. 5.22 shows measured transport coefficients for samples with chemical composition close to $x = 15$ extracted from Refs. [34] and [226]. The two samples from Ref. [34], labeled as Anno A (black unfilled circles) and Anno B (black unfilled triangles), and the sample from Ref. [226], labeled with Tsujii (black unfilled squares), have charge carrier concentrations at $n_{e,\text{Anno A}} \sim 9.71 \cdot 10^{20}\,1/\mathrm{cm}^{-3}$, $n_{e,\text{Anno B}} \sim 1.28 \cdot 10^{21}\,1/\mathrm{cm}^{-3}$, and $n_{e,\text{Tsujii}} \sim 3 \cdot 10^{21}\,1/\mathrm{cm}^{-3}$, respectively. The calculated transport coefficients of the GS and the canonical-ensemble average with $n_{e,1e}$ are in good agreement with experiment. S and σ calculated using the zero-band gap configuration show a rather different behavior at high temperatures $T \gtrsim 800\,\mathrm{K}$. For κ_{el}, thus also for κ, the calculations depart slightly from the measurements for $T \gtrsim 800\,\mathrm{K}$.

We turn now to the figure of merit ZT, that is shown in Fig. 5.22(f). Since it is obtained from $S^2\sigma$ divided by the almost constant value κ, the shape of the calculations is similar to the ones discussed for $S^2\sigma$. The results obtained for the GS and the canonical-ensemble average are in good agreement with the data corresponding to samples Anno A and B of Ref. [34], while the data corresponding to sample Tsujii of Ref. [226] with a significant larger n_e than expected for the composition $x = 15$ has much lower ZT values. The result obtained for the zero-band-gap configuration reveals a rather different change with temperature in comparison to the measurements, especially at $T \gtrsim 800\,\mathrm{K}$. The maximal ZT of ~ 0.7 is reached for the GS at $T = 1200\,\mathrm{K}$. The canonical-ensemble average, that takes into account also contributions of configurations with zero band gap in the electronic structure, give a smaller maximum ZT of ~ 0.5. This value is in agreement with a ZT in Ref. [34] predicted from an extrapolation of experimental data to $1200\,\mathrm{K}$ using a simplified BT model.

Since the samples measured and analyzed in Ref. [34] and [226] differ in their charge carrier concentration, we also explore different carrier concentrations in our calculations. We perform a canonical average with $n_{e,\text{high}} = 3 \cdot 10^{21}\,\mathrm{cm}^{-3}$

(light blue solid lines in Figs. 5.22(a), (c), (e) and (f)) that is higher than the estimated carrier concentration for $x = 15$, $n_{e,1e} = 8.415 \cdot 10^{20}\text{cm}^{-3}$, and corresponds to the carrier concentration determined for sample Tsujii of Ref. [226]. This choice leads to a reduction of S and an increase of σ. The resulting ZT is smaller and does not recover the values obtained for the sample of Tsujii. As expected from Ref. [34], the highest $ZT \geq 0.5$ is predicted for a charge carrier concentration around $n_{e,\text{low}} = 3 \cdot 10^{20}\,\text{cm}^{-3}$. The canonical averages of S, σ, $S^2\sigma$, and ZT evaluated at this concentration are shown with light blue dashed lines in Figs. 5.22(a), (c), (e), and (f), respectively. For $n_{e,\text{low}}$, the absolute value of S is larger with a maximum around $800\,\text{K}$ and σ is smaller in comparison to the canonical average with $n_{e,1e}$. ZT has a maximum of about 0.5 at $\sim 800\,\text{K}$. Thus, the lower carrier concentration does not improve the thermoelectric efficiency but lowers the temperature for which the highest ZT is achieved.

The largest ZT is observed for the well-ordered GS configuration. The canonical average including contributions of many configurations with different degree of disorder agrees well with experiments. This observation suggests that the synthesized samples are in a mixed state of several configurations, hampering to reach a thermoelectric efficiency with a ZT above 0.5.

5.8 CONCLUSION AND OUTLOOK

In this Chapter, we have studied the temperature-dependent electronic, structural, and transport properties of the type-I clathrate $\text{Ba}_8\text{Al}_x\text{Si}_{46-x}$ in the composition range $x \in [6, 16]$. They are obtained from canonical ensemble averages using MMC and WL samplings of the configurational space. These sampling routines have been implemented within the CE package `CELL`.

For the charge-compensated composition $x = 16$, the TD-EBS is computed by employing a novel method for calculating canonical-ensemble averages using configurational density of states $g(E)$. Here, first, a symmetrized energy spectrum is obtained by restoring the symmetry of the pristine primitive cell (according to [49, 50, 211]). Secondly, a canonical-ensemble average is performed over the symmetrized energy spectra of a set of configurations, whose energy and electronic properties are determined by *ab initio* calculations. $g(E)$ is used to assign statistical weights to these configurations. Due to the symmetrization, the resulting TD-EBS facilitates a comparison to angle-resolved photoemission spectra (APRES) [211]. Further, this method fully accounts for effects of the local atomic environment since the electronic properties are obtained purely from *ab initio* calculations. This is an advantage over effective-medium approximations, as *e.g.* the virtual-crystal approximation [53], the coherent-potential approximation [51, 52], and extensions thereof [54], which are commonly used to calculate the energy spectrum in the presence of disorder. Our method is

applicable to supercells and any complex alloy with many atoms in the primitive cell.

From the TD-EBS for $x = 16$, we observe a temperature-driven closing of the band gap. This transitions is concomitant with a partial order-disorder phase transition, revealed by the configurational (dis)order of Al atoms in the host structure. Its critical point in the macroscopic limit is determined from a finite-size scaling as $582\,\mathrm{K}$. This transition point significantly differs from the transition temperature obtained for the unit cell, being $820\,\mathrm{K}$, highlighting the importance of such a finite-size scaling to reach a macroscopic description. Such a phase transition leading to a closing of the band gap can dramatically impact the thermoelectricity efficiency, that favors semiconducting behavior. Consequently, clathrates samples annealed at different temperatures could exhibit large differences in their thermoelectric performance.

A closing of the band gap below the Fermi energy E_F that originates from a partial order-disorder transition is also observed for n-doped clathrates. For instance, for $x = 15$, the changes in electronic structure and configurational properties are similar to those observed for $x = 16$. For these compositions, the $24k$ site is preferred over the $16i$ site at low temperature. This preferences vanishes with increasing temperature, reaching a partially disordered state at temperatures above $1200\,\mathrm{K}$. The $6c$ site is preferred for all temperatures. For $x \in [6, 9]$, the band gap reduces with temperature, however the partial order-disorder transition behind has a different characteristic. Here, at low temperature, the $16i$ site is preferred over the $24k$ site. Still, with increasing temperature, a partially disordered state is approached that is similar as the one for $x \in [15, 16]$. For $x \in [12, 14]$, there is no clear ordering pattern due to a competition of the two above-described site preferences, resulting in QD states whose energy are close to the ones of the GS configurations but have opposite site-occupation preference. The competition of configurations with different ordering patterns leads also to zero or small band gaps for all temperatures for $x \in [10, 14]$, since there exists always a configuration with zero band gap.

Comparison of the temperature-dependent bond distances $b_{kk}(T)$ and $b_{ii}(T)$ to experiment in the composition range $x \in [6, 16]$ reveal that synthesized samples do not always resemble the GS configuration. Most of the samples are in very good agreement with our results at elevated temperatures $T \leq 900\,\mathrm{K}$, which are comparable to the annealing temperatures used in their synthesis. They are accessed by MMC samplings using a CE model to predict the bond distances of the visited configurations. Since they can be directly measured, while the occupation factors of the Wyckoff sites not (indistinguishable x-ray diffraction patterns of Al and Si host atoms), such a CE model is highly useful to identify the actual configuration of measured samples.

Finally, the transport properties have been investigated for $x = 15$, since for this composition there exists experimental data and it is near the charge-compensated composition [226]. They are calculated for the GS configuration,

a configuration with zero band gap having an energy $5\,\mathrm{meV/atom}$ above the GS energy, and a canonical-ensemble average obtained by a novel method for calculating these averages using $g(E)$. The largest ZT is found for the GS configuration, as expected, since its band structure corresponds to a doped semiconductor (band gap below E_F). The canonical-ensemble average consisting of contributions from configurations with and without band gap below E_F clearly has a smaller ZT, while that of the zero-band-gap configuration is well below. Good agreement with experiment is reached for the canonical-ensemble average. The GS configuration is also very close to it, while its increase at high temperatures is slightly more pronounced, thus reaches a larger ZT. Since we have demonstrated that configurational disorder has a significant impact on the transport coefficients for $x = 15$, we expect a similar scenario at $x = 16$. This can be subject of future studies.

Overall, our findings point out the crucial role of configurational disorder in complex thermoelectric materials. Different degrees of disorder can lead to significant differences in electronic and transport properties. By performing a multi-scale approach, bridging microscopic and macroscopic scales, we have obtained a reliable description of the macroscopic properties for complex materials, exemplified by clathrates.

A study of vibrational effects would be very interesting as a possible extension of this work. It has been demonstrated that such effects can significantly affect the stability [227]. However, we expect them to play a minor role in the electronic structure due to the following: The electronic and vibrational spectra of the empty and non-substituted clathrate Si_{46} resemble the one of bulk Si in the diamond structure due to the tetrahedral coordination of the host sites [191]. Thus, the band-gap renormalization of clathrates can be grossly estimated by the same as for bulk Si. The latter decreases monotonously with temperature and is found to be around $-0.1\,\mathrm{eV}$ at about $600\,\mathrm{K}$, which is close to the transition temperature of $582\,\mathrm{K}$ [228]. This value is smaller than the band gap of the GSs for $x \leq 9$ and $x \geq 15$ (*e.g.* being $0.4\,\mathrm{eV}$ for $x = 6$, $0.2\,\mathrm{eV}$ for $x = 9$, and $0.36\,\mathrm{eV}$ for $x = 16$). Thus, it is expected that vibrational effects may reduce the band gap and slightly lower the transition temperature, but not change the fact that there is a closing of the band gap driven by temperature-dependent disorder.

6

MEMORY-FUNCTION APPROACH FOR THE ELECTRICAL CONDUCTIVITY OF DISORDERED SOLIDS

The memory-function approach, as presented in Sec. 3.3.3, was originally formulated for the homogeneous electron gas [58]. This method is able to describe disordered systems at arbitrary coupling strength. It reproduces the classical Drude result for the conductivity in the weak coupling regime, in which the system behaves metallic. It can describe the transition to zero conductivity in the strong coupling regime, in which the system behaves as an insulator, as well as the neighborhood of the metal-to-insulator transition point. This presents a tremendous advantage as compared to the classical Drude theory and also BT, since these are not able to describe the insulating regime. In comparison to the Kubo-Greenwood approach, the memory-function method does not suffer from large numerical uncertainties originating from taking the zero-frequency limit. Also, supercell calculations can be avoided. Recently, the memory-function approach has been applied to study plasmons in quantum wells [229] and relaxation times in magnetic systems for weak disorder [165]. However, a general formalism of the memory-function approach for crystalline systems is still missing.

In this chapter, the memory-function approach for crystalline solids is presented. This novel method has been developed within a joint and long-term collaboration between the groups of Prof. J. Sofo from Pennsylvania State University and my supervisor Prof. C. Draxl from the Humboldt-University at Berlin, where I have been part of for six years. In the context of what is presented in my thesis, my main contribution was the implementation of the memory-function approach in **exciting** and its first application to bulk sodium. We choose sodium, since its electronic structure is very similar to the well-studied FEG [58]. Thus, a direct comparison between the two systems is enabled. For the FEG, a metal-to-insulator transition was reported by Götze [58]. An essential question to answer is if such a transition is also represent in bulk sodium.

The Chapter is organized as follows: In Sec. 6.1, the memory-function formalism for solids is presented. Its applicability on the example of bulk sodium is demonstrated in Sec. 6.2. A summary and conclusions are given in Sec. 6.3.

6.1 MEMORY-FUNCTION FORMALISM FOR CRYSTALLINE SOLIDS

The memory-function approach for crystalline systems differs from the one for the homogeneous electron gas (see Eqs. (134) and (135)) since here, the periodicity of the crystal lattice has to be taken into account. The explicit expressions for the density-density correlation function, the memory function, and the electrical conductivity, as implemented in **exciting**, are introduced in Sec. 6.1.1. Since the density-density response function is singular in the region where both, the frequency and the electron momentum, are small, the DC limit requires a careful treatment. This and the derivation of the accurate expressions for the DC limit are presented in Sec. 6.1.2. Section 6.1.3 discusses how to obtain the disorder potential from *ab initio* calculations.

6.1.1 *Equations for crystalline solids*

The Hamiltonian of crystalline systems with static disorder is defined as

$$H = H_0 + H' \ , \tag{159}$$

with

$$H_0 = \sum_{n\boldsymbol{k}} \epsilon_{n\boldsymbol{k}} c^\dagger_{n\boldsymbol{k}} c_{n\boldsymbol{k}} \tag{160}$$

and

$$H' = \sum_{\boldsymbol{q},\boldsymbol{G}} U_{\boldsymbol{G}}(\boldsymbol{q}) \rho^\dagger_{\boldsymbol{G}}(\boldsymbol{q}) \ . \tag{161}$$

Here, H_0 is the Hamiltonian of the clean, *i.e.*, the non-perturbed system (no disorder). $c^\dagger_{n\boldsymbol{k}}$ and $c_{n\boldsymbol{k}}$ are the creation and annihilation operator of the Bloch state with wave vector $\boldsymbol{k}$ and band index n. H' describes the interaction of this system with the disorder potential $U(\boldsymbol{r})$ (also called impurity potential). The Fourier transform of $U(\boldsymbol{r})$, calculated as

$$U_{\boldsymbol{G}}(\boldsymbol{q}) = \frac{1}{V} \int_V d\boldsymbol{r} e^{-\mathrm{i}(\boldsymbol{q}+\boldsymbol{G})\boldsymbol{r}} U(\boldsymbol{r}) \ , \tag{162}$$

depends on $\boldsymbol{q} + \boldsymbol{G}$, with $\boldsymbol{q}$ being a wave vector inside the first Brillouin zone and $\boldsymbol{G}$ being a reciprocal lattice vector. V is the volume of the simulation cell. The impurity potential is further discussed in Sec. 6.1.3.

To adapt the memory-function formalism for its application to crystals, we need to reformulate the expressions of the density operator ρ and the current operator j in terms of Bloch states and account for the fact that the wave

vector $\boldsymbol{q}$ is inside the first Brillouin zone. The Fourier transform of the density operator in a crystal is

$$\rho_{\boldsymbol{G}}(\boldsymbol{q}) \;=\; \sum_{nm\boldsymbol{k}} M_{nm\boldsymbol{k}}(\boldsymbol{q},\boldsymbol{G})\,\xi_{nm\boldsymbol{k}}(\boldsymbol{q})\;, \tag{163}$$

with $\xi_{nm\boldsymbol{k}}(\boldsymbol{q}) = c^{\dagger}_{n\boldsymbol{k}}c_{m\boldsymbol{k}+\boldsymbol{q}}$. In comparison to the definition used in Sec. 3.3.3, $\boldsymbol{q}$ is shifted by $\boldsymbol{q}/2$. $M_{nm\boldsymbol{k}}(\boldsymbol{q},\boldsymbol{G})$ are the plane-wave matrix elements, defined as

$$M_{nm\boldsymbol{k}}(\boldsymbol{q},\boldsymbol{G}) = \langle n\boldsymbol{k}|e^{-\mathrm{i}(\boldsymbol{q}+\boldsymbol{G})\boldsymbol{r}}|m\boldsymbol{k}+\boldsymbol{q}\rangle \tag{164}$$

with $|n\boldsymbol{k}\rangle = c^{\dagger}_{n\boldsymbol{k}}|0\rangle$. Using the continuity equation, given in Eq. (88), together with the commutation relation (Eq. (73)), the longitudinal current operator obeys the relation

$$\begin{aligned} j_{\boldsymbol{G}}(\boldsymbol{q}) \;&=\; -\frac{1}{|\boldsymbol{q}+\boldsymbol{G}|}\,[H,\rho_{\boldsymbol{G}}(\boldsymbol{q})] && (165)\\ &=\; -\frac{1}{|\boldsymbol{q}+\boldsymbol{G}|}\sum_{\boldsymbol{k}} M_{nm\boldsymbol{k}}(\boldsymbol{q},\boldsymbol{G})\,\epsilon_{nm\boldsymbol{k}}(\boldsymbol{q})\,\xi_{nm\boldsymbol{k}}(\boldsymbol{q})\;, && (166)\end{aligned}$$

with $\epsilon_{nm\boldsymbol{k}}(\boldsymbol{q}) = \epsilon_{n\boldsymbol{k}} - \epsilon_{m\boldsymbol{k}+\boldsymbol{q}}$. The expressions for $\rho_{\boldsymbol{G}}(\boldsymbol{q})$ and $j_{\boldsymbol{G}}(\boldsymbol{q})$ are analogous to the ones for the FEG (Eqs. (86) and (92), respectively), and consist of linear combinations of the dynamical variables $\xi_{nm\boldsymbol{k}}$, weighted by the matrix elements $M_{nm\boldsymbol{k}}(\boldsymbol{q},\boldsymbol{G})$. For given $\boldsymbol{q}$ and $\boldsymbol{G}$, the operators $\rho_{\boldsymbol{G}}(\boldsymbol{q})$ and $j_{\boldsymbol{G}}(\boldsymbol{q})$ fulfill the orthogonality condition $(\rho_{\boldsymbol{G}}(\boldsymbol{q})|j_{\boldsymbol{G}}(\boldsymbol{q})) = 0$ (see Eq. (95)). Thus, they can be assigned to the operators A_0 and A_1, respectively, of the set of operators A_α building the projector $\mathcal{P}_{\boldsymbol{G}}(\boldsymbol{q})$:

$$\mathcal{P}_{\boldsymbol{G}}(\boldsymbol{q})\,\bullet = \sum_{\alpha} |A_\alpha(\boldsymbol{q}+\boldsymbol{G}))\,(A_\alpha(\boldsymbol{q}+\boldsymbol{G})|\,\bullet)\;. \tag{167}$$

The analogous expression for the homogeneous electron gas is given in Eq. (93). Accordingly, we define:

$$\begin{aligned} A_0(\boldsymbol{q}+\boldsymbol{G}) \;&=\; (\rho_{\boldsymbol{G}}(\boldsymbol{q})|\rho_{\boldsymbol{G}}(\boldsymbol{q}))^{-1/2}\,\rho_{\boldsymbol{G}}(\boldsymbol{q}) && (168)\\ A_1(\boldsymbol{q}+\boldsymbol{G}) \;&=\; (j_{\boldsymbol{G}}(\boldsymbol{q})|j_{\boldsymbol{G}}(\boldsymbol{q}))^{-1/2}\,j_{\boldsymbol{G}}(\boldsymbol{q})\;. && (169)\end{aligned}$$

With the relevant subspace defined by $\mathcal{P}_{\boldsymbol{G}}(\boldsymbol{q})$, we can drive the equation of motion for the projected resolvent $\mathcal{R}$ (see Eq. (99)).

The density-density correlation function for the clean system, defined as $\phi^{(0)}_{\boldsymbol{G},\boldsymbol{G}'}(\boldsymbol{q},z) = (\rho_{\boldsymbol{G}}(\boldsymbol{q})|\mathcal{R}_0(z)|\rho_{\boldsymbol{G}'}(\boldsymbol{q}))$ with $\mathcal{R}_0 = (\mathcal{L}_0 - z)^{-1}$ (analogous expression for the FEG in Eq. (120)), reads:

$$\phi^{(0)}_{\boldsymbol{G},\boldsymbol{G}'}(\boldsymbol{q},z) = \frac{1}{V}\sum_{nm\boldsymbol{k}} \frac{M_{nm\boldsymbol{k}}(\boldsymbol{q},\boldsymbol{G})M^{*}_{nm\boldsymbol{k}}(\boldsymbol{q},\boldsymbol{G}')}{z+\epsilon_{nm\boldsymbol{k}}(\boldsymbol{q})}\,\frac{f_{nm\boldsymbol{k}}(\boldsymbol{q})}{\epsilon_{nm\boldsymbol{k}}(\boldsymbol{q})}\;, \tag{170}$$

with $f_{nm\boldsymbol{k}}(\boldsymbol{q}) = f_{n\boldsymbol{k}} - f_{m\boldsymbol{k}+\boldsymbol{q}}$. $f_{n\boldsymbol{k}}$ is the Fermi-Dirac distribution function:

$$f_{n\boldsymbol{k}} = \frac{1}{e^{\frac{1}{k_B T}(\epsilon_{n\boldsymbol{k}} - \mu)} + 1} \ . \tag{171}$$

Using the general relation between the correlation function and the Kubo linear-response function, Eq. (72), $\phi^{(0)}_{\boldsymbol{G},\boldsymbol{G}'}(\boldsymbol{q}, z)$ can be written in terms of the response function of the clean, non-interacting system $\chi^{(0)}_{\boldsymbol{G},\boldsymbol{G}'}(\boldsymbol{q}, z)$ as

$$\phi^{(0)}_{\boldsymbol{G},\boldsymbol{G}'}(\boldsymbol{q}, z) \ = \ -\frac{1}{z}\left[\chi^{(0)}_{\boldsymbol{G},\boldsymbol{G}'}(\boldsymbol{q}, z) - \chi^{(0)}_{\boldsymbol{G},\boldsymbol{G}'}(\boldsymbol{q}, 0)\right] \ , \tag{172}$$

with $\chi^{(0)}_{\boldsymbol{G},\boldsymbol{G}'}$ being

$$\chi^{(0)}_{\boldsymbol{G},\boldsymbol{G}'}(\boldsymbol{q}, z) = \frac{1}{V}\sum_{nm\boldsymbol{k}} \frac{f_{nm\boldsymbol{k}}(\boldsymbol{q})}{z + \epsilon_{nm\boldsymbol{k}}(\boldsymbol{q})} M_{nm\boldsymbol{k}}(\boldsymbol{q}, \boldsymbol{G}) M^*_{nm\boldsymbol{k}}(\boldsymbol{q}, \boldsymbol{G}') \ . \tag{173}$$

We define the static response function, *i.e.*, $z = 0$, as:

$$\chi_{\boldsymbol{G},\boldsymbol{G}'}(\boldsymbol{q}, z = 0) = (\rho_{\boldsymbol{G}}(\boldsymbol{q}) | \rho_{\boldsymbol{G}'}(\boldsymbol{q})) = g_{\boldsymbol{G},\boldsymbol{G}'}(\boldsymbol{q}) \ . \tag{174}$$

The memory function for solids can be defined as:

$$m_{\boldsymbol{G},\boldsymbol{G}'}(\boldsymbol{q}, z) \coloneqq m_{11,\boldsymbol{G},\boldsymbol{G}'}(\boldsymbol{q}, z) = \left(F_{1,\boldsymbol{G}}(\boldsymbol{q}) \left| \tilde{\mathcal{R}}(z) \right| F_{1,\boldsymbol{G}'}(\boldsymbol{q})\right) \ . \tag{175}$$

The equivalent expression for the FEG is given in Eq. (103). To evaluate Eq. (175), we need an expression for the fluctuating forces acting on the current $F_{1,\boldsymbol{G}}(\boldsymbol{q}) = \mathcal{Q}\mathcal{L} j_{\boldsymbol{G}}(\boldsymbol{q})$. Note that $F_{0,\boldsymbol{G}}(\boldsymbol{q}) = \mathcal{Q}\mathcal{L}\rho_{\boldsymbol{G}}$ is zero, as for the FEG. We obtain

$$\begin{aligned} F_{1,\boldsymbol{G}}(\boldsymbol{q}) = \frac{1}{\sqrt{N_e m_e}} \sum_{\boldsymbol{p},\boldsymbol{G}''} & U_{\boldsymbol{G}-\boldsymbol{G}''}(\boldsymbol{q} - \boldsymbol{p}) \\ & \times \left[|\boldsymbol{q} + \boldsymbol{G}| - |\boldsymbol{p} + \boldsymbol{G}''|_{\boldsymbol{q}+\boldsymbol{G}}\right] \rho_{\boldsymbol{G}''}(\boldsymbol{p}) \ , \end{aligned} \tag{176}$$

where $|\boldsymbol{q}+\boldsymbol{G}| = \widehat{(\boldsymbol{q}+\boldsymbol{G})} \cdot (\boldsymbol{q}+\boldsymbol{G})$ with $\widehat{(\boldsymbol{q}+\boldsymbol{G})}$ being the direction of the vector $\boldsymbol{q}+\boldsymbol{G}$ and $|\boldsymbol{p}+\boldsymbol{G}''|_{\boldsymbol{q}+\boldsymbol{G}} = \widehat{(\boldsymbol{q}+\boldsymbol{G})} \cdot (\boldsymbol{p}+\boldsymbol{G}'')$. In general, $\boldsymbol{G}'' \neq \boldsymbol{G}$. Applying the mode-coupling approximation, as defined by Eq. (121), the expression for the memory function then reads

$$\begin{aligned} m_{\boldsymbol{G},\boldsymbol{G}'}(\boldsymbol{q}, z) = \frac{1}{N_e m_e} \sum_{\boldsymbol{p},\boldsymbol{G}''} & \langle |U_{\boldsymbol{G}-\boldsymbol{G}''}(\boldsymbol{q} - \boldsymbol{p})|^2 \rangle_{\text{dis}} \\ & \times \left[|(\boldsymbol{q} + \boldsymbol{G})| - |\boldsymbol{p} + \boldsymbol{G}''|_{\boldsymbol{q}+\boldsymbol{G}}\right]^2 \phi_{\boldsymbol{G}'',\boldsymbol{G}'}(\boldsymbol{p}, z) \ . \end{aligned} \tag{177}$$

Using this expression, together with the equation of motion for the projected resolvent, given by Eq. (82), we arrive at the density-density correlation function

$\phi_{\boldsymbol{G},\boldsymbol{G}'}(\boldsymbol{q},z)$. Considering the projection onto the macroscopic mode $\boldsymbol{q}$, *i.e.*, $\boldsymbol{G}=\boldsymbol{G}'=0$, gives [1]:

$$\phi(\boldsymbol{q},z) \coloneqq \phi_{0,0}(\boldsymbol{q},z) = \frac{\phi^{(0)}_{0,0}(\boldsymbol{q},z+m_{0,0}(\boldsymbol{q},z))}{1-m_{0,0}(\boldsymbol{q},z)\,\phi^{(0)}_{0,0}(\boldsymbol{q},z+m_{0,0}(\boldsymbol{q},z))/\chi_{0,0}(\boldsymbol{q})} \ . \quad (178)$$

This equation has the same form as the corresponding expression for the FEG (see Eq. (118)).

Equations (177) and (178) can be solved self-consistently: Starting from $m_{0,0}=0$, Eq. (178) gives a ϕ that is equal to $\phi^{(0)}$. This ϕ is used to evaluate the updated $m_{0,0}$ with Eq. (177). This, in turn, can be plugged into Eq. (178) to update ϕ. One can iterate this procedure until convergence. Finally, the converged ϕ can be employed to evaluate the conductivity with:

$$\sigma(\boldsymbol{q},z) = \ \mathrm{i}\,\frac{z}{q^2}\left[z\phi(\boldsymbol{q},z)-\chi(\boldsymbol{q})\right] \ . \quad (179)$$

This expression is derived in Appendix A.2.4. The macroscopic conductivity is then obtained by the zero-wave-vector limit $\boldsymbol{q}\to 0$ of Eq. (179) evaluated at a positive infinitesimal imaginary part η of z:

$$\sigma(0,\omega) = \lim_{\eta\to 0}\lim_{\boldsymbol{q}\to 0}\sigma(\boldsymbol{q},\omega+\mathrm{i}\eta) \ . \quad (180)$$

6.1.2 *DC conductivity and disorder strength: Metal-to-insulator transition*

In the following, explicit expressions for the macroscopic DC conductivity in dependency of the disorder potential are derived. In the following, we neglect the $\boldsymbol{q}$-dependence of the memory function, *i.e.* $m_{0,0}\approx M_{0,0}(z)=M(z)$, as done in Ref. [58]. Then, considering $U_0(\boldsymbol{q})=U(\boldsymbol{q})$, the set of self-consistent equations reads:

$$M(z) \ = \ \frac{1}{3mN_e}\sum_{\boldsymbol{q}}\langle|U(\boldsymbol{q})|^2\rangle\, q^2\,\phi(\boldsymbol{q},z) \quad (181)$$

$$\phi(\mathbf{q},z) \ = \ \frac{\phi^{(0)}(\mathbf{q},z+M(z)}{1-M(z)\,\phi^{(0)}(\mathbf{q},z+M(z))/\chi^{(0)}(\mathbf{q},0)} \ . \quad (182)$$

Since we are interested in the DC conductivity, the special case $z=0$ is evaluated. At $z=0$, $M\coloneqq M(0)$. Furthermore, we write the disorder potential

1 Here, $\phi_{0,0}(\boldsymbol{q},z)$ should not be confused with $\phi_{00}(\boldsymbol{q},z)$, discussed in Sec. 3.3.3. $\phi_{00}(\boldsymbol{q},z)$ is the non-normalized density-density correlation function of the FEG and the indices indicate the independent variable A_α, where A_0 is proportional to the density operator $\rho_{\boldsymbol{G}}(\boldsymbol{q})$ (Eq. (168)).

as $U(\boldsymbol{q}) = UF(\boldsymbol{q})$, where U is the potential strength and $F(\boldsymbol{q})$ its space variation. Inserting Eq. (182) in Eq. (181), we obtain:

$$M = \frac{U^2}{3mN_e} \sum_{\boldsymbol{q}} |F(\boldsymbol{q})|^2 q^2 \chi^{(0)}(\boldsymbol{q},0) \frac{\phi^{(0)}(\boldsymbol{q},M)}{\chi^{(0)}(\boldsymbol{q},0) - M\phi^{(0)}(\boldsymbol{q},0)} \ . \tag{183}$$

Now, after inserting the relation (Eq. (172))

$$\phi^{(0)}(\boldsymbol{q},M) = -\frac{1}{M}\left(\phi^{(0)}(\boldsymbol{q},M) - \phi^{(0)}(\boldsymbol{q},0)\right) \ , \tag{184}$$

we arrive at an explicit expression of the potential strength in dependence on the memory function M:

$$\frac{1}{U^2} = \frac{1}{3mN_e} \sum_{\boldsymbol{q}} |F(\boldsymbol{q})|^2 \chi^{(0)}(\boldsymbol{q},0) \left[\frac{\chi^{(0)}(\boldsymbol{q},0)}{\frac{M^2}{q^2}\chi^{(0)}(\boldsymbol{q},M)} - \frac{q^2}{M^2} \right] \ . \tag{185}$$

Since U is purely real, the term on the r.h.s. also needs to be purely real. $\chi^{(0)}$ has the following properties:

$$\begin{aligned} \operatorname{Im}\chi^{(0)}(\boldsymbol{q},\pm\mathrm{i}\alpha) &= 0 & (186)\\ \operatorname{Re}\chi^{(0)}(\boldsymbol{q},+\mathrm{i}\alpha) &= \operatorname{Re}\chi^{(0)}(\boldsymbol{q},-\mathrm{i}\alpha) & (187)\\ \operatorname{Re}\chi^{(0)}(\boldsymbol{q},\pm\mathrm{i}\alpha) &< 0 \ , & (188) \end{aligned}$$

Therefore, a solution for Eq. (185) can be found for $M = \pm\mathrm{i}\alpha$:

$$\frac{1}{U^2} = -\frac{1}{3mN_e} \sum_{\boldsymbol{q}} |F(\boldsymbol{q})|^2 \chi^{(0)}(\boldsymbol{q},0) \left[\frac{\chi^{(0)}(\boldsymbol{q},0)}{\frac{\alpha^2}{q^2}\chi^{(0)}(\boldsymbol{q},\pm\mathrm{i}\alpha)} - \frac{q^2}{\alpha^2} \right] \ . \tag{189}$$

In the following, we use $M = -\mathrm{i}\alpha$.

An expression for the conductivity in terms of $\chi^{(0)}$ can be obtained from inserting Eq. (182) into Eq. (179). Then, we arrive at:

$$\sigma(\boldsymbol{q},\omega) = -\mathrm{i}\,\frac{\omega}{q^2} \frac{(\omega - \mathrm{i}\alpha)\chi^{(0)}(\mathbf{q},\omega - \mathrm{i}\alpha)}{\omega - \mathrm{i}\alpha\,\frac{\chi^{(0)}(\mathbf{q},\omega-\mathrm{i}\alpha)}{\chi^{(0)}(\mathbf{q},0)}} \ . \tag{190}$$

Here, we use a purely real $z = \omega$. $\chi^{(0)}(\boldsymbol{q},\omega - \mathrm{i}\alpha)$ goes to zero as q^2 for small $\boldsymbol{q}$ and finite frequency $\omega - \mathrm{i}\alpha$, while $\chi^{(0)}(\boldsymbol{q},0)$ in the limit of $\boldsymbol{q} \to 0$ goes to the negative density of states at the Fermi level $-\rho_F$ that is finite for metals. Thus, the leading term in the denominator of Eq. (190) in the limit $\boldsymbol{q} \to 0$ is:

$$q^2 \left(\omega - \mathrm{i}\alpha\,\frac{\chi^{(0)}(\mathbf{q},\omega - \mathrm{i}\alpha)}{\chi^{(0)}(\mathbf{q},0)} \right) \xrightarrow[q\to 0]{} q^2\omega \ . \tag{191}$$

This gives:

$$\sigma(\boldsymbol{q}\to 0,\omega) = -\mathrm{i}(\omega-\mathrm{i}\alpha)\lim_{\boldsymbol{q}\to 0}\frac{\chi^{(0)}(\mathbf{q},\omega-\mathrm{i}\alpha)}{q^2}\ . \tag{192}$$

The DC conductivity, *i.e.* $\omega = 0$, is then obtained as

$$\sigma_{\mathrm{DC}} = \sigma(\boldsymbol{q}=0,\omega=0) = -\alpha\ \lim_{\boldsymbol{q}\to 0}\frac{\chi^{(0)}(\boldsymbol{q},-\mathrm{i}\alpha)}{q^2}\ . \tag{193}$$

Equations (189) and (193) can be employed to obtain σ_{DC} for an arbitrary disorder potential strength U: For a given U, Eq. (189) can be solved numerically to find α, which, in turn, can be employed in Eq. (193) to find σ_{DC}.

In the following, we analyze under which conditions $\sigma_{\mathrm{DC}} = 0$, *i.e.*, the system is in the insulating regime. For this, we consider the expansion of $\chi^{(0)}(\boldsymbol{q},M)$ for small $\boldsymbol{q}$ [230]:

$$\begin{aligned}\chi^{(0)}(\boldsymbol{q},-\mathrm{i}\alpha) = &-\frac{1}{V}\frac{1}{\alpha^2}\boldsymbol{q}\left[\sum_{n\boldsymbol{k}}\frac{\partial f(\epsilon_{n\boldsymbol{k}})}{\partial\epsilon_{n\boldsymbol{k}}}\boldsymbol{p}_{nk}\boldsymbol{p}^{\star}_{nk}\right]\boldsymbol{q}\\ &+\frac{1}{V}\sum_{nm\boldsymbol{k}}\boldsymbol{q}\frac{\boldsymbol{p}_{nmk}\boldsymbol{p}^{\star}_{nmk}}{\left(\epsilon_{n\boldsymbol{k}}-\epsilon_{m\boldsymbol{k}}\right)^2}\boldsymbol{q}\ \frac{f(\epsilon_{n\boldsymbol{k}})-f(\epsilon_{m\boldsymbol{k}})}{-\mathrm{i}\alpha+\epsilon_{n\boldsymbol{k}}-\epsilon_{m\boldsymbol{k}}}\ .\end{aligned} \tag{194}$$

Here, the term in squared brackets is the square of the plasma frequency $\boldsymbol{\omega}_p^2$, and $\boldsymbol{p}_{nm\boldsymbol{k}} = \langle n\boldsymbol{k}|\hat{\boldsymbol{p}}|m\boldsymbol{k}\rangle$. It follows:

$$\begin{aligned}-\frac{\alpha^2}{q^2}\chi^{(0)}(\boldsymbol{q},-\mathrm{i}\alpha) = &\frac{1}{V}\ \hat{\boldsymbol{q}}\ \boldsymbol{\omega}_p^2\ \hat{\boldsymbol{q}}\\ &-\frac{1}{V}\alpha^2\sum_{nm\boldsymbol{k}}\hat{\boldsymbol{q}}\frac{\boldsymbol{p}_{nmk}\boldsymbol{p}^{\star}_{nmk}}{\left(\epsilon_{n\boldsymbol{k}}-\epsilon_{m\boldsymbol{k}}\right)^2}\hat{\boldsymbol{q}}\ \frac{f(\epsilon_{n\boldsymbol{k}})-f(\epsilon_{m\boldsymbol{k}})}{-\mathrm{i}\alpha+\epsilon_{n\boldsymbol{k}}-\epsilon_{m\boldsymbol{k}}}\ .\end{aligned} \tag{195}$$

For $\alpha\to 0$, only the first term survives. In this case, the DC conductivity (Eq. (193)) diverges and develops a Drude-like peak:

$$\sigma_{\mathrm{DC},\alpha\to 0} = \lim_{\alpha\to 0}\frac{1}{\alpha}\frac{1}{V}\omega_p^2\to\infty\ . \tag{196}$$

Using the Kramers-Kronig relations, the high-frequency limit $\alpha\to\infty$ of the density-density response function can be related to the f-sum rule (see Eq. (3.141) in Ref. [152]) in the following way:

$$\begin{aligned}\lim_{\alpha\to\infty} &-\frac{\alpha^2}{q^2}\mathrm{Re}\chi^{(0)}(\boldsymbol{q},-\mathrm{i}\alpha)\\ &= \frac{1}{q^2}\underbrace{\left[-\frac{2}{\pi}\int_0^\infty\alpha'\,\mathrm{Im}\chi^{(0)}(\boldsymbol{q},\alpha')\,\mathrm{d}\alpha'\right]}_{f\text{-sum rule}} = \frac{1}{q^2}\frac{nq^2}{m_e} = \frac{n}{m_e}\ .\end{aligned} \tag{197}$$

Here, n is the electronic density obtained as $n = N_e/V$. In this limit, the DC conductivity becomes zero (insulating regime):

$$\sigma_{\mathsf{DC},\alpha\to\infty} = \lim_{\alpha\to\infty} \frac{1}{\alpha}\frac{n}{m_e} = 0 \ . \tag{198}$$

Applying $\alpha \to \infty$ also in Eq. (185), we can estimate the critical potential strength U_{crit} for which the DC conductivity vanishes:

$$\frac{1}{U_{\mathsf{crit}}^2} = -\frac{V}{3N_e^2}\sum_{\boldsymbol{q}} |F(\boldsymbol{q})|^2 \left(\chi^{(0)}(\boldsymbol{q},0)\right)^2 \ . \tag{199}$$

This equation is highly useful, since it is a closed form of a general expression for the level of disorder required for the transition from a metal to an insulator.

6.1.3 *Impurity potential*

We consider a supercell with an impurity concentration n_{imp}. A configuration of the impurities in this supercell can be represented by the vector $\boldsymbol{\sigma} = \{\sigma_1, \sigma_2, \dots\}$, in the same way as introduced for the CE technique in Sec. 3.2.1. Each vector component corresponds to an atomic site i, that is occupied by a species type σ_i. For a given configuration $\boldsymbol{\sigma}$, the impurity potential $U_{\boldsymbol{\sigma}}(\boldsymbol{r})$ can be obtained from:

$$U_{\boldsymbol{\sigma}}(\boldsymbol{r}) = V_{\boldsymbol{\sigma},\mathsf{KS}}(\boldsymbol{r}) - V_{0,\mathsf{KS}}(\boldsymbol{r}) \ . \tag{200}$$

Here, $V_{\boldsymbol{\sigma},\mathsf{KS}}(\boldsymbol{r})$ is the KS potential of the supercell with configuration $\boldsymbol{\sigma}$, and $V_{0,\mathsf{KS}}(\boldsymbol{r})$ that of the pristine system. These potentials can be obtained, in principle, from DFT ground-state calculations. However, for large supercells this procedure is computationally very demanding and may even present an impossible task. To avoid this, we approximate $U_{\boldsymbol{\sigma}}(\boldsymbol{r})$ by a superposition of single-impurity potentials [177]:

$$U_{\boldsymbol{\sigma}}(\boldsymbol{r}) = \sum_{i=1}^{N} U_{\sigma_i}(\boldsymbol{r} - \boldsymbol{r}_i) \ . \tag{201}$$

Here, N is the total number of atoms in the crystal, $\boldsymbol{r}_i$ denotes the atomic position of site i, and $U_{\sigma_i}(\boldsymbol{r})$ is the impurity potential for an isolated impurity σ_i located at $\boldsymbol{r}$ in a clean (pristine) system. If $\sigma_i = 0$, *i.e.* site i is not substituted, the impurity potential is set to zero ($U_{\sigma_i=0}(\boldsymbol{r}) = 0$). The Fourier transform of Eq. (201) gives

$$U_{\boldsymbol{\sigma},\boldsymbol{G}}(\boldsymbol{q}) = \sum_{i=1}^{N} e^{\mathrm{i}(\boldsymbol{q}+\boldsymbol{G})\boldsymbol{r}_i} U_{\sigma_i,\boldsymbol{G}}(\boldsymbol{q}) \ , \tag{202}$$

with $U_{\sigma_i,\boldsymbol{G}}(\boldsymbol{q})$ being the Fourier transform of the isolated impurity potential.

In the case of a binary alloy, σ_i can be either 0 or 1. For $\sigma_i = 1$, *i.e.* site i contains a substituted atom, we define the corresponding impurity potential as $U_{1,\boldsymbol{G}}(\boldsymbol{q})$. Then, we can rewrite Eq. (202)

$$U_{\boldsymbol{\sigma},\boldsymbol{G}}(\boldsymbol{q}) = S_{\boldsymbol{\sigma}}(\boldsymbol{q}+\boldsymbol{G})\, U_{1,\boldsymbol{G}}(\boldsymbol{q}) \ , \tag{203}$$

with $S_{\boldsymbol{\sigma}}(\boldsymbol{q}+\boldsymbol{G})$ being the structure factor defined as

$$S_{\boldsymbol{\sigma}}(\boldsymbol{q}+\boldsymbol{G}) = \sum_{i=1}^{N} \delta_{\sigma_i,1}\, e^{\mathrm{i}(\boldsymbol{q}+\boldsymbol{G})\boldsymbol{r}_i}. \tag{204}$$

In the memory-function approach, the squared potential average $\langle |U_{\boldsymbol{G}}(\boldsymbol{q})|^2 \rangle_{\mathrm{dis}}$ is used. This ensemble average over different realizations of disorder (indicated with index dis) can be obtained as

$$\langle |U_{\boldsymbol{G}}(\boldsymbol{q})|^2 \rangle = \frac{1}{N_c} \sum_{c=1}^{N_c} |U_{\boldsymbol{\sigma}_c,\boldsymbol{G}}(\boldsymbol{G})|^2 = |U_{1,\boldsymbol{G}}(\boldsymbol{q})|^2 \, \frac{1}{N_c} \sum_{c=1}^{N_c} |S_{\boldsymbol{\sigma}_c}(\boldsymbol{q}+\boldsymbol{G})|^2 \ . \tag{205}$$

Here, the sum runs over N_c configurations. With the use of Eq. (203), it factorizes into two terms: The first term depends solely on the potential of an isolated impurity, U_1, and the second term is the squared structure factor. This expression offers several advantages: U_1 is independent from the actual configuration and needs to be calculated only once. Further, the simple expression of the structure factor averaged on configurations can be determined outside the DFT framework. This saves computational resources and enables the study of very large supercells without performing a DFT calculation. Here, a useful tool for calculating an averaged structure factor is the CE technique. Combined with finite-temperature simulations, as *i.e.* Monte-Carlo samplings, it allows for determining a temperature-dependent structure factor from ensemble averages. A special case is the high-temperature limit, *i.e.* the system with fully uncorrelated disorder. Starting from Eq. (204), we can derive for this limit the following analytic expression:

$$\begin{aligned}
\frac{1}{N_c} \sum_{c=1}^{N_c} |S_{\boldsymbol{\sigma}}(\boldsymbol{q}+\boldsymbol{G})|^2 &= \frac{1}{N_c} \sum_{c} \Big| \sum_{i=1}^{N} \delta_{\sigma_{ci},1}\, e^{\mathrm{i}(\boldsymbol{q}+\boldsymbol{G})\boldsymbol{r}_i} \Big|^2 && (206)\\
&= \frac{1}{N_c} \sum_{c=1}^{N_c} \sum_{i,j=1}^{N} \delta_{\sigma_{ci},1}\delta_{\sigma_{cj},1}\, e^{\mathrm{i}(\boldsymbol{q}+\boldsymbol{G})(\boldsymbol{r}_i-\boldsymbol{r}_j)} && (207)\\
&= \sum_{i,j=1}^{N} \left[\frac{1}{N_c} \sum_{c=1}^{N_c} \delta_{\sigma_{ci},1}\delta_{\sigma_{cj},1} \right] e^{\mathrm{i}(\boldsymbol{q}+\boldsymbol{G})(\boldsymbol{r}_i-\boldsymbol{r}_j)} \ . && (208)
\end{aligned}$$

The term in square brackets describes the density of impurity pairs, one of these impurities located at position i and the other at position j. For uncorrelated

disorder, this is per definition the product of the impurity density at those positions. Assuming a uniform impurity concentration n_{imp}, we obtain:

$$\frac{1}{N_c}\sum_{c=1}^{N_c}|S_{\boldsymbol{\sigma}}(\boldsymbol{q})|^2 = n_{\mathrm{imp}}^2\sum_{i,j=1}^{N} e^{\mathrm{i}(\boldsymbol{q}+\boldsymbol{G})(\boldsymbol{r}_i-\boldsymbol{r}_j)} \ . \tag{209}$$

Taking into account explicitly the lattice periodicity of the position $\boldsymbol{r}_i = \boldsymbol{s}_i+\boldsymbol{R}_i$, with $\boldsymbol{s}_i$ being the position of atom i in the unit cell and $\boldsymbol{R}_i$ being the lattice vector in real space, the sum on the right hand side can be written as:

$$\sum_{i,j=1}^{N} e^{\mathrm{i}(\boldsymbol{q}+\boldsymbol{G})(\boldsymbol{r}_i-\boldsymbol{r}_j)} = |L(\boldsymbol{q}+\boldsymbol{G})|^2|X(\boldsymbol{q}+\boldsymbol{G})|^2 \ . \tag{210}$$

Here, L is called the lattice factor and X the structure factor. These terms can be evaluated as

$$L(\boldsymbol{q}+\boldsymbol{G}) = \sum_i e^{\mathrm{i}\boldsymbol{R}_i(\boldsymbol{q}+\boldsymbol{G})} = \sum_i e^{\mathrm{i}\boldsymbol{R}_i\boldsymbol{q}} = N_\Omega\sum_{\boldsymbol{G}}\delta(\boldsymbol{q}-\boldsymbol{G}) \tag{211}$$

$$X(\boldsymbol{q}+\boldsymbol{G}) = \sum_i e^{\mathrm{i}\boldsymbol{s}_i(\boldsymbol{q}+\boldsymbol{G})} = \sum_i e^{\mathrm{i}\boldsymbol{s}_i(\boldsymbol{q}+\boldsymbol{G})} \ . \tag{212}$$

$N_\Omega = V/\Omega$ is the number of unit cells with volume Ω in the supercell with volume V. In the second term, the sum runs over the atomic positions in the unit cell only.

6.2 METAL-TO-INSULATOR TRANSITION IN SODIUM

As a first application of the memory-function approach in crystalline systems, we study sodium perturbed with a hypothetical square impurity potential in reciprocal space. Sodium has a single valence electron in the s subshell with spherical symmetry. Thus, its electronic structure is very similar to the one of the FEG, as will be evident in Sec. 6.2.1. As reported by Götze [58], the FEG perturbed with the same hypothetical square impurity potential reveals a metal-to-semiconductor transition, that is driven by the potential strength. We explore if such a metal-to-semiconductor transition is also present for sodium. This is discussed in Sec. 6.2.2.

6.2.1 *Electronic structure of sodium*

The band structure of bcc Na is shown in Fig. 6.1. It is calculated with **exciting** using the LDA-PW exchange-correlation functional [231]. The lattice parameter, determined by performing a volume relaxation, is 4.0598 Å (5% smaller than the experimental lattice parameter 4.2906 Å [232]). The band structure

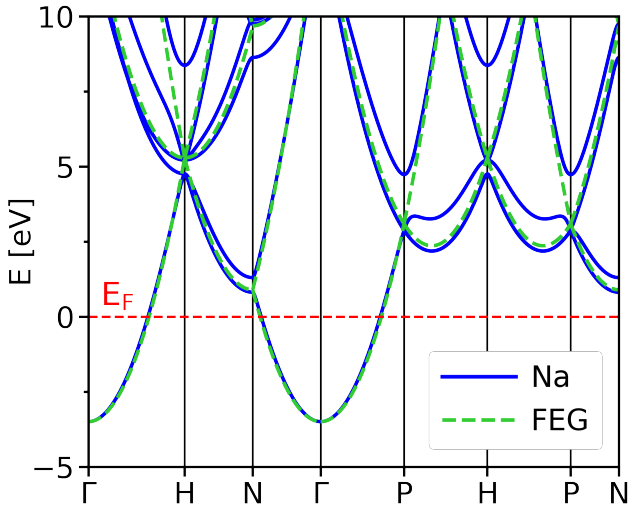

Figure 6.1: Band structure of Na (space group $Im3m$, No. 229) calculated with `exciting` using the LDA exchange-correlation functional [231] (blue lines). In addition, the band structure of the FEG folded to the first Brillouin zone of the Na lattice is shown (green dashed lines). The red dashed line indicates the Fermi energy E_F.

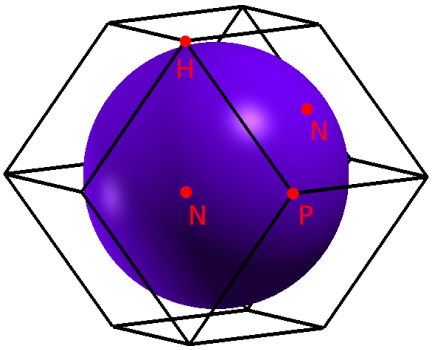

Figure 6.2: Fermi surface of Na calculated with `exciting`. The high-symmetry points H,N, and P are indicated with red points.

is almost parabolic below the Fermi energy E_F, with its minimum at the Γ point. The spherical symmetry of the Fermi surface of Na is evident from Fig. 6.2. With the aim of comparing our *ab initio* results for Na to the FEG, we extract two *ab initio* parameters from our calculations for Na: the Fermi wave vector k_F and the effective mass m_{eff} of the highest occupied band. These are used for the FEG model for comparison. Using a fine $\boldsymbol{k}$-point mesh of $128 \times 128 \times 128$, we determine $k_F = 0.51\, a_B^{-1}$.[2] m_{eff} can be estimated by using the *ab initio* density of states at E_F, $\rho_F = 12.077/\text{Ha}/\Omega$. From the FEG expression $\rho_F = m_{\text{eff}} k_F/\pi^2$, we obtain $m_{\text{eff}} = 1.039\, m_e$.

2 A similar value can be extracted from the electronic density $n = N_e/\Omega = k_F^2/(3\pi^2)$, knowing that for Na the number of electrons N_e is one and the unit cell volume Ω is $225.79\, a_B^{-3}$.

To further explore the similarity of Na to the FEG, we calculate the band structure of the FEG folded to the first Brillouin zone of the Na lattice with the use of the isotropic band model

$$E(\boldsymbol{k}+\boldsymbol{G}) + E_{\min} = \frac{1}{2\,m_{\text{eff}}}\,(\boldsymbol{k}+\boldsymbol{G})^2 \ . \tag{213}$$

Here, $m_{\text{eff}} = 1.038\,m_e$, $\boldsymbol{k}$ is a wave vector inside the first Brillouin zone and $\boldsymbol{G}$ is the reciprocal lattice vector of the Na lattice, which folds the bands back into the first Brillouin zone. The result is shown with light-green dashed lines in Fig. 6.1. Below E_F, the bands of the FEG match very well with the bands of Na. Also at higher energies, where the energy bands are folded according to $\boldsymbol{G} > 0$, there is a high similarity to the band structure of Na.

6.2.2 *Conductivity*

In the following, the DC conductivity is calculated for clean sodium perturbed with an impurity potential. For this, we use the explicit expressions of the memory-function approach, which are implemented in **`exciting`** and discussed in Sec. 6.1.2. The linear-response functions are projected on a macroscopic wave vector $\boldsymbol{q}$, *i.e.* local field effects are neglected ($\boldsymbol{G} = 0$ and $\boldsymbol{G}' = 0$). For the averaged impurity potential, we use

$$\langle |U(\boldsymbol{q})|^2 \rangle = U^2 |F(\boldsymbol{q})|^2 \tag{214}$$

with the space variation

$$|F(\boldsymbol{q})|^2 = \frac{6\pi^2}{q_0^3}\theta(|q_0 - q|) \ . \tag{215}$$

This is the same as the one used by Götze in Ref. [58] (see Eq. (125) in Sec. 3.3.3). U is the potential strength, and q_0 the momentum cut-off, defining the radius of a sphere with its origin at Γ. We choose $q_0 = 0.55\,a_B^{-1}$, which is larger than the radius of the Fermi surface with $k_F = 0.52\,a_B^{-1}$ (see Sec. 6.2.1) and describes a sphere fully inside the first Brillouin zone. Furthermore, a $\boldsymbol{q}$-independent and purely imaginary memory function $M = -\mathrm{i}\alpha$ is considered. Then, the DC conductivity, σ_{DC}, and the corresponding potential strength, U, are obtained from the following equations (Eqs. (189) and (193)):

$$\sigma_{\text{DC}} = -\alpha \lim_{\boldsymbol{q}\to 0} \frac{\chi^{(0)}(\boldsymbol{q}, -i\alpha)}{q^2} \tag{216}$$

$$\frac{1}{U^2} = -\frac{1}{3mN_e}\frac{6\pi^2}{q_0^3} \sum_{|\boldsymbol{q}|\le q_0} \chi^{(0)}(\boldsymbol{q},0) \left[\frac{\chi^{(0)}(\boldsymbol{q},0)}{\frac{\alpha^2}{q^2}\chi^{(0)}(\boldsymbol{q},-\mathrm{i}\alpha)} - \frac{q^2}{\alpha^2} \right] \ . \tag{217}$$

Before studying the conductivity, we first investigate the response functions for Na, which are used in the evaluation of Eqs. (216) and (217). $\chi^{(0)}(\boldsymbol{q},0)$ is shown in Fig. 6.3. The computed values for Na (black dots) are close to its counterpart for the FEG (black solid line). $\chi^{(0)}(\boldsymbol{q},0)$ for $|\boldsymbol{q}| > q_0$ are not computed, since they are not needed for the summation over $\boldsymbol{q}$-points performed in Eq. (217). At $\boldsymbol{q} = 0$, the limiting value $-\rho_F$ (black dashed line) is reached for Na and for the FEG, as expected from its corresponding expression (Eq. (132)). We note that the same limiting value is obtained for the crystal by analyzing the $\boldsymbol{q} \to 0$ limit of the static $\chi^{(0)}$, starting from Eq. (173). $\chi^{(0)}(\boldsymbol{q}, -i\alpha)$ has to fulfill the f-sum rule in the limit $\alpha \to \infty$ (Eq. (195)):

$$\Omega \lim_{\alpha\to\infty}(-1)\frac{\alpha^2}{q^2}\chi^{(0)}(\boldsymbol{q},\pm\mathrm{i}\alpha) = \frac{N_e}{m_e}\ , \tag{218}$$

with $m_e = 1$. In the case of the FEG, the limit of Eq. (218) is $N_e = 1$. This value is also reached for Na, as shown in Fig. 6.4 for $\boldsymbol{q} = 0$ and three finite wave vectors. Here, for the special case of $\boldsymbol{q} = 0$, a large contribution comes from the term of Eq. (194) containing the plasma frequency, ω_p (dashed line in Fig. 6.4).

Since the response function of Na behaves very similar as the FEG, we expect that also their conductivities with respect to the potential strength are similar. They are shown in Fig. 6.5. σ_{DC} for both, Na and the FEG, decreases in a similar manner with increasing U until it reaches zero at the critical potential strength U_{crit} (solid vertial lines). Above U_{crit}, both systems transition to the insulating regime. U_{crit} is $1.06\,E_0$ for Na (blue vertical line in Fig. 6.5), and

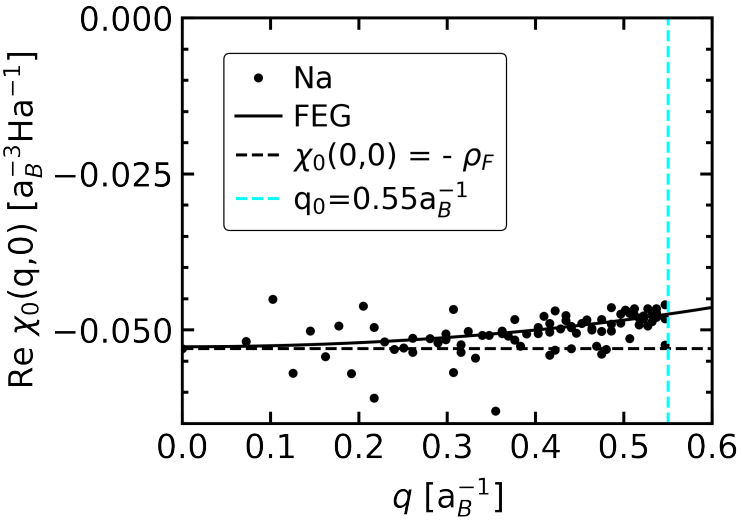

Figure 6.3: Kubo's linear-response function in the static limit, $\chi^{(0)}(\boldsymbol{q},0)$, versus the length of the wave vector $\boldsymbol{q}$, $q = |\boldsymbol{q}|$. The light blue line indicates the momentum cut-off q_0 of the averaged impurity potential (see Eq. (214)).

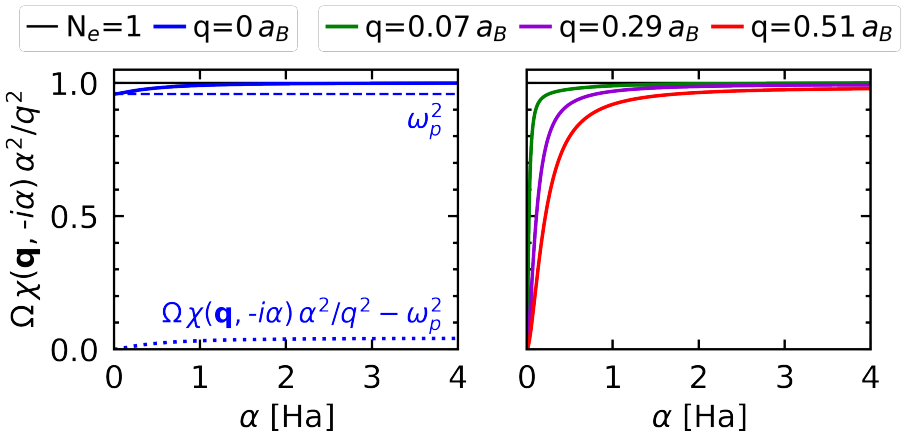

Figure 6.4: $\Omega\,\chi^{(0)}(\boldsymbol{q},-\mathrm{i}\alpha)\alpha^2/q^2$ versus α for $\boldsymbol{q}=0$ (left) and three finite wave vectors (right). $\chi^{(0)}(\boldsymbol{q},-\mathrm{i}\alpha)$ is Kubo's linear-response function of Na. For $\boldsymbol{q}=0$, the contribution from the plasma frequency ω_p is shown with a blue dashed line.

$1.05\,E_0$ for the FEG (red vertical line). The difference between these values is within the numerical precision. Table 6.1 summarizes the values of U_{crit} for Na calculated using Eq. (199) for different $\boldsymbol{k}$-point and $\boldsymbol{q}$-point meshes. They differ by less then $0.03\,E_0$ and show that we have reached convergence within this precision. A refinement of the $\boldsymbol{q}$-point grid beyond $8\times8\times8$ $\boldsymbol{q}$-points does not have a strong impact on the result.

For comparison, the classical Drude result for the FEG is added in Fig. 6.5 with a green dashed line. It is obtained from $M(0)$ calculated using Eq. (141) (zero-order result of $M(\omega)$ in the weak coupling regime). It does not show the transition to the insulating regime and has always a finite value for σ_{DC} even beyond U_{crit}. Thus, the classical result gives only the correct conductivity in the very weak coupling regime, *i.e.* at small potential strengths, as expected.

A different numerical strategy to study a metal-to-insulator transition, as presented here, consists of a self-consistent algorithm. This is implemented in **exciting**, and briefly discussed in Appendix A.2.5. Employing this implemen-

Table 6.1: Critical potential strength U_{crit} of Na for various $\boldsymbol{k}$- and $\boldsymbol{q}$-grids.

$\boldsymbol{k}$-grid	$\boldsymbol{q}$-grid	U_{crit} [E_0]
16×16×16	8×8×8	1.0731
16×16×16	16×16×16	1.0628
24×24×24	8×8×8	1.0824
24×24×24	12×12×12	1.0926
24×24×24	24×24×24	1.0803

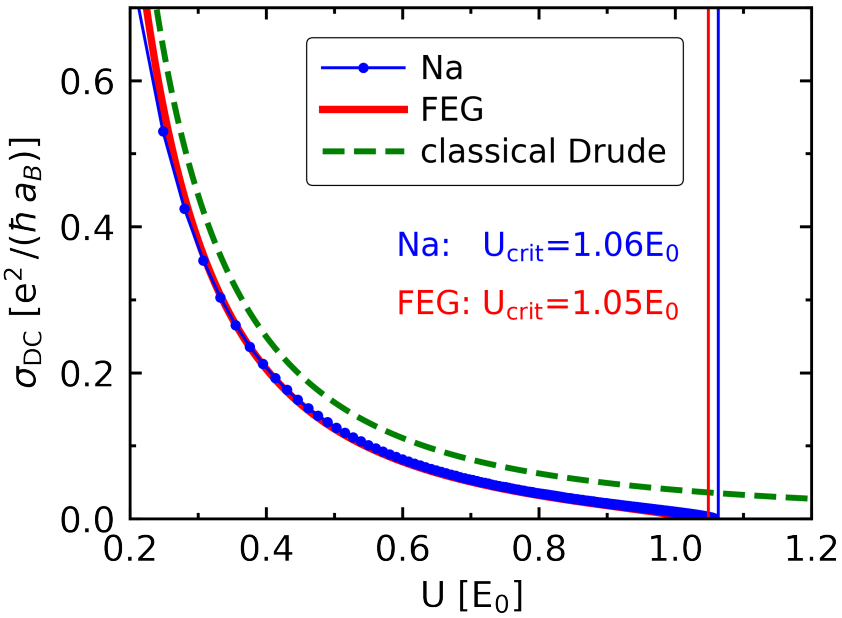

Figure 6.5: DC conductivity, σ_{DC}, with respect to the potential strength, U. The result obtained for Na is shown with blue dots, the result obtained for the FEG with a red solid line. In addition, the classical Drude result for the FEG calculated using the memory function of Eq. (141) with $k_F = 0.51\, a_B^{-1}$ is displayed with a green dashed line. The critical potential strengths for Na and the FEG are indicated with solid vertical lines in the corresponding color.

tation to obtain the self-consistent solution for Na, we find that it reproduces the same relation between the memory function M and the potential strength U, as obtained from using Eq. (217). Here, the self-consistent solution gives a converged M for a given U, while, using the explicit Eq. (217), U is obtained for a given $M = -\mathrm{i}\alpha$. In the self-consistent cycle, the converged result for M is independent of its starting value, that can be chosen to be purely real, purely imaginary or a mix of them.

6.3 CONCLUSIONS AND OUTLOOK

The *ab initio* memory-function approach for calculating the electrical conductivity limited by impurities has been derived for crystalline systems. Using this approach, the DC conductivity can be determined from the memory function without the complications arising from taking the static limit $\omega \to 0$, as encountered for the Kubo-Greenwood approach (see Sec. 3.3.2). Furthermore, we have presented a strategy that avoids *ab initio* calculations in large supercells. Here, the impurity potential is approximated by a superposition of single-impurity potentials.

The approach for solids has been demonstrated on bulk sodium perturbed with a square impurity potential in reciprocal space. Driven by the potential strength, a metal-to-insulator transition is observed, revealing the same trends as the homogeneous electron gas, discussed by Götze [58].

The here presented novel and fully quantum-mechanical approach is available in **exciting**. In the future, we will refine its self-consistent scheme in order to evaluate the dynamical conductivity. Furthermore, we plan to extend the implementation towards calculating the conductivity for complex alloys, that would be out of reach using the Kubo-Greenwood approach. For instance, for the complex clathrate compound, the application of the memory-function approach can bring key insights. In contrast to the semi-classical Boltzmann transport approach, as applied for them in Sec. 5.7, this method does not rely on an empirical parameter, as the relaxation time. An additional advantage is that, for $Ba_8Al_xSi_{46-x}$, we already have the CE models available to accurately access finite-temperature properties (see Sec. 3.2.1). Those tools of alloy theory can be used to attain a realistic model of the impurity potential at finite temperature.

A

APPENDIX

A.1 TEMPERATURE-DEPENDENT TRANSPORT PROPERTIES OF TYPE-I CLATHRATE

A.1.1 *Effect of the exchange-correlation function on the transition temperature*

To investigate the effect of the xc functional on the transition temperature, we perform a WL sampling using the CE model for the energy trained from the *ab-initio* data set based on the LDA exchange-correlation functional, obtained in Ref. [41]. From the resulting configurational density of states, we calculate the isobaric specific heat C_p for the unit cell in the same way as done in Sec. 5.5.1 for PBEsol. The result is shown in Fig. A.1. The transition temperature T_{trans} using the LDA exchange-correlation functional differs by less than 4% with respect to PBEsol. From this, we can conclude that the use of different local density functionals does not have a significant impact on T_{trans}.

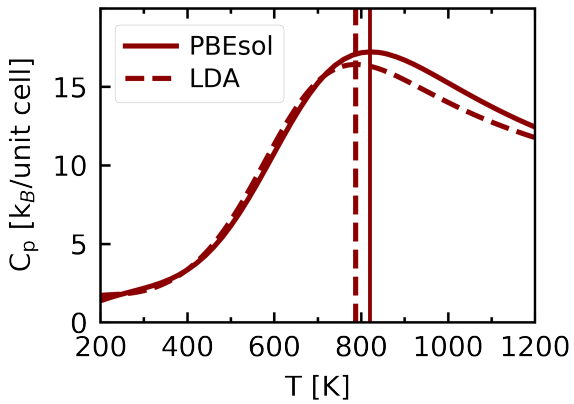

Figure A.1: Specific heat C_p with respect to temperature calculated with the use of $g(E)$ obtained from a WL sampling for LDA (dashed line) and PBE sol (solid line), for the unit cell. The vertical lines indicate the transition temperatures T_{trans}, estimated from the maximum of C_p: $T_{\text{trans}} = 787\,\text{K}$ for LDA and $T_{\text{trans}} = 820\,\text{K}$ for PBEsol.

A.1.2 *Convergence tests for transport coefficients of clathrates*

To obtain converged transport coefficients for clathrates using the BT approach, we perform a convergence study of the $\boldsymbol{k}$-grid used to evaluate the BT integrals. Figure A.2 shows the Seebeck coefficient $S(T, \mu)$ (panels (a) and (b)) and the electrical conductivity $\sigma(T, \mu)$ (panels (c) and (d)) calculated with different $\boldsymbol{k}$-meshes versus the chemical potential μ for the GS configuration (right panels) and a high-energy configuration with large disorder and a closed band gap (left panels). The coefficients calculated for a low temperature of $310\,\mathrm{K}$ are depicted in panels (a) and (c) and for a high temperature of $1300\,\mathrm{K}$ in panels

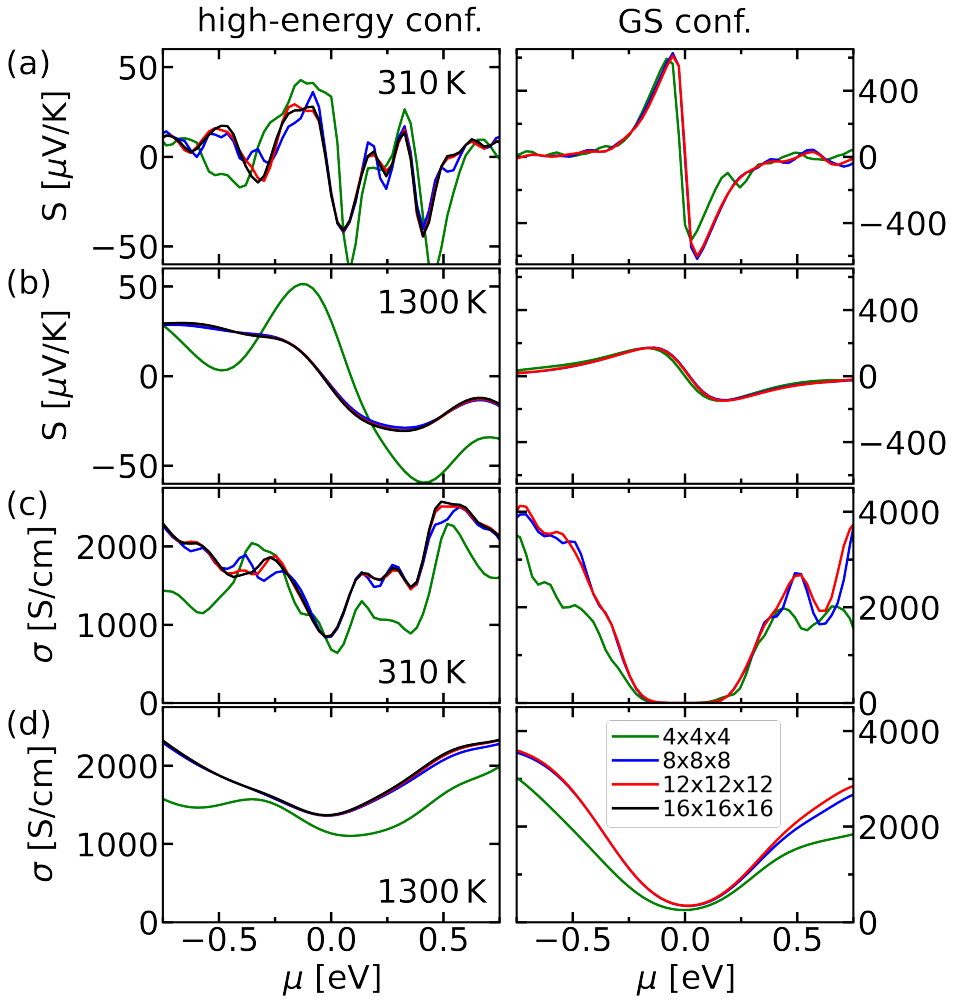

Figure A.2: Convergence test of the $\boldsymbol{k}$-mesh for the transport coefficients $S(T, \mu)$ ((a) and (b)) and $\sigma(T, \mu)$ ((c) and (d)) versus the chemical potential μ for $Ba_8Al_{16}Si_{30}$: The left panels show the transport coefficients for a high-energy configuration with a closed band gap and the right panels for the GS configuration. The results for $T = 310$ are shown in (a) and (c) and for $T = 1300\,\mathrm{K}$ in (b) and (d).

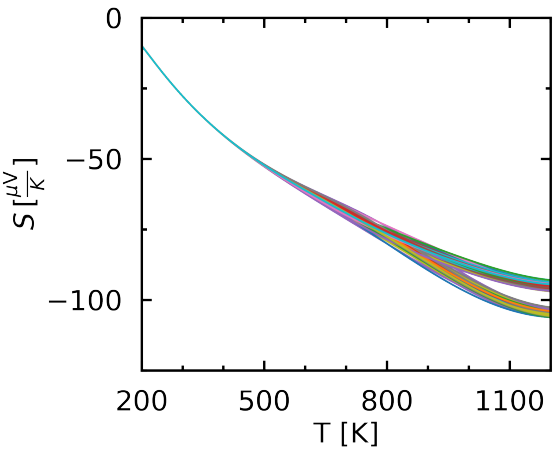

Figure A.3: Canonical-ensemble average of S obtained for 50 resamplings from Eq. (146).

(b) and (c). We observe that a $12\times12\times12$ $\boldsymbol{k}$-mesh and a $16\times16\times16$ $\boldsymbol{k}$-mesh yield similar results, especially for μ close to zero corresponding to low doping concentrations. For this, we consider coefficients calculated with a $12\times12\times12$ $\boldsymbol{k}$-mesh as converged.

To estimate the uncertainty of the canonical-ensemble average given by Eq. (146), we perform resamplings of the configurations used to calculate the canonical-ensemble average. On the example of the Seebeck coefficient S, shown in Fig. A.3, the resampled averages distribute in a bimodal way. The uncertainty is estimated by the difference of the minimum and maximum value of the obtained S_T's. Accordingly, the other transport coefficients show also same bimodal character and their uncertainty is estimated in the same way.

The transport coefficients obtained in Sec. 5.7 are calculated from configurations at composition $x = 16$. To effectively simulate the composition $x = 15$, the chemical potential μ in the BT calculation is adjusted to $n_e = 8.415 \cdot 10^{20}\,\mathrm{cm}^{-3}$, corresponding to one free electron in the unit cell. As a cross-check for this approach, transport coefficients of the actual GS at $x = 15$ are calculated. As shown in Fig. A.4, the results are almost identical.

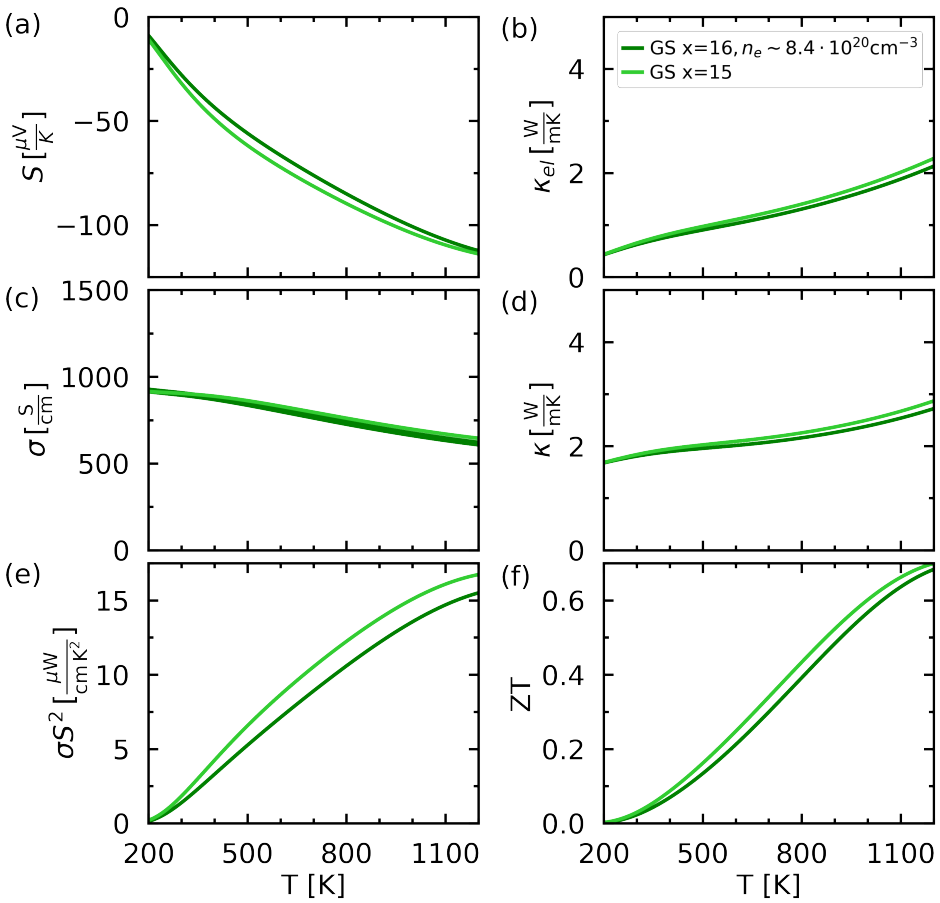

Figure A.4: (a) Seebeck coefficient S, (b) electronic part of the thermal conductivity κ_e, (c) electrical conductivity σ, (d) total thermal conductivity κ, (e) power factor $S^2\sigma$, and (f) the figure of merit ZT calculated with the BT approach. The results obtained for the GS configuration of $x = 16$ and setting the charge carrier concentration to $n_{e,1e} = 8.415{\cdot}10^{20}\,\mathrm{cm}^{-3}$ (corresponding to one free electron in the unit cell) are shown with dark green lines, and the results obtained for the GS configuration of $x = 15$ and $n_e = 0\,\mathrm{cm}^{-3}$ with light green lines.

A.2 MEMORY-FUNCTION APPROACH

A.2.1 *Time derivative of Kubo's internal product*

The time derivative of Kubo's internal product can be rewritten using the Liouville operator $\mathcal{L}$ as:

$$\frac{\mathrm{d}}{\mathrm{d}t}\phi_{AB}(t) = \left(\frac{\mathrm{d}}{\mathrm{d}t}A^\dagger(t)\middle|B\right) \tag{219}$$

$$\overset{\text{Eq. (73)}}{=} i(\mathcal{L}A^\dagger|B)\ . \tag{220}$$

$\mathcal{L}$ is Hermitian with respect to Kubo's internal product, *i.e.* $(\mathcal{L}A^\dagger|B) = (A^\dagger|\mathcal{L}B)$. Furthermore, the following relation can be derived:

$$\begin{aligned}
(A^\dagger|\mathcal{L}B) &= \int_0^\beta \mathrm{d}\lambda \left\langle e^{\lambda H} A^\dagger e^{-\lambda H} \, [H, B] \right\rangle && (221)\\
&= \int_0^\beta \mathrm{d}\lambda \left\langle \left(e^{\lambda H} A^\dagger e^{-\lambda H} \, H \, B - e^{\lambda H} A^\dagger e^{-\lambda H} \, B \, H \right) \right\rangle && (222)\\
&= \int_0^\beta \mathrm{d}\lambda \left\langle \left(e^{\lambda H} A^\dagger H e^{-\lambda H} \, B - e^{\lambda H} H A^\dagger e^{-\lambda H} B \right) \right\rangle && (223)\\
&= -\int_0^\beta \mathrm{d}\lambda \, \frac{\mathrm{d}}{\mathrm{d}\lambda} \left\langle e^{\lambda H} A^\dagger e^{-\lambda H} \, B \right\rangle && (224)\\
&= \langle e^{\lambda H} A^\dagger e^{-\lambda H} \, B \rangle + \langle A^\dagger B \rangle && (225)\\
&= \langle [A, B] \rangle \; . && (226)
\end{aligned}$$

Here, in the first step, Eq. (61) and (73) are used. Combining Eq. (220) and Eq. (226), we arrive at

$$\frac{\mathrm{d}}{\mathrm{d}t} \phi_{AB}(t) = i \langle [A^\dagger(t), B] \rangle \; . \tag{227}$$

The relations used for this derivation are taken from Refs. [23, 55, 233].

A.2.2 *Projected equation of motion*

We start from the equation of motion for the resolvent in reciprocal space $\mathcal{R}(z)$ (Eq. (78)):

$$(\mathcal{L} - z) \, \mathcal{R}(z) = 1 \; . \tag{228}$$

We apply to this equation, first, the projector of the relevant space $\mathcal{P}$ from the right side,

$$(\mathcal{L} - z) \mathcal{R}(z) \mathcal{P} = \mathcal{P} \; . \tag{229}$$

Then, from the left side, $\mathcal{P}$ and the projector of the outer space $\mathcal{Q}$ are multiplied by Eq. (229), respectively, resulting in the following two equations:

$$\begin{aligned}
\mathcal{P}(\mathcal{L} - z) \mathcal{R}(z) \mathcal{P} &= \mathcal{P}\mathcal{P} = \mathcal{P} \; , && (230)\\
\mathcal{Q}(\mathcal{L} - z) \mathcal{R}(z) \mathcal{P} &= \mathcal{Q}\mathcal{P} = 0 \; . && (231)
\end{aligned}$$

Here, $\mathcal{Q}\mathcal{P} = 0$, since the subspace of $\mathcal{Q}$ is orthogonal to the subspace of $\mathcal{P}$. Now, we insert $1 = \mathcal{P} + \mathcal{Q}$ between $(\mathcal{L} - z)\mathcal{R}(z)$ in Eq. (230) and Eq. (231):

$$\begin{aligned}
\mathcal{P}(\mathcal{L} - z) \mathcal{P} \mathcal{R}(z) \mathcal{P} + \mathcal{P}(\mathcal{L} - z) \mathcal{Q} \mathcal{R}(z) \mathcal{P} &= \mathcal{P} \; , && (232)\\
\mathcal{Q}(\mathcal{L} - z) \mathcal{P} \mathcal{R}(z) \mathcal{P} + \mathcal{Q}(\mathcal{L} - z) \mathcal{Q} \mathcal{R}(z) \mathcal{P} &= 0 \; . && (233)
\end{aligned}$$

From Eq. (233), we derive

$$\mathcal{Q}(\mathcal{L}-z)\mathcal{Q}\mathcal{Q}\mathcal{R}(z)\mathcal{P} = -\mathcal{Q}(\mathcal{L}-z)\mathcal{P}\mathcal{R}(z)\mathcal{P} \ , \tag{234}$$

$$\mathcal{Q}\mathcal{R}(z)\mathcal{P} = -\left[\mathcal{Q}(\mathcal{L}-z)\mathcal{Q}\right]^{-1}\mathcal{Q}(\mathcal{L}-z)\mathcal{P}\mathcal{R}(z)\mathcal{P} \ . \tag{235}$$

In Eq. (234), we make use of $\mathcal{Q} = \mathcal{Q}^2 = \mathcal{Q}\mathcal{Q}$. Since $\mathcal{Q}z\mathcal{P} = z\mathcal{Q}\mathcal{P} = 0$ (and also $\mathcal{P}z\mathcal{Q} = z\mathcal{P}\mathcal{Q} = 0$), it follows for Eq. (235):

$$\mathcal{Q}\mathcal{R}(z)\mathcal{P} = -\left[\mathcal{Q}(\mathcal{L}-z)\mathcal{Q}\right]^{-1}\mathcal{Q}\mathcal{L}\mathcal{P}\mathcal{R}(z)\mathcal{P} \ . \tag{236}$$

Substituting this relation into Eq. (232), we obtain

$$\mathcal{P}(\mathcal{L}-z)\mathcal{P}\mathcal{R}(z)\mathcal{P} - \mathcal{P}\mathcal{L}\mathcal{Q}\left[\mathcal{Q}(\mathcal{L}-z)\mathcal{Q}\right]^{-1}\mathcal{Q}\mathcal{L}\mathcal{P}\mathcal{R}(z)\mathcal{P} = \mathcal{P} \ , \tag{237}$$

$$\left\{\mathcal{P}(\mathcal{L}-z)\mathcal{P} - \mathcal{P}\mathcal{L}\mathcal{Q}\left[\mathcal{Q}(\mathcal{L}-z)\mathcal{Q}\right]^{-1}\mathcal{Q}\mathcal{L}\mathcal{P}\right\}\mathcal{P}\mathcal{R}(z)\mathcal{P} = \mathcal{P} \ . \tag{238}$$

This gives formally the projected equation of motion for $\mathcal{R}(z)$ (Eq. (82)):

$$\mathcal{P}\mathcal{R}(z)\mathcal{P} = \frac{\mathcal{P}}{\mathcal{P}(\mathcal{L}-z)\mathcal{P} - \mathcal{P}\mathcal{L}\mathcal{Q}\left[\mathcal{Q}(\mathcal{L}-z)\mathcal{Q}\right]^{-1}\mathcal{Q}\mathcal{L}\mathcal{P}} \ . \tag{239}$$

A.2.3 *Self-consistent equations for the homogeneous non-interacting system*

In the following, we express the self-consistent equations for the FEG perturbed with a square potential in dimensionless units, as used by Götze [58]. The functions and expressions in dimensionless units are indicated with $\bar{}$. Götze [58] uses the following dimensionless units for the wave vector $\boldsymbol{q}$ and the frequency z:

$$\bar{\boldsymbol{q}} = \frac{\boldsymbol{q}}{q_0} \tag{240}$$

$$\bar{z} = \frac{\hbar z}{E_0} \ . \tag{241}$$

Here, $E_0 = \frac{\hbar^2 q_0^2}{2m_e}$ with q_0 as the momentum cut-off of the square impurity potential, as defined in Eq. (125). Furthermore, we define the Fermi wave vector k_F, the Fermi velocity $v_F = \hbar k_F / m_e$ and the Fermi energy $E_F = \frac{\hbar^2 k_F^2}{2m_e}$, and the variables

$$\xi = \frac{2k_F}{q_0}, \qquad \lambda = \frac{3}{4}\frac{U}{E_F} \ , \tag{242}$$

where ξ measures the potential extension relative to the Fermi wave vector and λ the potential strength relative to the electronic kinetic energy E_F [58].

Kubo's linear response function in dimensionless units, $\bar{\chi}^{(0)}$, is defined in Eq. (19c) of Ref. [58] (therein labeled as κ^0) as

$$\bar{\chi}^{(0)}(x,y) = \frac{1}{2} + \frac{1}{8x}\left\{\left[1-(x-y/x)^2\right]\ln\left[\frac{x+1-y/x}{x-1-y/x}\right]\right. \tag{243}$$

$$\left. + \left[1-(x+y/x)^2\right]\ln\left[\frac{x+1+y/x}{x-1+y/x}\right]\right\} \ , \tag{244}$$

with $x = q/\xi = \frac{q}{2k_F}$ and $y = z/\xi^2 = \frac{1}{4}\frac{\hbar z}{\epsilon_F}$. $\chi^{(0)}$ can be written in terms of $\bar{\chi}^{(0)}$ as

$$\chi^{(0)}(\mathbf{q},z) = -\rho_F\ \bar{\chi}^{(0)}\left(\frac{q}{2k_F}, \frac{1}{4}\frac{\hbar z}{\epsilon_F}\right) = -\rho_F\ \bar{\chi}^{(0)}\left(\frac{\bar{q}}{\xi}, \frac{\bar{z}}{\xi^2}\right) \ . \tag{245}$$

The prefactor is the density of states at the Fermi level $\rho_F = m_e k_F/(\hbar^2\pi^2)$. The same relation is valid for the static limit

$$\chi^{(0)}(\mathbf{q},0) = -\rho_{\epsilon_F}\ \bar{\chi}^{(0)}\left(\frac{q}{2k_F}\right) = -\rho_{\epsilon_F}\ \bar{\chi}^{(0)}\left(\frac{\bar{q}}{\xi}\right) \tag{246}$$

with $\bar{\chi}^{(0)}(\bar{q}/\xi) = \bar{g}_0(q)$ as defined in Eq. (19a) of Ref. [58].

The density-density correlation function $\phi^{(0)}$, as defined in Eq. (126), can be expressed in terms of the density-density correlation function in dimensionless units, $\bar{\phi}^{(0)}$ (see Eq. (19b) of [58]), as follows:

$$\phi_0(\boldsymbol{q},z) = -\frac{1}{z}\left[\chi_0(\boldsymbol{q},z) - \chi_0(\boldsymbol{q},0)\right] \tag{247}$$

$$\overset{\text{Eq. 245}}{=} \frac{\rho_{\epsilon_F}}{z}\left[\bar{\chi}^{(0)}\left(\frac{\boldsymbol{q}}{2k_F}, \frac{z}{4\epsilon_F}\right) - \bar{\chi}^{(0)}\left(\frac{\boldsymbol{q}}{2k_F}, 0\right)\right] \tag{248}$$

$$= \frac{\rho_{\epsilon_F}}{E_0}\hbar\ \underbrace{\left\{\frac{1}{\bar{z}}\left[\bar{\chi}^{(0)}\left(\frac{\bar{\boldsymbol{q}}}{\xi}, \frac{\bar{z}}{\xi^2}\right) - \bar{\chi}^{(0)}\left(\frac{\bar{\boldsymbol{q}}}{\xi}, 0\right)\right]\right\}} \tag{249}$$

$$\phi_{0\sigma}(\boldsymbol{q},z) = \frac{\rho_\sigma(\epsilon_F)}{E_0}\hbar \times \qquad \bar{\phi}_0(\bar{\boldsymbol{q}},\bar{z}) \ . \tag{250}$$

Then, the density-density correlation function in dimensionless units, $\bar{\phi}$ (see Eq. (13) of Ref. [58]),

$$\bar{\phi}(\bar{\mathbf{q}},z) = \frac{\bar{\phi}_0(\bar{\mathbf{q}}, \bar{z}+\bar{M}(\bar{z}))}{1+\ \bar{M}(\bar{z})\,\bar{\phi}_0(\bar{\mathbf{q}}, \bar{z}+\bar{M}(\bar{z}))/\bar{\chi}^{(0)}(\bar{\mathbf{q}}/\xi, 0))} \tag{251}$$

is transformed using the relations defined in the Eqs. (250) and (246) to

$$\bar{\phi}(\mathbf{q},z) = \frac{\frac{E_0}{\rho_\sigma(\epsilon_F)\hbar}\phi^0(\mathbf{q}, z+M(z))}{1+\ \frac{\hbar}{E_0}M(z)\,\frac{E_0}{\rho_F\hbar}\phi^{(0)}(\mathbf{q}, z+M(z))/\left(-\frac{1}{\rho_F}\chi^{(0)}(\mathbf{q},0)\right)} \tag{252}$$

$$\phi_\sigma(\mathbf{q},z) = \frac{\phi^{(0)}(\mathbf{q}, z+M(z))}{1-M(z)\,\phi^{(0)}(\mathbf{q}, z+M(z))/\chi^{(0)}(\mathbf{q},0)} \ . \tag{253}$$

Here, $\bar{M}(z)$ is the memory function in dimensionless units ($\mathbf{q}$-independent) in units of E_0, *i.e.* $\bar{M}(\bar{z}) = \hbar/E_0\, M(z)$. The minus in Eq. (253) comes from replacing $\bar{\chi}^{(0)}$ by χ_0 using Eq. (246).

At the end, we demonstrate how the formula of the memory function (defined in Eq. (124)),

$$M(z) = \frac{1}{3nm_e}\frac{1}{V}\sum_{\boldsymbol{q}}\langle|U(\boldsymbol{q})|^2\rangle q^2\phi(\boldsymbol{q},z) \tag{254}$$

can be transformed to the integral (Eq. (16b) of Ref. [58])

$$\bar{M}(\bar{z}) = \lambda\xi^2\int_0^1 \mathrm{d}\bar{q}\,\bar{q}^4\,\bar{\phi}(\bar{\boldsymbol{q}},\bar{z})\ . \tag{255}$$

Here, $q = |\boldsymbol{q}|$ and V is the total volume. First, we insert the expression for the square potential average (see Eq. (125))

$$\langle|U(\boldsymbol{q})|^2\rangle = U^2\frac{6\pi^2}{q_0^3}\theta(q_0-q) \tag{256}$$

and then replace the sum by an integral as $1/V\sum_{\boldsymbol{q}} \to 1/(2\pi)^3\int\mathrm{d}\boldsymbol{q} = 1/(2\pi^2)\int\mathrm{d}q\,q^2$:

$$\begin{aligned} M(z) &= \frac{1}{3nm}\frac{1}{V}\sum_{\boldsymbol{q},q\le q_0} U^2\frac{6\pi^2}{q_0^3}q^2\phi(\boldsymbol{q},z) && (257)\\ &= \frac{1}{3nm}\frac{1}{2\pi^2}\int_0^{q_0}\mathrm{d}q\,q^4U^2\frac{6\pi^2}{q_0^3}\phi(\boldsymbol{q},z)\ . && (258)\end{aligned}$$

Then, we apply the dimensionless coordinates $\bar{q} = q/q_0$ and $\bar{U} = U/E_0$ and replace ϕ with using Eq. 250:

$$\begin{aligned} M(z) &= \frac{1}{3nm}\frac{1}{2\pi^2}\int_0^1\mathrm{d}\bar{q}\,\bar{q}^4q_0^5\,\bar{U}^2E_0^2\frac{6\pi^2}{q_0^3}\rho(\epsilon_F)\frac{\hbar}{E_0}\bar{\phi}(\bar{\boldsymbol{q}},\bar{z}) && (259)\\ &= \frac{1}{nm}\frac{1}{6\pi^2}6\pi^2\rho(\epsilon_F)\hbar\,q_0^2E_0\bar{U}^2\int_0^1\mathrm{d}\bar{q}\,\bar{q}^4\,\bar{\phi}(\bar{\boldsymbol{q}},\bar{z}) && (260)\\ &= \frac{6\pi^2}{k_F^3m}\frac{mk_F}{2\pi^2\hbar^2}\hbar\,q_0^2E_0\bar{U}^2\int_0^1\mathrm{d}\bar{q}\,\bar{q}^4\,\bar{\phi}(\bar{\boldsymbol{q}},\bar{z}) && (261)\\ &= \frac{E_0}{\hbar}\,3\frac{q_0^2}{k_F^2}\,\bar{U}^2\int_0^1\mathrm{d}\bar{q}\,\bar{q}^4\,\bar{\phi}(\bar{\boldsymbol{q}},\bar{z}) && (262)\\ &\overset{\text{Eq. (242)}}{=} \frac{E_0}{\hbar}\,12\frac{1}{\xi^2}\,\bar{U}^2\int_0^1\mathrm{d}\bar{q}\,\bar{q}^4\,\bar{\phi}(\bar{\boldsymbol{q}},\bar{z}) && (263)\\ \hbar\,M(z) &= E_0\ \lambda\xi^2\int_0^1\mathrm{d}\bar{q}\,\bar{q}^4\,\bar{\phi}(\bar{\boldsymbol{q}},\bar{z}) = E_0\,\bar{M}(\bar{z})\ . && (264)\end{aligned}$$

A.2.4 *Conductivity*

An expression for the longitudinal conductivity in terms of $\phi(\boldsymbol{q}, z)$ and $\chi(\boldsymbol{q})$ can be derived from Kubo's formula (Eq. (138)), Ref. [55]) as:

$$\begin{aligned}
\sigma(\boldsymbol{q}, z)\, q^2 &= -\mathrm{i}\, \boldsymbol{q} \left(j(\boldsymbol{q}) \left| (\mathcal{L} - z)^{-1} \right| j(\boldsymbol{q}) \right) \boldsymbol{q} && (265)\\
&\overset{\text{Eq. (88)}}{=} \mathrm{i} \left(\mathcal{L}\rho(\boldsymbol{q}) \left| (\mathcal{L} - z)^{-1} \right| \mathcal{L}\rho(\boldsymbol{q}) \right) && (266)\\
&= \mathrm{i} \left(\rho(\boldsymbol{q}) \left| \mathcal{L} \, (\mathcal{L} - z)^{-1} \right| \mathcal{L}\rho(\boldsymbol{q}) \right) && (267)\\
&= \mathrm{i} \left[\underbrace{(\rho(\boldsymbol{q}) | \mathcal{L}\rho(\boldsymbol{q}))}_{=0} + z \left(\rho(\boldsymbol{q}) | \mathcal{L} \, (\mathcal{L} - z)^{-1} \, \rho(\boldsymbol{q}) \right) \right] && (268)\\
&= \mathrm{i}\, z \left[(\rho(\boldsymbol{q}) | \rho(\boldsymbol{q})) + z \left(\rho(\boldsymbol{q}) | \, (\mathcal{L} - z)^{-1} \, \rho(\boldsymbol{q}) \right) \right] && (269)\\
&\overset{\text{Eq. (133)}}{=} \mathrm{i}\, z \left[-\chi(\boldsymbol{q}) + z\phi(\boldsymbol{q}, z) \right] \ . && (270)
\end{aligned}$$

Going from Eq. (267) to Eq. (268), and going from Eq. (268) to Eq. (269), the relation $\frac{1}{\mathcal{L}-z}\mathcal{L} = \mathcal{L}\frac{1}{\mathcal{L}-z} = \frac{\mathcal{L}-z}{\mathcal{L}-z} + z\frac{1}{\mathcal{L}-z}$ is used.

A.2.5 *Implementation*

The module for solving the self-consistent equations of the memory-function approach is integrated in the excited-states module of **`exciting`**. In this module, the Kubo's linear-response function, $\chi^{(0)}_{\boldsymbol{G},\boldsymbol{G}'}$, is available and can be further processed for the memory-function approach. All evaluated response functions are treated as ($\boldsymbol{G}$,$\boldsymbol{G}'$)-matrices. This keeps the option for a possible extension of the implementation towards calculating $\phi_{\boldsymbol{G},\boldsymbol{G}'}$ also for $\boldsymbol{G} > 0$ and $\boldsymbol{G}' > 0$ in the future.

The general workflow of the self-consistent memory-function approach in **`exciting`** is shown in Fig. A.5. For a given disorder potential with strength U, one self-consistent cycle is performed. It starts, first, with initializing $m^0_{\boldsymbol{G},\boldsymbol{G}'}(\boldsymbol{q}, z)$. It is set to a constant complex number z_0 for all frequencies z (iteration number $i = 0$). Furthermore, the static response function $\chi^{(0)}_{\boldsymbol{G},\boldsymbol{G}'}(\boldsymbol{q}, 0)$ is evaluated. Then, the self-consistent loop starts (blue frame in Fig. A.5). Each iteration i consists of the following steps: First, for given $m^i_{\boldsymbol{G},\boldsymbol{G}'}(\boldsymbol{q}, z)$, $\chi^{(0)}_{\boldsymbol{G},\boldsymbol{G}'}(\boldsymbol{q}, z + m^i_{\boldsymbol{G},\boldsymbol{G}'}(\boldsymbol{q}, z))$ or $\phi^{(0)}_{\boldsymbol{G},\boldsymbol{G}'}(\boldsymbol{q}, z + m^i_{\boldsymbol{G},\boldsymbol{G}'}(\boldsymbol{q}, z))$ is calculated. Second, $\phi^i_{\boldsymbol{G},\boldsymbol{G}'}(\boldsymbol{q}, z)$ is obtained (using Eq. (178)). The memory function is updated, yielding $m^{i+1}_{\boldsymbol{G},\boldsymbol{G}'}(\boldsymbol{q}, z)$. The self-consistent loop stops if the memory function is converged (light red diamond box). The convergence criterion is that the maxi-

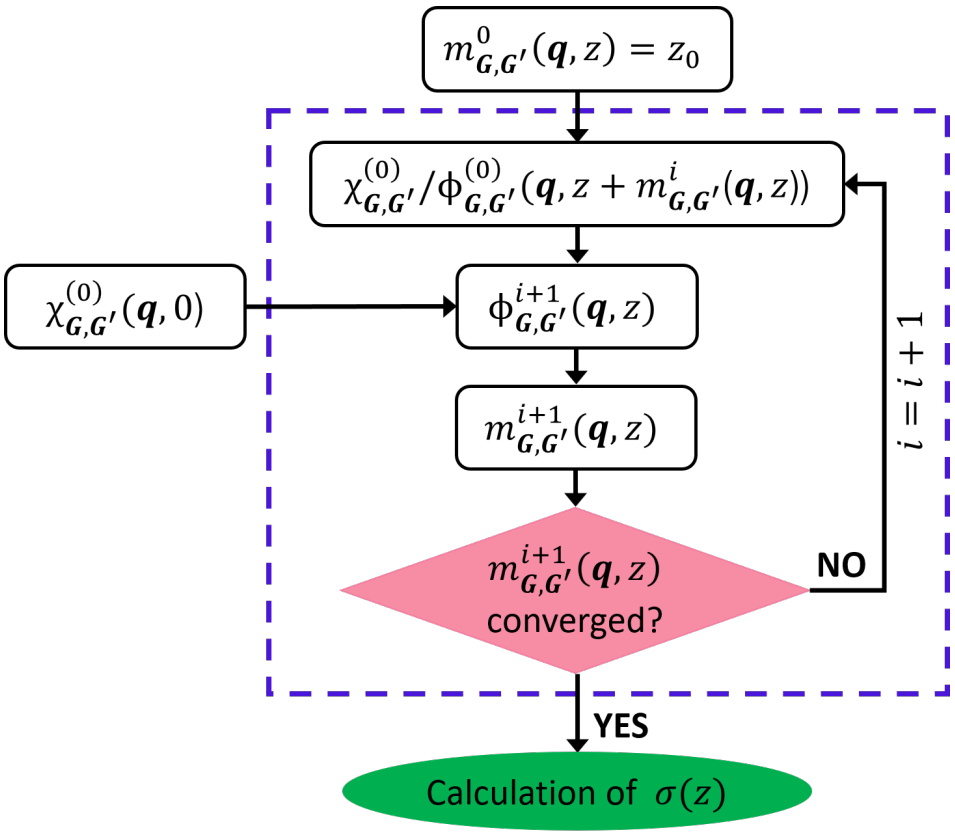

Figure A.5: Self-consistent scheme of the memory-function approach for crystalline systems as implemented in `exciting`.

mum difference between $m^{i+1}_{\boldsymbol{G},\boldsymbol{G}'}(\boldsymbol{q},z)$ and $m^{i}_{\boldsymbol{G},\boldsymbol{G}'}(\boldsymbol{q},z)$ should be less than a given tolerance m_{tol}:

$$\max\left(\mathrm{abs}\left(m^{i+1}_{\boldsymbol{G},\boldsymbol{G}'}(\boldsymbol{q},z) - m^{i}_{\boldsymbol{G},\boldsymbol{G}'}(\boldsymbol{q},z)\right)\right) < m_{\mathrm{tol}}\ . \tag{271}$$

When the self-consistent cycle reaches convergence, the conductivity $\sigma(\omega)$ can be calculated using Eq. (180) (green oval box).

ACKNOWLEDGEMENTS

In the first place, I would like to thank Prof. CLAUDIA DRAXL for supervising my thesis and giving me the opportunity to join the lively and joyful working environment of her group. She offered me manifold opportunities to interact and discuss my research results and plans with colleagues of the international scientific community. This encouraged me to fight for my goals and I am very grateful for her wonderful scientific guidance and advice in all these years. Especially in situations of strong deadlines, she was ready to meet for a careful strengthening of the results and the final polishing even at late evenings.

I am very grateful to Dr. SANTIAGO RIGAMONTI who supervised me during my time in Claudia's group with a lot of passion for cluster expansion, transport phenomena and material science. He provided great support for designing and writing proposals to expedite this PhD project. I highly value his carefulness and patience while exploring new concepts and thoughts. He was always ready for a thorough analysis of my results and came up with exciting ideas. It was a real pleasure to work with him. Even under tight time pressure I could be confident of bringing together any challenge to a solution.

I thank Prof. JORGE SOFO from Pennsylvania State University for energetic and intense discussions in our collaboration on electronic transport properties. I value his enthusiasm for the subject and his effort to push the project towards success. In addition, I especially want to thank him for his kind hospitality during my visits at Pennsylvania State University.

I enjoyed a lot my time in the solid-state theory group at the Humboldt Universität zu Berlin. Here I found a very pleasant atmosphere among loyal, helpful and amicable group members. At this point, I would like to thank PD Dr. PASQUALE PAVONE for reliable presence in all situations that required his wise assistance. Also many thanks to HELEN JURSCHA who is the great organizing soul of the group.

Thanks to my family and to all my friends for their patience and support. They always believed in me.

The work was supported by the Elsa Neumann Stiftung Berlin.

BIBLIOGRAPHY

[1] I. Johnson, W. T. Choate, and A. Davidson. "Waste Heat Recovery. Technology and Opportunities in U.S. Industry" (Mar. 2008). DOI: 10.2172/1218716.

[2] G. Bianchi et al. "Estimating the waste heat recovery in the European Union Industry." *Energy, Ecology and Environment* 4.5 (2019), pp. 211–221. DOI: 10.1007/s40974-019-00132-7.

[3] D. M. Rowe, ed. *CRC Handbook of Thermoelectrics*. 1st ed. CRC Press, 1995. DOI: 10.1201/9781420049718.

[4] J. R. Sootsman, D. Y. Chung, and M. G. Kanatzidis. "New and Old Conzepts in Thermoelectric Materials." *Angewandte Chemie International Edition* 48.46 (2009), pp. 8616–8639. DOI: 10.1002/anie.200900598.

[5] H. J. Goldsmid. *Introduction to Thermoelectricity*. Springer Series in Materials Science. Springer Verlag, 2010. DOI: 10.1007/978-3-642-00716-3.

[6] R. T. Balmer. *Modern Engineering Thermodynamics*. Elsevier, 2011. DOI: 10.1016/C2009-0-20199-1.

[7] M. G. Kanatzidis. "Advances in thermoelectrics: From single phases to hierarchical nanostructures and back." *MRS Bulletin* 40.8 (2015), 687–694. DOI: 10.1557/mrs.2015.173.

[8] A. R. M. Siddique, S. Mahmud, and B. Van Heyst. "A review of the state of the science on wearable thermoelectric power generators (TEGs) and their existing challenges." *Renewable and Sustainable Energy Reviews* 73 (2017), pp. 730–744. DOI: 10.1016/j.rser.2017.01.177.

[9] N. Jaziri et al. "A comprehensive review of Thermoelectric Generators: Technologies and common applications." *Energy Reports* 6 (2020), pp. 264–287. DOI: 10.1016/j.egyr.2019.12.011.

[10] L. S. Hewawasam et al. "Waste heat recovery from thermo-electric generators (TEGs)." *Energy Reports* 6 (2020), pp. 474–479. DOI: 10.1016/j.egyr.2019.11.105.

[11] L.-D. Zhao et al. "Ultralow thermal conductivity and high thermoelectric figure of merit in SnSe crystals." *Nature* 508.7496 (2014), pp. 373–377. DOI: 10.1038/nature13184.

[12] L.-D. Zhao et al. "Ultrahigh power factor and thermoelectric performance in hole-doped single-crystal SnSe." *Science* 351.6269 (2016), pp. 141–144. DOI: 10.1126/science.aad3749.

[13] L.-D. Zhao et al. "SnSe: a remarkable new thermoelectric material." *Energy & Environmental Science* 9.10 (2016), pp. 3044–3060. DOI: 10.1039/C6EE01755J.

[14] G. S. Nolas, G. A. Slack, and S. B. Schujman. "Chapter 6 Semiconductor clathrates: A phonon glass electron crystal material with potential for thermoelectric applications." *Recent Trends in Thermoelectric Materials Research I*. Ed. by Terry M. Tritt. Vol. 69. Semiconductors and Semimetals. Elsevier, 2001, pp. 255–300. DOI: 10.1016/S0080-8784(01)80152-6.

[15] K. A. Kovnir and A. V. Shevelkov. "Semiconducting clathrates: synthesis, structure and properties." *Russ. Chem. Rev.* 73 (2004), pp. 923–938. DOI: 10.1070/RC2004v073n09ABEH000916.

[16] G. J. Snyder and E. S. Toberer. "Complex thermoelectric materials." *Nature materials* 7 (2008), pp. 105–114. DOI: 10.1038/nmat2090.

[17] T. Takabatake et al. "Phonon-glass electron-crystal thermoelectric clathrates: Experiments and theory." *Rev. Mod. Phys.* 86 (2014), pp. 669–716. DOI: 10.1103/RevModPhys.86.669.

[18] M. Christensen, S. Johnsen, and B. B. Iversen. "Thermoelectric clathrates of type I." *Dalton Trans.* 39 (2010), pp. 978–992. DOI: 10.1039/B916400F.

[19] W. Kohn. "Electronic struture of matter-wave functions and density functionals." *Rev. Mod. Phys.* 71 (1999), pp. 1253–1266. DOI: 10.1103/RevModPhys.71.1253.

[20] R. O. Jones. "Density functional theory: Its origins, rise to prominence, and future." *Rev. Mod. Phys.* 87 (2015), pp. 897–923. DOI: 10.1103/RevModPhys.87.897.

[21] J. M. Ziman. "Principles of the Theory of Solids." 2nd ed. Cambridge University Press, UK, 1972. Chap. 7. DOI: 10.1017/CBO9781139644075.

[22] B. R. Nag. "Electron Transport on Compound Semiconductiors." Springer Series in Solid-State Sciences, Volume 11. Springer-Verlag Berlin Heidelberg NewYork, 1980. Chap. 7. DOI: 10.1007/978-3-642-81416-7.

[23] H. Mori. "Transport, Collective Motion, and Brownian Motion." *Progress of Theoretical Physics* 33.3 (1965), pp. 423–455. DOI: 10.1143/PTP.33.423.

[24] J. M. Skelton et al. "Anharmonicity in the High-Temperature $Cmcm$ Phase of SnSe: Soft Modes and Three-Phonon Interactions." *Phys. Rev. Lett.* 117 (2016), p. 075502. DOI: 10.1103/PhysRevLett.117.075502.

[25] G. Shi and E. Kioupakis. "Quasiparticle band structures and thermoelectric transport properties of p-type SnSe." *J. Appl. Phys.* 117 (2015), p. 065103. DOI: 10.1063/1.4907805.

[26] J. Ma, Y. Chen, and W. Li. "Intrinsic phonon-limited charge carrier mobilities in thermoelectric SnSe." *Phys. Rev. B* 97 (2018), p. 205207. DOI: 10.1103/PhysRevB.97.205207.

[27] K. Kutorasinski et al. "Electronic structure and thermoelectric properties of n- and p-type SnSe from first-principles calculations." *Phys. Rev. B* 91 (2015), p. 205201. DOI: 10.1103/PhysRevB.91.205201.

[28] A. Dewandre et al. "Two-Step Phase Transition in SnSe and the Origins of its High Power Factor from First Principles." *Phys. Rev. Lett.* 117 (2016), p. 276601. DOI: 10.1103/PhysRevLett.117.276601.

[29] A. Gulans et al. "exciting: a full-potential all-electron package implementing density-functional theory and many-body perturbation theory." *J. Phys. Condens. Matter* 26.36 (2014), p. 363202. DOI: 10.1088/0953-8984/26/36/363202.

[30] G. S. Nolas et al. "Semiconducting Ge clathrates: Promising candidates for thermoelectric applications." *Appl. Phys. Lett.* 73.2 (1998), pp. 178–180. DOI: 10.1063/1.121747.

[31] C. L. Condron et al. "Structure and Thermoelectric Characterization of $Ba_8Al_{14}Si_{31}$." *Inorg. Chem.* 45.23 (2006), pp. 9381–9386. DOI: 10.1021/ic061241w.

[32] J. H. Roudebush et al. "Neutron Diffraction Study of the Type I Clathrate $Ba_8Al_xSi_{46-x}$: Site Occupancies, Cage Volumes, and the Interaction between the Guest and the Host Framework." *Inorg. Chem.* 51.3 (2012), pp. 1805–1812. DOI: 10.1021/ic202095e.

[33] J. H. Roudebush et al. "Phase Range of the Type-I Clathrate $Sr_8Al_xSi_{46-x}$ and Crystal Structure of $Sr_8Al_{10}Si_{36}$." *Inorg. Chem.* 51.7 (2012), 4161––4169. DOI: 10.1021/ic2024814.

[34] H. Anno et al. "Crystallographic, thermoelectric, and mechanical properties of polycrystalline type-I $Ba_8Al_{16}Si_{30}$-based clathrates." *J. Mater. Sci.* 48.7 (2013), pp. 2846–2854. DOI: 10.1007/s10853-012-6977-y.

[35] H. Anno et al. "Crystallographic, Thermoelectric, and Mechanical Properties of Polycrystalline $Ba_8Al_xSi_{46-x}$ Clathrates." *J. Electron. Mater.* 42.7 (2013), pp. 2326–2336. DOI: 10.1007/s11664-012-2418-6.

[36] M. Bobnar et al. "Distribution of Al atoms in the clathrate-I phase $Ba_8Al_xSi_{46-x}$ at x=6.9." *Dalton Trans.* 44 (2015), pp. 12680–12687. DOI: 10.1039/C5DT01198A.

[37] N. P. Blake et al. "Band structures and thermoelectric properties of the clathrates $Ba_8Ga_{16}Ge_{30}$, $Sr_8Ga_{16}Ge_{30}$, $Ba_8Ga_{16}Si_{30}$, and $Ba_8In_{16}Sn_{30}$." *J. Chem. Phys.* 115.17 (2001), pp. 8060–8073. DOI: 10.1063/1.1397324.

[38] K. Akai et al. "First-Principles Study of Semiconducting Clathrate $Ba_8Al_{16}Ge_{30}$." *J. Electron. Mater.* 38.7 (2009), pp. 1412–1417. DOI: 10.1007/s11664-009-0727-1.

[39] M. Ångqvist, D. O. Lindroth, and P. Erhart. "Optimization of the Thermoelectric Power Factor: Coupling between Chemical Order and Transport Properties." *Chem. Mater.* 28.19 (2016), pp. 6877–6885. DOI: 10.1021/acs.chemmater.6b02117.

[40] M. Ångqvist and P. Erhart. "Understanding Chemical Ordering in Intermetallic Clathrates from Atomic Scale Simulations." *Chem. Mater.* 29.17 (2017), pp. 7554–7562. DOI: 10.1021/acs.chemmater.7b02686.

[41] M. Troppenz, S. Rigamonti, and C. Draxl. "Predicting Ground-State Configurations and Electronic properties of the Thermoelectric Clathrates $Ba_8Al_xSi_{46-x}$ and $Ba_8Al_xSi_{46-x}$." *Chem. Mater.* 29 (2017), pp. 2414–2424. DOI: 10.1021/acs.chemmater.6b05027.

[42] C. L Condron et al. "Structure and Thermoelectric Characterization of $Ba_8Al_{14}Si_{31}$." *Inorg. Chem.* 45 (2006), pp. 9381–9386. DOI: 10.1021/ic061241w.

[43] C. L. Condron et al. "Synthesis, Structure, and High-Temperature Thermoelectric Properties of Boron-Doped $Ba_8Al_{14}Si_{31}$ Clathrate I Phases." *Inorg. Chem.* 47.18 (2008), pp. 8204–8212. DOI: 10.1021/ic800772m.

[44] N. Metropolis et al. "Equation of State Calculations by Fast Computing Machines." *J. Chem. Phys.* 21.6 (1953), pp. 1087–1092. DOI: 10.1063/1.1699114.

[45] F. Wang and D. P. Landau. "Efficient, Multiple-Range Walk Algorithm to Calculate the Density of States." *Phys. Rev. Lett.* 86 (2001), pp. 2050–2053. DOI: 10.1103/PhysRevLett.86.2050.

[46] D. P. Landau, Shan-Ho Tsai, and M. Exler. "A new approach to Monte Carlo simulations in statistical physics: Wang-Landau sampling." *American Journal of Physics* 72.10 (2004), pp. 1294–1302. DOI: 10.1119/1.1707017.

[47] J.M. Sanchez, F. Ducastelle, and D. Gratias. "Generalized cluster description of multicomponent systems." *Physica A: Statistical Mechanics and its Applications* 128.1 (1984), pp. 334–350. DOI: 10.1016/0378-4371(84)90096-7.

[48] Alex Zunger et al. "Special quasirandom structures." *Phys. Rev. Lett.* 65 (1990), pp. 353–356. DOI: 10.1103/PhysRevLett.65.353.

[49] V. Popescu and A. Zunger. "Effective Band Structure of Random Alloys." *Phys. Rev. Lett.* 104 (2010), p. 236403. DOI: 10.1103/PhysRevLett.104.236403.

[50] V. Popescu and A. Zunger. "Extracting E versus $\vec{k}$ effective band structure from supercell calculations on alloys and impurities." *Phys. Rev. B* 85 (2012), p. 085201. DOI: 10.1103/PhysRevB.85.085201.

[51] P. Soven. "Coherent-Potential Model of Substitutional Disordered Alloys." *Phys. Rev.* 156 (1967), pp. 809–813. DOI: 10.1103/PhysRev.156.809.

[52] Paul Soven. "Application of the Coherent Potential Approximation to a System of Muffin-Tin Potentials." *Phys. Rev. B* 2 (1970), pp. 4715–4722. DOI: 10.1103/PhysRevB.2.4715.

[53] L. Bellaiche and D. Vanderbilt. "Virtual crystal approximation revisited: Application to dielectric and piezoelectric properties of perovskites." *Phys. Rev. B* 61 (2000), pp. 7877–7882. DOI: 10.1103/PhysRevB.61.7877.

[54] A. V. Ruban and I. A. Abrikosov. "Configurational thermodynamics of alloys from first principles: effective cluster interactions." *Reports on Progress in Physics* 71.4 (2008), p. 046501. DOI: 10.1088/0034-4885/71/4/046501.

[55] R. Kubo. "Statistical-Mechanical Theory of Irreversible Processes. I. General Theory and Simple Applications to Magnetic and Conduction Problems." *Journal of the Physical Society of Japan* 12 (1957), pp. 570–586. DOI: 10.1143/JPSJ.12.570.

[56] W. Götze and P. Wölfle. "Homogeneous Dynamical Conductivity of Simple Metals." *Phys. Rev. B* 6.4 (1972), pp. 1226–1238. DOI: 10.1103/PhysRevB.6.1226.

[57] W. Götze. "An elementary approach towards the Anderson transition." *Solid State Communications* 27.12 (Sept. 1, 1978), pp. 1393–1395. ISSN: 0038-1098. DOI: 10.1016/0038-1098(78)91579-X.

[58] W. Götze. "The mobility of a quantum particle in a three-dimensional random potential." *Philosophical Magazine B* 43.2 (1981), pp. 219–250. DOI: 10.1080/13642818108221896.

[59] T. J. Seebeck. "Abhandlungen der Deutschen Akademie der Wissenschaften zu Berlin" (1822), pp. 265–373.

[60] T. J. Seebeck. "Ueber die magnetische Polarisation der Metalle und Erze durch Temperaturdifferenz." *Annalen der Physik* 82 (1826), pp. 253–286. DOI: 10.1002/andp.18260820302.

[61] J. C. Peltier. *Ann. Chim. Phys.* 56 (1834), pp. 371–386.

[62] Z. H. Dughaish. "Lead telluride as a thermoelectric material for thermoelectric power generation." *Physica B: Condens. Matter* 322.1 (2002), pp. 205 –223. DOI: https://doi.org/10.1016/S0921-4526(02)01187-0.

[63] G. J. Snyder and A. H. Snyder. "Figure of merit ZT of a thermoelectric device defined from materials properties." *Energy Environ. Sci.* 10 (2017), pp. 2280–2283. DOI: 10.1039/C7EE02007D.

[64] G. Wiedemann and R. Franz. "Über die Wärme-Leistungsfähigkeit der Metalle." *Annalen der Physik* 165 (1853), pp. 487–531. DOI: 10.1002/andp.18531650802.

[65] G. A. Slack. "The Thermal Conductivity of Nonmetallic Crystals." Ed. by H. Ehrenreich, F. Seitz, and D. Turnbull. Vol. 34. Solid State Physics. Academic Press, 1979, pp. 1–71. DOI: 10.1016/S0081-1947(08)60359-8.

[66] A. J. Minnich et al. "Bulk nanostructured thermoelectric materials: current research and future prospects." *Energy & Environmental Science* 2 (2009), pp. 466–479. DOI: 10.1039/B822664B.

[67] A. Shakouri. "Recent Developments in Semiconductor Thermoelectric Physics and Materials." *Annual Review of Materials Research* 41 (2011), pp. 399–431. DOI: 10.1146/annurev-matsci-062910-100445.

[68] A. F. Ioffe. *Izv. Akad. Nauk USSR, Ser. Fiz.* 20 (1956), p. 76.

[69] M. V. Vedernikov and E. K. Iordanishvili. "A.F. Ioffe and origin of modern semiconductor thermoelectric energy conversion." *Seventeenth International Conference on Thermoelectrics. Proceedings ICT98 (Cat. No.98TH8365)*. 1998, pp. 37–42. DOI: 10.1109/ICT.1998.740313.

[70] V. L. Kuznetsov et al. "High performance functionally graded and segmented Bi_2Te_3-based materials for thermoelectric power generation." *Journal of Material Science* 37.14 (2002), pp. 2893–2897. DOI: 10.1023/A:1016092224833.

[71] Z.-G. Chen et al. "Nanostructured thermoelectric materials: Current research and future challenge." *Progress in Natural Science: Materials International* 22.6 (2012), pp. 535 –549. DOI: 10.1016/j.pnsc.2012.11.011.

[72] S. Twaha et al. "A comprehensive review of thermoelectric technology: Materials, applications, modelling and performance improvement." *Renewable and Sustainable Energy Reviews* 65 (2016), pp. 698 –726. DOI: 10.1016/j.rser.2016.07.034.

[73] J. He and T. M. Tritt. "Advances in thermoelectric materials research: Looking back and moving forward." *Science* 357.6358 (2017). DOI: 10.1126/science.aak9997.

[74] Z.-Y. Liu et al. "A review of $CoSb_3$-based skutterudite thermoelectric materials." *Journal of Advanced Ceramics* 9.6 (2020), pp. 647–673. DOI: 10.1007/s40145-020-0407-4.

[75] D. T. Morelli et al. "Low-temperature transport properties of p-type $CoSb_3$." *Phys. Rev. B* 51 (1995), pp. 9622–9628. DOI: 10.1103/PhysRevB.51.9622.

[76] G. S. Nolas, D. T. Morelli, and Terry M. Tritt. "SKUTTERUDITES: A Phonon-Glass-Electron Crystal Approach to Advanced Thermoelectric Energy Conversion Applications." *Annual Review of Materials Science* 29.1 (1999), pp. 89–116. DOI: 10.1146/annurev.matsci.29.1.89.

[77] B. C. Sales et al. "Filled skutterudite antimonides: Electron crystals and phonon glasses." *Phys. Rev. B* 56 (1997), pp. 15081–15089. DOI: 10.1103/PhysRevB.56.15081.

[78] Xun Shi et al. "Multiple-Filled Skutterudites: High Thermoelectric Figure of Merit through Separately Optimizing Electrical and Thermal Transports." *Journal of the American Chemical Society* 133.20 (2011), pp. 7837–7846. DOI: 10.1021/ja111199y.

[79] M. Rull-Bravo et al. "Skutterudites as thermoelectric materials: revisited." *RSC Adv.* 5 (2015), pp. 41653–41667. DOI: 10.1039/C5RA03942H.

[80] B. C. Chakoumakos et al. "Structural disorder and thermal conductivity of the semiconducting clathrate $Sr_8Ga_{16}Ge_{30}$." *Journal of Alloys and Compounds* 296.1 (2000), pp. 80–86. DOI: 10.1016/S0925-8388(99)00531-9.

[81] B. C. Sales et al. "Structural, magnetic, thermal, and transport properties of $X_8Ga_{16}Ge_{30}$ $(X = \mathrm{Eu}, \mathrm{Sr}, \mathrm{Ba})$ single crystals." *Phys. Rev. B* 63 (2001), p. 245113. DOI: 10.1103/PhysRevB.63.245113.

[82] A. Bentien et al. "Thermal conductivity of thermoelectric clathrates." *Phys. Rev. B* 69 (2004), p. 045107. DOI: 10.1103/PhysRevB.69.045107.

[83] M. A. Avila et al. "Glasslike versus crystalline thermal conductivity in carrier-tuned $Ba_8Ga_{16}X_{30}$ clathrates $(X = \mathrm{Ge}, \mathrm{Sn})$." *Phys. Rev. B* 74 (2006), p. 125109. DOI: 10.1103/PhysRevB.74.125109.

[84] T. Tadano, Y. Gohda, and S. Tsuneyuki. "Impact of Rattlers on Thermal Conductivity of a Thermoelectric Clathrate: A First-Principles Study." *Phys. Rev. Lett.* 114 (2015), p. 095501. DOI: 10.1103/PhysRevLett.114.095501.

[85] A. Saramat et al. "Large thermoelectric figure of merit at high temperature in Czochralski-grown clathrate $Ba_8Ga_{16}Ge_{30}$." *J. Appl. Phys.* 99.2 (2006), p. 023708. DOI: 10.1063/1.2163979.

[86] M. S. Dresselhaus et al. "New Directions for Low-Dimensional Thermoelectric Materials." *Advanced Materials* 19.8 (2007), pp. 1043–1053. DOI: 10.1002/adma.200600527.

[87] S. K. Bux, J.-P. Fleurial, and R. B. Kaner. "Nanostructured materials for thermoelectric applications." *Chemical Communications* 46 (2010), pp. 8311–8324. DOI: 10.1039/C0CC02627A.

[88] J. R. Szczech, J. M. Higgins, and S. Jin. "Enhancement of the thermoelectric properties in nanoscale and nanostructured materials." *J. Mater. Chem.* 21 (2011), pp. 4037–4055. DOI: 10.1039/C0JM02755C.

[89] L. D. Hicks and M. S. Dresselhaus. "Effect of quantum-well structures on the thermoelectric figure of merit." *Phys. Rev. B* 47 (1993), pp. 12727–12731. DOI: 10.1103/PhysRevB.47.12727.

[90] R. Venkatasubramanian et al. "Thin-film thermoelectric devices with high room-temperature figures of merit." *Nature* 413 (2001), pp. 597–602. ISSN: 1476-4687. DOI: 10.1038/35098012.

[91] A. I. Hochbaum et al. "Enhanced thermoelectric performance of rough silicon nanowires." *Nature* 451.7175 (2008), pp. 163–167. DOI: 10.1038/nature06381.

[92] M. Born and R. Oppenheimer. "Zur Quantentheorie der Molekeln." *Annalen der Physik* 389.20 (1927), pp. 457–484. DOI: 10.1002/andp.19273892002.

[93] C. Fiolhais, F. Nogueira, and M. A. L. Marques, eds. *A Primer in Density Functional Theory*. 1st ed. Springer Verlag, 2003. DOI: 10.1007/3-540-37072-2.

[94] Kieron Burke. "Perspective on density functional theory." *J. Chem. Phys.* 136.15 (2012), p. 150901. DOI: 10.1063/1.4704546.

[95] P. Hohenberg and W. Kohn. "Inhomogeneous Electron Gas." *Phys. Rev.* 136 (1964), B864–B871. DOI: 10.1103/PhysRev.136.B864.

[96] W. Kohn and L. J. Sham. "Self-Consistent Equations Including Exchange and Correlation Effects." *Phys. Rev.* 140 (1965), A1133–A1138. DOI: 10.1103/PhysRev.140.A1133.

[97] J. P. Perdew and K. Schmidt. "Jacob's ladder of density functional approximations for the exchange-correlation energy." *AIP Conference Proceedings* 577.1 (2001), pp. 1–20. DOI: 10.1063/1.1390175.

[98] J. P. Perdew et al. "Prescription for the design and selection of density functional approximations: More constraint satisfaction with fewer fits." *J. Chem. Phys.* 123.6 (2005), p. 062201. DOI: 10.1063/1.1904565.

[99] D. Ceperley. "Ground state of the fermion one-component plasma: A Monte Carlo study in two and three dimensions." *Phys. Rev. B* 18 (1978), pp. 3126–3138. DOI: 10.1103/PhysRevB.18.3126.

[100] D. M. Ceperley and B. J. Alder. "Ground State of the Electron Gas by a Stochastic Method." *Phys. Rev. Lett.* 45 (1980), pp. 566–569. DOI: 10.1103/PhysRevLett.45.566.

[101] J. P. Perdew, K. Burke, and M. Ernzerhof. "Generalized Gradient Approximation Made Simple." *Phys. Rev. Lett.* 77 (1996), pp. 3865–3868. DOI: 10.1103/PhysRevLett.77.3865.

[102] J. P. Perdew et al. "Restoring the Density-Gradient Expansion for Exchange in Solids and Surfaces." *Phys. Rev. Lett.* 100 (2008), p. 136406. DOI: 10.1103/PhysRevLett.100.136406.

[103] S. Kümmel and L. Kronik. "Orbital-dependent density functionals: Theory and applications." *Rev. Mod. Phys.* 80 (2008), pp. 3–60. DOI: 10.1103/RevModPhys.80.3.

[104] J. P. Perdew et al. "Understanding band gaps of solids in generalized Kohn–Sham theory." *Proceedings of the National Academy of Sciences* 114.11 (2017), pp. 2801–2806. DOI: 10.1073/pnas.1621352114.

[105] L. J. Sham and M. Schlüter. "Density-Functional Theory of the Energy Gap." *Phys. Rev. Lett.* 51 (1983), pp. 1888–1891. DOI: 10.1103/PhysRevLett.51.1888.

[106] P. Mori-Sánchez and A. J. Cohen. "The derivative discontinuity of the exchange–correlation functional." *Phys. Chem. Chem. Phys.* 16 (2014), pp. 14378–14387. DOI: 10.1039/C4CP01170H.

[107] P. Mori-Sánchez, A. J. Cohen, and W. Yang. "Localization and Delocalization Errors in Density Functional Theory and Implications for Band-Gap Prediction." *Phys. Rev. Lett.* 100 (2008), p. 146401. DOI: 10.1103/PhysRevLett.100.146401.

[108] M. K. Y. Chan and G. Ceder. "Efficient Band Gap Prediction for Solids." *Phys. Rev. Lett.* 105 (2010), p. 196403. DOI: 10.1103/PhysRevLett.105.196403.

[109] M. Ernzerhof and G. E. Scuseria. "Assessment of the Perdew–Burke—Ernzerhof exchange-correlation functional." *The Journal of Chemical Physics* 110.11 (1999), pp. 5029–5036. DOI: 10.1063/1.478401.

[110] A. D. Becke. "Density-functional thermochemistry. IV. A new dynamical correlation functional and implications for exact-exchange mixing." *The Journal of Chemical Physics* 104.3 (1996), pp. 1040–1046. DOI: 10.1063/1.470829.

[111] M. A. L. Marques et al. "Density-based mixing parameter for hybrid functionals." *Phys. Rev. B* 83 (2011), p. 035119. DOI: 10.1103/PhysRevB.83.035119.

[112] J. P. Perdew, M. Ernzerhof, and K. Burke. "Rationale for mixing exact exchange with density functional approximations." *J. Chem. Phys.* 105.22 (1996), pp. 9982–9985. DOI: 10.1063/1.472933.

[113] C. Adamo and V. Barone. "Toward reliable density functional methods without adjustable parameters: The PBE0 model." *J. Chem. Phys.* 110.13 (1999), pp. 6158–6170. DOI: 10.1063/1.478522.

[114] Jochen Heyd, Gustavo E. Scuseria, and Matthias Ernzerhof. "Hybrid functionals based on a screened Coulomb potential." *The Journal of Chemical Physics* 118.18 (2003), pp. 8207–8215. DOI: 10.1063/1.1564060.

[115] O. A. Vydrov et al. "Importance of short-range versus long-range Hartree-Fock exchange for the performance of hybrid density functionals." *J. Chem. Phys.* 125.7 (2006), p. 074106. DOI: 10.1063/1.2244560.

[116] L. Hedin. "New Method for Calculating the One-Particle Green's Function with Application to the Electron-Gas Problem." *Phys. Rev.* 139 (1965), A796–A823. DOI: 10.1103/PhysRev.139.A796.

[117] Mark S. Hybertsen and Steven G. Louie. "First-Principles Theory of Quasiparticles: Calculation of Band Gaps in Semiconductors and Insulators." *Phys. Rev. Lett.* 55 (13 1985), pp. 1418–1421. DOI: 10.1103/PhysRevLett.55.1418.

[118] F. Bechstedt. *Many-body approach to electronic excitations: concepts and applications*. 1st ed. Springer Verlag, 2015. DOI: 10.1007/978-3-662-44593-8.

[119] A. van de Walle. "Multicomponent multisublattice alloys, nonconfigurational entropy and other additions to the Alloy Theoretic Automated Toolkit." *CALPHAD: Computer Coupling of Phase Diagrams and Thermochemistry* 33 (2009), pp. 266–278. DOI: 10.1016/j.calphad.2008.12.005.

[120] A. van de Walle and G. Ceder. "Automating First-Principles Phase Diagram Calculations." *Journal of Phase Equilibria* 23 (2002), pp. 348–359. DOI: 10.1361/105497102770331596.

[121] G. D. Garbulsky and G. Ceder. "Linear-programming method for obtaining effective cluster interactions in alloys from total-energy calculations: Application to the fcc Pd-V system." *Physical Review B* 51 (1995), pp. 67–72. DOI: 10.1103/PhysRevB.51.67.

[122] B. Hülsen, M. Scheffler, and P. Kratzer. "Thermodynamics of the Heusler alloy $Co_{2-x}Mn_{1+x}Si$: A combined density functional theory and cluster expansion study." *Phys. Rev. B* 79 (2009), p. 094407. DOI: 10.1103/PhysRevB.79.094407.

[123] D. Lerch et al. "UNCLE: a code for constructing cluster expansion for arbitrary lattices with minimal user-input." *Modelling and Simulation in Materials Science and Engineering* 17 (2009), p. 055003. DOI: 10.1088/0965-0393/17/5/055003.

[124] R. Tibshirani. "Regression Shrinkage and Selection Via the Lasso." *Journal of the Royal Statistical Society: Series B (Methodological)* 58.1 (1996), pp. 267–288. DOI: 10.1111/j.2517-6161.1996.tb02080.x.

[125] T. Hastie, R. Tibshirani, and J. Friedman. *The Elements of Statistical Learning*. 2nd ed. Springer, 2009. DOI: 10.1007/978-0-387-84858-7.

[126] L. J. Nelson et al. "Compressive sensing as a paradigm for building physics models." *Phys. Rev. B* 87 (2013), p. 035125. DOI: 10.1103/PhysRevB.87.035125.

[127] N. Gauraha. "Introduction to the LASSO." *Resonance* 23.4 (2018), pp. 439–464. DOI: 10.1007/s12045-018-0635-x.

[128] M. Stone. "Cross-validation and multinomial prediction." *Biometrika* 61.3 (1974), pp. 509–515. DOI: 10.1093/biomet/61.3.509.

[129] D. M. Allen. "The Relationship Between Variable Selection and Data Agumentation and a Method for Prediction." *Technometrics* 16.1 (1974), pp. 125–127. DOI: 10.1080/00401706.1974.10489157.

[130] K.-C. Li. "Asymptotic Optimality for C_p, C_L, Cross-Validation and Generalized Cross-Validation: Discrete Index Set." *The Annals of Statistics* 15.3 (1987), pp. 958–975. DOI: 10.1214/aos/1176350486.

[131] K. Baumann. "Cross-validation as the objective function for variable-selection techniques." *TrAC Trends in Analytical Chemistry* 22.6 (2003), pp. 395–406. DOI: 10.1016/S0165-9936(03)00607-1.

[132] W. K. Hastings. "Monte Carlo sampling methods using Markov chains and their applications." *Biometrika* 57.1 (1970), pp. 97–109. DOI: 10.2307/2334940.

[133] D. P. Landau and Kurt Binder. "A Guide to Monte Carlo Simulations in Statistical Physics." 4th ed. Cambridge University Press, 2014. Chap. 4. DOI: 10.1017/CBO9781139696463.

[134] B. J. Schulz, K. Binder, and M. Müller. "Flat histogram method of Wang-Landau and N-fold way." *International Journal of Modern Physics C* 13.04 (2002), pp. 477–494. DOI: 10.1142/S0129183102003243.

[135] S. N. Khan and M. Eisenbach. "Density-functional Monte-Carlo simulation of CuZn order-disorder transition." *Phys. Rev. B* 93 (2016), p. 024203. DOI: 10.1103/PhysRevB.93.024203.

[136] K. Takeuchi, R. Tanaka, and K. Yuge. "New Wang-Landau approach to obtain phase diagrams for multicomponent alloys." *Phys. Rev. B* 96 (2017), p. 144202. DOI: 10.1103/PhysRevB.96.144202.

[137] M. Borg et al. "Density of Configurational States from First-Principles Calculations: The Phase Diagram of Al-Na Surface Alloys." *ChemPhysChem* 6.9 (2005), pp. 1923–1928. DOI: 10.1002/cphc.200400612.

[138] M. Troppenz, S. Rigamonti, Jorge Sofo, and C. Draxl, Partial order-disorder transition drives a closing of a band gap; submitted to *Phys. Rev. Lett.*. Available on arXiv: https://arxiv.org/abs/2009.11137.

[139] K. Binder. "Theory of first-order phase transitions." *Reports on Progress in Physics* 50.7 (1987), pp. 783–859. DOI: 10.1088/0034-4885/50/7/001.

[140] K. Binder. "Applications of Monte Carlo methods to statistical physics." *Reports on Progress in Physics* 60.5 (1997), pp. 487–559. DOI: 10.1088/0034-4885/60/5/001.

[141] P. Drude. "Zur Elektronentheorie der Metalle." *Annalen der Physik* 306.3 (1900), pp. 566–613. DOI: 10.1002/andp.19003060312.

[142] P. Drude. "Zur Elektronentheorie der Metalle; II. Teil. Galvanomagnetische und thermomagnetische Effecte." *Annalen der Physik* 308.11 (1900), pp. 369–402. DOI: 10.1002/andp.19003081102.

[143] J. C. Maxwell. "IV. On the dynamical theory of gases." *Philosophical Transactions of the Royal Society of London* 157 (1867), pp. 49–88. DOI: 10.1098/rstl.1867.0004.

[144] M. N. Kogan. "The Equations of the Kinetic Theory of Gases." *Rarefied Gas Dynamics*. Boston, MA: Springer US, 1969, pp. 29–104. DOI: 10.1007/978-1-4899-6381-9_2.

[145] H. Pauly. "Fundamentals of Kinetic Gas Theory." *Atom, Molecule, and Cluster Beams I: Basic Theory, Production and Detection of Thermal Energy Beams*. Berlin, Heidelberg: Springer Berlin Heidelberg, 2000, pp. 35–76. DOI: 10.1007/978-3-662-04213-7_2.

[146] N. W. Ashcroft and N. D. Mermin. *Solid State Physics*. New York [u.a.], 1976. ISBN: 0-03-083993-9.

[147] N. Singh. *Electronic Transport Theories: From Weakly to Strongly Correlated Materials*. 1st ed. CRC Press, 2016. DOI: 10.1201/9781315368962.

[148] C. Kittel. *Introduction to Solid State Physics*. John Wiley & Sons, Limited, 2004. ISBN: 978-1-119-45416-8.

[149] A . H. Wilson and Ralph Howard Fowler. "The theory of metals." *Proceedings of the Royal Society of London. Series A, Containing Papers of a Mathematical and Physical Character* 138.836 (1932), pp. 594–606. DOI: 10.1098/rspa.1932.0205.

[150] A. Sommerfeld and H. Bethe. "Elektronentheorie der Metalle." *Aufbau Der Zusammenhängenden Materie*. Berlin, Heidelberg: Springer Berlin Heidelberg, 1933, pp. 333–622. DOI: 10.1007/978-3-642-91116-3_3.

[151] G. D. Mahan. "Condensed Matter in a Nutshell." Princeton University Press, UK, 2011. Chap. 11. DOI: 10.2307/j.ctvcm4htt.

[152] G. Giuliani, G. Vignale, and Cambridge University Press. *Quantum Theory of the Electron Liquid*. Masters Series in Physics and Astronomy. Cambridge University Press, 2005. DOI: 10.1017/CBO9780511619915.

[153] J. Liouville. "Note sur la Théorie de la Variation des constantes arbitraires." *Journ. de Math.* 3 (1838), pp. 342–349.

[154] J. W. Gibbs. "On the Fundamental Formula of Statistical Mechanics, with Applications to Astronomy and Thermodynamics." *The Scientific papers*. Vol. 33. 1884, pp. 57–58.

[155] G. D. Mahan and J. O. Sofo. "The best thermoelectric." *Proceedings of the National Academy of Sciences* 93.15 (1996), pp. 7436–7439. DOI: 10.1073/pnas.93.15.7436.

[156] E. A. Stern. "Rigid-Band Model of Alloys." *Physical Review* 157 (1967), pp. 544–551. DOI: 10.1103/PhysRev.157.544.

[157] H. J. Goldsmid and J. W. Sharp. "Estimation of the thermal band gap of a semiconductor from seebeck measurements." *Journal of Electronic Materials* 28.7 (1999), pp. 869–872. DOI: 10.1007/s11664-999-0211-y.

[158] L. Onsager. "Reciprocal Relations in Irreversible Processes. I." *Phys. Rev.* 37 (1931), pp. 405–426. DOI: 10.1103/PhysRev.37.405.

[159] B. Holst, M. French, and R. Redmer. "Electronic transport coefficients from ab initio simulations and application to dense liquid hydrogen." *Phys. Rev. B* 83 (2011), p. 235120. DOI: 10.1103/PhysRevB.83.235120.

[160] S. R. de Groot and P. Mazur. "Non-equilibrium thermodynamics." Dover, New York, 1984. Chap. 3, pp. 20–29.

[161] D. A. Greenwood. "The Boltzmann Equation in the Theory of Electrical Conduction in Metals." *Proceedings of the Physical Society* 71.4 (1958), pp. 585–596. DOI: 10.1088/0370-1328/71/4/306.

[162] A. Arabi-Hashemi and S. G. Mayr. "Exploring electrical conductivity anomalies across the martensite transition in Fe_7Pd_3 ferromagnetic shape memory alloys: Experiments and ab-initio calculations." *Appl. Phys. Lett.* 106.9 (2015), p. 091906. DOI: 10.1063/1.4914004.

[163] O. Pfaffenzeller and D. Hohl. "Structure and electrical conductivity in fluid high-density hydrogen." *J. Phys. Condens. Matter* 9.50 (1997), pp. 11023–11034. DOI: 10.1088/0953-8984/9/50/008.

[164] P. L. Silvestrelli. "No evidence of a metal-insulator transition in dense hot aluminum: A first-principles study." *Phys. Rev. B* 60 (1999), pp. 16382–16388. DOI: 10.1103/PhysRevB.60.16382.

[165] F. V. Kyrychenko and C. A. Ullrich. "Temperature-dependent resistivity of ferromagnetic $Ga_{1-x}Mn_xAs$: Interplay between impurity scattering and many-body effects." *Phys. Rev. B* 80 (2009), p. 205202. DOI: 10.1103/PhysRevB.80.205202.

[166] M. French, T. R. Mattsson, and R. Redmer. "Diffusion and electrical conductivity in water at ultrahigh pressures." *Phys. Rev. B* 82 (2010), p. 174108. DOI: 10.1103/PhysRevB.82.174108.

[167] M. Pozzo, M. P. Desjarlais, and D. Alfè. "Electrical and thermal conductivity of liquid sodium from first-principles calculations." *Phys. Rev. B* 84 (2011), p. 054203. DOI: 10.1103/PhysRevB.84.054203.

[168] M. French and T. R. Mattsson. "Thermoelectric transport properties of molybdenum from *ab initio* simulations." *Phys. Rev. B* 90 (2014), p. 165113. DOI: 10.1103/PhysRevB.90.165113.

[169] A. Gold and W. Götze. "The mobility and dynamical conductivity of Na-doped Si-(100) MOS systems." *Solid-State Electronics* 28.1 (1985), pp. 87–91. DOI: 10.1016/0038-1101(85)90214-X.

[170] A. Gold et al. "The dynamical conductivity of a Na^+-doped interfacial charge layer on silicon." *Solid State Communications* 49.11 (1984), pp. 1085–1088. DOI: 10.1016/0038-1098(84)90429-0.

[171] A Gold and W Götze. "The metal insulator transition in two-dimensional systems with charged impurities." *Solid State Communications* 47.8 (1983), pp. 627–629. DOI: 10.1016/0038-1098(83)90765-2.

[172] A. Gold and W. Götze. "Localization and screening anomalies in two-dimensional systems." *Phys. Rev. B* 33.4 (1986), pp. 2495–2511. DOI: 10.1103/PhysRevB.33.2495.

[173] D. Belitz and S. Das Sarma. "Plasmon linewidth in metals and semiconductors: A memory-function approach." *Phys. Rev. B* 34.12 (1986), pp. 8264–8269. DOI: 10.1103/PhysRevB.34.8264.

[174] D. Belitz and W. Götze. "The temperature dependence of the d.c. conductivity near the Anderson transition in three-dimensional systems." *Philosophical Magazine B* 43.3 (1981), pp. 517–526. DOI: 10.1080/01418638108222113.

[175] S. Nakajima. "On Quantum Theory of Transport Phenomena: Steady Diffusion." *Progress of Theoretical Physics* 20.6 (1958), pp. 948–959. DOI: 10.1143/PTP.20.948.

[176] R. Zwanzig. "Ensemble Method in the Theory of Irreversibility." *J. Chem. Phys.* 33.5 (1960), pp. 1338–1341. DOI: 10.1063/1.1731409.

[177] W. Götze. "A theory for the conductivity of a fermion gas moving in a strong three-dimensional random potential." *Journal of Physics C: Solid State Physics* 12.7 (1979), pp. 1279–1296. DOI: 10.1088/0022-3719/12/7/018.

[178] K. Biswas et al. "High-performance bulk thermoelectrics with all-scale hierarchical architectures." *Nature* 489.7416 (2012), pp. 414–418. DOI: 10.1038/nature11439.

[179] H. J. Wu et al. "Broad temperature plateau for thermoelectric figure of merit ZT>2 in phase-separated $PbTe_{0.7}S_{0.3}$." *Nature Communications* 5.1 (2014), p. 4515. DOI: 10.1038/ncomms5515.

[180] Patrick Dieu. "Brillouin-Zone-Integration mit adaptiven Gittern." Bachelor Thesis. Humboldt-Universtät zu Berlin, 2019.

[181] M. Troppenz et al. Website. Tutorial about how to calculate the Boltzmann transport coefficients using the relaxation time approximation is online at http://exciting.wikidot.com/oxygen-boltzmann-equation.

[182] T. J. Scheidemantel et al. "Transport coefficients from first-principles calculations." *Phys. Rev. B* 68 (2003), p. 125210. DOI: 10.1103/PhysRevB.68.125210.

[183] G. K. H. Madsen and D. J. Singh. "BoltzTraP. A code for calculating band-structure dependent quantities." *Computer Physics Communications* 175.1 (2006), pp. 67 –71. DOI: 10.1016/j.cpc.2006.03.007.

[184] S. Nakajima. "The crystal structure of $Bi_2Te_{3-x}Se_x$." *Journal of Physics and Chemistry of Solids* 24.3 (1963), pp. 479 –485. DOI: 10.1016/0022-3697(63)90207-5.

[185] "The optical properties of p-type Bi_2Te_3[ ]Sb_2Te_3 alloys between 2-15 microns." *Journal of Physics and Chemistry of Solids* 23.9 (1962), pp. 1219 –1224. DOI: 10.1016/0022-3697(62)90169-5.

[186] H. J. Goldsmid. "The Thermal Conductivity of Bismuth Telluride." *Proceedings of the Physical Society. Section B* 69.2 (1956), pp. 203–209. DOI: 10.1088/0370-1301/69/2/310.

[187] D. Bansal et al. "Phonon anharmonicity and negative thermal expansion in SnSe." *Phys. Rev. B* 94 (2016), p. 054307. DOI: 10.1103/PhysRevB.94.054307.

[188] F. Giustino. "Electron-phonon interactions from first principles." *Rev. Mod. Phys.* 89 (2017), p. 015003. DOI: 10.1103/RevModPhys.89.015003.

[189] F. Caruso et al. "Thermally enhanced Fröhlich coupling in SnSe." *Phys. Rev. B* 99 (2019), 081104(R). DOI: 10.1103/PhysRevB.99.081104.

[190] F. Caruso and F. Giustino. "Theory of electron-plasmon coupling in semiconductors." *Phys. Rev. B* 94 (2016), p. 115208. DOI: 10.1103/PhysRevB.94.115208.

[191] D. Connétable. "First-principles calculations of carbon clathrates: Comparison to silicon and germanium clathrates." *Phys. Rev. B* 82 (2010), p. 075209. DOI: 10.1103/PhysRevB.82.075209.

[192] B. Eisenmann, H. Schäfer, and R. Zagler. "Die Verbindungen $A_8^{II}B_{16}^{III}B_{30}^{IV}$ ($A^{II} \equiv$ Sr, Ba; $B^{III} \equiv$ Al, Ga; $B^{IV} \equiv$ Si, Ge, Sn) und ihre käfigstrukturen." *Journal of the Less Common Metals* 118.1 (1986), pp. 43–55. DOI: 10.1016/0022-5088(86)90609-0.

[193] S.-J. Kim et al. "Structure and Thermoelectric Properties of Ba_6Ge_{25-x}, $Ba_6Ge_{23}Sn_2$, and $Ba_6Ge_{22}In_3$: Zintl Phases with a Chiral Clathrate Structure." *Journal of Solid State Chemistry* 153.2 (2000), pp. 321–329. DOI: https://doi.org/10.1006/jssc.2000.8777.

[194] A.V. Shevelkov and K. Kovnir. "Zintl Clathrates." *Zintl phases: Prinicples and Recent Developments*. Ed. by T. F. Fässler. Vol. 139. Springer Verlag, 2011, pp. 97–142. DOI: 10.1007/978-3-642-21150-8.

[195] R. Nesper. "The Zintl-Klemm Concept - A Historical Survey." *Zeitschrift für anorganische und allgemeine Chemie* 640.14 (2014), pp. 2639–2648. DOI: 10.1002/zaac.201400403.

[196] X. Shi et al. "On the Design of High-Efficiency Thermoelectric Clathrates through a Systematic Cross-Substitution of Framework Elements." *Advanced Functional Materials* 20 (2010), pp. 755–763. DOI: 10.1002/adfm.200901817.

[197] CELL documentation: https://sol.physik.hu-berlin.de/cell.

[198] S. Rigamonti *et al.*, CELL: a python package for cluster expansion with a focus on complex alloys, in preparation.

[199] A. H. Larsen et al. "The atomic simulation environment—a Python library for working with atoms." *J. Phys. Condens. Matt.* 29.27 (2017), p. 273002. DOI: 10.1088/1361-648x/aa680e.

[200] F. R. Lucci et al. "Atomic Scale Surface Structure of Pt/Cu(111) Surface Alloys." *The Journal of Physical Chemistry C* 118.6 (2014), pp. 3015–3022. DOI: 10.1021/jp405254z.

[201] M. S. S. Challa, D. P. Landau, and K. Binder. "Finite-size effects at temperature-driven first-order transitions." *Phys. Rev. B* 34 (1986), pp. 1841–1852. DOI: 10.1103/PhysRevB.34.1841.

[202] B. Efron. "Bootstrap Methods: Another Look at the Jackknife." *Annals of Statistics* 7.1 (1979), pp. 1–26. DOI: 10.1214/aos/1176344552.

[203] T. Hastie, R. Tibshirani, and J. Friedman. "The Elements of Statistical Learning." 2nd ed. Springer-Verlag, 2009. Chap. 7.11. DOI: 10.1007/978-0-387-84858-7.

[204] I. A. Abrikosov et al. "Locally self-consistent Green's function approach to the electronic structure problem." *Phys. Rev. B* 56 (1997), pp. 9319–9334. DOI: 10.1103/PhysRevB.56.9319.

[205] V. Blum et al. "Ab initio molecular simulations with numeric atom-centered orbitals." *Computer Physics Communications* 180.11 (2009), pp. 2175–2196. DOI: 10.1016/j.cpc.2009.06.022.

[206] J. Heyd, G. E. Scuseria, and M. Ernzerhof. "Hybrid functionals based on a screened Coulomb potential." *J. Chem. Phys.* 118.18 (2003), pp. 8207–8215. DOI: 10.1063/1.1564060.

[207] A. V. Krukau et al. "Influence of the exchange screening parameter on the performance of screened hybrid functionals." *J. Chem. Phys.* 125.22 (2006), p. 224106. DOI: 10.1063/1.2404663.

[208] J. Kim, A. Gulans, and C. Draxl. "Robust mixing in self-consistent linearized augmented planewave calculations." *Electronic Structure* 2.3 (2020), p. 037001. DOI: 10.1088/2516-1075/ababde.

[209] T. Uemura et al. "Electronic structure and thermoelectric properties of clathrate compounds $Ba_8Al_xGe_{46-x}$." *J. Appl. Phys.* 104.1 (2008), p. 013702. DOI: 10.1063/1.2947593.

[210] K. Koga et al. "Electronic Structure and Thermoelectric Properties of Si-Based Clathrate Compounds." *Journal of Electronic Materials* 38.7 (2009), pp. 1427–1432. DOI: 10.1007/s11664-009-0730-6.

[211] W. Ku, T. Berlijn, and C.-C. Lee. "Unfolding First-Principles Band Structures." *Phys. Rev. Lett.* 104 (2010), p. 216401. DOI: 10.1103/PhysRevLett.104.216401.

[212] Y. W. Tsang and M. L. Cohen. "Calculation of the Temperature Dependence of the Energy Gaps in PbTe and SnTe." *Phys. Rev. B* 3 (1971), pp. 1254–1261. DOI: 10.1103/PhysRevB.3.1254.

[213] C. Rincón, S. M. Wasim, and G. Marín. "Effect of thermal expansion coefficient on the temperature dependence of the band gap in CuInTe 2." *Materials Letters* 36 (Aug. 1998), pp. 245–248. DOI: 10.1016/S0167-577X(98)00041-X.

[214] M. Falmbigl et al. "Thermal expansion of thermoelectric type-I-clathrates." *Journal of Applied Physics* 108.4 (2010), p. 043529. DOI: 10.1063/1.3465637.

[215] W. L. Bragg and E. K. Williams. "The effect of thermal agitation on atomic arrangement in alloys." *Proc. Roy. Soc. A* 145.699-730 (1934). DOI: 10.1098/rspa.1934.0132.

[216] H. A. Bethe and H.H. Wills. "Statistical theory of superlattices." *Proc. Roy. Soc. A* 150.552-575 (1935). DOI: 10.1098/rspa.1935.0122.

[217] Y. Imry. "Finite-size rounding of a first-order phase transition." *Phys. Rev. B* 21 (1980), pp. 2042–2043. DOI: 10.1103/PhysRevB.21.2042.

[218] V. Privman and M. E. Fisher. "Finite-size effects at first-order transitions." *Journal of Statistical Physics* 33.2 (1983), pp. 385–417. DOI: 10.1007/BF01009803.

[219] K. Binder and D. P. Landau. "Finite-size scaling at first-order phase transitions." *Phys. Rev. B* 30 (1984), pp. 1477–1485. DOI: 10.1103/PhysRevB.30.1477.

[220] V. Privman and M. E. Fisher. "Finite-size rounding of first-order transitions." *Journal of Applied Physics* 57.8 (1985), pp. 3327–3328. DOI: 10.1063/1.335084.

[221] M. E. Fisher and A. N. Berker. "Scaling for first-order phase transitions in thermodynamic and finite systems." *Phys. Rev. B* 26 (1982), pp. 2507–2513. DOI: 10.1103/PhysRevB.26.2507.

[222] M. E. J. Newman and G. T. Barkema. *Monte Carlo Methods in Statistical Physics*. Clarendon Press, 1999. ISBN: 0198517971.

[223] S. Schnabel et al. "Microcanonical entropy inflection points: Key to systematic understanding of transitions in finite systems." *Phys. Rev. E* 84 (2011), p. 011127. DOI: 10.1103/PhysRevE.84.011127.

[224] R. T. Sanderson. "Electronegativity and bond energy." *Journal of the American Chemical Society* 105.8 (1983), pp. 2259–2261. DOI: 10.1021/ja00346a026.

[225] M. Baitinger, B. Böhme and Yu. Grin, private communication: Single-phase clathrate samples for x=8-15 were prepared at 900°C and the crystal structure of the clathrate phase was refined from synchrotron X-ray powder diffraction data.

[226] N. Tsujii et al. "Phase stability and chemical composition dependence of the thermoelectric properties of the type-I clathrate $Ba_8Al_xSi_{46-x}$ ($8 \leq x \leq 15$)." *Journal of Solid State Chemistry* 184.5 (2011), pp. 1293–1303. DOI: 10.1016/j.jssc.2011.03.038.

[227] A. Bhattacharya et al. "Formation of Vacancies in Si- and Ge-based Clathrates: Role of Electron Localization and Symmetry Breaking." *Phys. Rev. Lett.* 118 (2017), p. 236401. DOI: 10.1103/PhysRevLett.118.236401.

[228] P. Lautenschlager, P. B. Allen, and M. Cardona. "Temperature dependence of band gaps in Si and Ge." *Phys. Rev. B* 31 (1985), pp. 2163–2171. DOI: 10.1103/PhysRevB.31.2163.

[229] C. A. Ullrich and G. Vignale. "Time-dependent current-density-functional theory for the linear response of weakly disordered systems." *Phys. Rev. B* 65.24 (2002), p. 245102. DOI: 10.1103/PhysRevB.65.245102.

[230] Notes from Prof. Jorge Sofo with the title:"Memory function for periodic systems".

[231] J. P. Perdew and Y. Wang. "Accurate and simple analytic representation of the electron-gas correlation energy." *Phys. Rev. B* 45 (1992), pp. 13244–13249. DOI: 10.1103/PhysRevB.45.13244.

[232] Experimental lattice parameter taken from https://periodictable.com/Elements/011/data.html.

[233] D. N. Zubarev. "Double-Time Green Function in Statistical Physics." *Soviet Physics Uspekhi* 3.3 (1960), pp. 320–345. DOI: 10.1070/pu1960v003n03abeh003275.

PUBLICATION LIST

"Predicting Ground-State Configurations and Electronic Properties of the Thermoelectric Clathrates $Ba_8Al_xSi_{46-x}$ and $Sr_8Al_xSi_{46-x}$", M. Troppenz, S. Rigamonti, and C. Draxl, *Chem. Mater.* **29**, 2414 (2017). DOI: doi.org/10.1021/acs.chemmater.6b05027.

"Thermally enhanced Fröhlich coupling in SnSe", F. Caruso, M. Troppenz, S. Rigamonti, and C. Draxl, *Phys. Rev. B* **99**, 081104(R). DOI: doi.org/10.1103/physrevb.99.081104.

"First-principles study of Pd-alloyed Cu(111) surface in hydrogen atmosphere at realistic temperature", Z.-K. Han, D. Sarker, M. Troppenz, S. Rigamonti, C. Draxl, W. A. Saidi, and S. V. Levchenko, *J. Appl. Phys.* **128**, 145302 (2020). DOI: doi.org/10.1063/5.0020625.

"Partial Order-Disorder Transition Driving Closure of Band Gap: Example of Thermoelectric Clathrates", M. Troppenz, S. Rigamonti, J. O. Sofo, and C. Draxl (2020); submitted to *Phys. Rev. Lett.*. Available on arXiv: arxiv.org/abs/2009.11137.